XENON100 Dark Matter Search: Scintillation Response of Liquid Xenon to Electronic Recoils

Kyungeun Elizabeth Lim

Submitted in partial fulfillment of the
requirements for the degree
of Doctor of Philosophy
in the Graduate School of Arts and Sciences

COLUMBIA UNIVERSITY

2013

ABSTRACT

XENON100 Dark Matter Search: Scintillation Response of Liquid Xenon to Electronic Recoils

Kyungeun Elizabeth Lim

Dark matter is one of the missing pieces necessary to complete the puzzle of the universe. Numerous astrophysical observations at all scales suggest that 23 % of the universe is made of nonluminous, cold, collisionless, nonbaryonic, yet undiscovered dark matter. Weakly Interacting Massive Particles (WIMPs) are the most well-motivated dark matter candidates and significant efforts have been made to search for WIMPs.

The XENON100 dark matter experiment is currently the most sensitive experiment in the global race for the first direct detection of WIMP dark matter. XENON100 is a dual-phase (liquid-gas) time projection chamber containing a total of 161 kg of liquid xenon (LXe) with a 62 kg WIMP target mass. It has been built with radiopure materials to achieve an ultra-low electromagnetic background and operated at the Laboratori Nazionali del Gran Sasso in Italy. WIMPs are expected to scatter off xenon nuclei in the target volume. Simultaneous measurement of ionization and scintillation produced by nuclear recoils allows for the detection of WIMPs in XENON100. Data from the XENON100 experiment have resulted in the most stringent limits on the spin-independent elastic WIMP-nucleon scattering cross sections for most of the significant WIMP masses.

As the experimental precision increases, a better understanding of the scintillation and ionization response of LXe to low energy ($< 10\,\mathrm{keV}$) particles is crucial for the interpretation of data from LXe based WIMP searches. A setup has been built and operated at Columbia University to measure the scintillation response of LXe to both electronic and nuclear recoils down to energies of a few keV, in particular for the XENON100 experiment.

In this thesis, I present the research carried out in the context of the XENON100 dark matter search experiment. For the theoretical foundation of the XENON100 experiment,

the first two chapters are dedicated to the motivation for and detection medium choice of the XENON100 experiment, respectively. A general review about dark matter focusing on WIMPs and their direct detection with liquid noble gas detectors is presented in Chap. 1. LXe as an attractive WIMP detection medium is explained in Chap. 2. The XENON100 detector design, the detector, and its subsystems are detailed in Chap. 3. The calibration of the detector and the characterized detector response used for the discrimination of a WIMP-like signal against background are explained in Chap. 4. In an effort to understand the background, anomalous electronic recoils were studied extensively and are described in Chap. 5. In order to obtain a better understanding of the electronic recoil background of XENON100, including an estimation of the electronic recoil background contribution, as well as to interpret dark matter results such as annual modulation, measurement of the scintillation yield of low-energy electrons in LXe was performed in 2011, with the dedicated setup mentioned above. The results from this measurement are discussed in Chap. 6. Finally, the results for the latest science data from XENON100 to search for WIMPs, comprising 225 live-days taken over 13 months during 2011 and 2012 are explained in Chap. 7.

Table of Contents

List of Figures

List of Tables

Acknowledgments

I would like to thank first my advisor, Elena Aprile. Her enthusiasm for the XENON experiments and relevant projects, her persistence to attain her goals, her direct approaches to solving problems, along with her expectations and support have provided an almost perfect learning environment, which eventually guided me to become an experimental physicist.

I also thank Karl Giboni who made me want to be a detector designer someday with his creative ideas.

I was able to learn numerous things that I did not learn in class from the postdoctoral researchers I have met as part of the XENON Columbia group, Masaki Yamashita, Maria Elena Monzani, Roberto Santorelli, Kaixuan Ni, Antonio Jesus Melgarejo Fernandez, Rafael Lang, Ranny Budnik, Alfio Rizzo, Marcello Messina, and Guillaume Plante. Many of you have been great teachers and I am indebted to you for offering me the exact thing I needed at each stage of learning. My fellow graduate students in the group, Bin Choi, Luke Goetzke, and Hugo Contreras, helped me, too, to think harder through discussions. All of you in our group, including Junji Naganoma, made my time not only valuable but also enjoyable. Thank you.

Having an experiment in Italy and working with people from other institutes in different countries was an interesting and great experience. The success of the XENON100 experiment was only possible with passionate, hardworking, and dedicated scientists in various groups, without whom I would not be able to write this thesis. I thank all my colleagues in the XENON100 collaboration. It was such a pleasure to work closely with some of you during the commissioning phase of XENON100. Alfredo Davide Ferella, Marc Schumann, Yuan Mei, Peter Shagin, Eirini Tziaferi, Alexander Kish, Ali Askin, Ethan Brown, Emilija Pantic, and Antonio Ribeiro, all of you gave me unforgettable memories of late 2007 to early 2009. Francesco Arneodo has been a great help at every stay in Italy. I thank

Uwe Oberlack, Laura Baudis, and Teresa Marrodán Undagoitia for the valuable discussions about the analysis. I also thank some of the second generation of graduate students in the collaboration, Marc Weber, Sebastian Lindemann, and Kevin Lung for the discussions on various topics.

I would like to express my gratitude to Rino Persiani, Paolo Beltrame, and Hango Wang for their help on the measurement of the scintillation yield of low-energy electrons. My gratitude also goes to Masaki Yamashita and Aaron Manalaysay for their comments on the manuscript of the measurement.

Antonio Jesus Melgarejo Fernandez, Marc Schumann, Lucca Scotto Lavina, Marco Selvi, Kevin Lung, and Marc Weber kindly provided some of the figures in this thesis. Luke Goetzke, Antonio Jesus Melgarejo Fernandez, Aaron Veicht, and Andrew Brown read the manuscript and gave valuable feedback. Tae Hyun Yoon, André Loose, and Nelson Rivera supported me during the time of writing. I am thankful, too, to many of my friends in the same program at Columbia who shared the same passion and who could understand what obtaining a Ph.D. requires at $6\,\sigma$ C.L.. I also thank the thesis committee members, Szabolcs Márka, Lam Hui, Neil Weiner, and Flavio Cavanna, for their interest and feedback on my thesis.

I am grateful to Insik Hahn, and Yeongduk Kim, who discovered my potential to be a physicist and encouraged me to pursue a Ph.D. with a constant trust in me. You have changed the path of my life.

To my friends, relatives, and family, who have never tired of cheering me up and have been supportive of my decision throughout this time, pursuing a Ph.D. has been a rewarding but challenging endeavor and I might have been lost somewhere in the middle a while ago without you. I deeply appreciate you all. This thesis is dedicated to my parents, whose absolute belief and love helped me to be here today, and to my brother Chaewoo, who has been always my greatest backup.

Chapter 1

Dark Matter

Both observational and theoretical developments in cosmology over the last few decades point to the existence of dark components in the universe which are not yet well understood, along with the need to understand the evolution of perturbations around the zero order smooth universe and the hypothesized generator of these perturbations, inflation. One of the dark components is dark matter, which interacts with the normal matter only through gravity and possibly the weak force. The other dark component is dark energy, which is in a smooth, unclustered form that permeates all of space and tends to accelerate the expansion of the universe.

The mass-energy density in the universe can be determined from a combination of measurements of cosmic expansion and the cosmic microwave background, as shown in Fig. 1.1. In a universe composed of nonrelativistic matter and a cosmological constant (ΛCDM), the Friedmann equation, which comes from the energy conservation, is written as

$$H^2 \equiv \left(\frac{\dot{a}}{a}\right)^2 = \frac{8\pi G}{3}\rho_{\mathrm{tot}} - \frac{k}{a^2} \tag{1.1}$$

where $H = \dot{a}(t)/a(t)$ is the Hubble parameter, $a(t)$ is the scale factor, which relates the redshift to the size of universe, G is the gravitational constant, ρ_{tot} is the total average energy density of the universe, and k is the constant which describes the spatial curvature of the universe. The function $a(t)$ describes the evolution of the universe, which is completely determined by Einstein's field equation. In fact, Eq. 1.1 is a special case of Einstein's equation for a homogeneous and isotropic spacetime. The Hubble parameter explains how

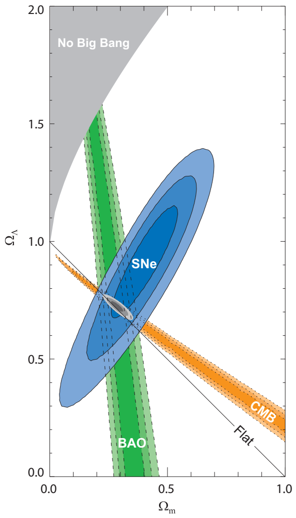

Figure 1.1: Constraints on matter density (Ω_m, x-axis) and the cosmological constant (Ω_Λ, y-axis) with 68.3 %, 95.4 %, 99.7 % contours obtained from supernovae, the cosmic microwave background [Dunkley *et al.*, 2009], and baryon acoustic oscillations [Eisenstein *et al.*, 2005]. Figure from [Kowalski *et al.*, 2008].

fast the universe is expanding (or contracting). Its present value H_0, the so-called "Hubble constant" is $73.8 \pm 2.4\,\mathrm{kms}^{-1}\mathrm{Mpc}^{-1}$ [Riess *et al.*, 2011]. If $k = 0$, the mass-energy density ρ_{tot} must be $3H^2/8\pi G$. Similarly, when $k = +1(-1)$, then ρ_{tot} must be greater than (less than) $3H^2/8\pi G$. Thus, if we measure the current density ρ_0 and the Hubble constant H_0 with sufficient precision, we can deduce the sign k of the curvature. By defining a density parameter Ω, the dimensionless ratio of the actual density ρ_{tot} to the critical density $\rho_c = 3H^2/8\pi G$, Eq. 1.1 is written as

$$\Omega - 1 = \frac{k}{a^2H^2} \tag{1.2}$$

It is clear that for $k = 0$, i.e. for the flat universe, ρ_{tot} should be the same as ρ_c, this is how the critical density picked up its name. By dividing the mass-energy budget into matter and vacuum energy, the density parameter is written as

$$\Omega = \frac{\rho_{\mathrm{tot}}}{\rho_c} = \frac{\rho_m + \rho_\Lambda}{\rho_c} = \Omega_m + \Omega_\Lambda \tag{1.3}$$

where ρ_m and ρ_Λ are the energy densities today of matter and the cosmological constant, and Ω_m and Ω_Λ are their values relative to the critical density ρ_c.

From cosmic microwave background measurements, which provide the curvature of universe by measuring the first peak of the power spectrum, the universe was measured to be flat, i.e., $\Omega \sim 1$. Combined with the measurements of red shift as a function of distance by use of the standard candle (e.g. type IA supernovae [Kowalski *et al.*, 2008]) or a standard ruler (e.g. baryon acoustic oscillations [Eisenstein *et al.*, 2005]), the mass-energy budget partitioning is given such that $\Omega_\Lambda \sim 0.73$ and $\Omega_m \sim 0.27$. With measurements of the primordial deuterium abundance along with a better understanding of how the light elements formed (i.e., big bang nucleosynthesis), Ω_m further breaks down into the baryon density, $\Omega_b \sim 0.04$, and the nonbaryon density, $\Omega_\chi \sim 0.23$. This tells us that our current knowledge is limited to only 4 % of the universe, and naturally compels us ask the fundamental question: “what is the nature of the dark components in our universe?” which is simply an updated version of why we are here and how we got here. In this thesis, I will focus on the dark matter, which seems to constitute 23 % of the universe.

In Sec. 1.1, we review several examples of observational evidence for the existence of dark matter in the whole scale of the universe, and what they suggest about the nature of dark matter. Some of theoretically plausible dark matter candidates are introduced in Sec. 1.2. Specific detection strategies of the most appealing dark matter candidates are explained in detail with the expected signal and detection medium choices, especially with liquid noble gas experiments, in Sec. 1.3.

1.1 Observational Evidence of Dark Matter

There exist substantial evidences of dark matter at all scales from many independent observations. In this section, we go through the observational evidences for the existence of dark matter at different spatial scales.

1.1.1 Galactic Scales: Galactic Rotation Curve

The galactic rotation curves of spiral galaxies are the earliest, and probably the most straightforward evidence of dark matter [Sofue and Rubin, 2001]. The rotation curve is measured using the 21 cm line of neutral hydrogen taking into account the Doppler shift [Begeman *et al.*, 1991]. Clouds of neutral hydrogen extend far beyond the galactic disk and thus allow the measurement of the orbital velocity much further out than the stars.

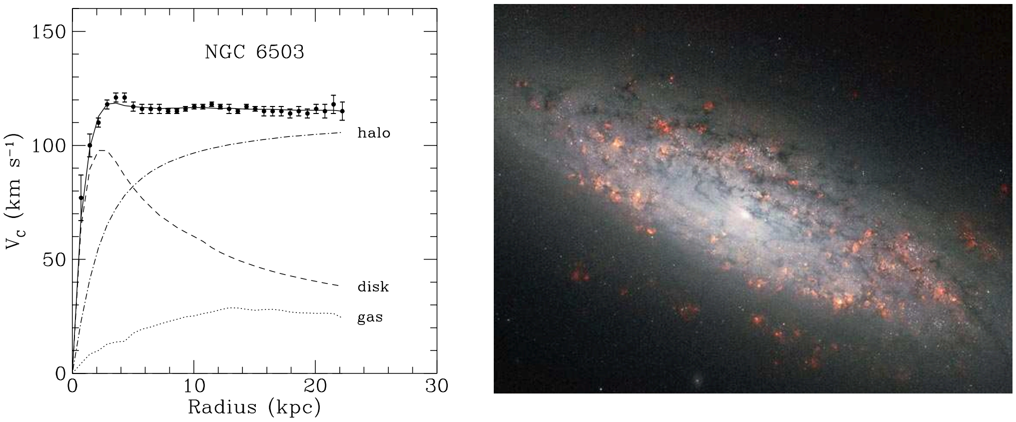

Figure 1.2: Measured rotation curve of NGC 6503 (left). The dotted, dashed and dash-dotted lines are the contributions of gas, disk and dark halo (dark matter), respectively. Figure (left) from [Begeman *et al.*, 1991]. Picture of NGC 6503 spiral galaxy (right). Pink-coloured puffs marking where stars have recently formed in NGC 6503's swirling spiral arms. Image credit (right): ESA/Hubble and NASA.

Fig. 1.2 (left) shows the rotational velocities of the stars and gas in NGC 6503 spiral galaxy as a function of their distances from the galactic center. In Newtonian Mechanics, rotational velocity v of an object with radius r around a galaxy is given by $v(r) = \sqrt{GM(r)/r}$, where $M(r)$ is the mass inside the orbit and G is the gravitational constant. If r lies outside the visible part of the galaxy and mass is given by this visible part, one would expect $v(r) \propto 1/\sqrt{r}$. However, the measured constant velocity distribution to the largest values of r where the rotation curve can be measured conflicts to the expectation from the contributions of only visible mass components such as luminous stars (disk) and interstellar gas (gas). By assuming an additional invisible mass component (dark halo), which follows $M(r) \propto r$, i.e. the mass density $\rho(r) \propto 1/r^2$, with the constraint that at some point $\rho(r)$ has to fall off faster (in order to keep the total mass of the galaxy finite), the data can be explained well.

Since this calculation is based on the Newtonian Mechanics, we are aware that the Modified Newtonian Dynamics (MOND) [Bekenstein, 2004] hypothesis can also explain the galactic rotation curves. Nevertheless, MOND faces several challenges [Dodelson, 2011] while the hypothesized existence of dark matter can account for various independent observations at different scales.

1.1.2 Extra-Galactic Scales: Galaxy Clusters

In 1933, during the examination of the great Coma galaxy clusters, Fritz Zwicky realized the mass of the cluster based on the speed of its galaxies was about ten times more than the mass of the visible component (luminous stars) of the cluster. He concluded that the cluster must contain an enormous quantity of unseen matter, with enough gravity to keep the rapidly moving galaxies from flying apart. Zwicky in effect discovered that most of the mass in the universe is invisible, and referred it as Dunkle Materie, which means “dark matter” [Zwicky, 1933].

In 1937, Zwicky came up with another idea of investigating dark matter. He posited that galaxy clusters could act as gravitational lenses due to the previously discovered gravitational lensing, which was first discussed by Orest Chwolson [Chwolson, 1924] but more commonly associated with Einstein because of his efforts on the quantitative studies [Einstein, 1936]. Gravitational lensing refers to the effect that a distribution of matter (such as a galaxy cluster or a black hole) between a distant source (a background galaxy) and an observer bends the spacetime around it. As a result, a magnified or distorted image of the source can be observed as light rays from the source propagate through the curved spacetime.

There exist three classes of gravitational lensing depending on the lensing strength : Strong lensing, weak lensing, and microlensing [Melia, 2007]. Strong lensing is responsible for the clearly visible distortions such as the formation of Einstein rings, giant arcs, and multiple images. Most lines of sight in the universe are thoroughly in the weak lensing regime, in which the deflection is impossible to be detected with a single background source but can be detected by analyzing a large numbers of sources. Microlensing is where no distortion in shape can be seen but the amount of light received from a background object changes in time. Among them, weak lensing can be used to reconstruct the background distribution of dark matter. By measuring the shapes and orientations of large numbers of distant galaxy clusters, which are among the largest gravitationally bound structures in the universe, with 80 % of the cluster content in the form of dark matter [Diaferio *et al.*, 2008], their orientations can be averaged to measure the shear of the lensing field in any region. The lensing shows up statistically as a preferred stretching of the background objects perpendicular to the direction to the center of the lens.

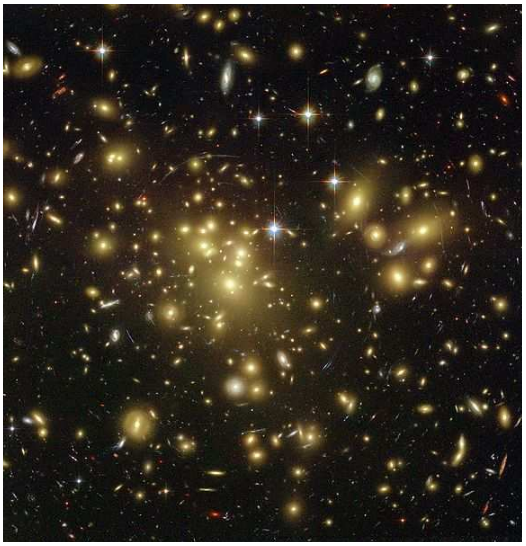

Figure 1.3: Galaxy cluster Abell 1689. Image credit: NASA, N. Benitez (JHU), T. Broadhurst (Racah Institute of Physics/The Hebrew University), H. Ford (JHU), M. Clampin (STScI),G. Hartig (STScI), G. Illingworth (UCO/Lick Observatory), the ACS Science Team and ESA.

Fig. 1.3 shows galaxy cluster Abell 1689, one of the biggest and massive galaxy clusters known, and hence one of the prominent lensing clusters. It is shown that background galaxies (red and blue) are gravitiationally lensed and stretched by the cluster itself (yellow).

Other compelling examples showing the existence and nature of dark matter at the extra-galactic scale are the “Bullet Cluster (1E 0657-558)” [Clowe *et al.*, 2004; Clowe *et al.*, 2006] and MACS J0025.4-1222 [Bradac *et al.*, 2008]. They are cluster mergers, consisting of two colliding galaxy clusters. In the ΛCDM paradigm, during the initial pass-through the dark matter particles and the galaxies are effectively collisionless while the X-ray halo is affected by ram pressure. Thus, the galaxies and dark matter halo are expected to remain spatially coincident following the interaction, while the X-ray halo is displaced toward the center of mass of the combined system. On the other hand, assuming MOND to be correct, the X-ray gas is the dominant mass component and the weak lensing mass reconstruction would therefore detect a primary mass peak consistent with the gas, which exhibits the spatial discrepancy with that from the galaxy distribution.

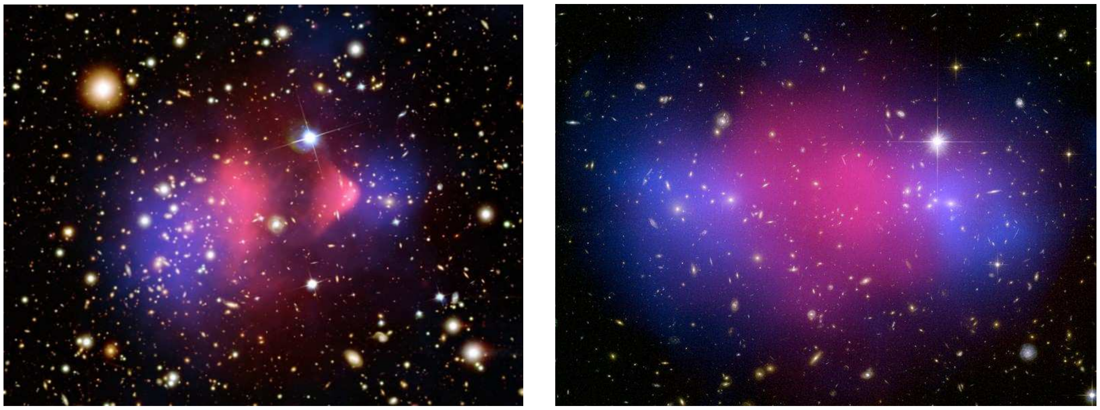

Figure 1.4: The matter in galaxy cluster 1E 0657-56, well-known as the "bullet cluster"(left) and MACS J0025.4-1222 (right) are shown as composite images. Composite credit (left): X-ray: NASA/CXC/CfA/ M.Markevitch *et al.*; Lensing Map: NASA/STScI; ESO WFI; Magellan/U.Arizona/ D.Clowe *et al.* Optical: NASA/STScI; Magellan/U.Arizona/D.Clowe *et al.*; Composite credit (right): X-ray (NASA/CXC/Stanford/S. Allen); Optical/Lensing (NASA/STScI/UC Santa Barbara/M. Bradac)

As shown in Fig. 1.4, the observed offsets of the lensing mass peaks (shown as blue) from the peaks of the dominant visible mass component (the X-ray gas, shown as magenta) directly demonstrate the presence, and dominance, of dark matter in this cluster and disfavors MOND.

1.1.3 Cosmological Scales: Big Bang Nucleosynthesis, Cosmic Microwave Background

Big Bang Nucleosynthesis

By knowing (or assuming) the conditions of the early universe and relevant nuclear cross-sections, it is possible to infer the primordial abundances of the light elements. Big Bang Nucleosynthesis (BBN) is the synthesis of the light nuclei, deuterium, ^{3}He, ^{4}He, and ^{7}Li, during the first few minutes after the Big Bang. Theoretical predictions of the light element abundances at the time of nucleosynthesis depend on the baryon density (the density of protons and neutrons) today since we know how those densities scale as universe evolves. Hence, the predictions of light element abundances are able to constraint the baryon density

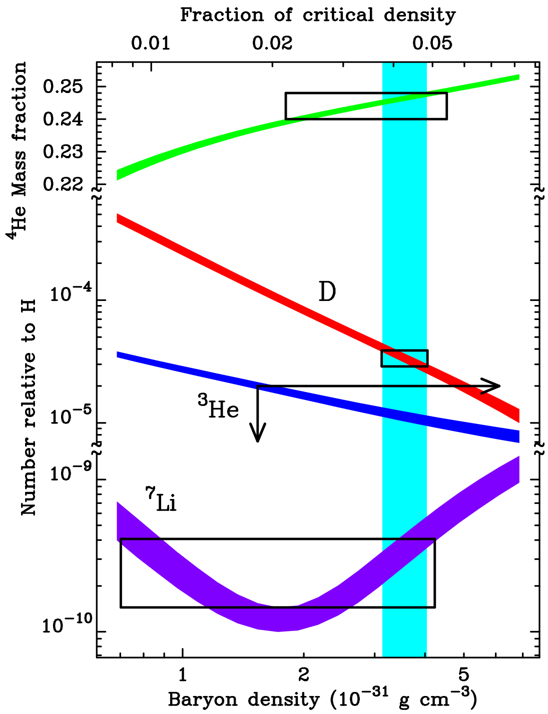

Figure 1.5: Constraints on the baryon density from Big Bang Nucleosynthesis (BBN) [Burles *et al.*, 1999]. Predictions are shown for four light elements - ^{4}He, D, ^{3}He, and ^{7}Li - spanning a range of 10 orders of magnitude. The solid vertical band is fixed by measurements of primordial deuterium. The boxes are the observations; there is only an upper limit on the primordial abundance of ^{3}He.

as shown in Fig. 1.5.

The deuterium measurements provide the most stringent constraint by measuring the D/H ratio in several high ($z > 3$) redshift intergalactic hydrogen clouds, far before the primordial abundances could have altered. These hydrogen clouds are "seen" by their distinctive Ly-α absorption features in the spectra of distant quasi-stellar objects (quasars, QSOs), with the deuterium features isotopically shifted to the blue by $0.33(1+z_{\mathrm{cloud}})$ [Burles and Tytler, 1998]. The primordial deuterium abundance pins down the baryon density (fraction of the critical density) to be $\Omega_b = 0.043 \pm 0.003$ (for $H_0 = 65\,\mathrm{km\,sec^{-1}\,Mpc^{-1}}$). Since the total matter density today is almost certainly larger than this (direct estimates give values of order $20 \sim 30\,\%$ [Dodelson, 2003]), BBN leads to a conclusion that most of the matter is nonbaryonic.

Cosmic Microwave Background

The cosmic microwave background (CMB) radiation is isotropic thermal black-body radiation that, as far as we can tell, permeates the entirety of the universe. The photons in the CMB last scattered off electrons at redshift $z \sim 1100$ [Dodelson, 2003]. Since then they traveled freely through space, therefore they literally came from the earliest moments of time, which makes the CMB the most powerful tool to view the early universe (379,000 years after the Big Bang). It is worthwhile to notice that the photons' collisions with electrons before last scatter off ensured that the photons were in thermal equilibrium and hence, they should have a black body spectrum. This strongly suggests that the Big Bang scenario is a good explanation of the early development of the universe and that the steady state model should be disregarded [Peebles *et al.*, 1991].

When it was discovered in the 1960s [Penzias and Wilson, 1965], the CMB was found to be remarkably uniform across the sky, as expected from black body radiation. It was not until 1992 that the COsmic Background Explorer (COBE) satellite discovered temperature variations (or ripples) at the level of 1 part in 100,000 in the CMB [Smoot *et al.*, 1992], which reflect tiny density fluctuations in the primordial soup of particles. COBE revealed what the large-scale fluctuations in the background look like by measuring temperature ripples from the 10 to 90 angular degree scale. This scale is so large that there has not been enough time for structure formation. Therefore COBE sees the so-called initial conditions of the universe. But to know the conditions in the early universe, small-scale examination (at the degree scale) is required. For a better understanding of the structure formation in the early universe, many ground and balloon-based experiments and the Wilkinson Microwave Anisotropy Probe (WMAP, the successor of COBE) have been launched and shown the ripples peak at the degree scale.

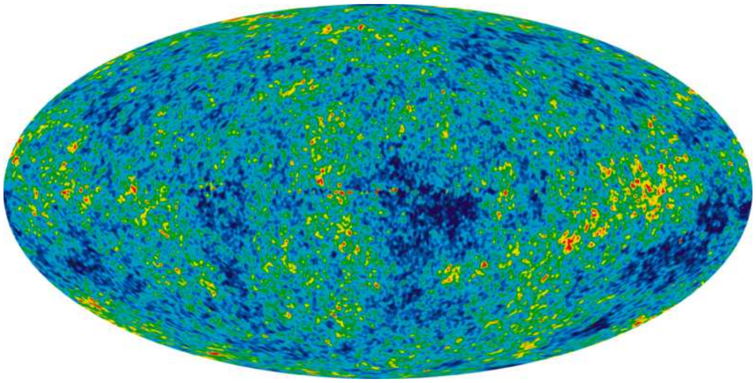

Figure 1.6: The cosmic microwave background temperature fluctuations from the 7-year Wilkinson Microwave Anisotropy Probe (WMAP) data seen over the full sky. The average temperature is 2.725 K and the colors represent the tiny temperature fluctuations (red regions are warmer and blue regions are colder by about 200 μK). This map is the ILC (Internal Linear Combination) map, which attempts to subtract out noise from the galaxy and other sources. (Other maps are typically used for detailed scientific analysis due to uncertain reliability, especially on smaller scales.) Credit: NASA / WMAP Science Team.

Fig. 1.6 shows Wilkinson Microwave Anisotropy Probe (WMAP) data image of 13.7 billion year old temperature fluctuations (shown as color differences) that correspond to the seeds that grew to become the galaxies. It is clearly shown that there exists spatial inhomogeniety in the temperature fluctuation. To interpret the temperature anisotropy in a more qualitative and quantitative way, what CMB experimentalists do is take a power spectrum of the temperature maps as function of the angular wavenumber (multipole moment l) which is related to the inverse of the angular scale ($l = 100$ is approximately 1 degree).

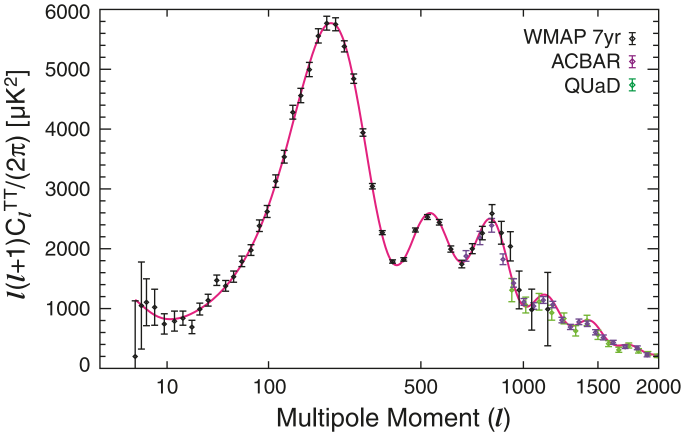

Figure 1.7: The WMAP 7-year temperature power spectrum [Larson *et al.*, 2011], along with the temperature power spectra from the ACBAR [Reichardt *et al.*, 2009] and QUaD [Brown *et al.*, 2009] experiments. Here the figure shows the ACBAR and QUaD data only at $l \geq 690$, where the errors in the WMAP power spectrum are dominated by noise. The solid line shows the best-fitting 6-parameter at ΛCDM model to the WMAP data alone. Figure from [Komatsu *et al.*, 2011].

Fig. 1.7 shows a power spectrum of WMAP [Larson *et al.*, 2011] along with Arcminute Cosmology Bolometer Array Receiver (ACBAR) [Reichardt *et al.*, 2009], Q and U Extragalactic Sub-mm Telescope at Degree Angular Scale Interferometer (QUaD) [Brown *et al.*, 2009], and best-fitting 6-parameter flat ΛCDM model to the WMAP data alone [Komatsu *et al.*, 2011]. This power spectrum can be divided into roughly 4 regions, the ISW rise ($l \lesssim 10$), Sachs Wolfe plateau ($10 \lesssim l \lesssim 100$), acoustic peaks ($100 \lesssim l \lesssim 1000$), and the damping tail ($l \gtrsim 1000$) [Scott and Smoot, 2011]. By measuring this power spectrum precisely, it is possible to infer most of the relevant parameters in standard cosmology. Here we will focus on the acoustic peaks since we are interested in the smaller scale of the universe for which we can see the features clearly.

Acoustic peaks can be understood as follows. CMB photons were hot enough to ionize hydrogen before recombination and they were "glued" to baryons by electrons via Thomson scattering, resulting in a photon-baryon fluid. Radiation pressure resists compression from gravity of the fluid setting up acoustic oscillations, analogous to a mass on a spring falling under gravity. These oscillations are frozen in at recombination and wave-modes caught at extrema of their oscillation represent peaks. They form a harmonic series based on the distance sound can travel by recombination, called the sound horizon at last scattering ($l \sim 100$). The first peak represents the mode that compressed once inside gravitational potential wells before recombination, the second the mode that compressed and then rarefied, the third the mode that compressed then rarefied then compressed, etc. Examination of acoustic peaks tells us many cosmological parameters such as curvature (from the first peak), physical density of dark baryons (from the second peak), etc. The dark matter density directly affects the overall amplitude of the peaks. Conclusively, the presence of the third peak is the cleanest test of dark matter since the self-gravity of the photons and baryons still plays a role in the first and second peaks [Hu, 2001].

WMAP itself has already provided stringent values for the various parameters of the standard model of cosmology with small uncertainties. For the mass-energy constituents of the universe, 7 years of WMAP results with the combination of baryon acoustic oscillation (BAO, [Percival *et al.*, 2010]) and H_0 ([Riess *et al.*, 2009]) measurements yield the baryon density, dark matter density, and dark energy density to be $\Omega_b = 0.0456 \pm 0.0016$, $\Omega_c = 0.227 \pm 0.014$, and $\Omega_\Lambda = 0.728^{+0.015}_{-0.016}$, respectively (Table 8 of [Jarosik *et al.*, 2011]).

1.2 Dark Matter Candidates

From the observational evidence of dark matter, we learned that the universe consists of 4 % baryons, 23 % nonbaryonic dark matter, and 73 % dark energy. We also learned nonbaryonic dark matter must fulfill several conditions: First, that the dark matter has to be dark, in the sense that it must generically have no (or extremely weak) interactions with photons. Otherwise it might have been detected by spectra of distant quasars [Profumo and Sigurdson, 2007]. Second, that the self-interaction of dark matter should be small-as shown in the bullet cluster, the two dark matter halos have passed through each other while the baryonic gas has shocked and is located between two halos. Third, that interaction with baryons must also be weak. If dark matter interacted with baryons other than gravitationally in the early Universe, the baryon-photon fluid would be effectively heavier (have a higher mass loading relative to radiation pressure) even before recombination so that the baryon acoustic oscillations in the matter power spectrum and the CMB angular power spectrum would be modified [Sigurdson *et al.*, 2004]. Lastly, that dark matter cannot be composed of standard model particles since most leptons and baryons are charged. The only potentially suitable standard model candidate is the neutrino, but it cannot be dark matter because of the celebrated Gunn-Tremaine bound [Tremaine and Gunn, 1979], which imposes a lower bound on the masses of dark matter particles that decoupled when relativistic. In other words, neutrinos fail to fulfill the condition that dark matter must be "cold" when they decoupled from ordinary matter. Therefore, the appealing candidates for the dark matter are still undetected, heavy elementary particles beyond the standard model.

There exist lots of dark matter candidates from many theories and they can be called the "Nonbaryonic Candidate Zoo". In this section, we will focus on two most plausible nonbaryonic dark matter candidates whose experimental searches are actively ongoing, these candidates are axions and weakly interacting massive particles (WIMPs).

1.2.1 Axions

The axion is a hypothetical elementary pseudoscalar particle [Weinberg, 1978; Wilczek, 1978] postulated by the Peccei-Quinn theory [Peccei and Quinn, 1977] to resolve the strong CP problem in quantum chromodynamics (QCD), which is posed by the nonobservation of an electric dipole moment of the neutron. If its mass is of order 10^{-5} eV, then a cosmologically interesting (i.e., matter density $\Omega \sim 1$) density of axions would have been produced at the QCD phase transition [Jungman *et al.*, 1996]. Since it has extremely feeble coupling to matter and radiation, it is hard to detect. Nevertheless, using the technique proposed by Sikivie [Sikivie, 1983], the axions two-photon coupling lends itself to a feasible search strategy with currently available technology. The main idea is that axions resonantly convert to single microwave photons by a Primakoff interaction, in a tunable microwave cavity permeated by a strong magnetic field. Further discussion about microwave cavity searches for dark matter axions can be found in [Bradley *et al.*, 2003]. For more general discussion about axion searches, refer to [Battesti *et al.*, 2008].

The Axion Dark Matter eXperiment (ADMX) is one of the experiments using Sikvie microcavity, searches for light, weakly interacting axions saturating the dark matter halo of our galaxy. With conventional amplifiers and SQUIDs, ADMX has excluded at 90 % confidence realistic axion models (KSVZ, DFSZ) in the 1.9 to 3.53 μeV range [Asztalos *et al.*, 2010; Asztalos *et al.*, 2004]. The CARRACK experiment [Shibata *et al.*, 2008] is another microwave cavity experiment, but using a Rydberg-atom microwave-photon detector in the cavity which can reach lower temperatures than ADMX. Given that the ADMX experiment is being upgraded and expected to explore more than two orders of magnitude lower sensitivity and the CARRACK experiment is being developed to reach 2 and 60 μeV with sensitivity to probe all plausible axion models, axions seem to be completely excluded or discovered soon.

1.2.2 Weakly Interacting Massive Particles

Weakly interacting massive particles (WIMPs) are stable particles which arise in extensions of the standard model of electroweak interactions (e.g., supersymmetry, universal extra dimensions). WIMP masses are typically in the range from 10 GeV to a few TeV, and they have interactions with ordinary matter which are characteristic of the weak interactions. The most well-motivated and certainly the most theoretically well-developed WIMP candidate is the neutralino, the lightest superparticle (LSP) in supersymmetric models with exact R-parity (which guarantees the stability of the LSP) [Jungman *et al.*, 1996].

The neutralino, χ, is a neutral spin-1/2 Majorana fermion (self annihilating, i.e., $\chi = \tilde{\chi}$), mathematically written as

$$\tilde{\chi} = \xi_\gamma \tilde{\gamma} + \xi_Z \tilde{Z}^0 + \xi_{h1} \tilde{h}_1^0 + \xi_{h2} \tilde{h}_2^0 \tag{1.4}$$

a linear combination of the supersymmetric partners of the photon, Z^0 boson, and neutral Higgs bosons. In theories with universal extra dimensions there exist Kaluza-Klein (KK) states γ_{KK}, Z^0_{KK}, H^0, which are neutral KK bosons. The candidates are stable (or quasi-stable; i.e., lifetimes greater than the age of the Universe) and the particle-theory models suggest masses $M_\chi \sim 10 - 10^3$ GeV [Matarrese *et al.*, 2011].

Within the standard cosmology, the present relic density of WIMPs can be calculated reliably if they were in thermal and chemical equilibrium with the hot soup of standard model particles after inflation (at temperatures $T \gg M_\chi$). Their equilibrium abundance at this time is maintained via rapid interconversion of $\chi\tilde{\chi}$ pairs and particle-antiparticle pairs of standard model particles (quark-antiquark, lepton-antilepton, and gauge-and/or Higgs-boson pairs). In many cases, the particle is a Majorana particle, in which case $\chi = \tilde{\chi}$. Later, when the temperature drops below the mass of the WIMP ($T \ll m_\chi$), the WIMP density would become exponentially (Boltzmann) suppressed until the rate for the annihilation reaction falls below the expansion rate H, at which point the interactions which maintain thermal equilibrium freeze out, and a relic cosmological abundance freezes in, i.e., the co-moving WIMP density remains essentially constant; if the Universe evolved adiabatically after WIMP decoupling, this implies a constant WIMP number to entropy density ratio.

This simple picture is described quantitatively by the Boltzmann equation, which characterizes the time evolution of the number density $n_\chi(t)$ of WIMPs:

$$\frac{dn_\chi}{dt} + 3Hn_\chi = -\langle\sigma_A v\rangle[(n_\chi)^2 - (n_\chi^{eq})^2] \tag{1.5}$$

where $\langle\sigma_A v\rangle$ is the thermally averaged total cross section for annihilation of $\chi\tilde{\chi}$ into lighter particles times the relative velocity v. The second term on the left-hand side accounts for the expansion of the Universe. In the absence of number-changing interactions, the right-hand side would be zero, and we would find $n_\chi \propto a^{-3}$, as we should. The first term in brackets on the right-hand side of Eq. (1.5) accounts for the depletion of WIMPs due to annihilation, and the second term arises from creation of WIMPs from the inverse reaction.

Fig. 1.8 shows numerical solutions to the Boltzmann equation [Kolb and Turner, 1988]. The equilibrium (solid line) and actual (dashed lines) abundances per comoving volume are plotted as a function of $x \equiv m_\chi/T$. As the annihilation cross section is increased the WIMPs stay in equilibrium longer, and we are left with a smaller relic abundance [Jungman *et al.*, 1996].

If we compute the WIMP density at freeze out, when the annihilation rate $\Gamma(T_f) \sim H(T_f)$, it is the WIMP density of today. Using the result from the CMB temperature measurement, the relic abundance of WIMPs is given by

$$\Omega_\chi h^2 \sim 3 \times 10^{-27}\,\mathrm{cm}^3\mathrm{s}^{-1}\langle\sigma_A v\rangle^{-1} + \text{ log corrections } (M_\chi). \tag{1.6}$$

If a new particle with weak-scale interactions exists, then its annihilation cross section can be

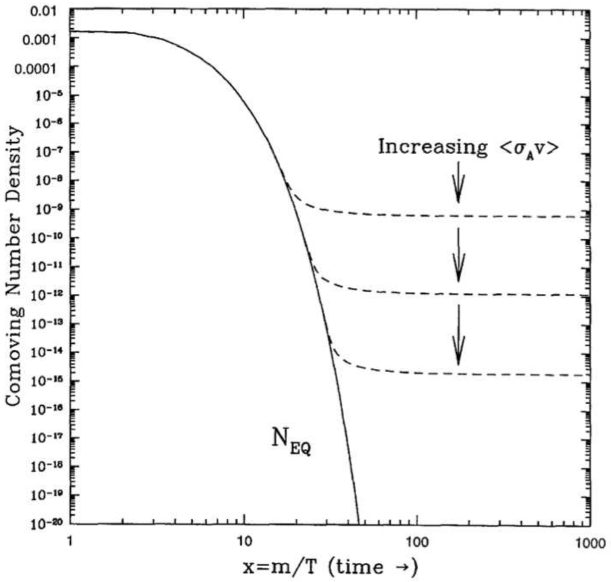

Figure 1.8: Comoving number density of WIMPs in the early Universe. The dashed curves are the actual abundance, and the solid curve is the equilibrium abundance. Figure from [Kolb and Turner, 1988].

estimated to be $\langle \sigma_A v \rangle \sim \alpha^2 (100\,\mathrm{GeV})^{-2} \sim 10^{-25}\mathrm{cm}^3\mathrm{s}^{-1}$, for $\alpha \sim 10^{-2}$. This is remarkably close to the value required to account for the dark matter in the Universe within an order of magnitude, especially if we realize that there is no *a priori* reason for a weak-scale interaction to have anything to do with closure density, a cosmological parameter. This striking coincidence suggests that if there is a stable particle associated with new physics at the electroweak scale, it is the dark matter. This is the so-called "WIMP miracle" which makes WIMPs as the most appealing dark matter candidate. Therefore, this idea has been followed by extensive theoretical work, and has led to an enormous experimental effort to detect these WIMPs. Detailed explanation of WIMP detection methods will be addressed in section 1.3.

Although not as attractive as the theories mentioned above, models based on the non-thermal WIMP production mechanisms have also been suggested. For more information, see [Nakamura, 2010] and references therein.

1.3 Direct Detection of Weakly Interacting Massive Particles

There exist three ways of detecting a WIMP. First, direct detection with a terrestrial detector on earth. Second, indirect detection by detecting secondary particles such as neutrinos, γ rays, positrons, antiprotons, and antinuclei from WIMP annihilation or decay [Bertone, 2010]. Last, production of WIMPs using a high-energy accelerator such as the LHC [Aad *et al.*, 2009], although it is difficult to claim a discovery of WIMPs with collider experiments since experimental understanding of the backgrounds is far more complicated. In this thesis, we confine our discussion to direct WIMP detection.

When it comes to direct detection, the cross section for elastic scattering of a WIMP from ordinary material is perhaps its most important property because it determines the detection rate. If WIMPs make up the halo of the Milky Way, then they have a local spatial density $n_\chi \sim 0.004\ (M_\chi/100\,\mathrm{GeV})^{-1}\mathrm{cm}^{-3}$ and are moving with velocities $v \sim 200\,\mathrm{km\,sec}^{-1}$. In addition, crossing symmetry between the annihilation $\chi\chi \to q\bar{q}$ and the elastic scattering $\chi q \to \chi q$ yields the cross section $\sigma(\chi q \to \chi q) \sim \sigma(\chi\chi \to q\bar{q}) \sim 10^{-36}\,\mathrm{cm}^2$. Therefore, it is possible to detect a WIMP directly by observing its interaction with some target nucleus in a low-background detector [Goodman and Witten, 1985; Wasserman, 1986; Drukier and Stodolsky, 1984].

Since at low energies quarks are bound into nucleons and nucleons in turn are bound into nuclei, the actual necessary cross section is $\sigma(\chi N \to \chi N)$ (where N stands for a nucleus) even though the WIMP-nucleus elastic-scattering cross section depends fundamentally on the WIMP-quark interaction strength. The calculation relating the χq interaction to the χN involves both QCD and nuclear physics. The required steps can be presented as follows:

$$\sigma(\chi q) \xrightarrow[\text{QCD}]{} \sigma(\chi n), \sigma(\chi p) \xrightarrow[\text{nuclear physics}]{} \sigma(\chi N).$$

Qualitatively, there are two different types of interactions, axial and scalar (or spin-dependent and spin-independent) [Goodman and Witten, 1985]. The first is described by the Lagrangian,

$$\mathscr{L}_{\mathrm{axial}} \propto \bar{\chi}\gamma^\mu\gamma_5\chi\bar{q}\gamma_\mu\gamma^5 q, \tag{1.7}$$

which couples χ to the spin of unpaired nucleons; this works only for nuclei with spin, and the coupling is different for unpaired protons or neutrons. Through this interaction one expects $\sigma \propto \bar{s}^2$, where $\bar{s}$ is the average spin $\sim 1/2$ of the unpaired proton or neutron in nuclei with odd atomic number.

The second interaction is described by the Lagrangian,

$$\mathscr{L}_{\text{scalar}} \propto \bar{\chi}\chi\bar{q}q, \tag{1.8}$$

which couples χ to the mass of the nucleus (coherent weak coupling), thus giving a cross section $\sigma \propto M^2 \propto A^2$ (where M and A are the nuclear mass and atomic number), which implies higher cross sections for larger A. However, this scaling is only valid up to a limit [Matarrese *et al.*, 2011].

In surveys of supersymmetric parameter space, one finds that the scalar interaction almost always dominates for nuclei with $A \gtrsim 30$. This has been noted and stressed in [Drees and Nojiri, 1993; Bednyakov *et al.*, 1994].

1.3.1 Interaction Rates and Recoil Spectra

WIMPs are expected to interact primarily with atomic nuclei, and since they are nonrelativistic, the most likely interaction is elastic scattering. The WIMP interaction rate per unit mass of the detection medium should follow

$$R \approx \frac{\rho_0}{m_\chi m_N}\sigma\langle v\rangle$$

where m_χ is the mass of the WIMP particles, ρ_0 is the local WIMP energy density near the Earth, which yields the WIMP number density is $n = \rho_0/m_\chi$, σ is the elastic-scattering cross section, $\langle v\rangle$ as the average speed of the WIMP relative to the target.

The differential scattering rate can be expressed as

$$\frac{dR}{dE_{\text{r}}} = \frac{\rho_0\sigma_0}{\sqrt{\pi}v_0 m_\chi {m_r}^2}F^2(E_{\text{r}})S(E_{\text{r}}) \tag{1.9}$$

where E_{r} is the recoil energy transferred to the detector nucleus, σ_0 is the zero-momentum transfer cross section, $F(E_{\text{r}})$ is a form factor correction due to the finite size of the nucleus, which depends on the energy transfered and on the nuclear radius, $S(E_{\text{r}})$ is a WIMP velocity dependent factor, m_r is the WIMP-nucleus reduced mass $m_r = m_\chi m_N/(m_\chi + m_N)$ and v_0 is the circular velocity of the Sun around the galactic center. In this section we mostly follow [Lewin and Smith, 1996] and [Jungman *et al.*, 1996].

WIMP Velocity Distribution

In Eq. 1.9, the WIMP velocity factor is defined as

$$S(E_{\mathrm{r}}) = \frac{\sqrt{\pi}}{2k} v_0 \int d\Omega \int_{v_{\min}}^{v_{\mathrm{esc}}} v f(\vec{v}, \vec{v}_e(t)) d^3 v$$

where $v_{\min} = \sqrt{E_{\mathrm{r}} m_N / (2 m_r{}^2)}$ is the minimum WIMP velocity that can produce a recoil of energy E_{r}, v_{esc} is the galactic WIMP escape velocity, the velocity distribution of the WIMPs $f(\vec{v}, \vec{v}_e(t))$, with the WIMP velocity relative to target, $\vec{v}$, and the Earth's velocity in the rest frame of the galaxy (which is a function of time t due to the Earth's motion rotating the Sun), $\vec{v}_e(t)$, and k is the normalization factor,

$$k = \int d\Omega \int_{v_{\min}}^{v_{\mathrm{esc}}} f(\vec{v}, \vec{v}_e(t)) d^3 v$$

Assuming a Maxwellian WIMP velocity distribution $f(\vec{v}, \vec{v}_e) \propto \exp[-(\vec{v} + \vec{v}_e)^2 / v_0^2]$, when the escape velocity v_{esc} is allowed to be at infinity, the integral gives $k_0 = (\pi v_0^2)^{3/2}$ and the normalization factor k becomes

$$k = k_0 \left[\mathrm{erf}\left(\frac{v_{\mathrm{esc}}}{v_0} \right) - \frac{2}{\sqrt{\pi}} \frac{v_{\mathrm{esc}}}{v_0} e^{-v_{\mathrm{esc}}^2 / v_0^2} \right] \tag{1.10}$$

This yields a WIMP velocity factor of

$$S(E_r) = \frac{1}{k} \left\{ \frac{\pi^{1/2}}{4} \frac{v_{\mathrm{esc}}}{v_0} \left[\mathrm{erf}\left(\frac{v_{\min} + v_{\mathrm{e}}}{v_0} \right) - \mathrm{erf}\left(\frac{v_{\min} - v_{\mathrm{e}}}{v_0} \right) \right] - e^{-v_{\mathrm{esc}}^2 / v_0^2} \right\} \tag{1.11}$$

Nuclear Form Factor Correction

When the momentum transfer $q = \sqrt{2 m_N E_{\mathrm{r}}}$, is such that the de Broglie wavelength h/q is no longer large compared to the nuclear radius, the effective cross section begins to fall with increasing q, even in the case of spin-dependent scattering which effectively involves a single nucleon. To take into account this effect, the nuclear form factor $F(q)$ is introduced and its dependence on cross section is given by

$$\sigma(q r_n) = \sigma_0 F^2(q r_n)$$

where r_n is an effective nuclear radius. For spin independent interactions, the nuclear form factor proposed by [Helm, 1956] provides

$$\sigma(q r_n) = 3 \frac{j_1(q r_n)}{q r_n} e^{-(qs)^2/2} \tag{1.12}$$

where $j_1(x)$ is the first order Spherical Bessel Function. Following a suggestion from [Engel, 1991], r_n is approximated as $r_n = \sqrt{r_v^2 - 5s^2}$, where $s = 1\,\mathrm{fm}$, $r_v = 1.2\,\mathrm{A}^{1/3}\,\mathrm{fm}$.

Differential Recoil Spectra

With all the mentioned information together, one can compute an expected differential recoil spectrum from WIMP-nucleon scattering using Eq. 1.9.

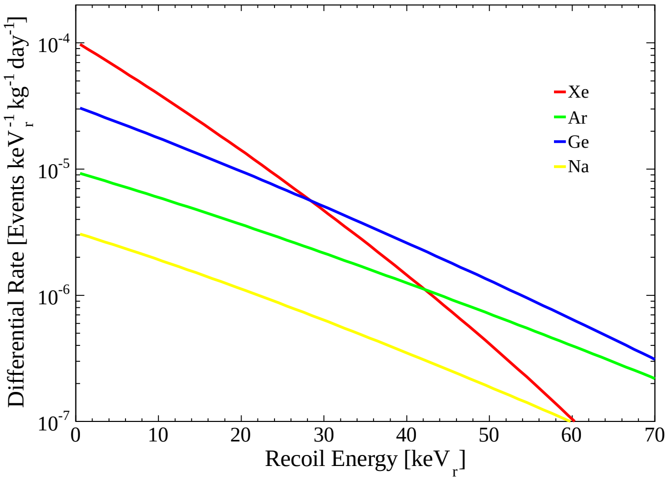

Figure 1.9: Expected differential recoil spectra from WIMP-nucleon scattering with different target nuclei, for a WIMP mass $m_\chi = 50\,\mathrm{GeV}$, and a WIMP-nucleon spin-independent cross section of $\sigma_{\chi N} = 1 \times 10^{-45}\,\mathrm{cm}^2$, $v_{\mathrm{esc}} = 544\,\mathrm{km/s}$, $v_0 = 220\,\mathrm{km/s}$, and $\rho_\chi = 0.3\,\mathrm{GeV}/c^3$.

Fig. 1.9 shows the expected differential recoil spectra from WIMP-nucleon spin-independent rate on xenon, argon, germanium, and sodium. Since the recoil spectrum decreases exponentially with the increase of the recoil energy, reaching a low energy threshold is important for WIMP detection. In addition, the rate depends on the target materials. Heavier targets exhibit an advantage of having a higher rate with the same energy threshold.

1.3.2 Annual Modulation

As mentioned in Sec. 1.3.1, the Earth velocity, $\vec{v}_e(t)$, is time dependent because of Earth's motion rotating the Sun. $v_e(t)$ is parametrized as

$$v_e(t) = v_0 \left[1.05 + 0.06 \cos\left(\frac{t - t_p}{1\,\mathrm{yr}}\right)\right]$$

where t_p is on June 2nd. Therefore, annual modulation of the WIMP-induced interaction rate is expected.

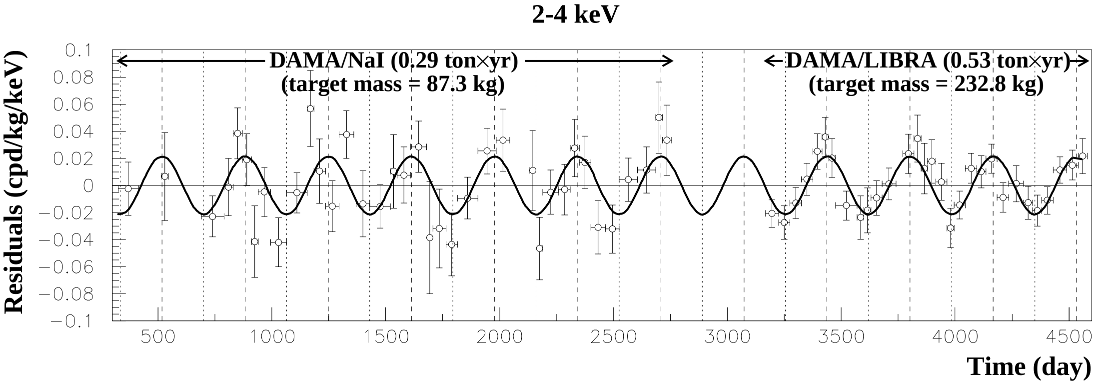

Figure 1.10: Annual modulation signature from the DAMA/NaI and DAMA/LIBRA experiments. Residual of rate of single hit interactions in the 2-4 keV energy interval as a function of time (points), along with a cosinudal function with a period of 1 year and a phase of 152.2 days. The modulation amplitude obtained from the best fit is $(0.0215 \pm 0.0226)\,\mathrm{counts\,day^{-1}\,kg^{-1}\,keV^{-1}}$. Figure from [Bernabei *et al.*, 2008].

An annual modulation of WIMPs was firstly reported by the DAMA/NaI experiment [Bernabei *et al.*, 2003] and it was confirmed by the DAMA/LIBRA experiment from the same collaboration [Bernabei *et al.*, 2008]. Fig. 1.10 shows an annual modulation signature from both DAMA/NaI and DAMA/LIBRA experiments. However, this observation of an annual modulation is inconsistent with null results from other experiments [Ahmed *et al.*, 2009; Aalseth *et al.*, 2008; Lee *et al.*, 2007; Angle *et al.*, 2008a], within the context of standard weak interactions motivated by supersymmetric model mentioned in Sec. 1.2.2. A lot of efforts have been made to reconcile the conflict between the DAMA results and other experimental results (e.g. [Chang *et al.*, 2009]), but none of them are satisfactory. However, one thing is clear about this modulation signal, namely that not only the signal but also the background contribution is included. It can very well be background which makes the modulation.

1.3.3 Detection Strategies

Given that WIMP detection is basically a rare event search, i.e., the expected signal rate is very low, the design concept of a detector focuses on the reduction of the background and increasing the total rate of the expected WIMP signal. Hence, the first common feature of all the direct WIMP searches is that the experiments are located underground to reduce background from cosmic rays. For example, Laboratori Nazionali del Gran Sasso (LNGS) in Italy provides 10^6 of muon flux suppression at a depth of 3600 m [Aglietta *et al.*, 1998; Ambrosio *et al.*, 1995]. Secondly, selecting detector materials with low radioactivity is also critical because the background contribution from the detector is predominant once the detector is deployed underground. In addition, reaching a very low energy threshold is desired since the typical differential rate of WIMP interactions exponentially decreases with recoil energy E_{r}, as shown in section 1.3.1. This can be achieved by designing the detector with higher signal collection efficiency and using a signal sensor with high efficiency. Another general feature of all the direct WIMP searches is making the target volume as large as possible. The number of target nuclei is linearly proportional to the total event rate and a larger detector means a shorter time for discovering or setting an upper limit for WIMPs.

The distinction among the direct WIMP experiments comes from the selection of the detection medium (target materials) and allied detection technique. When a particle has interactions with target atoms in the detector, it transfers its energy to target atoms and produces measurable signals through three types of elementary excitations: ionization, scintillation photons, and phonons.

Fig. 1.11 shows the various direct WIMP searches classified by the energy loss channel of the detection medium. As shown in the figure, direct WIMP searches can be categorized in six different types: three for each channel and the other three with combination of two channels. An advantage of a simultaneous measurement from two channels is that

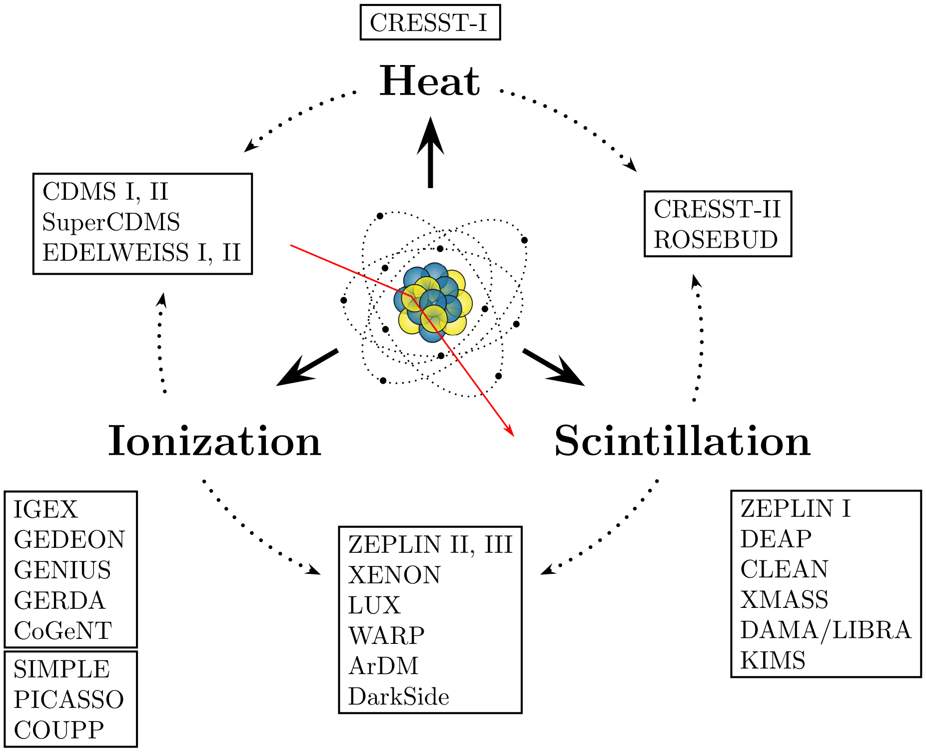

Figure 1.11: Past and present direct WIMP searches classified by the excitation channels measured. Figure from [Plante, 2012].

discrimination ability between WIMPs and electromagnetic background can be improved significantly. Since the interactions in the detection medium depend on the incident particle type and its energy, electromagnetic background interactions deposit energy in the detection medium in a different manner than do WIMP interactions. This results in the energy deposit partition through different channels of electromagnetic background interactions to be different than that from WIMP-induced interactions. Hence, the ratio of signal from one channel to signal from the other channel can be used as a good discriminant for the electromagnetic background rejection. A good example is making use of ionization signals in a solid-state detector by applying electric field, in addition to the use of the phonon signal. The Cryogenic Dark Matter Search (CDMS II) had reported discrimination of WIMP-like signal from electromagnetic background with a rejection power of $> 10^4$, using the ratio of ionization signal to the phonon signal [Ahmed *et al.*, 2009].

In the next section, we will focus on the noble gas detectors, which utilize scintillation, and in some cases ionization, too. Besides the "traditional" detection techniques, whose experiments are summarized in Fig. 1.11, there exist superheated liquid detectors and directional detectors. More information about the detectors using different detection techniques can be found in [Bertone, 2010] and references therein. For the status and prospects of direct WIMP searches, refer to [Beringer *et al.*, 2012].

1.3.4 Noble Gas Detectors

Historically, cryogenic detectors, detectors operating below 77 K, drew the attention of the direct WIMP search community earlier than noble gas detectors. Cryogenic detectors were utilized in the 1980s because of the excellent energy resolution and low threshold characteristics of semiconductors. The first searches for dark matter were performed with ultrapure semiconductors [Bertone, 2010]. On the other hand, noble gas detectors became popular in the 1990s, offering an excellent alternative for cryogenic detectors with their own advantages as a detection medium. First of all, they are available in large amounts as byproducts of the oxygen production from the steel industry. Argon is the third most abundant gas in the atmosphere, following nitrogen and oxygen, and the world production of xenon is about 27 tons per year. Secondly, it is relatively easy to purify the noble gases so as to remove intrinsic backgrounds in the detection medium [Aprile *et al.*, 2007a]. In addition, noble liquids are excellent scintillators and, with the exception of LNe, also very good ionizers in response to the passage of radiation [Bertone, 2010]. Lastly, it is easier to scale the target volume to have larger mass. For example, for cryogenic detectors, it is challenging and costly to grow the crystal without defect. The commonly used noble gases for the direct WIMP searches are argon and xenon due to their inherent high stopping powers, which can be utilized to suppress background significantly by choosing only the center volume of the detector (fiducialization) with the position information of the particle interaction. In this case, the outer layer of the target volume is used as an effective background shielding material (i.e., they are self-shielding). Equipped with these advantages, the experiments using the noble gases as the WIMP detection media are currently leading the field.

Using argon has an advantage compared to using xenon for the detection of scintillation signal, due to the large time separation between singlet and triplet state transitions in argon. The transition times differ by two orders of magnitude being $\tau_s = 7\,\mathrm{ns}$ and $\tau_t = 1.6\,\mu\mathrm{s}$ for the singlet and triplet state, respectively [Hitachi *et al.*, 1983; Lippincott *et al.*, 2008; Peiffer *et al.*, 2008]. Since the pulse shape differs significantly depending on the type of particle, this provides additional discrimination power to reject electromagnetic background. A discrimination power of $\sim 10^6$ against background has been achieved for nuclear recoil energies above $\sim 50\,\mathrm{keV}$ [Lippincott *et al.*, 2008]. There are several disadvantages to using argon over xenon. The biggest challenge of argon is the intrinsic background from ^{39}Ar, while the ^{85}Kr in xenon can be reduced by using a Kr distillation column, since its boiling point is different from that of xenon. The shorter wavelength of the argon scintillation light (128 nm) compared to that of xenon (178 nm) demands the use of wavelength shifters, to shift the wavelength of the scintillation photon to the range of detection by commercial photomultiplier tubes (PMTs). In addition, since xenon has a higher atomic number Z and a higher density, it is favored in terms of self-shielding power. Further comparisons between two elements are possible based on the difference in their properties. In Chap. 2, we will focus on liquid xenon in more details as the detection medium for a WIMP search.

As mentioned in Sec. 1.3.3, noble gas detectors are divided into two groups depending on the use of ionization signal or not: Ionization-scintillation detectors and scintillation detectors. For the ionization-scintillation detectors, they can be subdivided into single phase detectors and dual phase detectors. In the WIMP searches, ionization-scintillation dual-phase (liquid-gas) detectors and scintillation single-phase detectors with liquid are common. XMASS [Sekiya, 2011] in Japan is a single-phase 800 kg liquid xenon detector installed in a large, pure water shield at the SuperKamiokande site. DEAP-3600 [Boulay, 2012] and MiniCLEAN [Hime, 2011] are other single-phase detectors being assembled at SNOLab and will operate with 3600 kg of liquid argon and 500 kg of liquid argon/neon, respectively.

For the dual-phase experiments, WARP, ArDM, and DarkSide are argon based. WARP is the only LAr detector that has set a competitive WIMP-nucleon scattering cross section limit so far [Benetti *et al.*, 2008]. ArDM [Marchionni *et al.*, 2010] is being installed at the Canfranc laboratory with a 1,100 kg mass. DarkSide [Alton *et al.*, 2011] with 50 kg of ^{39}Ar depleted argon, is being installed in the Gran Sasso laboratory. Xenon-based dual-phase experiments are very active in the field. XENON100 has placed currently the best limits at all masses on the spin-independent interactions of WIMPs [Aprile *et al.*, 2012a]. The XENON100 experiment is the main topic of this thesis and its details will be discussed extensively in Chap. 3−7. The XENON10 limit for spin-dependent WIMPs with pure neutron couplings in still the best published limit at all masses [Angle *et al.*, 2008b]. XENON1T [Aprile, 2012], the successor of XENON100 is planned to be operated at the Gran Sasso laboratory. ZEPLIN III, which had set competitive limits on spin-independent interactions of WIMPs [Akimov *et al.*, 2012], has been upgraded with a lower background and has finished data taking. PANDA-X is planned to be housed in the Jinping laboratory in China [Beringer *et al.*, 2012]. The LUX detector [McKinsey *et al.*, 2010] is planned to be operated in the new SURF laboratory.

Chapter 2

Liquid Xenon as WIMP Detection Medium

In this chapter, we will resume the discussion of the properties of liquid xenon (LXe) as a radiation detection medium, and see that LXe is a good medium for the detection of rare events such as WIMPs. As a particle detection medium, probably the most critical characteristic is its ability to absorb radiation and transform the absorbed energy into measurable signals. In the case of LXe, both ionization electrons and scintillation photons are produced in response to radiation. In addition, the ionization and the scintillation signals are highly complementary and anti-correlated. Therefore, when detected simultaneously and with high efficiency, the two signals enable a precise measurement of the particle's properties, from its energy and interactions history to its type.

It might be also worth remembering that noticeable progress in relevant techniques helped make full use of LXe as a particle detection medium. Advancement in photodetectors with high quantum efficiency at the 178 nm wavelength of the LXe scintillation, and cryocoolers with sufficient power to liquefy and maintain LXe in a liquid state, enabling reliable detector operation, are of note. Additionally, commercial purifiers have demonstrated effective removal of electronegative contaminants which do not freeze out at LXe temperature ($\sim -110\,^{\circ}$C).

In Sec. 2.1 we summarize the properties of LXe as a particle detection medium. Particle dependence of energy loss in LXe is reviewed in Sec. 2.2. We will explain details about the two available signals in LXe in Sec. 2.3 (scintillation) and Sec. 2.4 (ionization), along with the use of both signals in background rejection for WIMP searches.

2.1 Properties

Xenon was discovered by William Ramsay and Morris Travers in 1898, shortly after their discovery of the elements krypton and neon, through the study of liquefied air. The earth's atmosphere is about 0.0000087 % xenon. Xenon is obtained as a byproduct from liquefaction of air and its separation into oxygen and nitrogen. The resulting liquid oxygen mixture contains both krypton and xenon, which can be extracted by fractional distillation. The last stage is the extraction of xenon from the krypton/xenon mixture by distillation [Plante, 2012]. Due to its rarity, xenon costs far more than other noble gases, about $1000/kg.

Xenon is one of the heaviest noble gases, only behind radon. Given that radon is radioactive, it is not suitable for a radiation based detector. As mentioned briefly in Sec. 1.3.4, the high atomic number and high density of LXe make it very efficient at stopping penetrating radiation. By selecting only the center volume of the target, and using the outer layer as shielding material, external electromagnetic background can be suppressed significantly.

Naturally occurring xenon is made of eight stable isotopes, as listed in Tab. 2.1. (^{124}Xe, ^{126}Xe, and ^{134}Xe are predicted to undergo double-beta decay, but this has never been observed, so they are considered to be stable.). Beyond these stable forms, there are over 30 unstable isotopes and isomers that have been studied, the longest-lived of which is ^{136}Xe which undergoes double-beta decay with a half-life of 2.11×10^{21} yr [Ackerman *et al.*, 2011]. Since this is basically an extremely rare process, ^{136}Xe is considered to be a stable isotope in Tab. 2.1. The next longest-lived unstable isotope is ^{127}Xe with a half-life of 36.345 days. Xenon is essentially free from intrinsic radioactive naturally occurring Xe isotopes, which makes it an attractive rare event search detection medium. Because ^{129}Xe and ^{131}Xe constitute about half of the stable isotopes, xenon is also sensible for spin-dependent dark matter interactions.

Fig. 2.1 shows a phase diagram of xenon. At atmospheric pressure, the liquid phase of

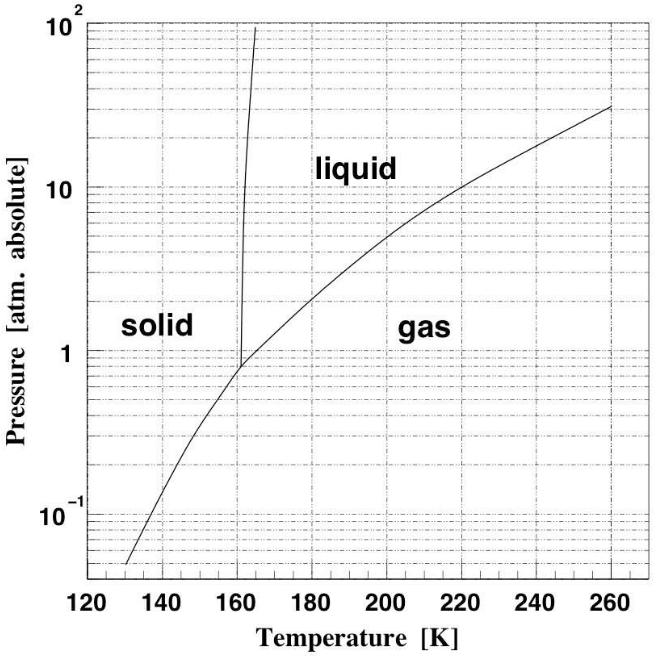

Figure 2.1: Phase diagram of xenon. Figure from [Aprile and Doke, 2010].

xenon extends over a narrow temperature range, from about 162 to 165 K. The relatively high boiling point temperature of LXe, compared to other liquid noble gases, necessitates only a modest cryogenics system for gas liquefaction. At the same time, the high boiling point is a disadvantage, since electronegative impurities are not frozen out. Thus, the LXe must undergo extra purification. Tab. 2.1 summarizes some of the physical properties mentioned above.

The very high scintillation photon yield of LXe is beneficial to measure the signals from LXe. For relativistic electrons, the scintillation photon yield is $\sim$ 42 photons/keV [Doke and Masuda, 1999], which is more than 70 % of that from NaI(Tl) [Miyajima *et al.*, 1993]. Another advantage of LXe is that xenon is essentially transparent to its own scintillation, since the energy of a scintillation photon from the exciton is smaller than the absorption band of the free exciton (see Sec. 2.3). This also allows LXe detectors to be built at large scales without significantly losing scintillation photons, which is mandatory for achieving the low-energy threshold required for dark matter detection. Tab. 2.1 lists some physical properties of Xe and Tab. 2.3 some properties of LXe related to particle detection.

Table 2.1: Physical properties of liquid xenon. Table from [Plante, 2012].

Property	Value
Atomic Number Z	54
Molar mass	131.29 g mol^{-1}
Isotopic Abundance	^{124}Xe (0.095 %), ^{126}Xe (0.089 %), ^{128}Xe (1.91 %)
	^{129}Xe (26.4 %), ^{130}Xe (4.07 %), ^{131}Xe (21.2 %)
	^{132}Xe (26.9 %), ^{134}Xe (10.4 %), ^{136}Xe (8.86 %)
Gas density (273 K, 1 atm)	5.8971 g L^{-1}
Liquid density (165.05 K, 1 atm)	3.057 g cm^{-3}
Melting point, (1 atm)	161.4 K
Boiling point, (1 atm)	163.05 K
Triple point, (1 atm)	161.31 K, 0.805 atm, 3.08 g cm^{-3}
Critical point, (1 atm)	289.74 K, 57.65 atm, 1.155 g cm^{-3}
Latent heat of fusion	17.29 kJ g^{-1}

2.2 Energy Loss

For the detection of radiation, the capability to stop incident particles, which enables a measurement of the full incident particle energy, is one of the critical characteristics of a detection medium, along with the ability to transform the energy absorbed into measurable signals. Interactions in the detection medium in general depend on the type of incident particle. To organize the discussions that follow, it would be helpful to arrange the four major categories of radiations as shown in Tab. 2.4.

The entries in the left column of Tab. 2.4 represent the charged particulate radiations that continuously interact via the Coulomb force with the electrons present in the medium through which they pass. Upon entering any absorbing medium, the charged particle immediately interacts with many electrons simultaneously. The electron feels an impulse from the Coulomb force as the particle passes its vicinity. Depending on the proximity of the

Table 2.2: Physical properties of liquid xenon (continued). Table from [Plante, 2012].

Property	Value
Thermal properties	
Heat conductivity (gas, 273 K, 1 atm), λ	5.192 mW $m^{-1}K^{-1}$
Heat conductivity (liquid, 178 K), λ	71.1 mW $m^{-1}K^{-1}$
Electrical properties	
Relative permittivity (gas), ϵ_r	1.00
Relative permittivity (liquid), ϵ_r	1.96 [a]
Dielectric strength	$\gtrsim$ 400 $kVcm^{-1}$ [b]
Optical properties	
Refractive (178 nm)	1.69 [c]
Rayleigh scattering length (178 nm), $\lambda_{\mathrm{Rayleigh}}$	29 cm [d]

[a] [Schmidt, 2001]

[b] [Jones and Kunhardt, 1995]

[c] [Solovov *et al.*, 2004]

[d] [Ishida *et al.*, 1997]

Table 2.3: Properties of liquid xenon related to particle detection. From [Plante, 2012].

Property	Value
Avg. energy per electron-ion pair, W_{i}	15.6 eV [a]
Avg. energy per scintillation photon, $W_{\mathrm{ph}}(\mathrm{max})$	13.8 eV [b]
Ratio of excitons to ionization $N_{\mathrm{ex}}/N_{\mathrm{i}}$	0.06 [a]
Scintillation properties	
Scintillation wavelength, λ_s	178 nm [c]
Excimer singlet lifetime, τ_1	2.2 ns [d]
Excimer triplet lifetime, τ_3	27 ns [d]

[a] [Takahashi *et al.*, 1975]

[b] [Doke *et al.*, 2002]

[c] [Jortner *et al.*, 1965]

[d] [Kubota *et al.*, 1978b]

Table 2.4: Four categories of radiation depending on the type. Table from [Knoll, 2000] and modified.

Charged Particulate Radiations		Uncharged Radiations
Heavy charged particles	$\Leftarrow$	Neutrons (mean free path in LXe $\sim 10\,\mathrm{cm}$ [a])
Fast electrons	$\Leftarrow$	X-rays and γ rays (mean free path in LXe $\sim 2\,\mathrm{cm}$ [b])

[a] Mean free path at a few tens of keV to 10 MeV

[b] Mean free path at $\sim 300\,\mathrm{keV}$

encounter, an impulse may be sufficient either to raise the electron to a higher-lying shell within the absorber atom (excitation) or to remove completely the electron from the atom (ionization). This results in the creation of a track of free electrons and ionized atoms. For heavy charged particles, the particle interacts with many electrons so the net effect is to decrease its velocity continuously until the particle is stopped. For fast electrons, they lose energy at a lower rate and follow a much more tortuous path through absorbing media since its mass is equal to that of orbital electrons with which it is interacting. In addition, electron-nuclear interactions sometimes occur, which can abruptly change the electron direction.

The radiations in the right column of Tab. 2.4 are uncharged and hence not subject to the Coulomb force. Instead, these radiations first undergo a “catastrophic” interaction that radically alters the properties of the incident radiation in a single encounter. Cases of interest are when the interaction results in the full or partial transfer of energy of radiation to electrons (X- or γ rays) or nuclei of the constituent atoms (neutrons), or to charged particle products of nuclear reactions (neutrons). The left arrows illustrate the results of such catastrophic interactions [Knoll, 2000]. The mean free paths for γ rays and neutrons are also shown.

At high velocities, energy loss can also occur through bremsstrahlung radiation. However, this radiation contribution is not significant at the energies we are interested in ($< 1\,\mathrm{MeV}$). Inelastic collisions with atomic electrons, which produce excitation and ionization (both included under the name of electronic excitation), are the dominant mechanism for the energy loss of electrons and α particles in LXe. Non-relativistic heavy charged particles, such as a recoiling nuclei, lose a sizable amount of energy through elastic collisions with atomic nuclei as well. Since the measurable signals in LXe come from electronic excitation, this leads to a quenching of the signal (nuclear quenching, see Sec. 2.3.4).

In the track, excited atoms (excitons) rapidly form excited dimers (excimers), which decay afterwards and emit scintillation photons. Without application of an electric field, ionization electrons will recombine and also form excimers which eventually produce scintillation photons. Hence, scintillation photons are produced both from direct excitation and from ionization (see Sec. 2.3.1). Strong evidence for this comes from the observation that a higher electric field reduces the scintillation signal, by reducing the fraction of electrons that recombine [Kubota *et al.*, 1978b]. Even with an absence of external electric field, only partial recombination would occur if some electrons thermalize too far from their parent ion [Doke *et al.*, 1988] in a timescale useful for the collection of signals.

The efficiency of the conversion of absorbed energy into measurable signals is often characterized by W_i, the average energy required to produce an electron-ion pair (the so-called W-value), and W_ph, the average energy required to produce a scintillation photon. The value of W_i for LXe (15.6 eV) is larger than the ionization energy of xenon because of other mechanisms by which the particle loses energy which do not produce ionization, excitation for example. If one assumes that recombination is complete and one exciton produces one scintillation photon and one recombined electron-ion pair also produces one scintillation photon, W_ph can be written as

$$W_\mathrm{ph} = E/(N_\mathrm{i} + N_\mathrm{ex}) = W_\mathrm{i}/(1 + N_\mathrm{ex}/N_\mathrm{i}) \tag{2.1}$$

where N_i and N_ex are the number of electron-ion pairs and excitons, respectively, produced by a recoil of energy E, and where we have used the definition $W_\mathrm{i} = E/N_\mathrm{i}$. The ratio of excitons to electron-ion pairs in LXe is estimated to be $N_\mathrm{ex}/N_\mathrm{i} \approx 0.06$ from a calculation based on oscillator strengths of solid xenon obtained from absorption spectra [Takahashi *et al.*, 1975]. A upper bound of 0.20 on $N_\mathrm{ex}/N_\mathrm{i}$ was obtained by [Doke *et al.*, 2002], which estimates the maximum scintillation yield in LXe to be $W_\mathrm{ph(max)} = 13.8 \pm 0.9\,\mathrm{eV}$ (see Sec. 2.3.3).

2.2.1 Interaction of Charged Particles: Electronic Stopping Power

As mentioned earlier, the final carriers of the energy deposited in the detection medium are electrons and charged particles. To know the energy deposition of an incident particle, it is required to know how the charged particles lose their energy in the detection medium. Since the charged particles lose energy with small steps, it is possible to measure the energy loss of the particle per unit path length.

Stopping power is defined as the average energy loss of the particle per unit path length. The stopping power depends on the type and energy of the particle and on the properties of the material through which it passes. Since the production of an electron-ion pair requires a fixed amount of energy, the density of ionization along the path is proportional to the stopping power of the material. "Stopping power" is treated as a property of the material, while "energy loss per unit path length" describes what happens to the particle. Nevertheless, the numerical value and units are identical for both quantities.

Electronic stopping means slowing down due to the inelastic collisions between bound electrons in the medium and the ion moving through it. Thus, the collisions may result both in excitations of bound electrons of the medium, and in excitations of the electron cloud of the ion. By the same analogy, nuclear stopping refers to slowing down due to the elastic collisions, even though it is misnomer since it is not attributed to the nuclear force. We do not consider nuclear stopping here because for very light ions slowing down in heavy materials such as Xe, the nuclear stopping is weaker than the electronic stopping at all energies.

Because it is difficult to describe all possible interactions for all possible ions states through the passage of a particle, the electronic stopping power is typically given as an average over all energy loss processes for different charge states, with a simple function of energy,

$$S_e(E) = -\frac{dE}{dx} \tag{2.2}$$

where E is energy of the particle, and x is the path length. Negative sign in the right hand is to make $S_e(E)$ positive to describe the "loss" of energy.

Locally, the ionization density is determined by the electronic stopping power for the recoiling particle, while the local electric field is the applied drift field minus any screening from the ionization in the track. Globally, both of these are influenced by the track structure: since stopping power is energy dependent, the division of energy among daughter recoils will affect the ionization density distribution, and the track geometry may impact screening of the electric field.

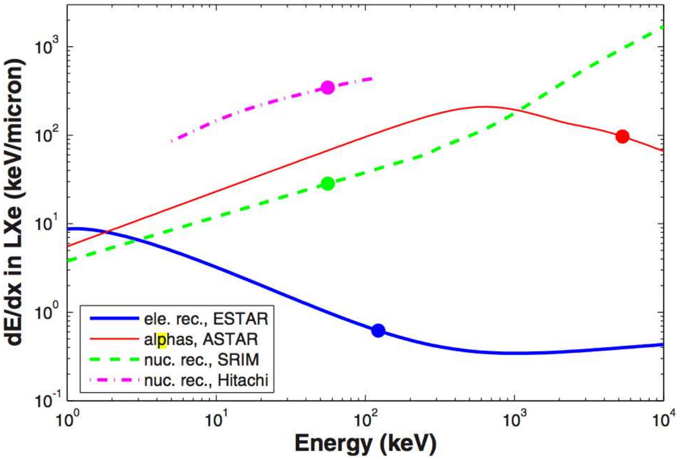

Figure 2.2: Predicted electronic stopping power (dE/dx) for electrons (blue) [Beger *et al.*, 2005b], for α particles (red) [Beger *et al.*, 2005a], and for nuclear recoils (dashed green) [Ziegler, 2011] in LXe, along with calculation for nuclear recoils (magenta) [Hitachi, 2005]. Figure from [Aprile *et al.*, 2006].

Fig. 2.2 shows the predicted electronic stopping power versus of energy for electrons (blue), α particles (red), and Xe nuclei (dashed green) in LXe. Higher electronic stopping power corresponds to higher ionization density, and, in most situations, greater recombination. The highest stopping power corresponds to the lowest ionization signal yield (α particles), and the lowest stopping power corresponds to the highest ionization signal yield (electrons). At the region of interest for a WIMP search (besides below 3 keV), nuclear recoils have a higher ionization density than electronic recoils. Because of the proportionality of recombination to ionization density, one would expect less quenching of scintillation for nuclear recoils than electronic recoils with increase of electric field, and indeed it has been observed (Sec. 2.4.3). It is worth noting, however, that while the charge yield for α particles and electrons shows a strong dependence on the drift field, nuclear recoils, which have an absolute charge yield between that of α particles and electrons, show almost no field dependence. This is the first indication that recombination in small tracks is qualitatively different than in large tracks [Dahl, 2009].

2.2.2 Interaction of γ rays

Among a large number of possible interaction mechanisms for γ rays, three major types play an important role in γ ray detection: photoelectric absorption, Compton scattering, and pair production. All these processes lead to the partial or complete transfer of the γ ray photon energy to electron energy. The created energetic electrons (positrons for pair production) lose their energies through electronic excitation and produce excitons and electron-ion pairs. In contrast to the charged particles, which slow down gradually through continuous, simultaneous interactions with many detection medium atoms, the three processes result in sudden changes in the γ ray photon history, in that the photon either disappears entirely or is scattered through a significant angle.

Photoelectric Absorption

In the photoelectric absorption process, a photon undergoes an interaction with an detection medium atom in which the photon is completely absorbed. As a result, an energetic photoelectron is ejected by the photon absorbing atom from one of its bound shells. The interaction is with the atom as a whole and can not take place with free electrons. For γ rays of sufficient energy, the most probable origin of the photoelectron is the most tightly bound, or K-shell, of the atom. The photoelectron appears with an energy given by

$$E_{\mathrm{e}^-} = h\nu - E_{\mathrm{b}} \tag{2.3}$$

where E_{b} represents the binding energy of the photoelectron in its original shell. For γ ray energies of more than a few hundred keV, the photoelectron carries off the majority of the original photon energy.

In addition to the photoelectron, the interaction also creates an ionized atom in the detection medium with a vacancy in one of its bound shells. This vacancy is quickly filled through capture of a free electron from the medium and/or rearrangement of electrons from other shells the atom. Therefore, one or more characteristic X-ray photons may also be generated. Although in most cases these X-rays are reabsorbed close to the original site through photoelectric absorption involving less tightly bound shells, their migration and possible escape from radiation detectors can influence their response. In some fraction of the cases, the emission of an Auger electron may substitute for the characteristic X-ray in carrying away the atomic excitation energy.

The process is enhanced for detection media of high atomic number Z, and LXe has the benefit of being a self-shielding material from photoabsorbed γ rays due to its high Z compared to other detection media. Fig. 2.3 shows the total, photoelectric absorption, Compton scattering, and pair production γ ray mass attenuation coefficients in Xe, as a function of energy. As shown in the figure, the photoelectric absorption is predominant mode of interaction for γ rays (or X-rays) of relatively low energy. With a LXe density of $2.86\,\mathrm{g\,cm^{-3}}$, the attenuation length is $\sim 2\,\mathrm{cm}$ at $300\,\mathrm{keV}$. Therefore, we can conclude that most of the external low-energy γ rays are photoabsorbed in the outer layer of the target volume and do not reach the inner volume, which makes fiducialization an effective tool for

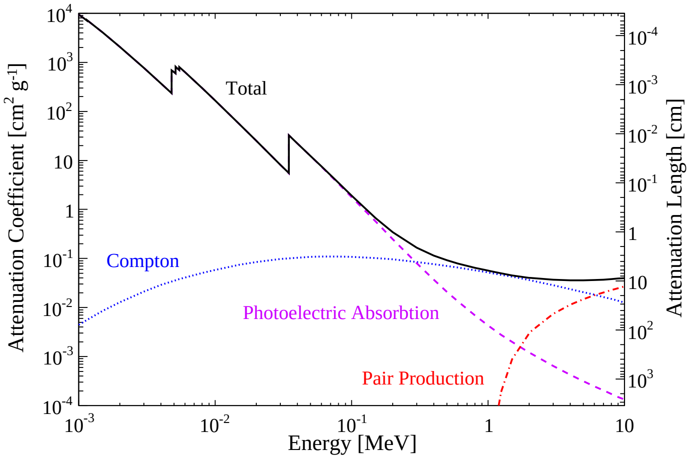

Figure 2.3: Total (black), photoelectic absorption (dashed violet), Compton scattering (dotted blue), and pair production (dash-dotted red) γ ray mass attenuation coefficients in Xe. The right axis indicates the attenuation length in LXe, using a density of $2.86\,\mathrm{g\,cm^{-3}}$. Data from XCOM database [Beger *et al.*, 2010]. Figure from [Plante, 2012].

the external γ background suppression (see Chap. 4).

The discontinuities in the photoelectric absorption curve, so-called "absorption edges", appear at γ-ray energies that correspond to the binding energies of electrons in the various shells of the absorber atom. The edge lying highest in energy corresponds to the binding energy of the K-shell electron. For γ-ray energies slightly above the edge, the photon energy is just sufficient to undergo a photoelectric interaction in which a K-electron is ejected from the atom. For γ-ray energies slightly below the edge, this process is no longer energetically possible and hence the interaction probability drops abruptly. Similar absorption edges occur at lower energies for the L, M, etc electron shells of the atom [Knoll, 2000].

Compton Scattering

Compton scattering takes place between the incident γ-ray photon and an electron in the detection medium. It is a dominating interaction process when the γ ray energy is between 300 keV and a few MeV. In Compton scattering, the incoming photon is deflected through an angle θ with respect to its original direction. The photon transfers a portion of its energy to the electron (assumed to be initially at rest), which is then known as a "recoil electron". Because all angles of scattering are possible, the energy transferred to the electron can vary continuously from zero to a large fraction of the γ-ray energy according to Eq. 2.4 given by

$$h\nu' = \frac{h\nu}{1 + \frac{h\nu}{m_e c^2}(1 - \cos\theta)} \tag{2.4}$$

where $m_e c^2$ is the electron rest mass energy, $h\nu$ is the energy of the incoming γ ray, $h\nu'$ is the energy of the Compton-scattered γ ray, and θ is the scattering angle. For forward scattering (small θ), very little energy is transferred. Some of the original energy is always retained by the scattered γ ray and it can continue its path and produce other energetic electrons via subsequent interactions. From Fig. 2.3, one could expect that most of the external background, which produces electronic recoils in the energy region of interest for dark matter searches, would arise from the low-energy single Compton scatters with forward scattering.

Pair Production

If the γ-ray energy exceeds twice the rest-mass energy of an electron (1.02 MeV), the process of pair production is energetically possible. The probability of this interaction remains very low until the γ-ray energy approaches several MeV and therefore pair production is predominantly confined to high-energy γ rays, outside of the energy region of interest for a dark matter search. In the interaction, the γ ray photon converts to an electron-positron pair. All the excess energy carried by the photon above the 1.02 MeV required to create the pair goes into kinetic energy shared by the positron and the electron. Because the positron will subsequently annihilate after slowing down in the absorbing medium, two back-to-back annihilation photons are normally produced as secondary products [Knoll, 2000].

Coherent Scattering

Besides the three major interaction mechanisms mentioned above, coherent scattering or "Rayleigh scattering" can occur in the detection medium as well. Since Rayleigh scattering neither excites nor ionizes the atom, the photon retains its initial energy after the scattering and virtually no energy is transferred. However, this process changes the direction of the scattered photon and it is one of the mechanisms which affects to the detection of scintillation photons in LXe (see Sec. 2.3.5).

2.2.3 Interaction of Neutrons

When a neutron undergoes an interaction, it is with a nucleus of the detection medium. As a result of the interaction, the neutron may either be totally absorbed and replaced by one or more secondary radiations, or else the energy and direction of the neutron is changed significantly. In contrast to the γ rays, the secondary radiation resulting from neutron interactions is mostly heavy charged particles. These particles are produced either as a result of neutron-induced nuclear reactions or may be the nuclei of the detection medium itself, which have gained energy through neutron collisions. The relative probabilities of the various types of neutron interactions depends strongly on the neutron energy.

The secondary radiations due to fast neutron ($> 0.5\,\mathrm{eV}$) interactions are recoil nuclei, which have picked up a detectable amount of energy from neutron collisions. At each scattering site, the neutron loses energy and is moderated or slowed to lower energy. If the energy of the fast neutron is sufficiently high ($\sim 1\,\mathrm{MeV}$), inelastic scattering with nuclei can take place. The recoil nucleus is elevated to one of its excited states during the collision and quickly deexcites, emitting a γ ray. The neutron loses a greater fraction of its energy during recoil than it would in an equivalent elastic collision. This inelastic scattering of the neutron with Xe nuclei can be used to calibrate LXe detectors with low-energy γ rays. More uniform irradiation of the detector is possible compared with the case of using the same energy γ ray sources due to the longer penetration depth of the neutrons. Tab. 2.5 lists inelastic neutron interactions in LXe along with their decay half-lives and γ ray energies.

Table 2.5: Table of the most likely inelastic neutron interactions with production of low-energy γ rays on Xe. Data from the ENDF/B-VII.0 database [Chadwick *et al.*, 2006]. Table from [Plante, 2012].

Reaction	Cross Section [a] (barns)	Decay Half-Life	γ Energy (keV)
$^{129}\mathrm{Xe}(n,n')^{129}\mathrm{Xe}$	0.28	0.97 ns	39.58
$^{131}\mathrm{Xe}(n,n')^{131}\mathrm{Xe}$	0.15	0.48 ns	80.19
$^{129}\mathrm{Xe}(n,n')^{129m}\mathrm{Xe}$	0.011	8.88 d	236.14
$^{131}\mathrm{Xe}(n,n')^{131m}\mathrm{Xe}$	0.054	11.84 ns	163.93

[a] Cross section at 1 MeV

While neutron inelastic interactions with Xe do not contribute to a background for a dark matter search, since the associating γ rays have a high energy, outside of the region of interest, elastic interactions of neutrons constitute an irreducible neutron background. Fortunately, fast neutrons tend to scatter multiple times in a large detector (the neutron elastic mean free path is ~ 10 to $20\,\mathrm{cm}$ at energies of a few tens of keV to $10\,\mathrm{MeV}$) unlike WIMPs and hence, they can be rejected by using the single-to-multiple scatter ratio. However, at the current scale of LXe detectors ($\sim 30\,\mathrm{cm}$), making use of the single-to-multiple scatter ratio does not provide significant rejection. Therefore, detector materials must be chosen such that the total neutron production rate is far less than one neutron interaction, in the region of interest during a dark matter search.

2.3 Scintillation Signal

2.3.1 Mechanism of Scintillation

Scintillation, the emission of luminescence, from liquid rare gases is attributed to the decay of excimers (Xe_2^*) to the ground state. Both direct excitation of atoms and electron-ion recombination lead to the formation of excimers. Thus, the origin of the scintillation photons in LXe is attributed to two separate processes involving excited atoms (Xe^*) and ions (Xe^+), both produced by ionizing radiation.

$$\mathrm{Xe}^* + \mathrm{Xe} \rightarrow \mathrm{Xe}_2^* \tag{2.5}$$

$$\begin{aligned} \mathrm{Xe}^+ + \mathrm{Xe} &\rightarrow \mathrm{Xe}_2^+, && \text{(2.6a)} \\ \mathrm{Xe}_2^+ + \mathrm{e}^- &\rightarrow \mathrm{Xe}^{**} + \mathrm{Xe}, && \text{(2.6b)} \\ \mathrm{Xe}^{**} &\rightarrow \mathrm{Xe}^* + \mathrm{heat}, && \text{(2.6c)} \\ \mathrm{Xe}^* + \mathrm{Xe} &\rightarrow \mathrm{Xe}_2^* && \text{(2.6d)} \end{aligned}$$

$$\mathrm{Xe}_2^* \rightarrow 2\mathrm{Xe} + h\nu \tag{2.7}$$

Eq. 2.5 indicates the process from excitation and Eq. 2.6 shows the sequential processes due to ionization. Both processes lead the production of vacuum ultraviolet (VUV) scintillation photons, whose wavelengths are centered at 178 nm with width of 14 nm [Jortner *et al.*, 1965], via Eq. 2.7. Note that Eq. 2.5 and Eq. 2.6d are identical, i.e., even for the ionization process, the final VUV scintillation photons are produced by excimers. In addition, it is clear that the presence of a strong enough external electric field would influence the process of Eq. 2.6b.

Although it is not a fundamental process for the production of scintillation photons, an additional process may play a role in the amount of scintillation photons produced. At high ionizing densities, as is the case for the high linear energy transfer (LET) tracks, such as α particles and fission fragments, and nuclear recoils, quenching of the amount of scintillation photons is observed. The fact that lifetimes of the VUV emission do not depend on the LET (or the existence of quenching itself) suggests that quenching occurs prior to the creation of the excitons [Hitachi, 2005]. Hitachi proposed the "bi-excitonic collision" quenching mechanism

$$\mathrm{Xe}^* + \mathrm{Xe}^* \rightarrow \mathrm{Xe}_2^{**} \rightarrow \mathrm{Xe} + \mathrm{Xe}^+ + e^- \tag{2.8}$$

By collision of two excitons, an electron-ion pair and an electron are produced. The ejected electron, e^- may recombine with an ion to reform an exciton and the overall result is that two excitons are required for one photon. As the name states, a collision of two excitons is required for this mechanism and hence, it is possible only at high LET tracks.

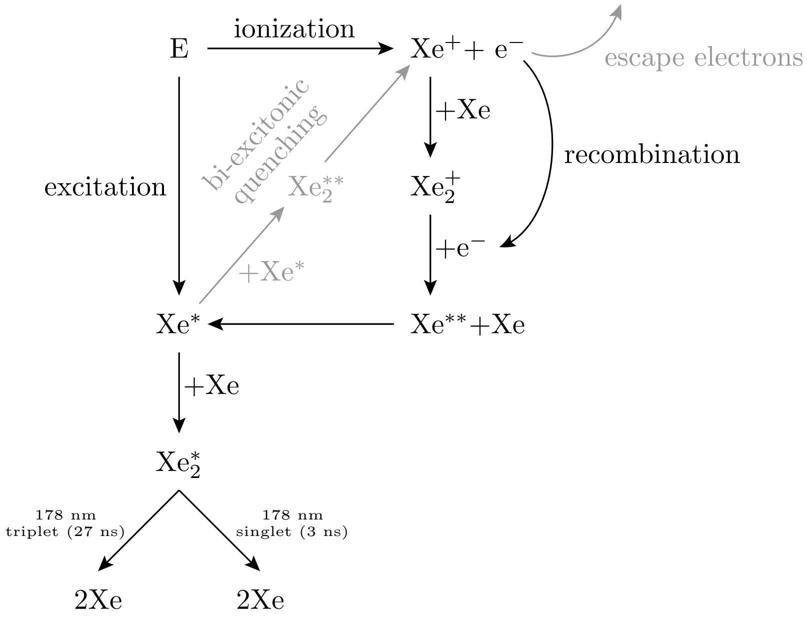

Figure 2.4: Scintillation mechanism in LXe (black) and different processes that can lead to the quenching of the scintillation light (gray). Figure from [Plante, 2012].

Fig. 2.4 summarizes schematically scintillation mechanism in LXe (black) and different processes that can lead to the quenching of the scintillation light (gray).

2.3.2 Scintillation Pulse Shape

The scintillation photon from LXe has two decay components due to deexcitation of the singlet ($^1\Sigma_u^+$) and triplet states ($^3\Sigma_u^+$) of the excimer Xe_2^*. The shorter decay shape is produced by the deexcitation of singlet states and the longer is from the deexcitation of triplet states. While the singlet and triplet lifetimes depend only weakly on the density of excited species, the intensity ratio of singlet to triplet states is larger at higher deposited energy density.

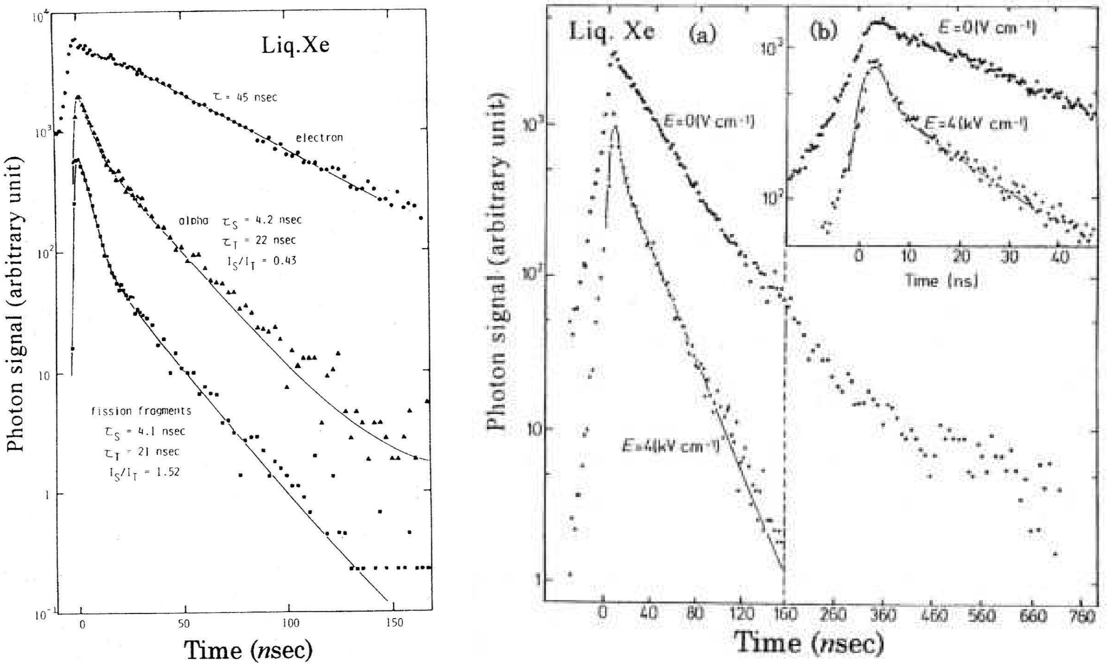

Figure 2.5: Decay curves of scintillation from LXe excited by electrons, α particles, and fission fragments, without electric field (left). Figure from [Hitachi *et al.*, 1983]. Decay curves of scintillation from LXe with and without an electric field of 4 kV/cm, over a long time scale and short time scale (right). Note the change in time scale at 160 ns in long time scale. Figure from [Kubota *et al.*, 1978a].

Fig. 2.5 (left) shows the decay curves of the scintillation photons for electrons, α particles, and fission fragments in LXe, without an electric field. The short and long decay times are 4.2 and 22 ns for α particles and 4.1 and 21 ns for fission fragments, respectively [Hitachi *et al.*, 1983]. These decay times make LXe one of the fastest scintillators. For relativistic electrons, the scintillation has only one decay component for relativistic electrons, with a decay time of 45 ns [Kubota *et al.*, 1979; Hitachi *et al.*, 1983]. The short decay time for relativistic electrons is 2.2 ± 0.3 ns and the long decay time is 27 ± 1 ns, with an electric field of 4 kV/cm [Kubota *et al.*, 1978a] (Fig. 2.5 (right)). The disappearance of two decay components without electric field seems to be attributed to the slow recombination between electrons and ions produced by relativistic electrons. The difference in the scintillation pulse decay shape for different types of particle in liquid rare gases can be used to effectively discriminate these particles. Pulse shape discrimination (PSD) is, however, difficult for LXe given the small time separation of the two decay components unlike liquid argon (LAr).

2.3.3 Scintillation Yield

The scintillation yield is given as E/W_{ph}, where E is the energy deposited by the ionizing radiation and W_{ph} is the average energy required for the production of a single photon. As explained in Sec. 2.3.1, the amount of scintillation photons produced is subject to the effects of external electric fields or quenching processes. If the strength of an external electric field in LXe increases, the recombination process is suppressed and it results in reduced scintillation yield. The scintillation yield also depends on the linear energy transfer (LET) because the recombination probability between electrons and ions increases with the density of electron-ion pairs.

The LET dependence of scintillation yield in LXe is shown in Fig. 2.6 for various types of particles [Doke *et al.*, 2002]. In the low LET region, the scintillation yield gradually decreases with decreasing LET. Relativistic electrons (solid squares) and electronic recoils from γ rays (open squares) are understood to have a reduced scintillation yield due to escape electrons which do not recombine with parent ions for an extended period of time (on the order of few ms) in the absence of electric field. In the high LET region, the scintillation yield curve shows saturation above $100\,\mathrm{MeV\,g^{-1}\,cm^{-2}}$ from relativistic heavy ions (solid circles). Significantly lower scintillation yield from α particles and fission fragments can be understood by bi-excitonic collision. The flat behavior of the LET in LXe assumed to be corresponding to the maximum scintillation yield (absolute scintillation yield). It is

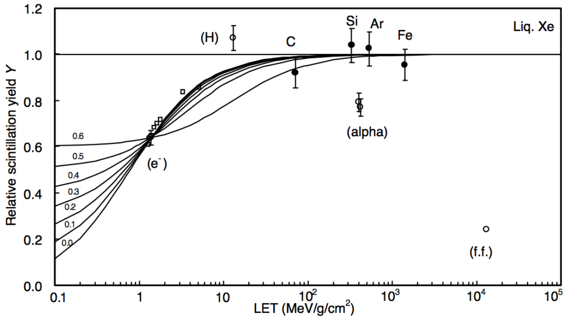

Figure 2.6: Dependence of scintillation yield on LET in LXe for various types of particles. Relativistic heavy ions (solid circles) at high LET have a scintillation yield regardless of LET and assumed to be the maximum scintillation yield in LXe. Relativistic electrons (solid square) and electronic recoils from γ rays (open squares) are interpreted to have a reduced scintillation yield due to the effect of escape electrons. The reduced scintillation yield of α particles is attributed to biexcitonic quenching [Hitachi, 2005]. Figure from [Doke *et al.*, 2002].

not straightforward to verify this from the measurements at high LET since ionization and scintillation signals were not observed simultaneously. However, the similar result using LAr by measuring simultaneously both signals supports this assumption. From the simultaneous measurement of ionization and scintillation of 1 MeV electrons (solid square) and with the maximum scintillation yield assumption on the flat behavior, the average energy required to produced a scintillation photon is estimated as $W_{\mathrm{ph}}(\mathrm{max}) = 13.8\,\mathrm{eV}$ [Doke *et al.*, 2002].

2.3.4 Nuclear Quenching on Scintillation Yield: Lindhard Factor

As mentioned earlier, recoiling electrons lose almost all of their energy through electronic excitation in electronic recoils, but recoiling nuclei also lose energy through elastic collisions with other nuclei. While some of these nuclei create further ionization, most have energies below the ionization threshold. This energy loss is not detectable in LXe, so what we observe is an overall suppression of electronic excitation for nuclear recoils.

Lindhard calculated the total electronic energy loss in a nuclear recoil [Lindhard *et al.*, 1963]. The energy dependent Lindhard factor $\mathcal{L}$, defined as the fraction of the initial recoil energy eventually lost to electronic excitation, is parameterized as [Lewin and Smith, 1996]

$$\mathcal{L} = \frac{kg(\epsilon)}{1 + kg(\epsilon)} \tag{2.9}$$

where

$$\epsilon = 11.5E_{\rm nr}(\,{\rm keV})Z^{-7/3}, k = 0.133Z^{2/3}A^{-1/2}, g(\epsilon) = 3\epsilon^{0.15} + 0.7\epsilon^{0.6} + \epsilon \tag{2.10}$$

for a recoil of energy $E_{\rm nr}$.

Eq. 2.9 provides the generic prediction for $\mathcal{L}$ in any material, and precisely describes the nuclear quenching of ionization signals in semiconductors [Chasman *et al.*, 1968; Jones and Kraner, 1975; Messous, 1995]. In LXe, nuclear quenching alone cannot explain the observed scintillation yield at low energies [Aprile *et al.*, 2005], but reasonable agreement can be obtained when electronic quenching is considered [Hitachi, 2005; Mei *et al.*, 2008]. Recently it has been suggested that if both the scintillation and ionization signals are included, the Lindhard prediction is compatible with the observed quenching [Sorensen and Dahl, 2011]. The lower scintillation yield observed is attributed to a change in the fraction of energy that ultimately goes in to ionization instead of scintillation.

Experimentally, the Lindhard factor is inferred from the measurement of the relative scintillation efficiency of nuclear recoils, $\mathcal{L}_{\rm eff}$, the so-called "effective Lindhard factor". Detailed use of $\mathcal{L}_{\rm eff}$ will be explained in Sec. 4.2.3.

2.3.5 Detection of Scintillation Photons: Absorption, Scattering, Refraction, and Reflection

From Sec. 2.3.1 to Sec. 2.3.3, we have learned about the production of scintillation photons in LXe. However, measuring the scintillation signal requires additional considerations related to the detection efficiency of the scintillation photons. Absorption, scattering of scintillation photons in LXe, the refraction index of LXe, and reflection of scintillation photons to the detector materials heavily influence the scintillation photon collection efficiency.

LXe is essentially transparent to its own scintillation photons because the energy of a scintillation photon released from the relaxation of the exciton ($\sim 7\,$eV) is not sufficient to cause atomic excitation [Schwentner *et al.*, 1985]. Nevertheless, impurities dissolved in LXe may absorb the VUV photons, reducing the observed scintillation yield. Light attenuation is described by

$$I(x) = I(0)\exp(-x/\lambda_{\mathrm{att}}) \tag{2.11}$$

where λ_{att} is the photon attenuation length, which consists of two separate components, the absorption length λ_{abs}, describing true absorption and loss of photons by impurities, and the scattering length λ_{sca}, representing elastic scattering of photons without any loss. The latter is dominated by Rayleigh scattering. Since Rayleigh scattering effectively makes the travel path of a scintillation photon to reach a photosensor longer, it increases the chance that a scintillation photon be absorbed by the detector materials on its way, resulting in attenuation of the scintillation yield. The two are related by

$$1/\lambda_{\mathrm{att}} = 1/\lambda_{\mathrm{abs}} + 1/\lambda_{\mathrm{sca}} \tag{2.12}$$

The attenuation length can be measured after removing the contribution from Rayleigh scattering. The Rayleigh scattering length is measured to be $\lambda_{\mathrm{Rayleigh}} = 29\,\mathrm{cm}$ [Ishida *et al.*, 1997].

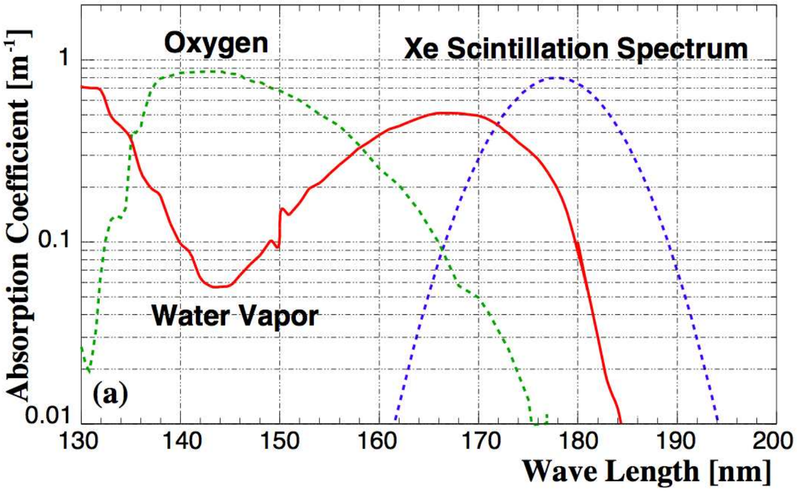

Figure 2.7: Absorption coefficient for VUV photons in 1 ppm water vapor and oxygen. The Xe scintillation spectra is superimposed. Figure from [Ozone, 2005].

The absorption length λ_{abs} of the VUV scintillation photons in LXe depends on the amount of impurities in LXe. The most serious impurity for the VUV scintillation photons of LXe is water vapor, which is largely contributed by the outgassing of the liquid containment vessel and other detector materials placed inside the liquid, followed by oxygen. Fig. 2.7 [Ozone, 2005] shows the absorption coefficient for VUV scintillation photons in 1 ppm water vapor and oxygen. The absorption spectra of water and oxygen largely overlap with the xenon scintillation spectrum.

The higher refractive index of LXe than that of gaseous xenon (GXe) (See Tab. 2.1) affects the scintillation photon detection in dual-phase detectors. Scintillation photons produced in LXe will undergo total internal reflection at the liquid-gas interface and the amount of scintillation photon detected in each phase will be influenced accordingly.

The inner surface of a LXe detector is often made of polytetrafluoroethylene (PTFE) due to its high VUV reflectivity. Measurements of the reflectivity of PTFE for Xe scintillation photons have ranged from 60 % [Barabanov *et al.*, 1987a] to values as large as 95 % [Yamashita *et al.*, 2004]. Recent measurements of the reflectivity of PTFE at LXe scintillation wavelengths for different types of PTFE yield values ranging from 47 to 66 %, but there exist indications that when immersed in LXe the reflectivity could be considerably higher [Silva *et al.*, 2010]. The most recent measurements of the same quantity found a range of values from 49 to 80 % [Choi, 2012].

2.4 Ionization Signal

In addition to the scintillation signal, LXe converts its deposited energy in the form of the ionization signal via production of electron-ion pairs. LXe has band structures like a semiconductor or an insulator [Asaf and Steinberger, 1974] and its large band gap energy E_g (the energy difference between the bottom of the conduction band and the top of the valence band) of 9.28 eV makes it a good insulator.

As shown in Tab. 2.3, the average energy required to produce an electron-ion pair is 15.6 eV, less than other liquid noble gases [Miyajima *et al.*, 1974; Aprile *et al.*, 1993], and hence it makes LXe the liquid noble gas with the largest ionization yield. Since electron-ion pairs tend to recombine to neutral atoms, an external electric field across the detection medium is required to collect electrons and ions separately. Given that a Xe ion is much heavier than an electron, the ionization signal is usually measured by drifting the electrons through LXe without loss of electrons. Therefore, keeping LXe ultra-pure to prevent the attachment of electrons to impurities is critical to obtain ionization signal. The detailed processes are explained in the followings sections.

2.4.1 Drift Velocity

The conduction electrons created by ionizing radiation remain as a localized small cloud as they drift along the electric field line. The drift velocity of electrons, v_d, is proportional to the applied electric field at low values of the electric field. The proportionality constant is called the electron mobility, μ ($v_d = \mu$E). At high fields, the electron drift velocity saturates. Fig. 2.8 shows the electron drift velocity dependence on the ratio of electric field to gas density in LXe and GXe [Atrazhev *et al.*, 2005].

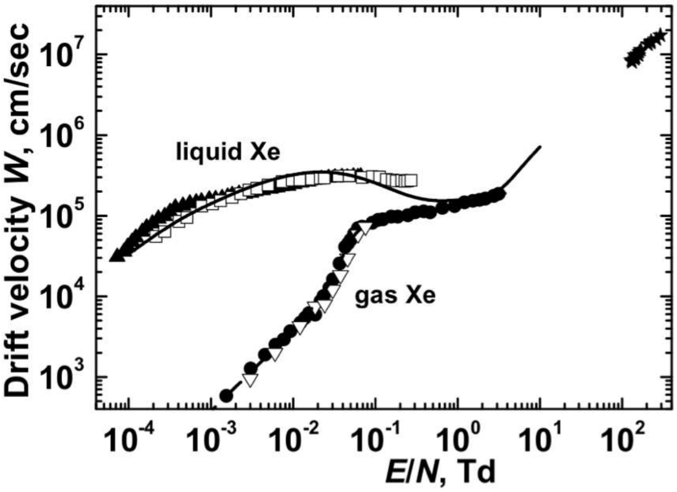

Figure 2.8: Electron drift velocity in LXe and GXe as a function of the ratio of electric field to gas density (E/N) from several measurements [Gushchin *et al.*, 1982; Pack *et al.*, 1992; Huang and Freeman, 1978], along with a calculation [Atrazhev *et al.*, 2005]. $1\,\mathrm{Td} = 10^{-17}\,\mathrm{V\,cm^2}$. Figure from [Atrazhev *et al.*, 2005].

The drift velocity of Xe ions is several orders of magnitude smaller than that of electrons [Hilt and Schmidt, 1994].

2.4.2 Electron Attachment

Since LXe is operated at the highest temperature among liquid noble gases, some of the impurities are not frozen out. When conduction electrons drift in LXe and collide with electronegative impurities, they form ions which drift far slower, due to their heavier masses and this electron attachment to impurities causes reduction of the ionization signal. The average time before the collision of a conduction electron with an electronegative impurity is the electron lifetime, τ_e. Under the assumption that impurities are distributed uniformly in LXe, the number of electrons remaining free after drifting across a distance z, $N_e(z)$, is,

$$N_e(z) = N_{e|z=0}\mathrm{exp}\left(-\frac{z}{v_d\tau_e}\right) \tag{2.13}$$

where $N_{e|z=0} = N_e(0)$. The probability that the electrons be captured by impurities is a function of electron energy and hence the applied electric field. The most common impurity is O_2, whose attachment rate to electrons can be reduced by increasing the electric field. The rate constants dependence on the electric field for O_2, N_2O, and SF_6 can be seen in Fig. 2.9.

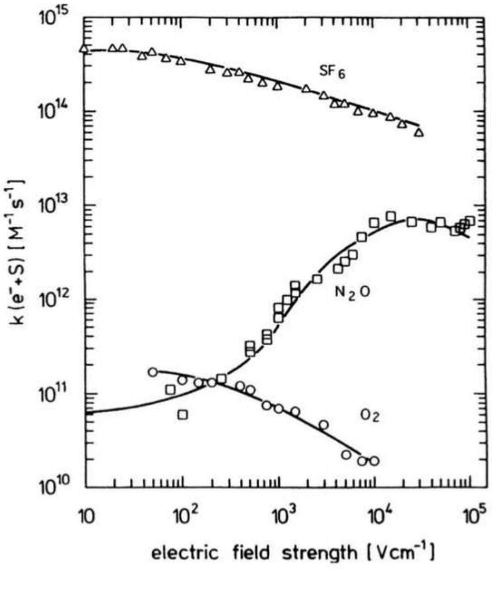

Figure 2.9: Electric field dependence of the rate constants of electron attachment to O_2, N_2O, and SF_6 in LXe. Figure from [Bakale *et al.*, 1976].

2.4.3 Recombination

With the application of an external electric field across LXe, the recombination of electron-ion pairs (Eq. 2.6b) is suppressed. This leads to the reduction of scintillation photon production, and the amount of quenching of the scintillation signal depends on the field strength. The scintillation quenching due to the electric field was first observed in LXe and LAr by [Kubota *et al.*, 1978b]. The quenching is accompanied by the increase of ionization electron collection since the electrons that do not recombine produce a corresponding ionization signal. There exists an ionization density dependence in recombination. In higher ionization density tracks, such as α particles or nuclear recoils, more electrons can recombine even in the presence of a strong electric field compared with lower ionization density like electronic recoil tracks. This ionization density dependence of recombination is the key mechanism of discrimination which benefits the electronic recoil background suppression at low energies in a WIMP search. Fig. 2.10 shows the electric field dependence of the relative scintillation

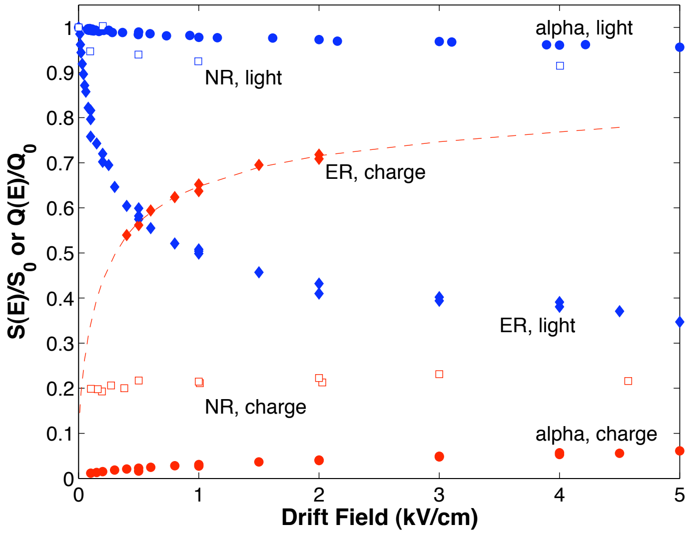

Figure 2.10: Drift field dependence of relative scintillation and ionization yields of α particles, electronic recoils, and nuclear recoils in LXe. Figure from [Aprile *et al.*, 2006].

and ionization signals for α particles, nuclear recoils and electronic recoils [Aprile *et al.*, 2006].

The recent measurement of [Conti *et al.*, 2003] indicates the clear evidence of anti-correlation between ionization and scintillation fluctuations in LXe. It is observed that at a given energy, a smaller scintillation signal is always accompanied by a larger ionization signal as if the total quanta of ion-electron pairs and excitons is fixed. By measuring both signals on an event by event basis, the energy resolution can be improved to the level predicted by the Fano factor [Aprile *et al.*, 2007b].

2.4.4 Electroluminescence: Electron Emission and Amplification

In a dual-phase detector with a sufficiently high electric field, the drifted electrons can acquire kinetic energies which exceed the potential barrier of the liquid-gas interface (due to the larger dielectric constant of LXe than that of GXe), and be extracted into the gas phase. This electron emission allows for the amplification of the ionization signal through the collision of electrons with Xe atoms in the gas gap. With high enough electric field in GXe, proportional scintillation photons are created via excitation of atoms. This is called proportional scintillation or electroluminescence, because the size of the signal is proportional to the number of electrons drifted. The photon yield per unit length per electron dN_{ph}/dx is empirically determined to be

$$\frac{dN_{\mathrm{ph}}}{dx} = \alpha \left(\frac{E_g}{p} - \beta \right) p \tag{2.14}$$

where $\alpha = 70\,\mathrm{photons\,kV^{-1}}$, $\beta = 1\,\mathrm{kV\,cm^{-1}\,atm^{-1}}$, E_g is the electric field in the gas gap, and p is the pressure [Belogurov *et al.*, 1995].

The benefit of amplification is reaching a lower energy threshold without suffering worse energy resolution than without amplification. It can even lead to detection of single electron signals in the LXe TPC [Edwards *et al.*, 2008].

2.4.5 Discrimination

As explained in Sec. 2.4.3, the ionization density dependence in recombination leads to the discrimination of nuclear recoils from electronic recoils. In a dual-phase LXe detector, the ratio of proportional scintillation over (prompt) scintillation is used as a particle type discriminant.

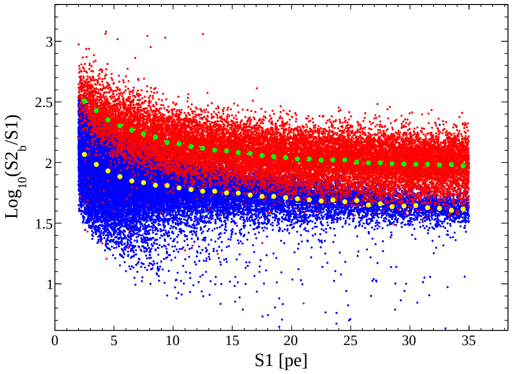

Figure 2.11: Discrimination between electronic recoils (red) and nuclear recoils (blue) in XENON100. The green circles and yellow circles indicate the means of electronic recoils and nuclear recoils, respectively. Y-axis shows discrimination parameter, the log of ratio of proportional scintillation signal to scintillation signal, and the x-axis indicates energy. As shown in the figure, electronic recoils and nuclear recoils can be separated well in this parameter space. Details about the bands will be explained in Sec. 4.4 and we will revisit this figure in the same section. Credit: XENON100 collaboration.

Fig. 2.11 shows the discrimination ability of XENON100. Red data points indicate the response of electronic recoils using ^{60}Co and ^{232}Th sources, and the blue data points indicate the response of nuclear recoils using an ^{241}AmBe(α, n) source. The separation between the two bands allows for $\sim 99.5\,\%$ electronic recoil events rejection while still keeping $50\,\%$ of the nuclear recoil events acceptance. The rejection power increases as the electronic recoil energy decreases, and the width of the electronic recoil band becomes narrower.

The origin of the discrimination in LXe is not well understood at the microscopic level. The recombination model [Dahl, 2009] correctly reproduces the energy and electric field dependence of the band centroids but not recombination fluctuations. Nevertheless, for practical purpose of rejecting electronic recoil background, the ratio of proportional scintillation signal to prompt scintillation signal in LXe provides a good method to distinguish nuclear recoils (WIMP-like signal) from electronic recoils (background).

Chapter 3

The XENON100 Experiment

The motivation of dark matter searches and the reasons why WIMPs are one of the most plausible theoretical candidates for dark matter were presented in Chap. 1. In Chap. 2, we presented LXe as an attractive WIMP detection medium. Now we turn to one of the most successful WIMP search experiments using LXe, which has set the most stringent limits on the spin-independent elastic WIMP-nucleon scattering cross section for WIMP masses above $8\,\mathrm{GeV}/c^2$ to date [Aprile *et al.*, 2012a].

The XENON100 experiment uses LXe as both the WIMP target and detection medium. The detector is a cylindrical dual-phase (gas-liquid) time projection chamber (TPC) enclosing a LXe target mass of 62 kg, and is operated at the Laboratori Nazionali del Gran Sasso in Italy. The LXe TPC is the key technique on which the success of XENON100 is supported. The excellent electronic stopping power of LXe combined with the position reconstruction capabilities of a dual-phase ionization-scintillation TPC lead to effective fiducialization. This allows for the use of only the inner volume of the full active volume as a WIMP target, with the outer volume used as a self-shielding material. This fiducialization helps to suppress the electronic recoil background significantly and hence benefits the low background requirements for a WIMP search. In addition, the ionization density dependence of recombination of ionized Xe molecules with electrons allows further background rejection using the discriminating power of nuclear recoils (expected from a WIMP signal) from electronic recoils (electromagnetic background).

In this chapter, we review the principle of a generic XENON type dual-phase TPC and describe the XENON100 detector and its subsystems.

3.1 Principle of the XENON dual-phase TPC

Dual-phase ionization-scintillation liquid noble gas TPCs measure both the prompt scintillation light, emitted as a particle recoils in the liquid target, and the ionization electrons produced, via the proportional scintillation light emitted as they are accelerated in the gas phase. A schematic of the XENON dual-phase TPC is shown in Fig. 3.1. A particle interaction in the XENON TPC (left) is shown along with sketch of the waveforms of two types of events (right). The TPC is enclosed by optically reflective side walls, a cathode grid on the bottom, a gate grid a few mm below the liquid-gas interface, and an anode grid on the top, a few mm above the liquid-gas interface. The cathode is connected to a negative high voltage. The gate grid is fixed at the ground potential to separate the electric fields in the

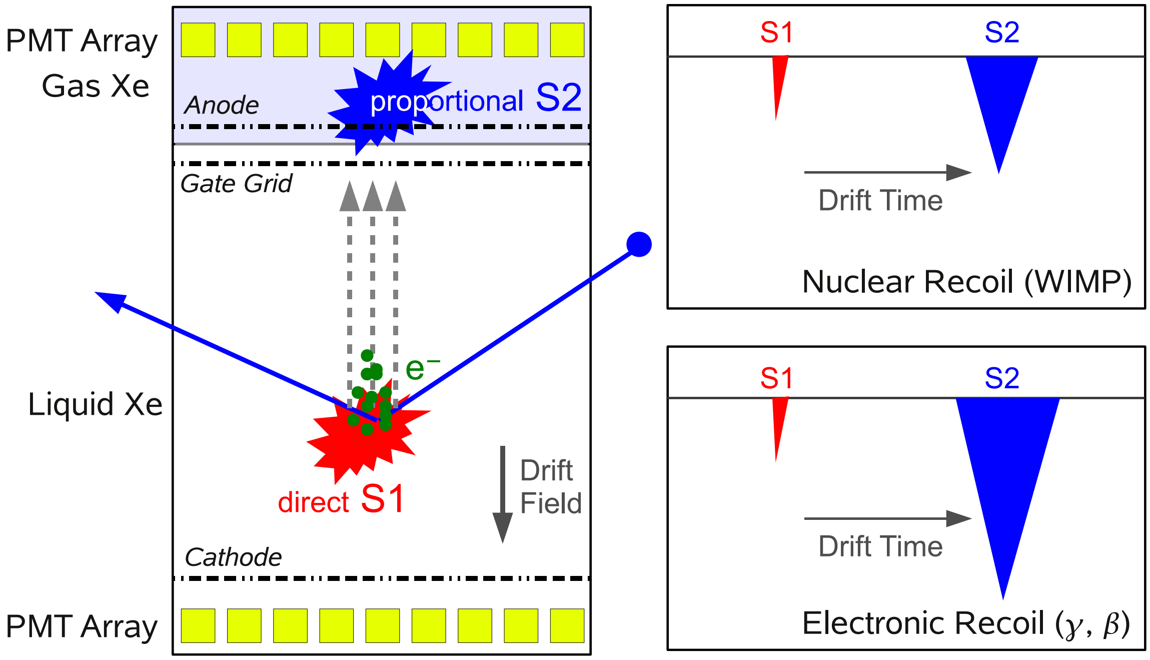

Figure 3.1: Working principle of the XENON dual-phase liquid-gas TPC (left) and sketch of the waveforms of electronic (right, top) and nuclear (right, bottom) recoils with both S1 and S2 signals. Figure from [Aprile *et al.*, 2012c].

bulk of LXe from those in the vicinity of liquid-gas interface, and the anode is maintained at a positive high voltage. Two photomultiplier tube (PMT) arrays, one above the anode and one below the cathode are used to collect the prompt scintillation and proportional scintillation photons.

When a particle interacts in the LXe active volume, both scintillation photons and ionization electrons are produced at the interaction site. The prompt scintillation signal is detected by the PMTs immediately after the interaction, producing a fast rising pulse that we refer to as S1. The ionized electrons are drifted by the applied electric field between the cathode and the gate grid to the liquid-gas interface. A stronger electric field between the gate grid and the anode there extracts the electrons into the gas phase. Proportional scintillation photons, whose total number is proportional to the number of ionization electrons, are emitted as the electrons are accelerated in this high field region and are measured by the PMTs, producing a delayed proportional scintillation pulse that we refer to as S2. The time difference between the S1 and the S2 signals is used to measure the depth (z) coordinate while the spatial distribution of the S2 signal on the PMTs of the top array provides a way to reconstruct the (x, y) position in the transverse plane. (See Sec. 4.1.3 for the details of the 3D vertex reconstruction of XENON100.) Thus, the XENON100 TPC provides full 3D vertex reconstruction on an event-by-event basis allowing for the fiducialization of the target volume to reduce backgrounds. Further background reduction can be performed using the discrimination of nuclear recoils from electronic recoils through the ratio of the ionization signal to the scintillation signal, with a discrimination power often set at the 99.5 % level at low energies while maintaining 50 % of the nuclear recoil acceptance, as mentioned in Sec. 2.4.5.

3.2 Detector Design

The design goal of XENON100 was an order of magnitude increase in target mass and two orders of magnitude reduction of the low-energy γ background level compared to its predecessor, XENON10 [Aprile *et al.*, 2011a; Angle *et al.*, 2008a], for ~ 50 times greater sensitivity. Most of the ideas to achieve this goal came from the experience of XENON10 and many of them were focused on the improvements of XENON10. First of all, an extensive campaign of detector materials radioactivity screening was performed to find those with an acceptable activity for detector construction, and to measure the intrinsic radioactivity of several commercial components used in the assembly. The description of the facility, measurement, and the results are reported in [Aprile *et al.*, 2011d].

In addition, minimization of the detector subsystems housed inside the passive shield was pursued to reduce the γ background from detector materials. In XENON10, the pulse tube refrigerator (PTR) was mounted inside the passive shield to cool the LXe. In XENON100, the PTR was moved outside of the passive shield and a remote cooling of the LXe has been implemented. Details of the cryogenic system are provided in Sec. 3.5. All of the other equipment, such as pressure sensors, turbo molecular pumps, diaphragm pumps, and vacuum gauges, are also attached to the cryostat volume outside of the passive shield. The total mass of steel within the shield cavity was reduced from 180 kg for the much smaller XENON10 detector to about 70 kg for XENON100.

From the data analysis of XENON10, a certain class of events was found to contribute to background due to the detector design, the so-called “anomalous leakage events” [Angle *et al.*, 2008a]. Anomalous leakage events were identified as electronic-recoil multiple scatters that give rise to signals indistinguishable from single scatters due to the scatter geometry. In these events, one scatter occurs in a part of the detector that is sensitive to the scintillation (S1) signal only. This could be below the cathode, where the detector is particularly charge insensitive. The other scatter then occurs in the light and charge sensitive volume. The resulting signal then has a reduced discrimination power against nuclear recoils, due to a reduced S2/S1 ratio with respect to single-scatter electronic recoils. Therefore, particular effort was made to minimize the occurrence of this type of event in the design stage of the detector. Two decisions were made for this purpose. First, minimize the charge insensitive volume below the cathode by keeping the distance between the cathode and the bottom PMT array as short as possible. Second, the idea of using an active LXe veto to tag these events was introduced. This was under the reasoning that γ rays responsible for anomalous leakage events from additional scatters in the charge insensitive volumes should escape to the volume on the side or on the bottom. This topology was considered mostly likely due to the Compton scatter of high energy γ rays which lose only a few keV energy in the sensitive volume and travel in all directions. If they keep traveling in the sensitive volume, they fail to fulfill both the single scatter selection cuts and the energy of interest cut, and are thus not a problem. But if they escape to the bottom or side of the TPC, they can be tagged by instrumenting those volumes with PMTs which can actively veto them. Anomalous leakage events in XENON100 will be discussed thoroughly in Chap. 5.

The LXe veto idea also provides another practical advantage, the reduction of the γ background from the inner surface of the detector vessel. Due to the self-shielding by the LXe, having only a few cm of LXe volume outside of the TPC is already helpful to suppress the background from the inner surface of the detector vessel [Aprile *et al.*, 2011e]. However, by “turning on the eyes” outside of the TPC through instrumenting the optical separation with PMTs, about two orders of magnitude greater low-energy γ background suppression can be achieved, even with relatively low quantum efficiency (QE) PMTs. Moreover, this reduction of event rate in the sensitive volume helps to reduce the overall data volume, of benefit to data transfer (see Sec. 3.9).

Finally, a radially symmetric pattern in the top PMT array with an extension of one PMT width beyond the radius of the sensitive volume was adopted for a more precise (x, y) position reconstruction.

After these considerations, extensive Monte Carlo simulations based on the GEANT4 simulation toolkit [Agostinelli *et al.*, 2003] were performed to estimate the performance of the detector, with the final output of the projected sensitivity for the spin-independent WIMP-nucleon scattering cross section. Details of design considerations and simulations are explained in [Plante, 2012]. Fig. 3.2 shows a technical drawing of the final detector design approved for construction.

3.2.1 Time Projection Chamber

The almost cylindrical XENON100 TPC has dimensions 30.5 cm in height and 15.3 cm in radius with the capacity to contain 62 kg of LXe target. Fig. 3.3 shows the top and bottom copper ring frames of the TPC during the installation of the side polytetrafluorethylen (PTFE) panels and the fabrication of the field shaping copper wires. The walls delineating

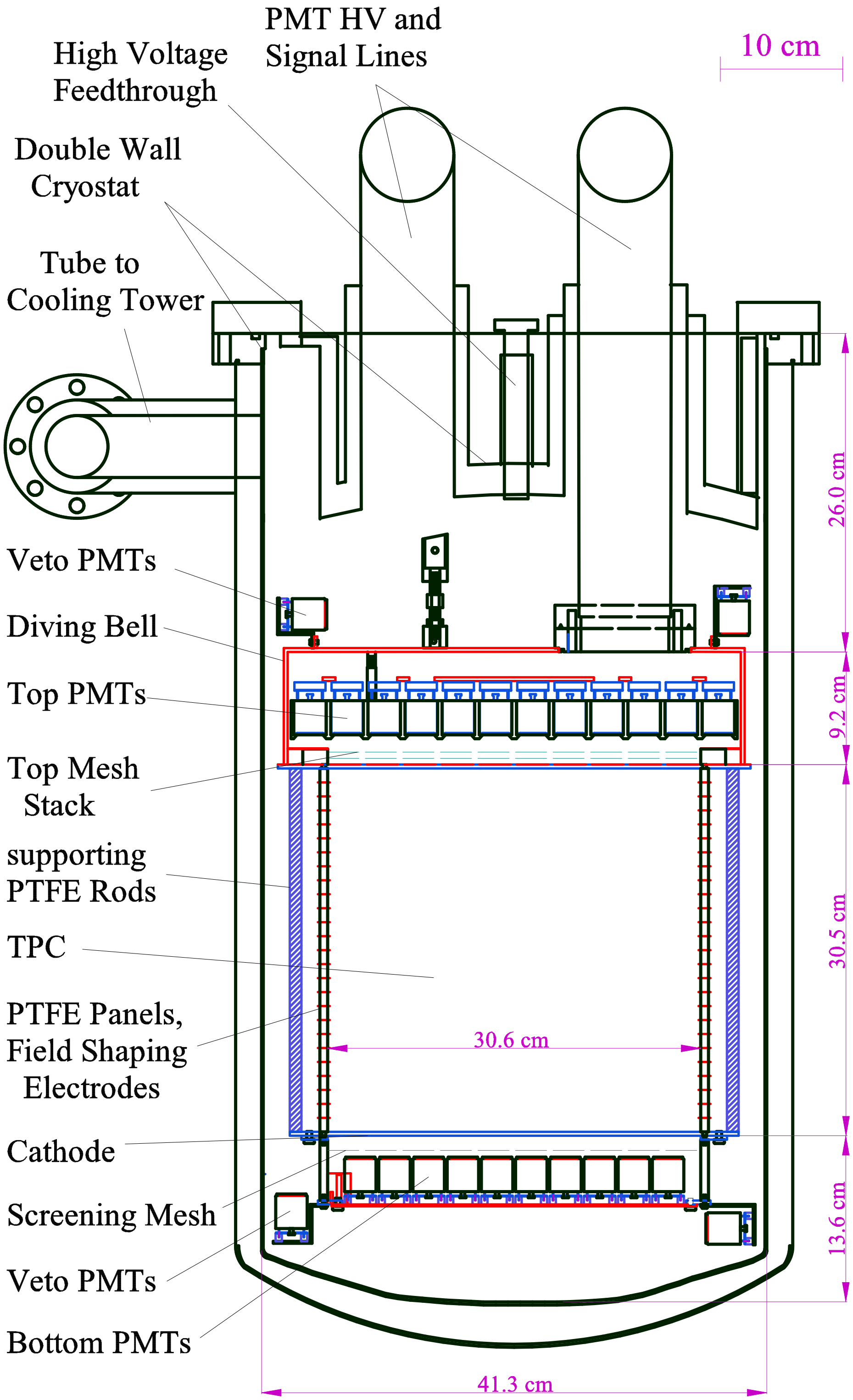

Figure 3.2: Drawing of the XENON100 dark matter detector with its dimensions. Original technical drawing by Dr. K. Giboni. Figure from [Aprile *et al.*, 2012c].

Figure 3.3: Picture of the top and bottom copper ring frames of the TPC, along with 16 PTFE support rods and two interlocking PTFE panels during panel installation (left), and a picture of the TPC during the fabrication of the field shaping copper wires (right). From left to right: the author and M. Schumann (Rice University).

the cylindrical volume and separating it from the active LXe veto shield, which surrounds the target, are made of 24 interlocking panels of 1/4 inch-thick PTFE. PTFE is chosen both for its properties as an electrical insulator and as a good reflector of VUV scintillation photons as mentioned in Sec. 2.3.5. The TPC is closed on the bottom by the cathode, and on the top by the gate grid (see Sec. 3.3).

Since the detector is operated in LXe at a temperature of $-91°\mathrm{C}$, shrinkage of the PTFE panels must be taken into account for the correct target mass computation and the position reconstruction of particle interactions. PTFE has a rather large linear thermal expansion coefficient $A \sim 1.2 \times 10^{-4}\,\mathrm{K}^{-1}$ as measured for the PTFE used in XENON100. This leads to a few mm of contraction of the TPC height compared to room temperature. Radial contraction is negligible because the PTFE panels are mounted between copper support rings which have a much smaller thermal expansion coefficient ($A_{\mathrm{Cu}} \sim 1.5 \times 10^{-5}\,\mathrm{K}^{-1}$).

3.2.2 Diving Bell: Liquid Level Adjustment for Proportional Scintillation

The key ingredient of dual-phase operation is the proportional scintillation signal in addition to the prompt scintillation signal. Hence it is critical to have a reliable S2 signal. As shown in Eq. 2.14 of Sec. 2.4.4, the amount of proportional scintillation depends on the pressure of the Xe gas and the electric field in the gas gap. The integral form of Eq. 2.14 yields

$$N_{\mathrm{ph}} = C\left(\frac{E_g}{P} - 1.0\right)P\chi \tag{3.1}$$

where N_{ph} is the number of generated proportional scintillation photons, C a scaling constant, E_g the electric field in the gas gap (in kV/cm), P the pressure of the Xe gas (in bar), and χ the height of the gas gap between LXe surface and the anode (in cm).

One thing to notice is that E_g is a function of the liquid level and the distance from the gate grid to the liquid surface, which is the distance between the gate grid and the anode - χ. The electric field in the gas gap is determined by the electric potential difference between the gate grid and the anode, the dielectric constants of LXe and GXe, and the liquid level. The maximum voltage between the anode and the gate grid is usually limited by the high voltage (HV) feedthrough. Given that the dielectric constants of the LXe and GXe are fixed, the liquid level is the parameter which has to be fine tuned last to achieve the optimum amplification which gives the best resolution of the S2 signal. A precise control of the liquid level is an essential element of successful dual-phase operation.

To minimize the impact of liquid density variations due to temperature changes, as well as fluctuations in the gas recirculation rate, a diving bell design was chosen to keep the liquid at a precise level. An additional advantage of using a bell is that the liquid in the detector vessel can be at an arbitrarily high level outside of the bell. In XENON100, this makes it possible to fill the vessel to a height of about 4 cm above the bell, enabling a 4π coverage of the TPC by the LXe veto.

Fig. 3.4 shows the bell connected to the TPC (left) and the bell attached to the cryostat lid (right). The bell keeps the liquid level at the desired height when a constant stream of gas pressurizes it. This is accomplished by feeding the Xe gas returning from the gas recirculation system into the bell. The pressure is released through a small pipe that reaches out into the LXe veto volume. The height of the LXe level inside the bell is the same as

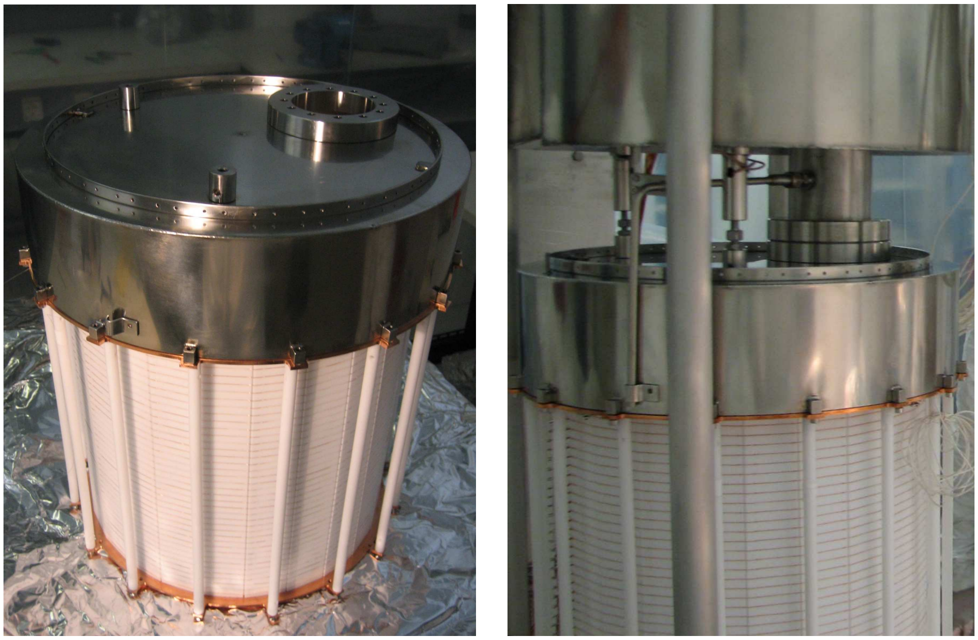

Figure 3.4: TPC with the bell on top (left) and bell attached to the cryostat lid along with a gas pipe to adjust the liquid level (right).

the height of the open end of the pipe, and this can be vertically adjusted by actuating a motion feedthrough to which the pipe is connected [Aprile *et al.*, 2012c].

3.2.3 Photomultiplier Tubes (PMTs)

The XENON100 PMTs are 2.5 cm square Hamamatsu R8520-06-Al PMTs specially selected for low radioactivity [Aprile *et al.*, 2011d]. The PMTs have a special bialkali photocathode for low-temperature operation down to −110°C, and are optimized for the detection of 178 nm Xe scintillation photons.

Fig. 3.5 shows the top and bottom PMT arrays for the scintillation photon detection in the TPC. The top PMT array is composed of 98 tubes held in a PTFE structure, arranged in concentric circles to improve the resolution of radial position reconstruction while minimizing the number of tubes required. Since PTFE is a good VUV photon reflector, the radially symmetric pattern enhances the light collection efficiency even with a reduced number of PMTs compared to a square grid arrangement. The outmost ring extends beyond

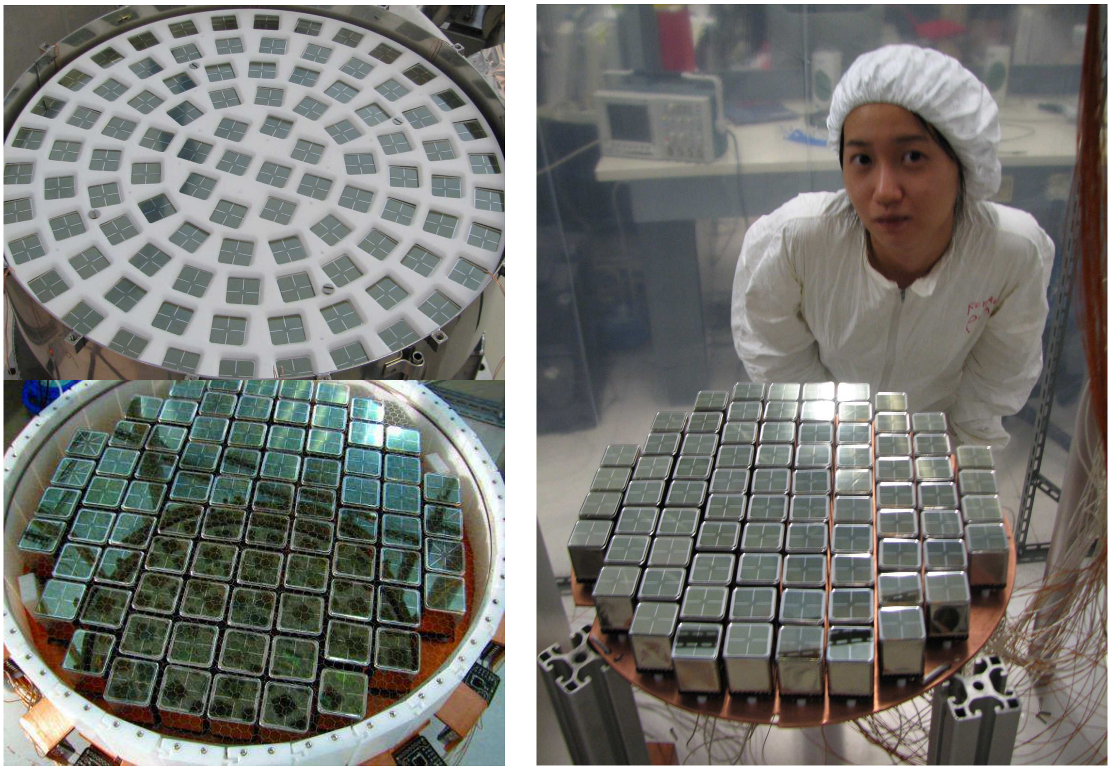

Figure 3.5: Top PMT array inside the bell (left, top), bottom PMT array with the screening mesh (left, bottom), and the author just after mounting the bottom PMTs on the copper plate (right). The difference of PMT patterns between the top and bottom arrays allows for better position reconstruction and light collection efficiency, respectively.

the TPC radius to improve position reconstruction at the edges. The bottom array consists of 80 tubes mounted in a copper plate. While the top PMT array arrangement was driven by the position reconstruction of particle interactions, the bottom PMT arrangement was optimized for with the idea of maximum coverage of the TPC bottom area. This was based on the fact that total reflection at the liquid-gas interface due to the large refractive index of LXe (1.69 ± 0.02 [Solovov *et al.*, 2004]) results in more scintillation photons propagation in the downward direction. For this reason, PMTs with higher QE were used for the bottom PMT array compared to the top PMT array. The average QE of the bottom and top PMT arrays are ~ 33 and $\sim 23\,\%$, respectively.

A LXe layer of about 4 cm thickness surrounds the TPC on all sides and is observed by 64 PMTs of the same type as used for the TPC readout. Fig. 3.6 shows the veto PMTs on the top and bottom of the TPC. The top and bottom veto arrays have 32 tubes each arranged alternating between inward and down or inward and up. This allows a simultaneous view of the top, bottom and side portions of the active veto volume. In total, this volume contains 99 kg of LXe. The presence of this LXe veto, operated in anti-coincidence mode, is very effective for background reduction [Aprile *et al.*, 2011e] and is one major difference in design compared to XENON10 as mentioned earlier.

The PMTs are operated in the ground anode scheme, that is, with the photocathode at a negative potential and the anode at a ground voltage. The PMT base circuit is printed on a Cirlex® substrate with surface mount components. The total resistance of the PMT base voltage divider resistor chain is $125\,\mathrm{M\Omega}$, chosen to minimize the heat influx from the PMTs to the LXe. At the maximum operating voltage of $-900\,\mathrm{V}$, the power dissipation is 6.5 mW/PMT, resulting in a necessary cooling power of 1.6 W to compensate for the heat influx from the total PMTs. Fig. 3.7 shows the schematic of the PMT base electrical circuit. Compared to XENON10, the design was modified and the number of electronic components was reduced in order to decrease the background contribution. The maximum S2 signal on any given PMT without suffering PMT non-linearity is estimated to be ~ 8700 pe [Plante, 2012]. In reality, the only way to observe this effect in data is through worsening of position reconstruction. This value is then consistent with the observed value, which depending on the PMT can start between ~ 6000 and 9000 pe.

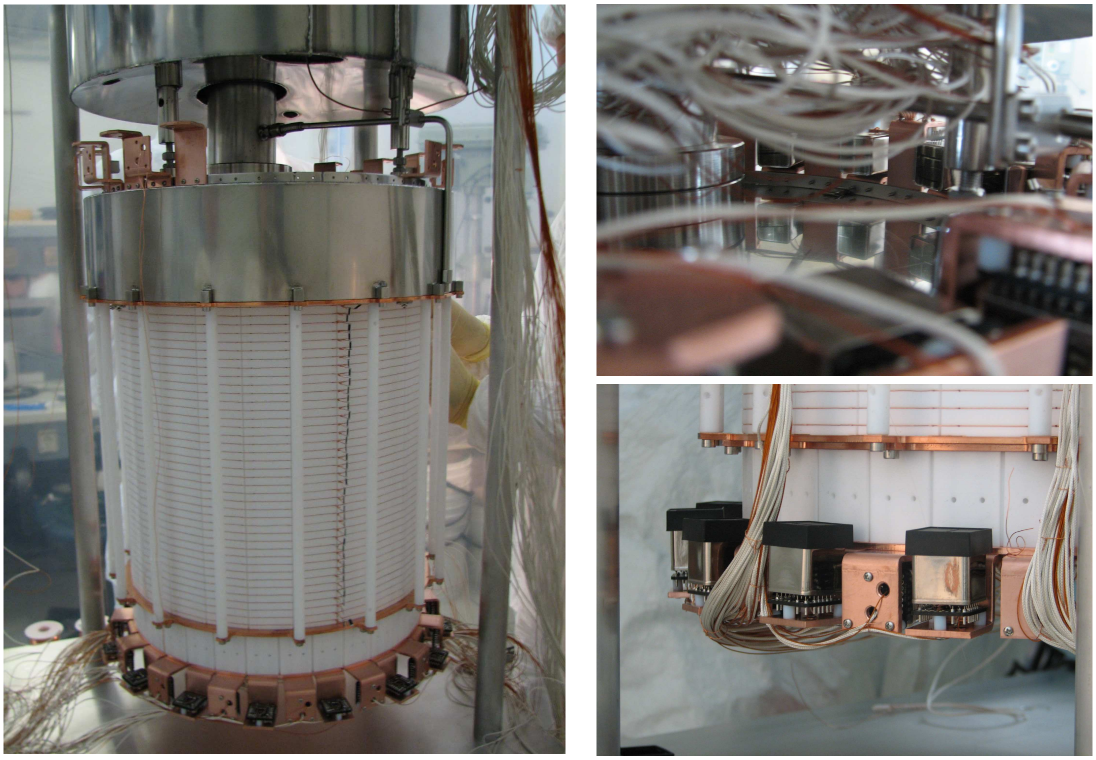

Figure 3.6: Picture of the inner detector structure during the veto PMT installation (left). Completed top veto ring of downwards-inwards alternating PMTs (right, top) and bottom veto ring of upwards-inwards bottom PMTs (right, bottom).

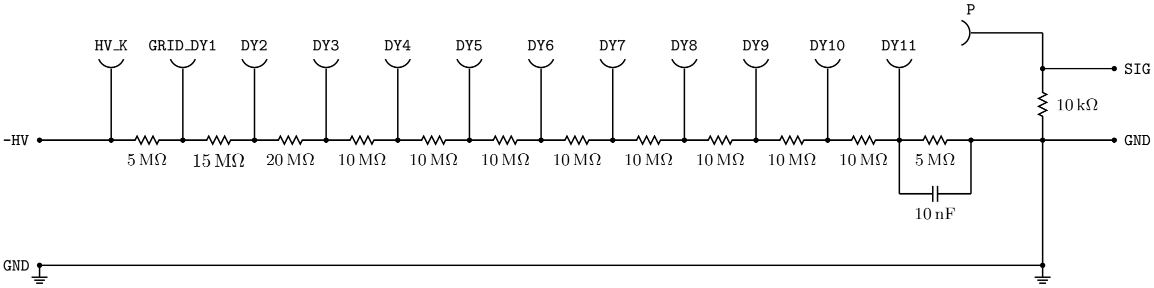

Figure 3.7: Schematic of the XENON100 grounded-anode PMT voltage divider. Figure from [Plante, 2012]

Each PMT is connected with a PTFE insulated coaxial cable to read the signal as well as a Kapton insulated single wire cable to supply the operating voltage. The outer insulation of the coaxial cable was removed to prevent a potential impact of the trapped air on the LXe purity. This choice resulted in a common ground for all PMT anodes. The cables of the top PMTs are guided out of the passive shield through a pipe connected to the bell. All other cables are grouped into four bunches which are fixed to the PTFE support structure, and guided on top of the bell where they are collected and routed out of the shield through a second pipe. Each pipe is equipped with commercial 48-pin vacuum feedthroughs at the end providing a connection to the atmosphere, outside of the shielding.

Non-functional PMTs were only 5 % (four on the top array, four on the bottom array, and four in the active veto) of the total PMTs in 3 years of detector operation after the last opening for maintenance.

3.2.4 Cryostat

The TPC is mounted in a double-walled 316Ti stainless steel (a titanium stabilized version of 316 molybdenum-bearing austenitic stainless steel) cryostat, selected for its low activity, especially in ^{60}Co [Aprile *et al.*, 2011d]. The connection to the outside of the shield is established via three stainless steel pipes, one double-walled to the cooling system, the others single-walled to the PMT feedthroughs and pumping ports. Fig. 3.8 shows the inside of the cryostat along with the recirculation pipe and the LXe dripping pipe coming through the double-walled pipe connected to the cooling tower (left) and the top assembly of the cryostat and cooling tower connection (right). The motion feedthrough to adjust the liquid level is shown on the left of the top flange.

3.3 Electric Field Configuration

Thin metal meshes are used to create the electric fields required to operate XENON100 as a dual-phase TPC. They were chemically etched from stainless steel foils and spot-welded onto rings made of the same low radioactivity stainless steel used for the cryostat. Before welding, the meshes were stretched to minimize sagging.

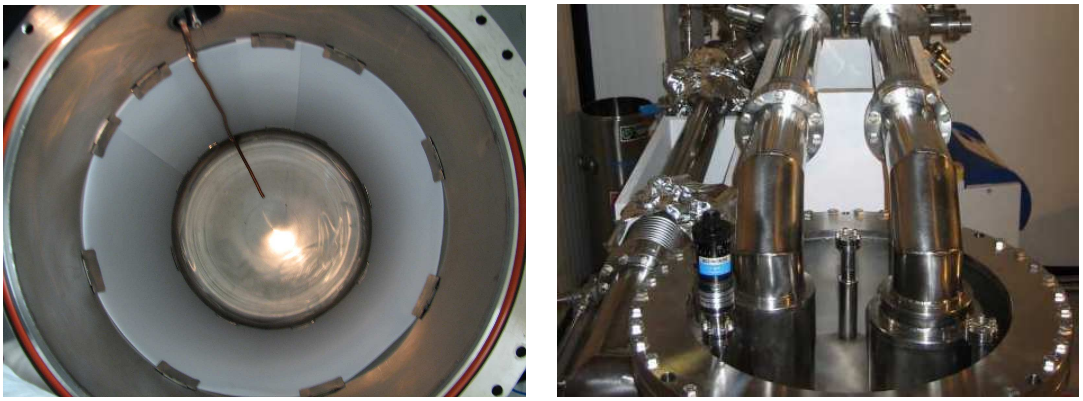

Figure 3.8: Picture of the inside of the cryostat (left) and picture of entire top assembly and cooling tower connection (right). The veto PTFE lining is kept in place by welded steel holders. LXe flowing from the cooling tower funnel reaches the main cryostat and drips down at the end of center pipe. LXe from the bottom of the detector is extracted via the recirculation line shown in the left. The white wooden supports in the right figure represents the position of the passive shield door underground.

Fig. 3.9 shows the meshes used for the electric field configuration of XENON100 and the electric field cage along with the voltage divider. About 15 mm below the top PMTs, the TPC is closed with a stack of three stainless steel meshes with a hexagonal pattern: a central anode (125 μm thick, 2.5 mm pitch) between two grounded meshes with a spacing of 5 mm (right, top). An extraction field of $\sim 12\,\mathrm{kV/cm}$ is obtained by applying +4.5 kV to the anode, and adjusting the height of the liquid level, yielding $\sim 100\,\%$ extraction efficiency [Aprile *et al.*, 2004; Gushchin *et al.*, 1982]. The grounded mesh above the anode shields the amplification region from external fields especially due to the negative electric potential of the top PMTs and provides a more homogeneous S2 signal.

The cathode mesh is 75 μm thick with a hexagonal pattern and a pitch of 5 mm. A grounded screening mesh, also of a hexagonal pattern and 5 mm pitch, but 50 μm thick, is placed 12 mm below the cathode, and 5 mm above the bottom PMTs to shield them from the cathode high voltage (Fig. 3.9 (right,bottom)). To bias the cathode and the anode, custom-made hermetically sealed HV feedthroughs, of a similar design as those

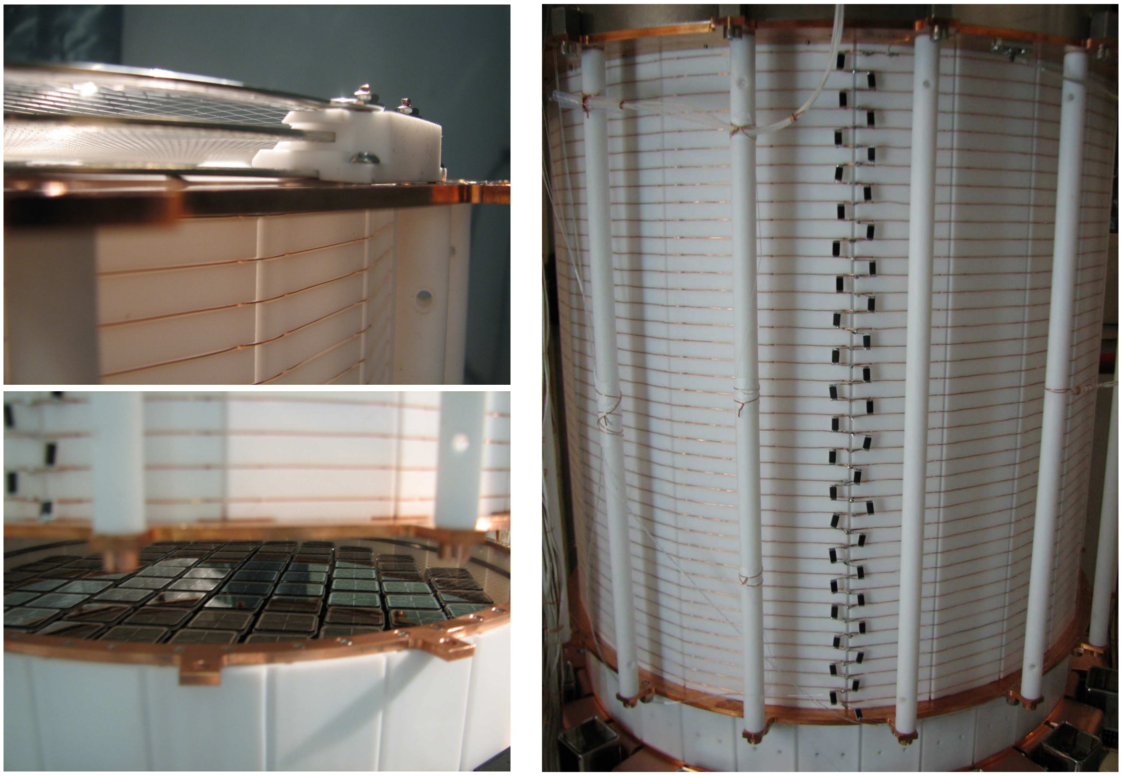

Figure 3.9: Top stack of three stainless meshes: top mesh, anode and gate grid from top to bottom (left, top), screening mesh below the cathode and above the bottom PMTs (left, bottom), and field cage structure with voltage divider composed of 700 MΩ resistors (right).

developed for XENON10 [Aprile *et al.*, 2011a], are used also for XENON100. They are made of a stainless steel core with a PTFE insulation layer, to achieve a reduced radioactive contamination compared to commercial HV feedthroughs. The cathode feedthrough was designed to withstand a voltage of -30 kV. However, during the initial operation of the detector, a production of scintillation pulses near the bottom PMT array was observed when this voltage was too high. Hence, it was decided to run the detector with a reduced voltage of -16 kV, resulting in a drift field of 0.53 kV/cm across the TPC. The pulses are most likely caused by electron field emission and subsequent scintillation in the strong electric field near sharp features of the cathode mesh. As mentioned in Sec. 3.2, the unavoidable LXe layer between cathode and bottom PMT array is responsible for most of the anomalous leakage events.

In order to optimize the S2 signal extraction, the anode could be moved horizontally with respect to the gate grid and the top grid. It was aligned at a half-pitch offset under a microscope and fixed with set screws. The whole stack is optimized for optical transparency and minimal impact on the S2 energy resolution. The spread of the S2 signal due to the varying electron path length is only 4 %, independent of the S2 energy. Averaged over all angles of incidence, the optical transparencies of the top mesh stack and of the cathode plus the screening mesh are 47.7 and 83.4 %, respectively [Aprile *et al.*, 2012c].

The uniformity of the electric field across the ~ 30 cm long TPC drift gap is achieved by a field cage structure made of thin copper wires. Two wires, at the same potential, one running on the inside and one on the outside of the PTFE panels, are used to emulate a $1/4''$-wide field shaping electrode. Forty equidistant field shaping electrodes, connected through 700 MΩ resistors are used (Fig. 3.9 (right)).

The penetration of the electric field lines through the cathode, facilitated by the large mesh pitch and the thin wire diameter chosen to optimize light collection, distorts the electric field at large radii, just above the cathode. The correction of this effect is explained in detail in Sec. 4.1.3.

3.4 Passive Shield

A passive shield surrounding of the detector is prerequisite for low background search experiments to reduce background contributions from the detector environment. Since the decision to operate XENON100 at the same site as XENON10 but with a goal of 100 times lower background was made, improvements of XENON10's passive shielding were performed.

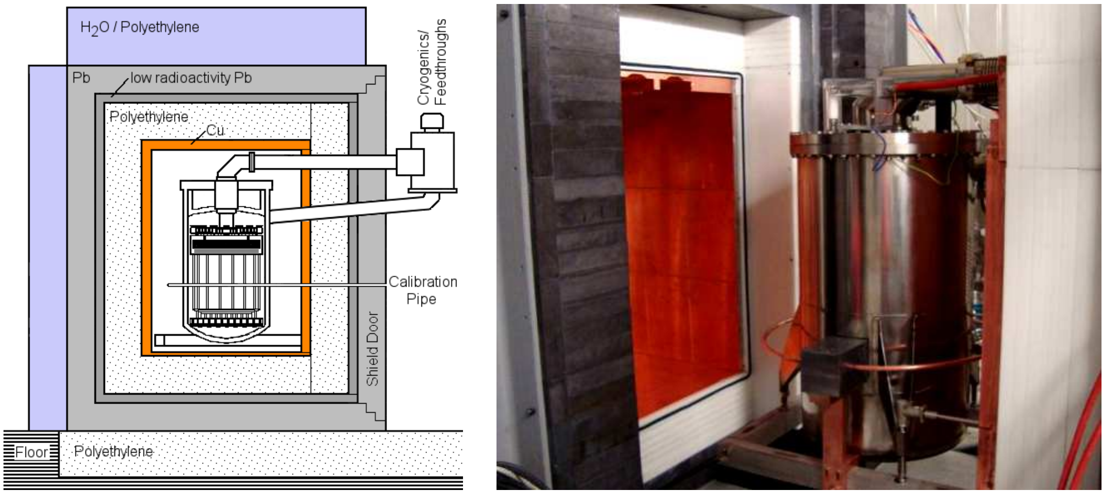

Figure 3.10: Drawing of the XENON100 detector and its passive shield made of OHFC, polyethylene, lead, and water containers (left) and XENON100 the shield door open (right). The Pb-brick along the calibration pipe around the cryostat is a γ ray shield used during ^{241}AmBe(α, n) neutron calibrations. Figure from [Aprile *et al.*, 2012c].

Fig. 3.10 (right) shows a sketch of XENON100 inside the shield. The detector is surrounded (from inside to outside) by 5 cm of oxygen-free high thermal conductivity (OFHC) copper, followed by 20 cm of polyethylene, and 20 cm of lead, where the innermost 5 cm consist of lead with a low ^{210}Pb contamination of (26 ± 6) Bq/kg [Aprile *et al.*, 2011d]. The entire shield rests on a 25 cm thick slab of polyethylene. An additional outer layer of 20 cm of water or polyethylene has been added on the top and on three sides of the shield to reduce the neutron background further.

During the detector operation, the inner shield cavity is constantly purged with high purity nitrogen gas at a rate of 17 standard liters per minute (SLPM) in order to reduce the amount of radioactive radon penetrating into the shield. The remaining radon concentration is constantly monitored with a commercial radon detector and is below the limit of the detector sensitivity ($< 1\,\mathrm{Bq/m^3}$) [Aprile *et al.*, 2012c].

3.5 Cryogenic System

Given that LXe's operating temperature is about 120 K lower than room temperature, a reliable, uncomplicated cooling system with long-term stability is a mandatory requirement for LXe dark matter experiments.

Pulse tube refrigerators (PTRs) [Baldini *et al.*, 2005], specifically designed for high cooling power at LXe temperatures, were employed from the start of the XENON project. The PTR for XENON100 is an Iwatani PC150, driven by a 6.5 kW helium compressor. The cooling power for this combination is measured to be 200 W at 170 K.

Fig. 3.11 shows the cooling tower of XENON100 during the installation of the components (right) and zoom of the top (left, top) and bottom (left, bottom) of the cooling tower. The PTR cold-head is mounted on a cylindrical copper block that closes off the inner detector vessel and acts as a cold-finger. The cold-finger is sealed to the inner detector vessel with a pure aluminum wire seal. The PTR can thus be serviced or replaced without exposing the detector volume to air. As shown in (left, top) of the figure, a copper cup with electrical heaters is inserted between the PTR cold-head and the cold-finger. The temperatures above and below the heater are measured with precise temperature sensors. A proportional-integral-derivative (PID) controller regulates the heating power required to keep the temperature of the cold-finger, and hence the Xe vapor pressure in the detector, at the desired value. The bottom of the cooling tower is composed of a funnel and a stainless steel pipe to guide collected LXe to the detector vessel (left, bottom).

A schematic of the cryogenic system is shown in Fig. 3.12. The PTR is mounted in a separate double-walled vacuum insulated vessel, placed outside the passive shield, along with many auxiliary modules, including the motor valve and buffer tank, which have to be within 50 cm of the PTR cold-finger for optimal performance. This remote cooling system

Figure 3.11: The PTR, heater cup, cold finger coupling at the top of the cooling tower (left, top). Funnel and bottom flange of the inner vessel of the cooling tower along with the stainless steel pipe in the center of the double-wall vacuum insulated pipe for the dripping of LXe to the detector vessel (left, bottom), and the XENON100 Cooling Tower during the installation of the components. The motor-valve and the buffer tank are mounted on the frame that supports the cooling tower.

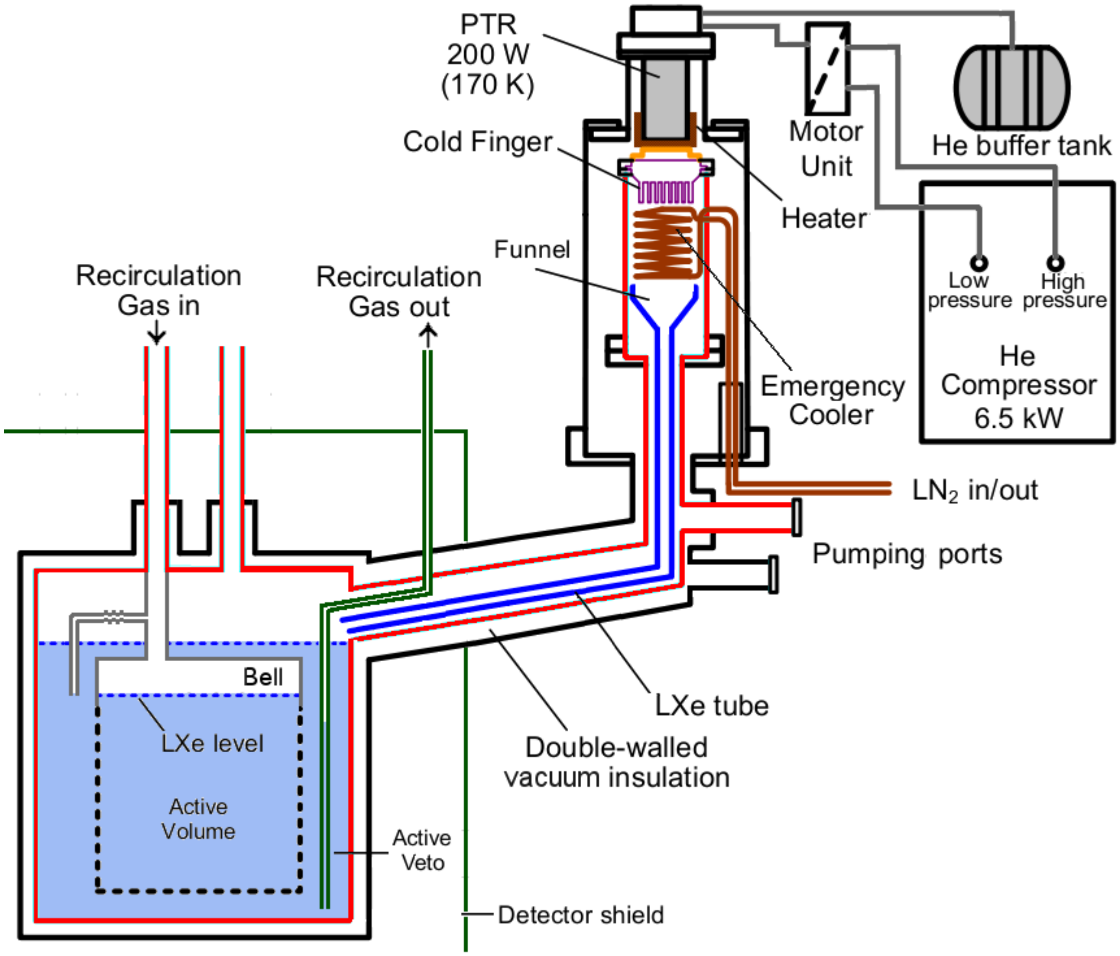

Figure 3.12: Sketch of the XENON100 cryogenic system. Cooling is provided by a 200 W pulse tube refrigerator (PTR) installed outside the shield. The PTR is connected to the main cryostat by a double-walled vacuum insulated pipe. Not drawn to scale. Figure from [Aprile *et al.*, 2012c].

is used to reduce the radioactive background as mentioned in Sec. 3.2. The bottom of this cooling tower is connected to the main cryostat through a vacuum insulated pipe that returns the LXe above the liquid level. The liquid drops are collected by a funnel and flow back into the detector through a smaller diameter stainless pipe at the center of the insulated pipe shown in Fig. 3.11 (right, bottom). This pipe is inclined by 5° with respect to the horizontal to drive the liquid flow to the detector vessel.

In case of emergency, such as a prolonged power failure or a failure of the primary cooling system, the detector can be cooled by liquid nitrogen (LN_2). A stainless steel coil is wound around the cold finger and is connected to an external LN_2 dewar, always kept full during the detector operation. The LN_2 flow through the coil is controlled by an actuated valve and triggered when the detector pressure increases above a defined set-point. Tests have shown that the detector can be kept stable for more than 24 h without any human intervention using the emergency LN_2 cooling system [Aprile *et al.*, 2012c].

3.6 Gas Handling and Purification System

A total of 161 kg of LXe is necessary to fill the target volume and the active veto. It is stored in four large (75 *l* volume) high-pressure aluminum gas cylinders, which are surrounded by custom-made insulated LN_2 dewars. Both Xe filling and recovery take place in the gas phase, through a stainless steel pipe connecting the storage with the purification system. All pipes, flow controllers, regulators, and valves are metal sealed.

To fill the detector with LXe, the temperature of the cold finger is set to the liquid temperature of $-91°$C at the pressure of GXe filling (usually kept around 2 atm) by the PTR. GXe is liquefied on the surface of the cold finger and the LXe is gathered through the funnel and dripped into the detector vessel along the inclined stainless steel pipe. At the beginning of filling, the dripped liquid immediately evaporates since the detector vessel is not at the temperature of the liquid, and hence the filling speed is limited. Once the detector vessel is cooled down to the liquid temperature, Xe starts to condensate and begins to fill the detector from the bottom of the detector vessel. The filling speed reaches a maximum of 3 kg/h once the detector is filled with enough LXe. At this stage, the limitation of the filling speed is the cooling power of the PTR.

Since Xe is expensive (see Sec. 2.1), it is recovered when the detector is not operated. For Xe recovery, the dewars around the storage bottles are filled with LN_2 to cool the cylinders in contact. Any remaining Xe gas in the cylinders is frozen and the pressure inside the cylinders reaches almost 0 atm. This pressure gradient between the detector system and the cylinders forces the gas in the detector to be recovered into the cylinders. To help this process, a double-diaphragm pump is used to extract the gas from the detector and the insulation vacuum in the detector vessel is broken which results in the warming of and a pressure increase in the detector.

During Xe purification from Kr through a dedicated cryogenic distillation column (see Sec. 3.7), the gas stored in the cylinders is passed through the distillation column before being filled directly into the detector. Since the Kr-rich Xe produced as off-gas during distillation is not used, more Xe than is needed for a complete fill of XENON100 is stored in the cylinders.

As mentioned in Sec. 2.3.5 and Sec. 2.4.2, impurities in LXe attenuate both S1 and S2 signals. Therefore, it is important to purify the LXe constantly to keep a desired purity level. This is done by recirculating Xe gas through a high temperature zirconium getter (SAES MonoTorr PS3-MT3-R/N-1/2, see Fig. 3.13), which removes impurities by chemically bonding them to the getter material. At a rate of about 5 SLPM, liquid from the bottom of the detector vessel is evaporated and pushed through the getter by a double diaphragm pump (KNF N143.12E), before it is returned to the detector [Aprile *et al.*, 2012c].

For the first filling of the detector, the detector was heated to 50°C to speed up the purification process, with the temperature limit set by the PMTs, while the detector vacuum was monitored with a residual gas analyzer (RGA). After this “baking” of detector materials, the detector was cleaned by 2 atm of hot Xe gas recirculation through the getter for several weeks starting at the end of 2008, relying on the polarizability of Xe which makes it an effective solvent [Rentzepis and Douglas, 1981]. During this process, decrease of the water content from ~ 500 to a 1 ppb level was monitored with a dedicated detector (Tigeroptics HALO) using the spectral absorption technique [Aprile *et al.*, 2012c].

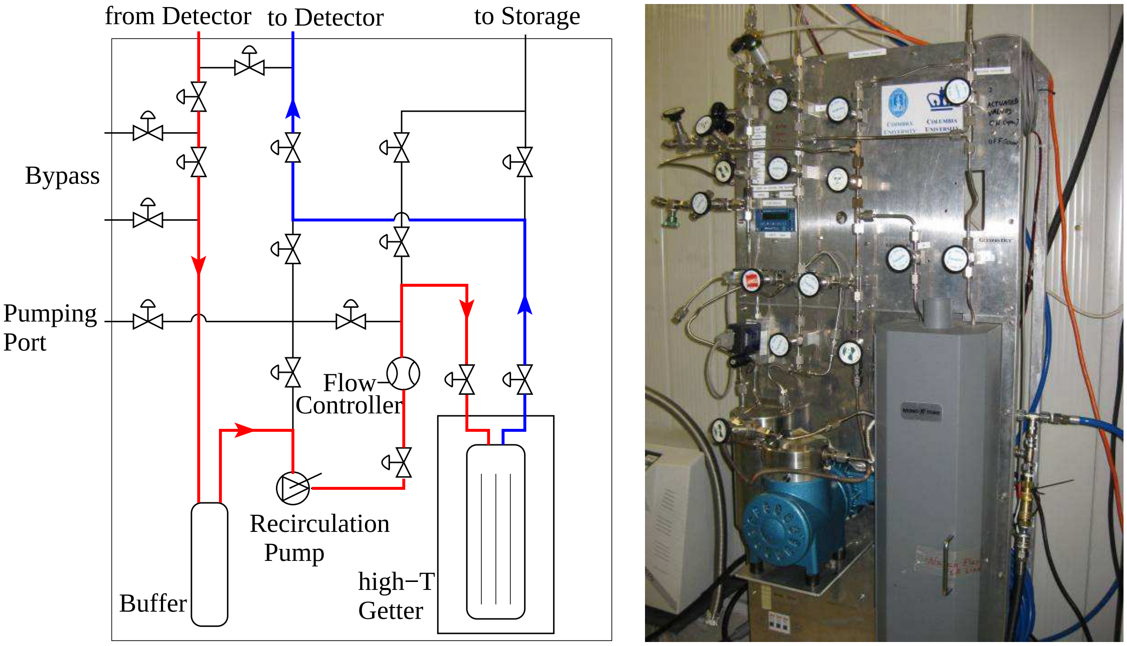

Figure 3.13: Schematic of the XENON100 purification system (left, figure from [Aprile *et al.*, 2012c]) and picture of gas panel with the hot getter and the recirculation pump on-site (right). LXe is extracted from the detector using recirculation pump and evaporates in the gas line in between. It passes through a high temperature getter for purification and it is pushed back in to the detector. The different valves are used to bypass the components for special operations such as filling, recovery or maintenance. The arrows in the left figure indicate the standard gas flow for the detector operation.

3.7 Krypton Distillation Column

As explained in Sec. 2.1, Xe does not have any long-lived radioactive isotopes thus Xe itself hardly contributes to the intrinsic γ background. The main intrinsic γ background in commercially available Xe is attributed to ^{85}Kr, which has an isotopic abundance of ^{85}Kr/^{nat}Kr 2×10^{-11} [Du *et al.*, 2004]. This isotope, which has a half-life of 10.76 yrs, is produced in uranium and plutonium fission and is released into the environment in nuclear weapon tests and by nuclear fuel reprocessing plants.

Commercial Xe gas contains ^{nat}Kr at the ppm level. Most of the gas used in XENON100 was processed by Spectra Gases Co. to reduce the ^{nat}Kr content to the 10 ppb level, using their cryogenic distillation plant [Aprile *et al.*, 2012c]. During the very first XENON100 run, with a total mass of only 143 kg, a ^{nat}Kr level of 7 ppb was measured via a delayed coincidence analysis, consistent with the value provided by Spectra Gases. To ensure the background contribution from ^{85}Kr is subdominant, the fraction of ^{nat}Kr in Xe must be about a factor of 100 lower than this processed value. Therefore, a small-scale cryogenic distillation column was procured and integrated into the XENON100 system underground [Aprile *et al.*, 2012c].

The schematic of the XENON100 Kr-distillation column (left) and its picture on-site (right) are shown in Fig. 3.14. The Xe gas is cooled using a cryocooler before entering the column at half height. A constant thermal gradient is kept using a heater at the bottom of the column and another cryocooler at the top. Thanks to the different boiling temperatures of Kr (120 K at 1 atm) and Xe (165 K), a Kr-enriched mixture will develop at the top of the column and a Kr-depleted one at the bottom. The Xe with a high Kr concentration is separated by freezing into a gas bottle, while the Xe at the bottom is used to fill the detector.

After installation and an initial commissioning run of the column, a second distillation of the full xenon inventory was performed in summer 2009. For the commissioning run leading to the first science results [Aprile *et al.*, 2010], the Kr concentration was (143^{+135}_{-90}) ppt (90 % C.L.), as measured with the delayed coincidence method. This concentration agrees with the value inferred from a comparison of the measured background spectrum with a Monte Carlo simulation [Aprile *et al.*, 2011e]. A small leak in the recirculation pump before the

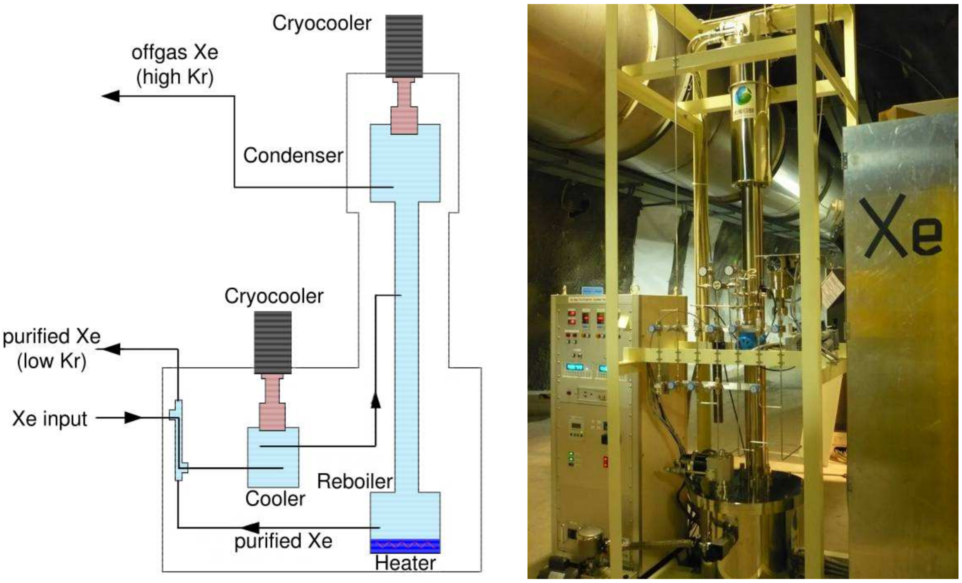

Figure 3.14: The schematic of the cryogenic distillation column used to separate krypton from xenon (left, figure from [Aprile *et al.*, 2012c]) and a picture of the setup underground during the installation (right). The height of the column is about 3 m.

first science run [Aprile *et al.*, 2011b] led to a Kr increase of a factor ~ 5. However, this higher level did not have a large impact on the scientific reach, as demonstrated by the results. In the meantime, a lower Kr concentration, comparable to the one in [Aprile *et al.*, 2010], was achieved by further distillation in late 2010.

The Kr contamination in the second science run [Aprile *et al.*, 2012a] was measured to be $(19 \pm 4\,\mathrm{ppt})$ and $(18 \pm 8\,\mathrm{ppt})$, with ultra-sensitive rare gas mass spectrometry combined with a sophisticated Kr/Xe separation technique and the analysis of delayed β-γ coincidences associated with the ^{85}Kr beta decay $(18 \pm 8\,\mathrm{ppt})$, respectively.

3.8 Slow Control System and Detector Stability

A Java-based client-and-server system is used to monitor all relevant XENON100 parameters for the stable detector operation, such as detector and environmental pressures and temperatures, LXe level, Xe gas recirculation rate, PMT voltages and currents, anode and cathode high voltage, nitrogen purge flow, radon-level in the shield cavity and the environment, cryostat vacuum, etc. It is called “slow” control since those parameters are recorded with tens of seconds interval, unlike the detector data taking which can go up to a few kHz. The slow control system is constantly monitored by two independent alarm servers physically located in different countries to deal with any emergency situation of the detector operation effectively.

XENON100 shows excellent stability with time. Fig. 3.15 shows the evolution of some of the parameters measured by the slow control for the science data reported in [Aprile *et al.*, 2012a], covering a period of ~ 13 months. Pressure and temperature were measured to be stable within 0.7 and 0.16 %, respectively. The periods where the fluctuations were larger than these values were discarded from data analysis. As mentioned in Sec. 2.4.4, the amplification of proportional scintillation strongly depends on the pressure of the GXe. At the XENON100 operating conditions, pressure fluctuations of 0.7 % lead to negligible S2 signal fluctuations of < 0.08 %.

3.9 Data Acquisition System (DAQ)

Using flash ADCs (FADCs) allows for a detailed time analysis of triggered events as if storing oscilloscope images, which is useful for extracting relevant information about the events. However, the main challenge is that the data volume is large. Digitizing the full waveforms of the 242 PMTs requires quite amount of data storage. The adopted solution to reduce the event size was to implement a data reduction algorithm on the field programmable gate array (FPGA) [Plante, 2012]. The company manufacturing the FADCs chosen for the experiment, CAEN Technologies, agreed to modify their firmware to include our specification for a baseline suppression algorithm. This data reduction before the transfer to the DAQ computer allows for faster data taking rates, still limited by the VME transfer speed, but now mostly given by the average duration of the S2 signal [Plante, 2012]. The S2 pulse width sets the limit because it is much wider than the S1 pulse width.

The XENON100 data acquisition system is divided into three subsystems: the trigger, the waveform acquisition subsystem, and the rate and time accounting subsystem. The

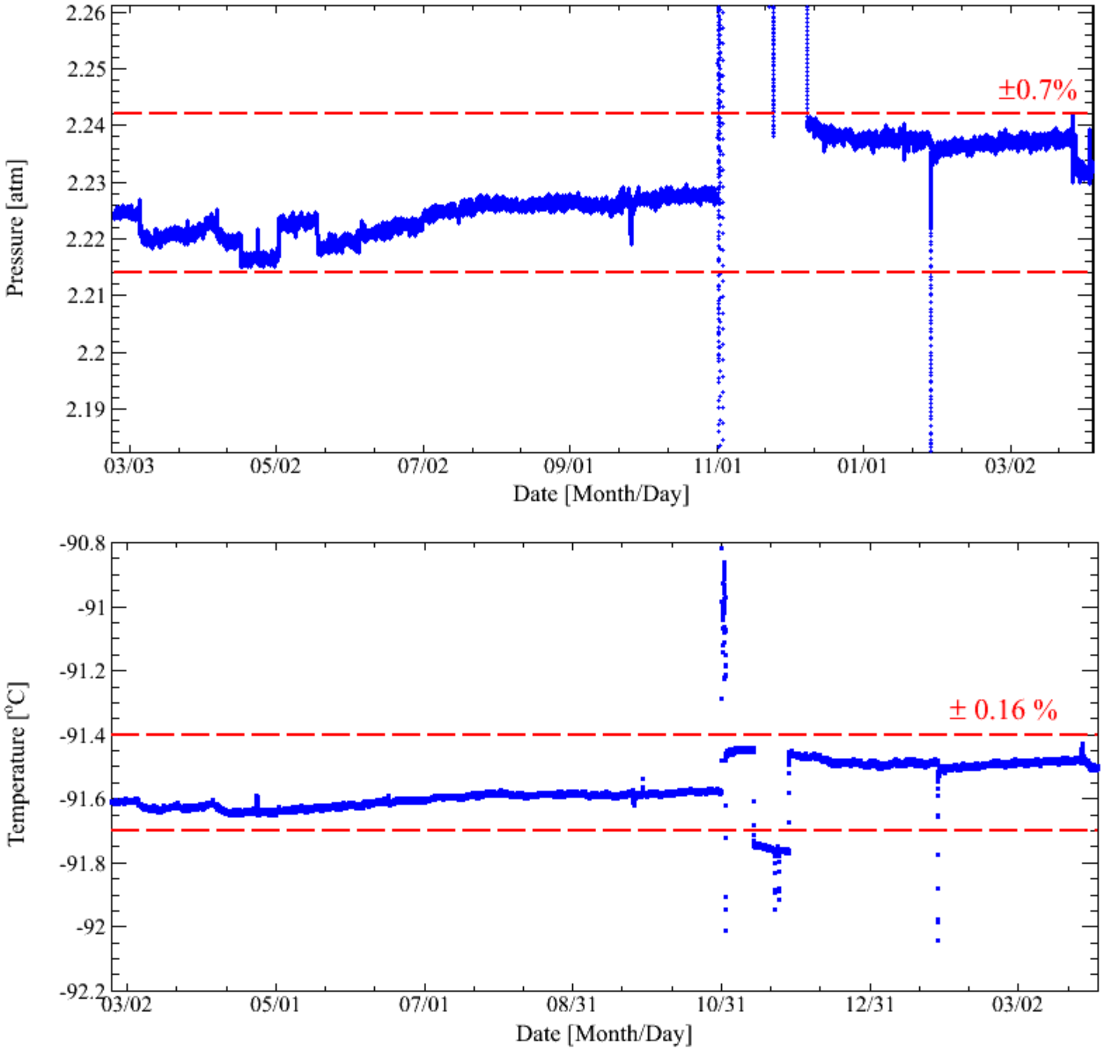

Figure 3.15: Pressure (top) and temperature (bottom) stability of XENON100 during `run_10`. The continuous data taking was interrupted maintenance of the detector. Red dashed lines show ±0.7 and ±0.16 % variation of pressure and temperature, respectively. The data taken outside of these variations were not used for the analysis. Credit: XENON100 collaboration.

trigger uses an S2-based trigger scheme to limit the rate to events within the TPC. The waveform acquisition subsystem is composed of 31 CAEN FADCs (V1724, 14 bit, 100 MS/s). The FADCs have an input bandwidth of 40 MHz and a full scale range of 2.25 V. The modules are housed in two VME crates and connected to the DAQ computer via an optical fiber connection. Fig. 3.16 shows a diagram of the XENON100 DAQ system.

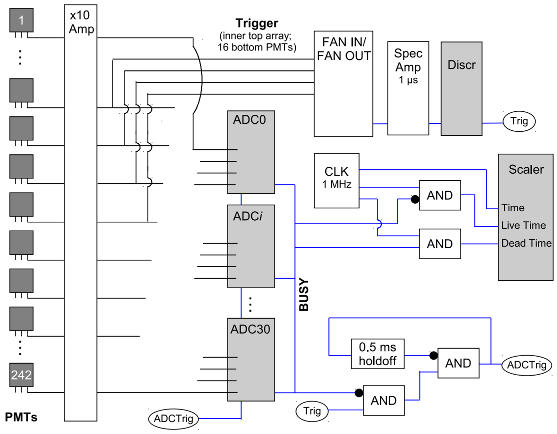

Figure 3.16: DAQ schematic of XENON100 for the dark matter search. All 242 PMTs are digitized at 100 MHz sampling rate with Flash ADCs. A hardware trigger is generated using 68 top and 16 bottom PMTs. Figure from [Aprile *et al.*, 2012c].

The signals from all 242 PMTs are fed into Phillips 776 ×10 amplifiers. The Phillips 776 ×10 amplifier outputs two copies per channel of the amplified analog signal. The first copy of each channel is digitized by the FADCs. The second copy of the 68 inner PMT channels of the top array and the 16 inner PMT channels of the bottom array are summed in the Phillips 740 fan-ins. The summed signal is amplified and filtered with an ORTEC research amplifier (model 450) using an integration time constant of 1 μs. The integrated signal is discriminated and constitutes the preliminary trigger logic signal. This trigger signal is combined into an AND gate with a logic signal indicating whether or not the FADCs are in a *busy* state and subsequently combined with a holdoff logic signal that prevents the generation of a secondary trigger signal for 500 μs. The resulting logic signal is distributed simultaneously to the 31 FACDs modules.

At low trigger rates, the CAEN V1724 FADC permits operation in a deadtime-less mode where data is written to a circular buffer with 512 kB of memory per channel, and where multiple events can be stored before they are read via the VME bus. Additionally, an on-board FPGA allows on-line zero-length encoding of the digitized samples, that is, only the relevant portions of the signal trace are stored to the module memory and transferred from the module to the data acquisition computer. S1 and S2 signals have typical time scales of $< 150\,\mathrm{ns}$ and $1\,\mu\mathrm{s}$, respectively, but the time the ionization electrons take to travel from the interaction site to the liquid level ranges from 0 to $\sim 175\,\mu\mathrm{s}$ at a drift field of $0.53\,\mathrm{kV/cm}$. The acquisition window is set at $400\,\mu\mathrm{s}$, more than twice the maximum drift time, with the trigger positioned in the middle of the window, such that all features of an event are recorded, whether the trigger occurred due to an S1 signal or an S2 signal. Thus, large portions of the digitized waveform are essentially free of signals and consist mostly of baseline samples. This idea is behind the adoption of the zero-length encoding algorithm to reduce the size of events. By recording only parts of the waveform where the voltage exceeds a predefined threshold, with a fixed number of samples before and after the excursion above threshold, the baseline samples can be discarded. For XENON100 the encoding threshold is set at 30 digitizer counts ($\sim 4\,\mathrm{mV}$) and pre- and post-excursion segments of 50 samples ($500\,\mathrm{ns}$). The threshold corresponds to ~ 0.3 photoelectrons (pe). For more details of the zero-length encoding algorithm for XENON100 data taking, see [Plante, 2012].

For low energy events, this zero-length encoding results in a reduction of the event size by a factor ten. At higher energies however, large S2 signals followed by a series of a few electron S2 signals result in larger event sizes and the reduction is not as remarkable. Nevertheless, this data reduction allows for much higher calibration rates, as the data volume to be transfered to the host computer is reduced. For high energy γ sources the maximum rate achievable is $\sim 30\,\mathrm{Hz}$. The maxium rate of the VME crate optical fiber and the maximum writing speed of the RAID array are the limiting factors which determine the transfer speed to the DAQ computer. However, it is not recommended to calibrate a detector with high rates since the accidental coincidence probability within the event window is proportional to the event rate (e.g., $30\,\mathrm{Hz} \cdot 400\,\mu\mathrm{s} \sim 1\,\%$). For the PMT waveforms from veto PMTs, data size is not an issue since they hardly occupy disc space due to the absence of S2 signals.

The DAQ trigger also includes a high-energy veto subsystem that inhibits triggers by the S1 signal so as to suppress high-energy events triggering. Given that the data transfer rate between the VME crates with the FADCs and the DAQ computer is limited by a combination of the fiber optical connection and the writing speed to disk, it is beneficial to prevent the transfer of events outside of the energy range of interest. Since the trigger generation is set by discrimination of the signal with a certain threshold, a large S1 pulse due to a high-energy event can generate a trigger if its pulse height is comparable to that of an S2 pulse. By selecting peaks with a narrow width, the events triggered by S1 signals can be rejected. The threshold of the high-energy veto is set high enough such that no distortion of the spectrum at low energies occurs. In order to prevent triggers generated by subsequent S2 peaks, further triggers are inhibited for the next $500\,\mu$s. The high-energy veto is used for all low-energy calibrations such as the electronic recoil band and nuclear recoil band calibrations (Sec. 4.4).

The rate and time accounting subsytem of the DAQ is responsible for measuring the time, live time, dead time, trigger rate, and event rate of the measurement. A clock module generates a logic signal at a frequency of 1 MHz that is combined with the *busy* signal and its complement to compute the dead time and live time, respectively. A CAEN V830 scaler is used to count the number of clock cycles, dead cycles and live cycles. The scaler also counts the number of triggers, before any inhibition due to the *busy* signal or a high energy veto signal, and the number of events of the measurement. The effect of the trigger holdoff is taken into account separately. The deadtime during science data taking is about 1 % [Aprile *et al.*, 2012c].

The efficiency of the XENON100 trigger was measured initially by feeding a square voltage pulse with a width of $1\,\mu$s width and variable height to the research amplifier. At a pulse height of 24 mV a trigger was generated for every voltage pulse (i.e. this is the voltage required for 100 % trigger efficiency). At a PMT gain of 2×10^6 pe/e$^-$ and after the ×10 amplification, a photoelectron corresponds to a charge signal of 160 mV ns in the $50\,\Omega$ input resistor of the FADC. This means that the $24\,\mathrm{mV}\,\mu\mathrm{s}$ square pulse was equivalent to a 150 pe signal. Since the PMTs used for the trigger collect $\sim 52\,\%$ of the S2 scintillation photons, the 100 % efficiency trigger threshold is 290 pe. This value was confirmed afterwards by a direct measurement. By recording the normal trigger signal utilizing an unused ADC channel with the events triggered by energy deposits in the veto, the fraction of S2 signals that generated a trigger to the total number of S2 signals was obtained as a function of S2 signal size, which enables a computation of the trigger threshold and efficiency.

For the runs whose results were published in [Aprile *et al.*, 2011b; Aprile *et al.*, 2010] (run_08, run_07), the trigger was based on the analog sum of the signal. However, for the second science run (run_10), the trigger has been modified to lower the energy threshold. The new trigger is configured such that if a channel exceeds the 0.5 pe threshold, the FADC adds a 125 mV square-wave to its majority output for a time of one bin (10 ns). The majority ouputs of all top and bottom PMT FADCs that comprise the trigger are summed up and fed into the spectral amplifier. The integrated majority signal, using a spectroscopy amplifier with an integration time of 1 μs, is fed into a low threshold discriminator to create the trigger. Fig. 3.17 shows a trigger efficiency comparison between run_10 (blue) and run_08 (black) as a function of S2. The improved trigger threshold for run_10 is $>$ 99 % above S2 $\sim$ 150 pe, a factor of two lower than that of run_08.

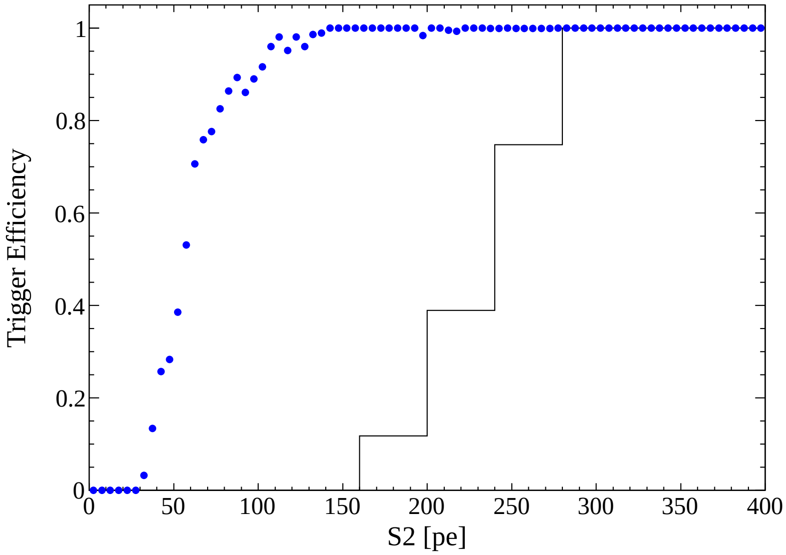

Figure 3.17: Trigger efficiency comparison between run_10 (blue) and run_08 (black) as a function of S2. Compared to run_08, S2 threshold was lowered about a factor of two, from 300 pe to 150 pe. Credit: XENON100 collaboration.

For easier access to the raw waveforms of a particular event, the data are stored in an indexed file format that can be compressed further using standard compression tools during data taking. The extraction of physical parameters from the waveforms is done offline on a computing cluster separated from the DAQ system. For details about the raw data processing program, refer to [Plante, 2012].

Chapter 4

Calibration of XENON100

Once a detector is operational, it is necessary to calibrate its response according to the goal of the experiment. For a direct WIMP search experiment, the key ingredient is to differentiate background events from possible WIMP events, as well as to set up the correct energy scale in the region of interest. In a dual-phase LXe detector, background suppression is done via two techniques: fiducializing the target volume and discriminating the electronic recoil background from nuclear recoils. To achieve this, basic calibrations such as the calibration of hardware components, scintillation and proportional scintillation signals, vertex reconstruction, and signal correction due to the position dependence are a prerequisite.

Both setting the energy scale and the electronic recoil background rejection level are based on irradiation of the detector with radioactive sources. XENON100 uses external calibration sources inserted in a copper tube wound around the cryostat (see Fig. 3.10). The vertical position of the tube is restricted to the TPC center, while the source can be placed at all polar angles. To build energy scales, ^{137}Cs, ^{60}Co, and various γ lines from neutron irradiation by a ^{241}AmBe(α, n) source are used. For the characterization of electronic recoils and nuclear recoils, ^{60}Co, ^{232}Th, and ^{241}AmBe(α, n) are used.

For the sake of clarity, we will divide detector calibration into different categories. Basic calibrations, whose final step is signal correction, i.e., the adjustment of the detected signal size due to the spatial dependence of the signal, will be explained in Sec. 4.1. Energy scales will be introduced in Sec. 4.2. The electronic recoil background is explained in Sec. 4.3 with a comparison with Monte Carlo simulation. Nuclear and electronic recoil band characterization for further rejection of the electronic recoil background will be explained in Sec. 4.4.

4.1 Basic Calibrations

4.1.1 Basic Hardware Components Calibration

For the basic hardware components, the calibration of the level meter and PMTs is the main task to determine the height of the liquid level and to equalize the 242 PMTs gains, respectively. The former is closely related to the amplification of proportional scintillation (Sec. 2.4.4) and its optimization, while the latter aims at minimizing the position dependence of the signal in the first step of particle detection. Details of the level meter and PMT calibration can be found in [Plante, 2012] and [Kish, 2011], respectively.

4.1.2 Basic Calibration of the Scintillation and Proportional Scintillation: S1 Stability and Electron Lifetime

As discussed previously (Sec. 2.3.5, 2.4.2), the impurities in LXe affect the size of both the scintillation signal (S1) and the proportional scintillation signal (S2) and hence the energy thresholds. In addition, monitoring the signal size is also important for checking the signal stability and signal corrections. Signal monitoring was done regularly throughout detector operation by using the 662 keV full absorption peak from a ^{137}Cs source. Due to the high electronic stopping power of LXe, it is almost impossible to probe the whole sensitive volume of XENON100 with 122 keV photoabsorbed γ rays from ^{57}Co source. Hence, the S1 light yield for the 662 keV full absorption peak, the peak position in S1 over the deposited energy in LXe with unit of pe/keV, was monitored for the scintillation signal stability. Regarding the S2 signal, however, the more interesting and critical quantity is the electron lifetime, τ_{e}, given that the electronegative impurities are mostly from the outgassing of the detector vessels which decreases with operation time in the air-tight system. The electron lifetime is defined as the average drift time required for the initial number of drifting electrons to be diminished by factor of 1/e from capture by impurities (see Sec. 2.4.2). It can be inferred from a distribution of the S2 signal vs drift time. For the electron lifetime computation, the S2 signal seen by only the bottom PMTs ($\mathsf{S2}_b$) is used, so as to avoid PMT saturation and also because its response is more homogeneous compared to that of top PMTs.

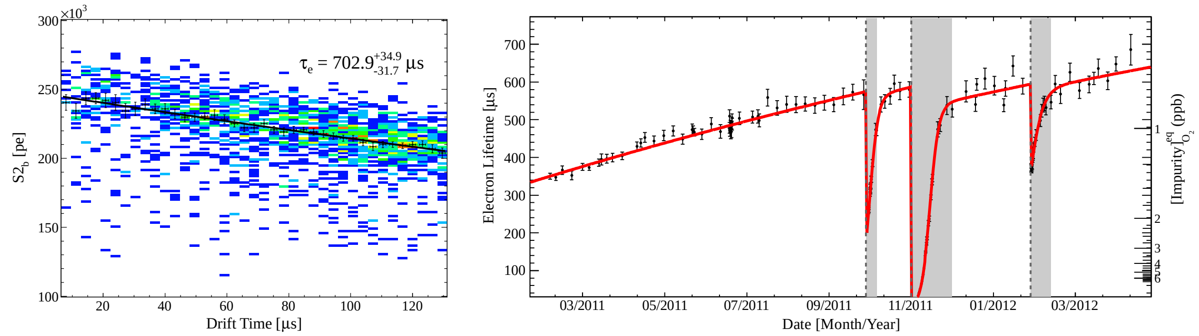

Figure 4.1: Example of electron lifetime measurement from $\mathsf{S2}_b$ vs drift time space (left) and the electron lifetime evolution of `run_10` (right). The three dips in the right figure are attributed to interruptions for detector maintenance. See the text for more details. The electron lifetime evolution increases with detector operation time. It is thus necessary to correct the data due to this time evolution of electron lifetime. Credit: XENON100 collaboration.

Fig. 4.1 shows an example of electron lifetime measurement from $\mathsf{S2}_b$ vs drift time space (left) and the evolution of the electron lifetime for the second science run (`run_10`) (right). The electron lifetime is obtained by an exponential fit of the median of $\mathsf{S2}_b$ as a function of drift time, as shown in the right figure. During `run_10`, the electron lifetime increased from 374 to 611 μs, with the average being $\tau_{\rm e} = 514\,\mu$s [Aprile *et al.*, 2012a]. The three dips in the electron lifetime in the right figure are attributed to interruptions in the purification cycle for detector maintenance. The dips correspond to pulse tube refrigerator (PTR) interruption due to the change of the power line of the motor valve unit for the PTR, PTR interruption due to the failure of a compressor (caused by chiller faliure due to fan blocking), and getter interuption due to the failure of the air compressor. The first two dips in the electron lifetime are most likely related to the liquid level change in the detector which caused introduction of impurities from the detector surface, while the last dip is related to the failure of purification system itself. However, the general behavior of the electron lifetime evolution is that it increases with detector operation time due to constant cleaning of the LXe by the purification system. It is thus necessary to correct the data due to this time evolution of the electron lifetime. Further explanations about electron lifetime behavior are described in [Plante, 2012].

4.1.3 3D Vertex Reconstruction

When a particle interacts at position (x, y, z) in the detector, scintillation light $\mathsf{S1}$ and charge (free electrons) are produced simultaneously at that position. The 3D interaction position is reconstructed from the spatial and temporal information of each event recorded in the data. If the electric field inside of the TPC were uniform, electrons would drift straight up so that the $\mathsf{S2}$ would have exactly the same (x, y) position as the primary interaction $\mathsf{S1}$. In reality, this is not the case since the pitch of the cathode is large enough to allow leakage of the electric field to the outer cryostat, without field shaping rings below the cathode. This results in a systematically skewed electric field towards the center of the TPC. Therefore, this effect must be taken into account to infer the right position of a particle interaction. More details on the electric field correction can be found in [Mei, 2011].

After the electric field correction, the position reconstruction procedure breaks down into two parts. First, the z position is determined from the time difference between the prompt $\mathsf{S1}$ and the delayed $\mathsf{S2}$ signal, $\Delta t = t_{\mathsf{S2}} - t_{\mathsf{S1}}$, assuming a constant drift velocity. t_{S1} and t_{S2} are determined at the maxima of the pulses. From the maximum drift time and the known TPC length, this can be converted to the space coordinate z. Fig. 4.2 shows the waveform of a low-energy event from background data. The top figure shows the $\mathsf{S1}$ peak (blue marker) of 5.1 photoelectrons (pe) at $\sim 47\,\mu$s and the $\mathsf{S2}$ peak (red marker) of 460 pe at $\sim 200\,\mu$s, yielding a Δt of $151\,\mu$s in this case. The z position resolution of XENON100 is 0.3 mm $(1\,\sigma)$, inferred from events in background data at well known positions near the top liquid layer, the gate grid, or the cathode. However, because of the finite width of the $\mathsf{S2}$ signal, two $\mathsf{S2}$ pulses can only be separated if they are more than 3 mm in z apart [Aprile *et al.*, 2012c].

Second, the (x, y) position is reconstructed from the $\mathsf{S2}$ top array PMT pattern. The $\mathsf{S2}$ signal from the charge cloud is generated at a very localized spot right above the liquid-gas interface. This leads to a highly clustered $\mathsf{S2}$ signal on the array of top PMTs. Accounting

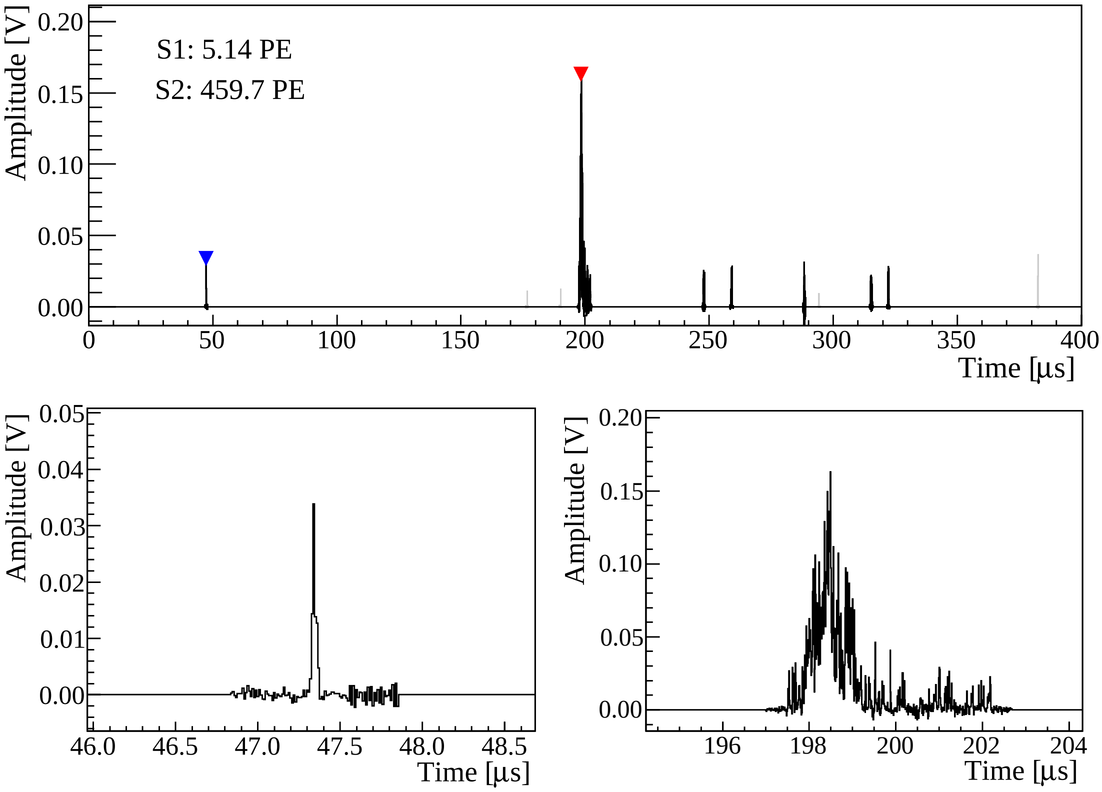

Figure 4.2: Waveform example of a low-energy event from background data: The full waveform (400 μs) with the sum of 178 PMTs of the TPC (top). The blue marker and red maker indicate the S1 and S2 pulses, respectively. No position-dependent corrections have been applied. The time difference is 151 μs. The small pulses after the S2 peak are S2 signals from single electrons extracted into the gas phase [Plante, 2012]. A zoom of the S1 (bottom, left) and S2 (bottom, right) exhibits the different features of S1 and S2 signals. The S1 has very sharp rise time and short decay time, while the S2 has a much wider pulse shape due to amplification in the gas. Figure from [Aprile *et al.*, 2012c].

for the granularity of the 1″ × 1″ PMTs, the (x, y) position of a particle interaction can be reconstructed with a precision of < 3 mm. This precision is verified by placing a ^{57}Co source on the top flange of the detector without liquid on top due to the short penetration depth of 122 keV γ rays in LXe. Three different position reconstruction algorithms (χ^2, support vector machine (SVM), and Neural Network (NN) algorithm) have been developed to obtain the (x, y) position from a comparison of the measured top array PMT hit pattern with the ones generated by a Monte Carlo simulation. Fig. 4.3 shows the S2 PMT hit pattern for both top and bottom PMT arrays along with the reconstructed position using NN. The left figure was used for the (x, y) position reconstruction. Details about the position reconstruction algorithms of the XENON100 data can be found in [Mei, 2011; Kish, 2011].

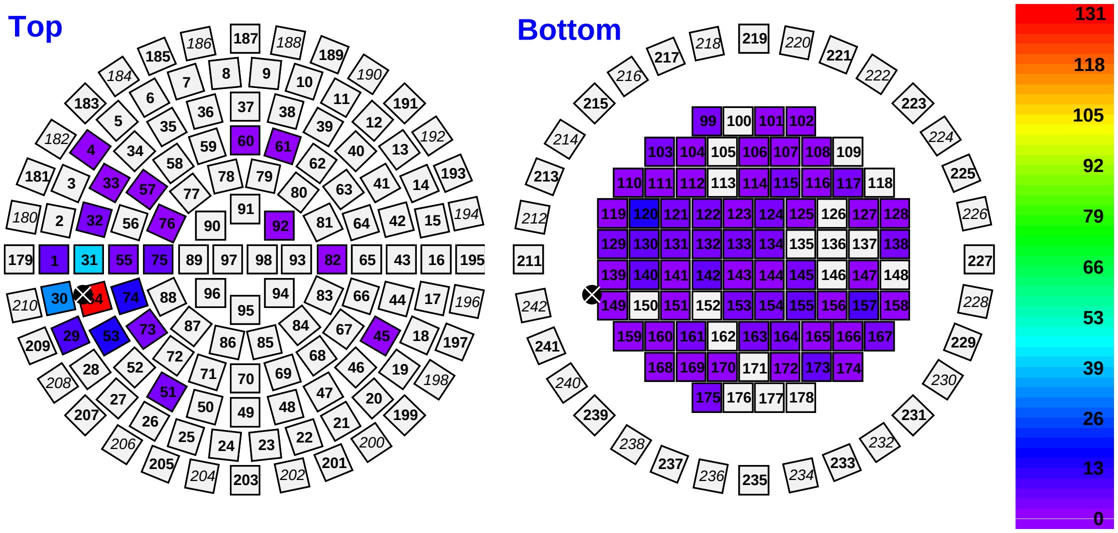

Figure 4.3: S2 PMT hit pattern of the event displayed in Fig. 4.2 with NN algorithm results. Numbers indicate individual PMTs, PMTs 179-242 are in the active veto. The color code is proportional to the signal seen by each PMT. The hit pattern on the top array (left) is used for the (x, y) position reconstruction. The black circled x is the reconstructed position. Figure from [Aprile *et al.*, 2012c].

4.1.4 Position Correction on Signal

Both S1 and S2 are spatially dependent. The primary factor for the spatial dependence of the signals is the light detection efficiency variation in the target volume. For S1, the scintillation photon detection efficiency depends on: the solid angle of a generated scintillation photon at the interaction position to the PMTs; the propagation of the scintillation photons, which is affected by the reflectivity of the detector materials; the absorption length and Rayleigh scattering length of LXe; the refractive index of LXe (see Sec. 2.3.5); the configuration of PMTs with different quantum efficiency including nonfunctional PMTs; the optical transparencies of the meshes, as well as other factors. Due to the axial symmetry of the TPC, the (x, y) dependence is expected to be enfolded in r dependence and an S1(r, z) correction map was used for the results published in [Aprile *et al.*, 2010; Aprile *et al.*, 2011b]. For the results during the commissioning run (run_07), the correction was performed with a ^{137}Cs source and with low anode voltage (2.2 kV) to avoid PMT saturation of the S2 at 662 keV, which would impact the linearity of the signal and the reconstruction of the positions. For the first science run (run_08), the correction was inferred from 40 keV γ rays during the ^{241}AmBe(α, n) neutron calibration. 40 keV γ rays produced by inelastic neutron scatterings on ^{129}Xe have the advantage of a higher event rate at the center of the TPC due to the longer mean free path of MeV neutrons compared to that of γ rays in LXe. The consistency check with other γ lines (236, 164, 80 keV γ rays) showed agreement at the 3 % level. For run_10, a S1(r, θ, z) correction was performed with low anode ^{137}Cs data for more accurate position correction, especially to improve the full absorption peak resolution near the bottom of the TPC. However, the difference between S1(r, z) and S1(r, θ, z) was verified to be less than 1 %. The correction was done with respect to the value at the center of the detector.

For the S2 signal correction, detector leveling is a prerequisite. The detector leveling was performed by looking at the width of the S2 pulse, which is sensitive to the gas gap width. After detector leveling [Plante, 2012; Aprile *et al.*, 2012c], the S2(x, y) width correction was carried out so as to take into account the (x, y) dependence of S2 width due to the mesh warping. Then, the S2 spatial correction was done in a similar way as the S1 spatial correction, but divided into two steps, in z and in x-y. The necessity for this two step method is attributed to the difference in signal generation between S2 and S1. The critical difference is that S1 is prompt (from the excitation of Xe atom) while S2 is produced by electrons drifted across LXe, which are subject to quenching of the signal by the capture by impurities and consequently, S2 exhibits a clear z dependence. Therefore, the S2(z) correction requires electron lifetime correction in addition to the solid angle variation. A linear fit to the electron lifetime evolution yields the z correction for the S2 signals with a small systematic uncertainty ($< 1.3\,\%$).

The S2(x, y) correction is influenced by the light detection efficiency variation which depends on the same factors as the S1 correction, however additionally including nonuniformity in the proportional scintillation gap. Fig. 4.4 shows the S2 response of the top (left)

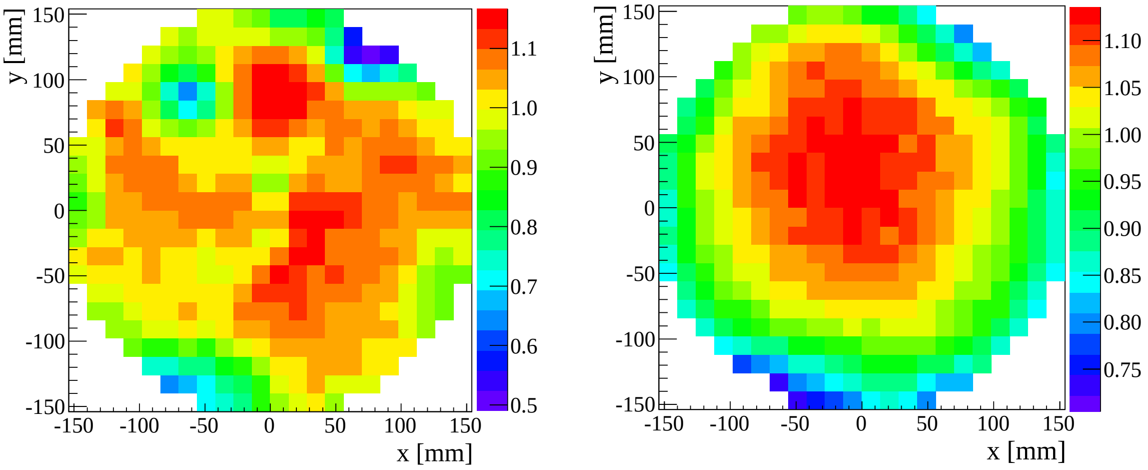

Figure 4.4: S2 response of the top (left) and bottom (right) PMT arrays, measured with 40 keV γ rays from inelastic neutron scattering off ^{129}Xe. The color code is the relative change compared to the mean. The bottom PMT array shows a more uniform response while top PMT array shows more fluctuations due to nonworking PMTs, such as at ($x \sim -50\,\mathrm{mm}$, $y \sim 100\,\mathrm{mm}$). Figures from [Aprile *et al.*, 2012c].

and the bottom (right) PMT array. S2 signals from the top and bottom PMT arrays are corrected independently with two different correction functions. Since the S2 signal is produced very close to the top array PMTs, positions close to nonfunctional top array PMTs suffer a greater reduction in signal and the spatial nonuniformity is more pronounced, as shown. In contrast, the S2 is distributed much more uniformly on the bottom array PMTs, resulting in a far more smoothly varying response function. This smaller uncertainty in the correction function led to the choice of using only the bottom PMT array S2 signal for the dark matter analysis presented in Chap. 7.

4.2 Energy Scales

One of the purposes of the detector calibration is to set the correct energy scale (e.g. convert pe to keV), allowing conversion between measured signal and energy deposit. As mentioned in Sec. 2.2, for the same amount of energy deposition, nuclear recoils and electronic recoils produce different amounts of S1 and S2. Therefore, the nuclear (E_{nr}) and electronic (E_{er}) recoil energy scales must be established separately.

The energy scale in LXe detectors is solely based on the prompt scintillation signal S1. One of the reasons for this is that many LXe detectors do not detect the ionization signal at all. Another reason, more relevant to dark matter detection, is that only the prompt scintillation yield of nuclear recoils has been measured down to very low nuclear recoil energy [Plante *et al.*, 2011], while the ionization yield remains largely unknown in the low energy region [Aprile *et al.*, 2006; Sorensen and Dahl, 2011]. Building energy scales on S1 alone results in highly nonlinear energy scale functions.

The relationship between the energy deposit and the amount of photons and electron-ion pairs produced in LXe detectors only depends on the LXe properties as a detection medium. Therefore, dedicated small setups are preferred to study the energy dependence of signals in LXe. However, it is mandatory for the energy calibration of practical detectors to use the same reference sources as were used in the dedicated setup. Moreover, it is still desirable to verify the energy dependence of signals from LXe in the WIMP search detector. The energy dependence of S1 is typically expressed with S1 scintillation yield, $L_y(E_{\mathrm{r}})$, defined as the size of the S1 over the recoil energy in the LXe, E_{r}, with units of pe/keV. $L_y(E_{\mathrm{r}})$ is obtained by the multiplication of absolute scintillation yield (see Sec. 2.3) and scintillation photon detection efficiency. Hence, $L_y(E_{\mathrm{r}})$ is detector specific and must be calibrated for each detector. Consequently, every detector has its own energy scale, even if these can be related through the use of a common energy calibration source.

One thing to keep in mind is that the response of photoabsorbed γ rays is different from the response of electrons. A photoabsorbed γ ray deposits its energy with multiple energetic electrons produced as a result of the photoabsorption. Hence, the scintillation yield obtained is then the convolution of the distribution of electron energies produced with the scintillation response of LXe to electrons, instead of that of an electron of that energy. Therefore, β and γ would have different energy scales, although the final carriers depositing energy in the LXe are the same - an electron for both cases. Since the main electronic recoil background contribution at low energies is attributed to the Compton electrons from high-energy γ rays (originating from the residual radioactive isotopes in the detector materials), it is necessary to know the scintillation response of LXe to electronic recoils with a single electron in order to set up the electronic recoil background energy scale. This topic will be covered in detail in Chap. 6.

4.2.1 Electronic-Recoil Equivalent Energy (γ rays)

The electronic-recoil equivalent energy scale is defined using a γ-ray source to obtain the conversion between energy deposited and detector response. This response is measured in photoelectrons (pe) for the scintillation signal, or electrons for the ionization signal. Reconstructed energies with such a scale will have units of $\mathrm{keV_{ee}}$, keV electron-equivalent. If the scintillation signal alone or the ionization signal alone is used to define the scale, the scale will in general not be linear over a large range of energies, since the fraction of electrons that recombine varies with energy. Consequently, implicitly attached to the unit of $\mathrm{keV_{ee}}$ is the energy at which the calibration was performed.

Fig. 4.5 shows the γ-ray response of XENON100 to several sources along with the Monte Carlo simulation expectation using the NEST model [Szydagis *et al.*, 2011]. ^{137}Cs is used to obtain the S1 light yield $L_y(662\,\mathrm{keV_{ee}})$. In addition, ^{241}AmBe(α, n) calibration provides several lower γ lines from inelastic neutron interactions with Xe nuclei. 40 and 80 keV γ rays are obtained from inelastic neutron scattering on ^{129}Xe and ^{131}Xe. 164 and 236 keV γ rays are obtained from the deexcitation of neutron-activated ^{131m}Xe and ^{129m}Xe. (Tab. 2.5 shows the inelastic neutron interactions with Xe mentioned above.) It is clear that the

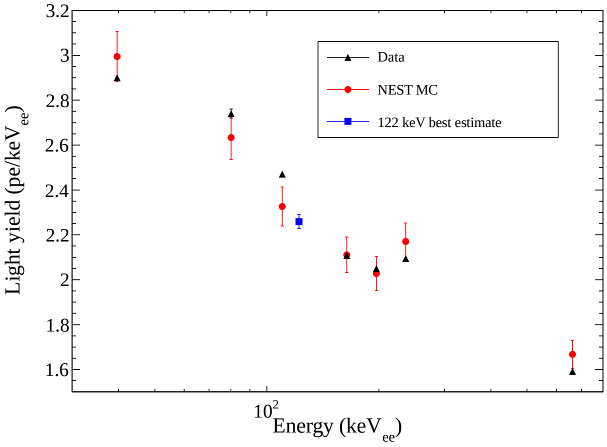

Figure 4.5: S1 light yields to several γ rays. 40 and 80 keV γ rays are due to the inelastic neutron scattering of Xe, 164 and 236 keV γ rays are from activated Xe, 110 and 197 keV are from activated F, and 662 keV full absorption peak is from ^{137}Cs source. The S1 light yield at 122 keV was inferred using these data with the energy dependence of S1 light yield from NEST model [Szydagis *et al.*, 2011]. Credit: XENON100 collaboration.

$L_y(E_{\mathrm{er}})$ shows nonlinear behavior with energy. 236 keV is a good example of the manifest energy dependence of $L_y(E_{\mathrm{er}})$. Its unusually high L_y value is expected because it is from a two-step deexcitation, each step having lower energies: a 196 keV γ ray followed immediately by a 40 keV γ ray. $L_y(E_{\mathrm{er}})$ increases as E_{er} decreases due to the variation in the fraction of electron-ion pairs that recombine as a function of energy, resulting in a higher apparent L_y for the two consecutive γ rays when compared to a monoenergetic γ ray at the same energy. Therefore, the 236 keV γ ray is excluded when inferring $L_y(E_{\mathrm{er}})$ for γ rays. Neutrons from ^{241}AmBe(α, n) also interact with the F nuclei in the PTFE walls of the TPC, via inelastic scattering. ^{19}F then deexcites emitting 110 and 197 keV γ rays, with half-lives of 0.6 and 89.3 ns, respectively. However, due to their short mean free path in LXe, these γ rays can only be observed at the edge of the target volume.

Conventionally, the S1 light yield is reported using 122 keV γ rays. The volume-averaged S1 light yield of XENON100 at 122 keV was inferred as $L_y(122\,\mathrm{keV_{ee}}) = (2.28 \pm 0.04)\,\mathrm{pe/keV_{ee}}$ for run_10 (see Fig. 4.5).

4.2.2 Electronic-Recoil Combined Energy Scale

Since variations in the recombination fraction induce an anticorrelation between the scintillation and ionization signals, it is possible to construct a linear energy scale in which those recombination fluctuations are canceled by adding the two signals with appropriate factors, an idea suggested in [Seguinot *et al.*, 1992]. This electronic recoil energy scale is called the combined energy scale and several γ sources are usually used to construct it, hence units of $\mathrm{keV_{ee}}$ are also used for energies reconstructed with it.

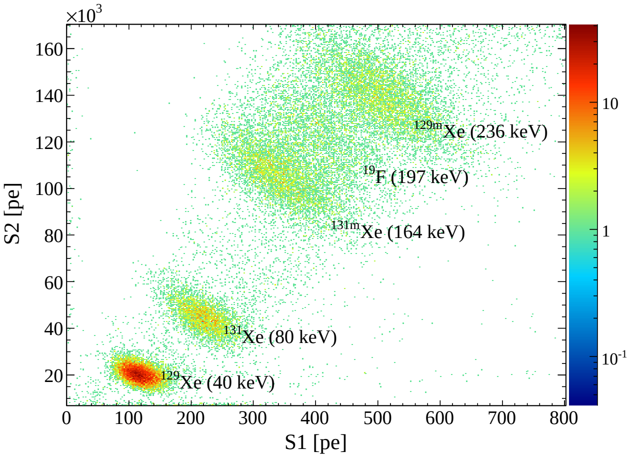

Figure 4.6: γ lines from the ^{241}AmBe(α, n) calibration data in position-corrected S2 vs S1. All the γ lines due to the inelastic neutron interactions in LXe, along with the inelastic neutron interactions with the F nuclei are shown. All the lines exhibit clear anticorrelation between S2 and S1, which decreases with the decrease of energy. Credit: XENON100 collaboration.

Fig. 4.6 shows the anticorrelation between ionization signal (S2) and scintillation signal (S1) of the γ lines from ^{241}AmBe(α, n) calibration data. All the γ lines due to the inelastic neutron interactions in LXe, along with the 197 keV γ line attributed to the inelastic scattering of the neutron with F are shown. All the γ lines exhibit clear anticorrelation, which decreases with the decrease of energy. Therefore, it is possible to obtain a lower energy resolution by utilizing the anticorrelation between S2 and S1.

Fig. 4.7 shows how to define the anticorrelation angle θ (left) and how much the energy

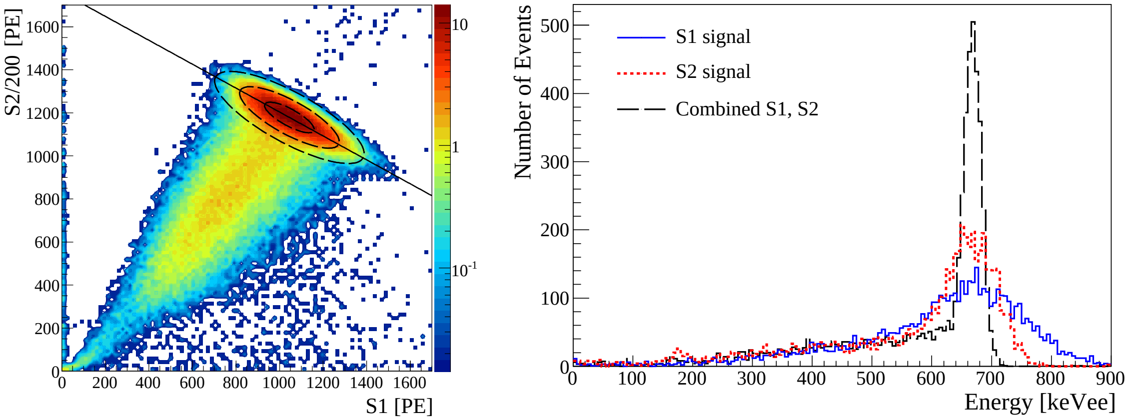

Figure 4.7: Definition of anticorrelation angle with the ^{137}Cs calibration data (left). The main population showing anticorrelation is photoabsorbed 662 keV γ rays while the lower energy tail is attributed to Compton scattering or partial energy deposition by γ rays. The projection along the line shown in the figure improves the resolution significantly. The spectral comparison between S1, S2, and projection along the line is shown in the right figure. S1 has the worst peak resolution because the number of generated scintillation photons is smaller than that of S2, and the S1 signal size has more pronounced position dependence compared to the S2 signal. As expected, the width of the combined energy peak is much narrower. Figures from [Aprile *et al.*, 2012c]

resolution can be improved by using the S2-S1 combined energy scale compared with S1 alone or S2 alone (right), using a ^{137}Cs source. By defining an ellipse in the S2-S1 plane described by a two-dimensional Gaussian, the anticorrelation angle θ, the angle between the line shown in Fig. 4.7 (left) and the horizon can be determined. The projection of the peak along this angle allows for an improved energy resolution. From the mean positions and angles obtained from calibration data, the combined energy scale for electronic recoil events has been defined. All the γ sources mentioned in Sec. 4.2.1, together with 1173, 1333 keV γ rays from ^{60}Co were used to set up the electronic-recoil combined energy scale.

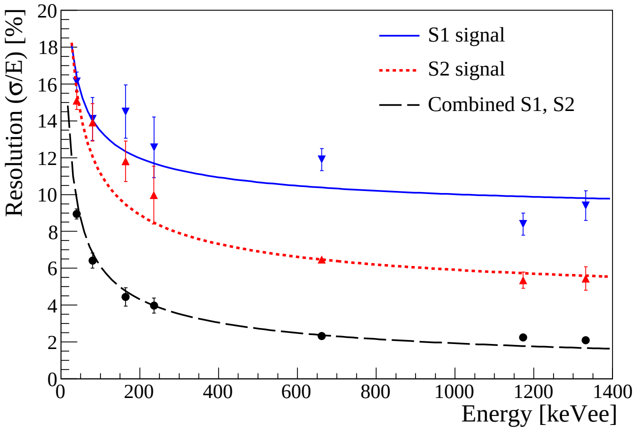

Figure 4.8: Measured relative energy resolution (σ/E) of γ calibration lines between 40 and 1333 keV$_{ee}$ in S1, S2, and combined energy scale, along with the fits with $1/\sqrt{E}$ dependence of σ/E. Figure from [Aprile *et al.*, 2012c].

Fig. 4.8 shows the γ-ray energy resolution of XENON100 as a function of energy. The energy resolution depends on the intrinsic resolutions of the scintillation and ionization processes in LXe, the spatial dependence of light collection efficiency in the LXe target volume, statistical fluctuations of observed photoelectrons, and the PMT gain fluctuation.

The energy resolution, R_c, is given by Eq.(5) from [Aprile *et al.*, 2007b]

$$R_c{}^2 = \frac{\sin^2\theta R_{\mathsf{S1}}{}^2 + \cos^2\theta R_{\mathsf{S2}}{}^2 + 2\sin\theta\cos\theta R_{\mathsf{S1,S2}}}{(\sin\theta + \cos\theta)^2} \tag{4.1}$$

where θ is the anticorrelation angle mentioned above, R_{S1} and R_{S2} are the energy resolutions from scintillation and ionization spectra, respectively. The covariance $R_{\mathsf{S1,S2}}$ is the contribution from the correlation of the two signals, which is typically expressed using correlation coefficient $\rho_{\mathsf{S1},\mathsf{S2}}$,

$$\rho_{\mathsf{S1},\mathsf{S2}} = \frac{R_{\mathsf{S1},\mathsf{S2}}}{R_{\mathsf{S1}} \cdot R_{\mathsf{S2}}} \tag{4.2}$$

The obtained values of $\rho_{\mathsf{S1},\mathsf{S2}}$ are between -0.7 and -0.9 [Kish, 2011], which indicate strong anticorrelation between S1 and S2 signals.

The energy resolution was obtained from a fit with a functional form of

$$\frac{\sigma(E)}{E} = a + \frac{b}{\sqrt{E}} \tag{4.3}$$

where a and b are constants that are different for the three scales. The function is described with $1/\sqrt{E}$ dependence since the mean and the resolution of the energy are proportional to the number of observed photoelectrons and the square root of the number of observed photoelectrons, respectively. It is shown that a resolution of 2 % can be reached with the combined energy scale at energies higher than 600 keV.

The combined energy scale is used for the comparison of background spectra with Monte Carlo simulation expectations since the improved resolution greatly helps in the separation of lines.

4.2.3 Nuclear-Recoil Equivalent Energy

Although the nuclear recoil equivalent energy scale is the most relevant for a WIMP search, it is hard to obtain the $E_{\mathrm{nr}}(\mathsf{S1})$ directly from the detector. The major difficulty lies in the determination of the true nuclear recoil energy of particles interacting with Xe nuclei. The probability of having a nearly monoenergetic neutron source in the energy region of interest for a WIMP search is negligible. Therefore, an independent measurement of LXe responses to nuclear recoils with a good knowledge of neutron energy deposition is required. This can be achieved by recording elastic scattered monoenergetic neutrons with far detectors at a fixed angle. This method measures the energy dependence of nuclear recoils directly. There exists another way of inferring the energy dependence of the scintillation response of LXe to nuclear recoils, namely by comparing experimental data of the recoil energy spectrum obtained with a neutron source with a Monte Carlo simulation of the expected nuclear recoil energy spectrum. However, this indirect method tends to have high systematic uncertainty since any neglected factors such as uncertainties in the energy spectrum of the neutron source, efficiency losses near threshold, energy dependence of selection cuts, etc, which are typically difficult to measure precisely, are absorbed in the energy dependence of scintillation response of LXe to nuclear recoils. Several measurements have been reported with this indirect method [Horn *et al.*, 2011; Sorensen *et al.*, 2009].

Given that one has to rely on energy dependence measurements from an independent detector to set the energy scale, the determination of the nuclear recoil energy scale in WIMP search LXe detectors is a two-step procedure. First, using the full absorption peak of a known γ ray source, determine the $\mathsf{S1}$ light yield L_y at fixed γ energy, as explained in Sec. 4.2.1. The conventional value is $L_{y,\mathrm{er}}(E_{\mathrm{er}} = 122\,\mathrm{keV}) = L_y(122\,\mathrm{keV_{ee}})$. Second, use the result from the energy dependence measurement of $\mathcal{L}_{\mathrm{eff}}$, the relative nuclear recoil $\mathsf{S1}$ light yield with respect to $L_y(122\,\mathrm{keV_{ee}})$ at zero electric field

$$\mathcal{L}_{\mathrm{eff}}(E_{\mathrm{nr}}) = \frac{L_{y,\mathrm{nr}}(E_{\mathrm{nr}})}{L_{y,\mathrm{er}}(E_{\mathrm{er}} = 122\,\mathrm{keV})} \tag{4.4}$$

where subscripts “nr” and “er” refer to nuclear and electronic recoils. Here, $L_y(122\,\mathrm{keV_{ee}})$ serves as an anchor point, its value determined separately in both the WIMP search detector and the small setup for $\mathcal{L}_{\mathrm{eff}}$ measurement. The choice of 122 keV γ rays as an anchor point is mainly because of common use of ^{57}Co sources for small LXe detectors energy calibration. $L_y(122\,\mathrm{keV_{ee}})$ can be directly determined in a small LXe detector, but in XENON100 it is inferred by interpolation of the measurements of several γ rays with different energies (Sec. 4.2.1).

Since $\mathcal{L}_{\mathrm{eff}}$ is typically measured at zero electric field, the electric field quenching for electronic recoils and nuclear recoils has to be considered in using $\mathcal{L}_{\mathrm{eff}}$ to set $E_{\mathrm{nr}}(\mathsf{S1})$ in a dual-phase detector. An external electric field suppresses recombination and this quenching in scintillation signal is different for electronic and nuclear recoils (see Sec. 2.4.3). $S_{\mathrm{er}}(E)$ and $S_{\mathrm{nr}}(E)$ are the $\mathsf{S1}$ electric field quenching factors for electronic and nuclear recoils, respectively, where E is the applied electric field.

With all factors together, the nuclear recoil energy $E_{\mathrm{nr}}(\mathsf{S1})$ is computed by

$$E_{\mathrm{nr}} = \frac{\mathsf{S1}}{{L_y}^*}\frac{1}{\mathcal{L}_{\mathrm{eff}}}\frac{S_{\mathrm{er}}}{S_{\mathrm{nr}}} \tag{4.5}$$

where ${L_y}^* = L_y(122\,\mathrm{keV_{ee}})$ is the $\mathsf{S1}$ light yield of photoabsorbed 122 keV γ rays, $\mathcal{L}_{\mathrm{eff}}$ is the relative scintillation efficiency of LXe to nuclear recoils at zero electric field, and $S_{\rm er}$ and $S_{\rm nr}$ are the S1 electric field quenching factors for electronic and nuclear recoils, respectively. $S_{\rm er}$ and $S_{\rm nr}$ are measured to be 0.58 and 0.95 under the XENON100 operating conditions with an electric field of 0.53 kV/cm [Aprile *et al.*, 2006]. The unit "$\rm keV_{nr}$" is employed for energies reconstructed with the nuclear recoil equivalent energy scale. This is similar to the electronic recoil equivalent energy scale, but for nuclear recoils.

$\mathcal{L}_{\rm eff}$ has been directly measured independently with numerous detectors by several groups [Arneodo *et al.*, 2000; Bernabei *et al.*, 2001; Akimov *et al.*, 2002; Aprile *et al.*, 2005; Chepel *et al.*, 2006; Aprile *et al.*, 2009; Manzur *et al.*, 2010]. Even though measurement accuracy and the understanding of systematic uncertainties has been improving over the years, there is still sizable disagreement present in $\mathcal{L}_{\rm eff}$ measurements, especially at low energies. The most recent direct measurement of $\mathcal{L}_{\rm eff}$ from our group [Plante *et al.*, 2011] reached the lowest energy (3 $\rm keV_{nr}$) ever measured with significantly reduced uncertainty. Nevertheless, to make the best estimate of $\mathcal{L}_{\rm eff}$ for XENON100 results, we took all the available direct measurements of $\mathcal{L}_{\rm eff}$ and performed a fit assuming that $\mathcal{L}_{\rm eff}$ can be described by a Gaussian at each $E_{\rm nr}$ value. The measurements and fits are shown in Fig. 4.9.

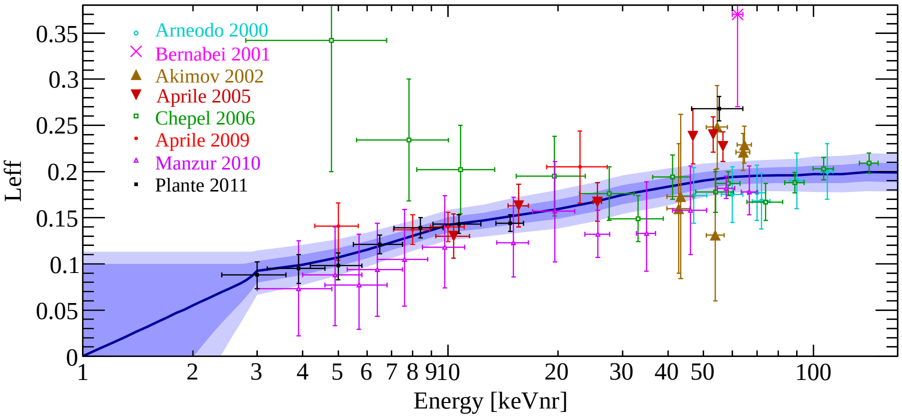

Figure 4.9: All direct measurements of $\mathcal{L}_{\rm eff}$ along with a fit described by a Gaussian distribution to obtain the mean (solid line) and the uncertainty band (1 and 2 σ). Below 3 $\rm keV_{nr}$ the trend is logarithmically extrapolated to $\mathcal{L}_{\rm eff} = 0$ at 1 $\rm keV_{nr}$. Figure from [Aprile *et al.*, 2011b].

The trend observed is of slowly decreasing $\mathcal{L}_{\text{eff}}$ towards low energies. One thing to notice is that the fit on the estimation of $\mathcal{L}_{\text{eff}}$ must be extrapolated below 3 keV, since no direct measurements exist below this energy. Given that this lowest nuclear recoil energy measurement was only possible due to very high light detection efficiency of the LXe detector used in [Plante *et al.*, 2011] and that it is almost at the lowest possible measurable nuclear recoil energy for $\mathcal{L}_{\text{eff}}$ measurement, this extrapolation at low energies is currently unavoidable. To be conservative, extrapolation below 3 keV was performed with a logarithmically decreasing function to have zero scintillation at 1 keV.

4.3 Electronic Recoil Background

After setting the combined energy scale, it is possible to compare the measured electronic recoil background from the detector materials with a simulation. GEANT4 simulations which utilize a detailed geometry of the concrete realization of the detector were used to estimate the electronic recoil background of XENON100 [Aprile *et al.*, 2011e]. The inputs to the simulation are the radioactive screening measurements listed in [Aprile *et al.*, 2011d]. The main electronic recoil background contribution from detector materials originates from radioactive contamination in the PMTs. High-energy γ rays from the residual radioactive isotopes, mainly ^{238}U, ^{232}Th, ^{40}K, and ^{60}Co, Compton scatter in the target volume and deposit their energies in the WIMP search region. The intrinsic radioactive impurities in the LXe, such as ^{85}Kr and ^{222}Rn, and the contribution from two neutrino double-beta decays of ^{136}Xe, were added separately to obtain the total Monte Carlo simulation spectra.

Fig. 4.10 shows the comparison of the measured single scatter electronic recoil background in a 10 kg fiducial volume with the prediction from simulation for `run_10`, without the active veto cut. Since WIMPs are expected to interact only one time in the target volume due to their small elastic scattering cross-section, the particle interactions of interest are only single scatter events, regardless of their types. In fact, all the data selection cuts are tuned for the detection of single scatter events at low energies. A small fiducial volume is chosen to minimize losing events by PMT saturation at high energy (see Sec. 3.2.3), which forces the event's position to be reconstructed towards the center of the TPC. No scaling

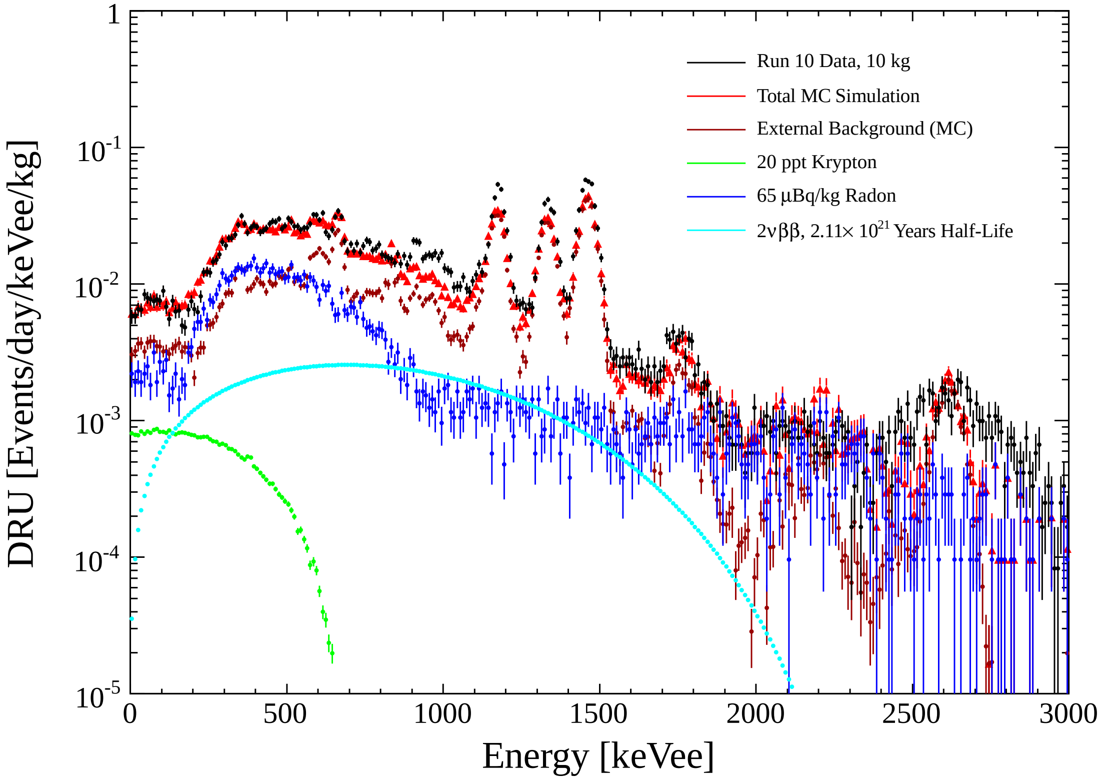

Figure 4.10: Measured electronic recoil background from single scatter events in a 10 kg fiducial volume during the second science run (`run_10`) and the predicted rate from simulation, without the active veto. No scaling of the activities was applied for the radioactive isotopes. (See the text for the detailed information about the radioactive isotopes.) The agreement below 800 keV is very good given this fact. The agreement is expected to be worse at high energies since all the single scatter cuts are optimized for the low energy event detection. Credit: XENON100 collaboration.

of the activities was applied for the radioactive isotopes. 20 ppt of krypton concentration was used based on the results from ultra-sensitive rare gas mass spectrometry combined with a sophisticated Kr/Xe separation technique (19 ± 4 ppt) and the analysis of delayed β-γ coincidences associated with the ^{85}Kr beta decay (18 ± 8 ppt) [Aprile *et al.*, 2012a]. The radon activity is given by Bi-Po delayed coincidence and α analyses, where the most conservative value is taken to be $\sim 65\,\mu$Bq/kg. ^{136}Xe two-neutrino double-beta decay spectrum is obtained from the measurement of [Ackerman *et al.*, 2011]. The active veto cut is not applied to reduce systematic uncertainties since it exact behaviour is hard to model in the Monte Carlo simulation. The agreement between the prediction and the measurement below 800 keV is very good. The agreement is actually expected to worsen at higher energies since most of the data analysis selection cuts are optimized for the low-energy events detection (below 100 keV) as previously mentioned.

The predicted rate of single scatter electronic recoil events in the energy region between 10 and 100 keV, without veto coincidence cut, is $(14.5 \pm 0.9) \times 10^{-3}$ events keV^{-1} day^{-1} kg^{-1} for 34 kg fiducial volume used in the results from `run_10` [Aprile *et al.*, 2012a]. With the application of the veto coincidence cut with an energy threshold of 100 keV in the veto, the rate reduces to $(5.3 \pm 0.6) \times 10^{-3}$ events keV^{-1} day^{-1} kg^{-1}, by a factor of three. The background reduction factor of the veto coincidence cut is only moderately senstive to the energy threshold below ~ 200 keV [Aprile *et al.*, 2011e]. Since veto PMTs are closer to the external source, a more pronounced spatial dependence in S1 size (and hence in the energy threshold) in the veto volume is expected than in the target volume. The averaged energy threshold in the veto measured with a collimated ^{137}Cs source is 90 % at ~ 200 keV [Kish, 2011].

4.4 Electronic and Nuclear Recoil Band Calibration

The ratio of proportional scintillation (S2) over prompt scintillation (S1) is a good discriminant due to the ionization density dependence in recombination. Hence it can be used to distinguish electronic recoil background from the WIMP-induced nuclear recoils (see Sec. 2.4.5). An accurate knowledge of the response of the detector to both electronic and nuclear recoils in terms of discrimination is essential for the further rejection of electronic recoil background. The discrimination band is defined in a 2D parameter space, with a discrimination parameter plotted against an energy parameter. Traditionally, $\log_{10}(\mathsf{S2}/\mathsf{S1})$ is used as the discrimination parameter and $\mathsf{S1}$ is used for energy scale determination.

To characterize the electronic recoil band, the detector was irradiated with 1.17 and 1.33 MeV γ rays from a 100 kBq ^{60}Co source, and several γ lines (with the highest of 2.6 MeV) from a 1.53 kBq ^{232}Th source. While the contribution from intrinsic electronic recoil backgrounds such as ^{85}Kr, ^{222}Rn, and ^{136}Xe is independent of the fiducial volume, the electronic recoil background contribution due to the radioactive isotopes in the detector materials changes significantly with the fiducial volume choice. If the intrinsic background is kept small enough, the main contribution to the electronic recoil background is from the radioactive isotopes in the detector materials. In this case, the mechanism for the low-energy background is Compton scattering of high-energy γ rays originating from radioactive decays in the detector materials. These scatterings deposit energies through Compton electrons, mostly with forward scattering. Consequently, irradiating the detector with a high-energy γ ray source imitates the electronic recoil background at low energy well.

For `run_08`, electronic recoil background calibrations were performed using a small ^{60}Co source (encapsulated in a A3029 capsule) placed at three different positions in the copper tube (see Fig. 3.10). In `run_10`, a wire-shaped ^{232}Th source was introduced additionally, mainly for more uniform irradiation of the detector. Fig. 4.11 shows the (x,y) distribution of single scattered electronic recoil events at low energies ($2\,\text{pe} < \mathsf{S1} < 35\,\text{pe}$) with the active veto cut applied, from ^{60}Co (left) and ^{232}Th (right). No significant difference in (x,y) position is evident between the two sources. The reason is that the Compton scattering cross section varies very mildly above 30 keV and it decreases with energy above ~100 keV as shown in Fig. 2.3. With an attenuation length of $\sim 10\,\text{cm}$, the wire shape of the ^{232}Th source does not provide a significant advantage compared to taking data with a ^{60}Co source at three different positions 120° apart. In addition, band shape comparison between ^{60}Co and ^{232}Th was also performed and the differences in the mean (μ_{er}) and the width (σ_{er}) of the band were verified to be less than 0.4 and 1 %, respectively.

The detector response to nuclear recoils is important not only to determine the electronic

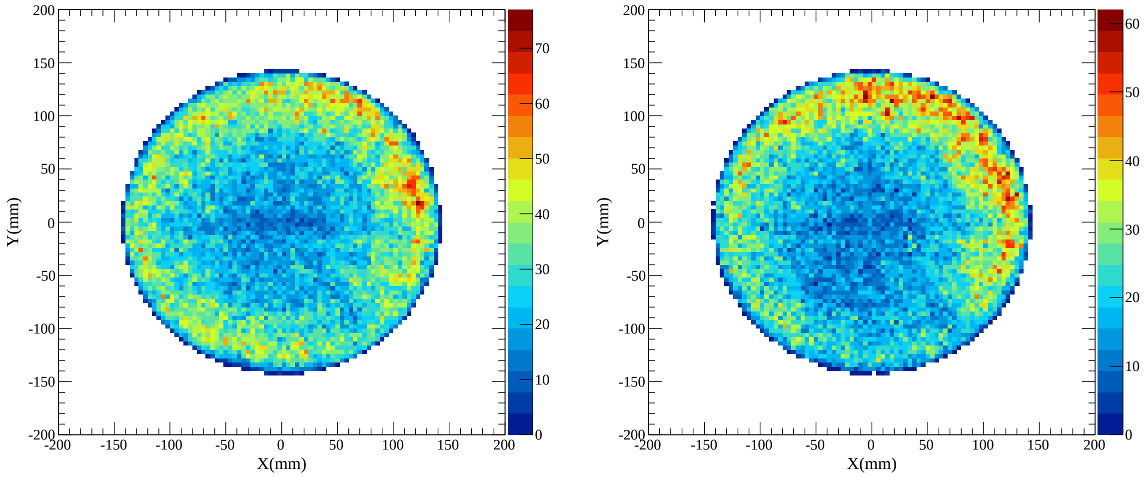

Figure 4.11: (x,y) position distribution of single scattered electronic recoil events from ^{60}Co (left) and ^{232}Th (right). Credit: XENON100 collaboration.

recoil background contamination in the WIMP-induced signal region but also to estimate the acceptance of the different data selection cuts. For the nuclear recoil band calibration, an ^{241}AmBe(α, n) source with $\sim$ 200 n/s activity was placed at one point inside a lead brick shield. The lead shield was used to reduce accompanying γ rays as shown in Fig. 3.10. It would be desirable to irradiate the detector with several source positions to probe the detector volume uniformly, as was done for ^{60}Co calibration. However, the risk of activating surrounding detector materials is high and the allowed exposure time to neutrons is limited by LNGS. In addition, neutrons have a longer mean free path than γ rays ($\sim$ 10 and $\sim$ 6 cm for MeV neutrons and MeV γ rays, respectively in LXe) and hence, the position dependence of an interaction due to the external source position is less pronounced.

Fig. 4.12 shows the electronic recoil and nuclear recoil band with a single scatter event selection cut in 34 kg fiducial volume. Red points indicate electronic recoil events from ^{60}Co and ^{232}Th data combined, and blue points indicate nuclear recoil events from ^{241}AmBe(α, n) data. Green circles are the mean of the electronic recoil band and yellow circles are the mean of the nuclear recoil band. For the discrimination parameter, only the bottom PMT array S2 signal (S2$_{\mathsf{b}}$) was used due to its more uniform response compared to the top PMT

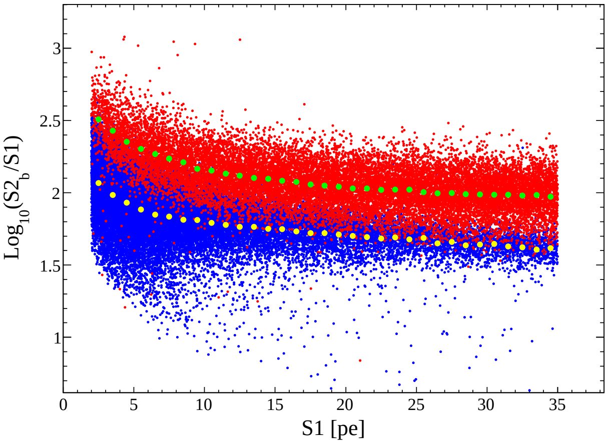

Figure 4.12: Electronic (red) and nuclear (blue) recoil bands from the XENON100 calibration along with the means of the electronic (green circles) and nuclear (yellow circles) recoil bands. The nuclear recoil band is lower than the electronic recoil band due to recombination. Most of the electronic recoil events can be described as Gaussian with small amounts of events leaking far down to the nuclear recoil band. Credit: XENON100 collaboration.

array $\mathsf{S2}$ signal, as explained in Sec. 4.1.4.

The first thing to notice in the figure is that $\log_{10}(\mathsf{S2_b}/\mathsf{S1})$ decreases with an increase in recoil energy for both the electronic and nuclear recoil bands. Second, the $\log_{10}(\mathsf{S2_b}/\mathsf{S1})$ mean of the electronic recoil band is higher than that of the nuclear recoil band. Since the purpose of discrimination is to estimate the electronic recoil background contamination in the expected WIMP search region, characterizing the electronic recoil band shape is critical. As shown in the figure, the major population of electronic recoil events can be described by a Gaussian distribution in the discrimination parameter in a small $\mathsf{S1}$ interval, with a mean $\mu_{\mathrm{er}}(\mathsf{S1})$, and width $\sigma_{\mathrm{er}}(\mathsf{S1})$. Why the electronic recoil band exhibits Gaussianity in $\log_{10}(\mathsf{S2_b}/\mathsf{S1})$ space is not known, but has been verified with data to be the case [Aprile *et al.*, 2012b]. In addition to the events which follow the Gaussian distribution of the electronic recoil band, there exist a small number of electronic recoil events deviating from the Gaussian shape of the electronic recoil band, with lower discriminant values.

It is possible to separate the electronic recoil background into two types, depending on this non-Gaussian feature in the discrimination parameter vs energy. $Type\,I$ background follows a Gaussian distribution and $Type\,II$ background does not. $Type\,II$ background is anomalous background in a sense that it carries lower S2/S1 than the majority of electronic recoil events. The $Type\,II$ events are problematic because they leak into the nuclear recoil band. While $Type\,I$ background behavior is obvious, a study on the mechanism of the $Type\,II$ background is required to describe the behavior of $Type\,II$ background. As mentioned in Sec. 3.2, from the design stage of XENON100 one mechanism responsible for this $Type\,II$ background was known. The following chapter is dedicated to a study on the anomalous background events in XENON100.

Chapter 5

Anomalous Background Events in XENON100

As discussed in Chap. 4, there exists a type of electronic recoil background which mimics nuclear recoils in terms of the `S2/S1` ratio. This is the so-called “anomalous background” since it does not follow the major electronic background population in the discrimination parameter. It is important to have a good understanding of anomalous background so as to complete the understanding of the electronic recoil background of XENON100. To achieve this goal, one can make a sequential procedure. First, make a hypothesis on the mechanism of the anomalous background. Second, build a model based on it and verify the model with an estimation of anomalous background contribution. Last, make a prediction on the estimation of anomalous background contribution with the model.

We also developed an analysis cut to reject these events in parallel with the estimation of the anomalous background contribution. The events tagged by the anomalous background events rejection cut was extensively studied and its comparison with the model will be explained as well in this chapter.

This chapter is organized as follows: The mechanism of anomalous background events is described in Sec. 5.1, how to build a model using Monte Carlo simulation to estimate the anomalous background contribution in Sec. 5.2, verification of the model with electronic recoil band calibration data in Sec. 5.3, and development of the cut to reject the anomalous background in Sec. 5.4. Finally, this chapter ends with the discussion (Sec. 5.5). The data used in this chapter is from the first science run (run_08) of XENON100.

5.1 Mechanism of Anomalous Background Events

Since the defining characteristic of anomalous background is a reduced S2/S1 ratio, it is reasonable to come up with two possibilities for this scenario, quenched S2 or enhanced S1. When one thinks of the LXe enclosed by the PTFE structure and PMT arrays, one realizes that there exist S2 insensitive volumes because of the distance that must necessarily be maintained between the grids at HV and detector instruments such as PMTs. In addition, it is not possible to make a perfect realization of the electric field even inside the field cage and S2 insensitive region coexists in the field cage volume. Hence, the quenched S2 possibility looks plausible. For an enhanced S1, given that the light collection efficiency (LCE) map obtained from the S1 scintillation yield is well understood in the sensitive volume and is verified with the Monte Carlo simulation (which can be extended to outside of the sensitive volume), we can discard this possibility.

Now let us think of the data selection cut of the band calibration data for the discrimination between electronic and nuclear recoils. As mentioned previously, we are interested in only single scatters in the target volume, since that is what is expected from WIMP interactions. The way to select single scatter events in XENON100 is to find events with one S1 and one S2 as shown in Fig. 4.2. This means an event without S2 does not fulfill the single scatter selection cut. Thus the "real" single scatter in the S2 insensitive volume would be discarded. However, this implies if multiple scatters happen with one scatter in the S2 sensitive volume providing single S2 and another scatter(s) in S2 insensitive volume, we would select them even though they are "fake" single scatters. This is because prompt scintillation photons travel through the LXe with the speed of light and it is impossible to distinguish individual S1s from multiple scatters, they just sum up and result in one larger S1 signal.

Both electrons and γ rays contribute to the electronic recoil background. Electrons lose their energies in the detection medium with many small steps along the track, kind of in a continuous manner. In addition, the high electronic stopping power of electrons in combination with the high density of LXe makes the track size of electrons point-like at low energies (at 60 keV, the track length is 4.6 μm [Mozumder, 1995]). Therefore, multiple scatters are not expected from electrons. On the other hand, γ rays can make multiple scatters via Compton scattering in the LXe or the coincidence of two γ rays, one in S2 sensitive volume and the other in S2 insensitive volume, can provide the mechanism mentioned above. Anomalous background events with this mechanism are dubbed γ-X events for these reasons.

Fig. 5.1 shows possible particle interactions in XENON100 along with the waveforms and discrimination parameter vs S1 spaces. In the bottom of the figure, an example of a γ-X event is shown as a single γ interaction in the sensitive volume accompanied by a “X” interaction in the S2 insensitive region which results in the reduced S2/S1 and cause the event to leak into the WIMP search region. Since it can not be distinguished from a WIMP event, it is essential to estimate the γ-X event contribution to the background.

Given that it is impossible to know the position of an interaction from the data without a S2 signal, a Monte Carlo simulation is mandatory to estimate the γ-X event contribution. The GEANT4 simulation toolkit [Agostinelli *et al.*, 2003], version 4.9.1p02, was used with a full detector geometry description incorporating the detailed structure of the S2 insensitive regions such as the bottom PMT screening mesh, PTFE light-emitting diode (LED) holders, PTFE bottom reflector below cathode, and field shaping rings at large radii inside the TPC. Calibration and background simulations were performed using the company provided source activities and the screening results of the detector materials [Aprile *et al.*, 2011d].

Since the main background contribution of the first science run (run_08) was attributed to ^{85}Kr, the possibility of its contribution as γ-X was investigated. The only possible physical process is β-γ delayed coincidence, $^{85}\mathrm{Kr}(\beta, 173\,\mathrm{keV}) \rightarrow {}^{85m}\mathrm{Rb}(\gamma, 514\,\mathrm{keV}) \rightarrow {}^{85}\mathrm{Rb}$ with a 1.46 μs lifetime and a 0.454 % branching ratio. However, unlike the two immediate prompt scintillation generations, resulting in summed S1 signal (e.g., from Compton scattering), the 1.46 μs of time difference between β and γ decays from ^{85}Kr yields a few percent probability that the S1 from the β overlap with the S1 from the γ. On top of this, the branching ratio of this process further suppresses the possibility that the delayed coincidence of ^{85}Kr acts as

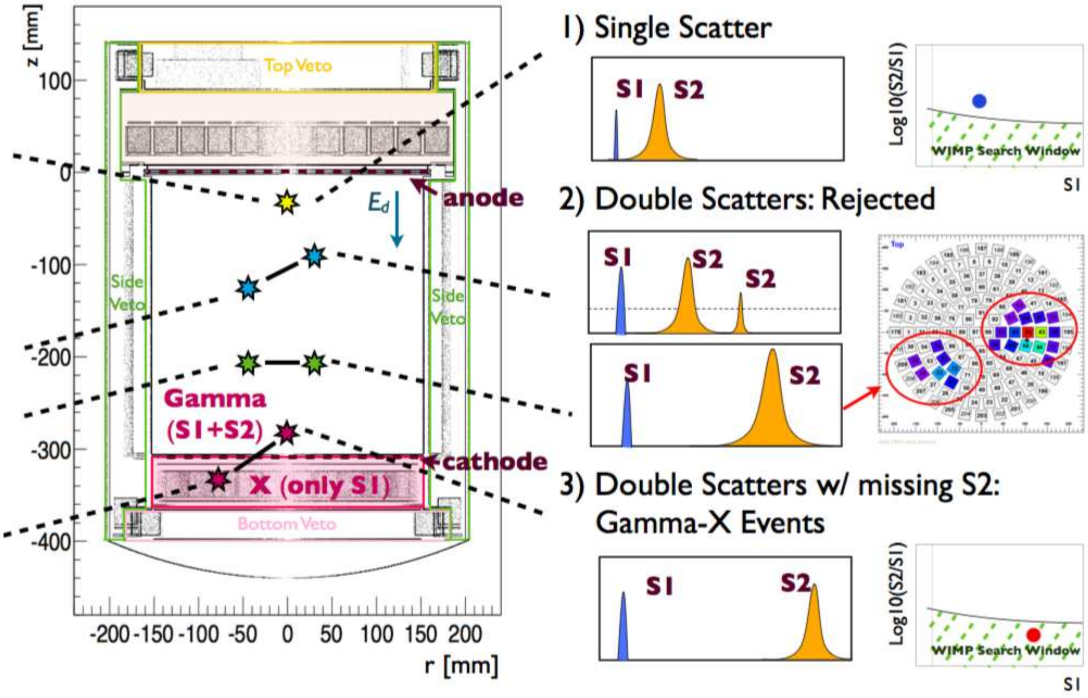

Figure 5.1: Particle interactions in XENON100 including an example of γ-X event along with the waveforms and discrimination parameter vs S1 spaces. Single scatter (top, yellow star) is a desired event. Double scatters (blue stars) can be rejected with the requirement of legitimate single S1 and single S2 signals. When the double scatters happen in the same z in the sensitive volume (green stars), it results in larger single S2 signal in the waveform, but these events can be rejected by looking at the S2 Top PMT hit pattern. In addition, it is not a problem in terms of discrimination because a nuclear recoil carries lower S2/S1 than an electronic recoil. Lastly, a γ-X event (red stars) which scatter once in the S2 insensitive volume and another time near the bottom of the sensitive volume fulfills the single scatter selection cut in waveform, but it leaks into the WIMP search region in discrimination parameter.

a γ-X event. From the Monte Carlo simulation, the contribution of ^{85}Kr to γ-X is expected to be less than $1.6 \times 10^{-4}\,\text{events}^{-1}\text{d}^{-1}$ in the total target volume below 100 keV, assuming a 400 ppt(particle/particle) concentration of Kr, and a $^{85}\text{Kr}/^{nat}\text{Kr}$ ratio of 2×10^{-11}.

5.2 Building γ-X Model

As mentioned previously, γ-X studies require Monte Carlo simulation to estimate its contribution to the electronic background. Therefore, building a model includes the energy calibration of the signal to make a reliable prediction from the simulation. This energy calibration is not trivial in a large detector and requires accurate knowledge of the energy dependence of the signal, which is not linear when only one signal is measured (Sec. 4.2). In addition, unlike the $\mathcal{L}_{\text{eff}}$ measurements for nuclear recoils (see Sec. 4.2.3), hardly any measurements exist for electronic recoils in LXe, especially at low energies ($\lesssim 100\,\text{keV}$). Even if so, at these energies, in most cases, scintillation light-yield measurements have been carried out with monoenergetic sources [Barabanov *et al.*, 1987a; Obodovskii and Ospanov, 1994; Yamashita *et al.*, 2004] where photoelectric absorption is the dominant interaction. Recently our group measured it with low-energy electrons in zero electric field, which will be discussed extensively in Chap. 6. However, at the time of this study, this result was not available and the energy dependence of recombination ratio exhibits nonlinear field dependence for electronic recoils while it shows linear field dependence for nuclear recoils [Dahl, 2009].

In addition, an S2 insensitive region may have a nonzero electric field and hence requires proper electric field quenching of the signal. Nevertheless, only scarce measurements of the field quenching were performed with photoabsorbed γ rays and the highest applied electric field was 5 kV/cm [Aprile *et al.*, 2006].

All of these point to the need to make assumptions on the energy calibration of the model due to lack of measurements. In this section, we start with the requisite assumptions related to energy calibration due to lack of our knowledge without measurements. Then we define the S2 insensitive region (X-region). We explain how to generate S1 with the S1 energy calibration, taking into account the interactions in the S2 insensitive regions. We generate S2 using the information from the electronic recoil band. Finally, we explain how we select γ-X events.

5.2.1 Assumptions on the Model

Energy Dependence of S1 Scintillation Yield and Its Extrapolation

We will use the S1 scintillation yield measurement of XENON100 with γ ray sources to calibrate S1. We are aware that the response of the photoabsorbed γ rays is different from that of electrons and the behavior at low energies is extrapolated. However, it was our best knowledge at the time of this study.

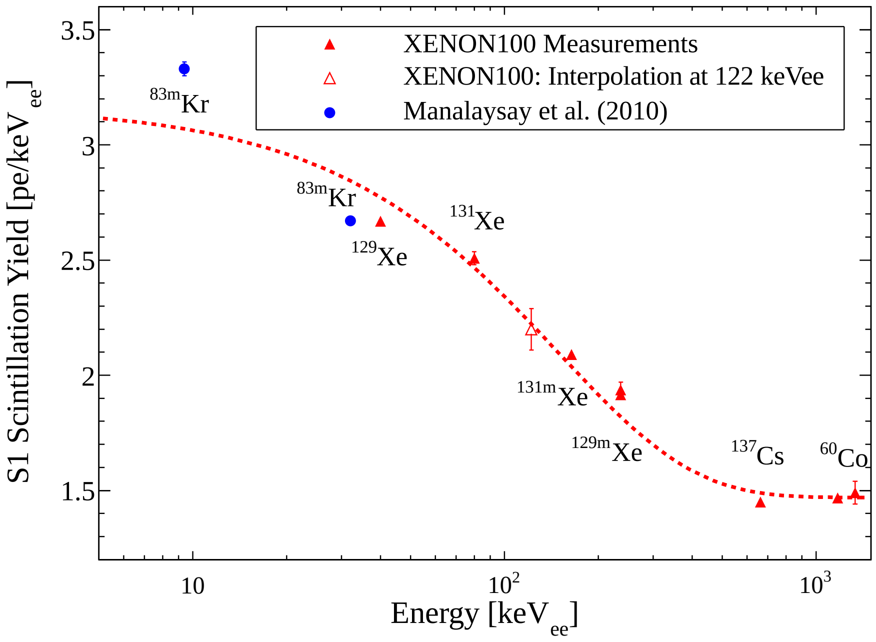

Figure 5.2: S1 scintillation yield measurements of XENON100 along with the model (dashed line) used for S1 calibration. As mentioned in Sec. 4.2.1, the scintillation yield at 122 keV$_{ee}$ was inferred due to its low penetration depth ($\sim$ 3 mm). The scintillation yield measurement of ^{83m}Kr decays (32.1, 9.4 keV) [Manalaysay *et al.*, 2010] is shown as well. Scintillation yields of ^{83m}Kr decays will be discussed in detail with the more recent measurement described in Chap. 6. Figure from [Aprile *et al.*, 2012c] and updated.

Fig. 5.2 shows S1 scintillation yield measurements of XENON100 using photoabsorbed γ rays from various radioactive sources along with the model (dashed line) used for S1 calibration. The dashed line was used to describe the energy dependence of the S1 scintillation yield. To infer low-energy behavior, the results from the scintillation yield measurement of ^{83m}Kr decays [Manalaysay *et al.*, 2010] were used. We will get back to the scintillation yields of ^{83m}Kr decays with thorough discussion in Chap. 6.

Electric Field Dependence on S1 Scintillation Yield and Its Extrapolation

Another critical requisite assumption was on the S1 field quenching. Only a few measurements exist for S1 and S2 electric field quenching and the measurements were performed only up to 5 kV/cm and with 122 keV photoabsorbed γ rays from a ^{57}Co source. Therefore, we assume that the field quenching of the 122 keV photoabsorbed γ rays represents the field quenching of the low-energy electrons. In addition, some of the S2 insensitive region experiences higher electric field than the measured value and the extrapolation was unavoidable too. We use the Fig. 2.10 to obtain S1 field quenching and the field quenching at higher electric field than 5 kV/cm was assumed to be the same as the value at 5 kV/cm.

Correlation between S1 and S2

Since the electric field quenching measurements accompany the anticorrelation between S1 and S2 and none of the measurements were performed with low-energy electrons, anticorrelation was not considered in the current model. The way we correlate S1 and S2 is not at the microscopic level, which fixes the sum of excitons and ions and allows the fluctuations of them, but rather in the macroscopic level using the electronic recoil band feature. It will be further explained in Sec. 5.2.4.

5.2.2 S2 Insensitive Region (X-region)

From the design stage of XENON100, special care was taken to reduce S2 insensitive regions in the LXe enclosed by the top and bottom PMT arrays and PTFE panels where both top and bottom PMTs detect prompt scintillation photons, especially below the cathode and above the bottom PMTs. However, this region still contributes the most to γ-X events, resulting in reduced S2/S1 due to the sizable Xe mass and high light collection efficiency in this region. This region was subdivided into several regions according to the S1 LCE and S1 electric field quenching, which is listed in Tab. 5.3 and Tab. 5.1 .

Another region is inside the TPC, near the inner wall of the PTFE panels at large radii. Although it is inside the field cage, this region is S2 insensitive because the electric field lines deviate from the z direction.

Fig. 5.3 shows the detailed S2 insensitive regions below cathode (left) and at large radii in the TPC (right). Fig. 5.13b was obtained using the COMSOL field simulation (credit Y. Mei). Note that 0 mm corresponds to 152.4 mm in Fig. 5.13a. The black volume is where charge collection is 0 which extends to ~ -1 mm in radius. Therefore, the S2 insensitive region at large radii was approximated as 0.6 mm thick radially with the sensitive volume radius and its height such as tube shape.

5.2.3 Energy Conversion: S1 Generation from the Simulation

As mentioned in Sec. 5.2.1, energy calibration of the signal requires accurate knowledge on the energy dependence of the signal in LXe and the detector response parameters such as the position dependence of electric field quenching and LCE, and the quantum efficiency (QE) of photomultiplier tubes (PMTs). Because we will be using the energy dependence of S1, we are interested in the relationship between recoil energy and S1 given by,

$$E_{\mathrm{r}} \times W_{\mathrm{ph}}(E_{\mathrm{r}}) \times S_{\mathrm{r,i}}(E) \times \mathrm{LCE}_{\mathrm{j}}(r, z) \times \mathrm{QE}(\mathrm{T}, \theta) = \mathsf{S1} \tag{5.1}$$

where E_{r} is recoil energy, W_{ph} is average energy to create scintillation photon, S_{r} is electric field quenching, E is drift field, r is radial position of the interaction, z is vertical position of the interaction, T is the temperature of the PMTs, and θ is an incident angle of a scintillation photo to photocathode. i and j are indices for the subdivision of the X-region according to the effective electric field and LCE, respectively. E_{r} is given by the simulation, and the other inputs are needed to obtain S1 correctly. In the following subsections, we will go through each of the terms.

The energy smearing of S1 consists of three steps. First, the number of created photons after the first four terms of the left-hand of Eq. 5.1 is Poisson smeared before they

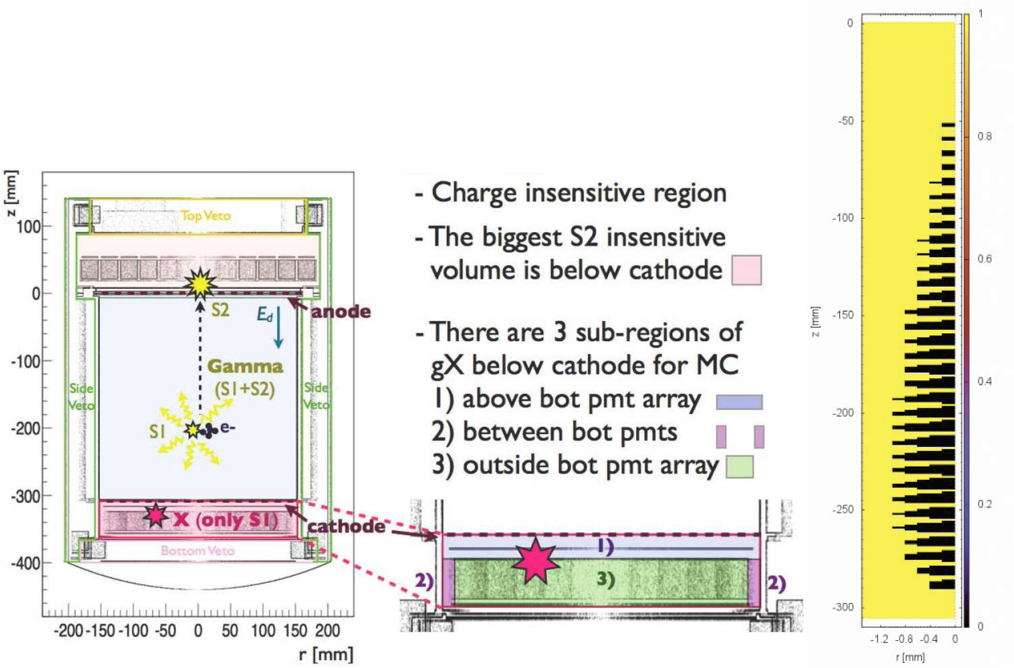

(a) Below cathode with 3 LCE subdivision.

(b) At large radii.

Figure 5.3: S2 insensitive regions in XENON100: Below the cathode (left) and at large radii inside the TPC (right). The regions below the cathode were subdivided into three different regions according to S1 LCE, above the bottom PMT array, between the bottom PMTs, and outside of the bottom PMT array. The region above the bottom PMT array is subdivided into two regions according to effective electric field. LCE simulation at each subregion is described in Sec. 5.2.3. The S2 insensitive region at large radii inside the TPC (black) was obtained from the COMSOL electric field simulation. Note that 0 mm in the right figure corresponds to 152.4 mm in the left figure. Right figure credit: Y. Mei.

hit the photocathodes of the PMTs. Second, when photons hitting the photocathode are converted to photoelectrons using the QE of the PMT, the number of photoelectrons is Poisson smeared again. Lastly, the number of photoelectrons obtained from step two is Gaussian smeared with the resolution given as half of the number of photoelectrons, which is observed from the single photoelectron spectra of the PMTs.

Quantum Efficiency (QE) of XENON100 PMTs

The QE of a PMT is the probability that a photon incident on the photocathode be converted to a photoelectron, and hence simply defined as the ratio of the number of photoelectrons emitted from a photocathode over number of incident photons [Knoll, 2000]. As shown in Eq. 5.1, QE is one of the terms to obtain the energy conversion relation between S1 (given by pe) and recoil energy (given by $\mathrm{keV_{ee}}$) and it is important to take it into account properly. The QE of Hamamatsu R8520 PMTs at LXe temperature was measured to be $\sim 10\,\%$ higher than the one measured at room temperature [Aprile *et al.*, 2012d]. In addition, the QE value is expected to be different when it is immersed in LXe compared with the QE measured in vacuum due to the dependence of the QE on the incident photon angle, which is affected by the refraction between LXe and the PMT window. However, since there exists no QE measurement in LXe, we use the averaged values of top and bottom PMTs obtained from the room temperature measurement of XENON100 PMTs.

Fig. 5.4 shows the measured QE of XENON100 PMTs at room temperature. As shown in the figure, high QE PMTs are used for the bottom PMTs (99−178) to increase the light detection efficiency of S1. The PMTs which have 0 values are not measured. It would be desirable to use its own measured QE for each PMT but the S1 signal is dominated by bottom PMTs. In addition, given that only a few of them are measured, we treat the top and bottom PMT arrays as two large PMTs on top and bottom, with averaged QEs for the top and bottom PMTs of 24.61 and 29.02 %, respectively. Since 18 % of S1 signal is seen by the top PMTs and 78 % of it is seen by the bottom PMTs, the average QE in the TPC is assumed to be 28.04 %. In addition, the QE at the X-region below the cathode was assumed to be the same as that of the bottom PMTs.

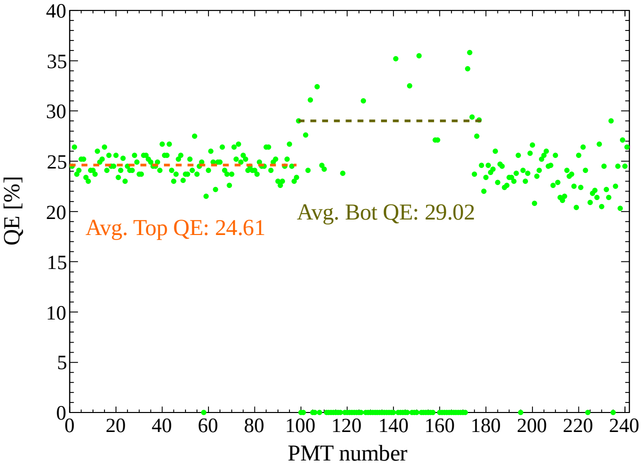

Figure 5.4: Measured QE of XENON100 PMTs at room temperature along with averaged QE values of top PMTs (1−98) and bottom PMTs (99−178). High QE PMTs were mounted in the bottom PMT array due to higher LCE near the bottom of the TPC. The QEs of 62 PMTs were not measured and their QE values are shown as 0. Credit: XENON100 collaboration.

S1 Field Quenching in X-region

As mentioned in Sec. 5.2.1, only a few measurements exist for S1 field quenching, with the highest field of 5 kV/cm. Therefore, we use the result from this measurement (Fig. 2.10) to obtain the electric field quenching factor, S_{r}. Because $S_{\mathrm{er,S1}}$ shows only mild field dependence above 2 kV/cm, we assume that S1 field quenching at higher electric field than 5 kV/cm is the same as that at 5 kV/cm. Tab. 5.1 lists the geometric subdivision of the X-region below the cathode depending on effective electric field. Due to the ground potential of the bottom PMT screening mesh and the negative HV of the PMT body, the effective electric field below the cathode varies from region to region. The relative $S_{\mathrm{r}}(E)$ to $S_{\mathrm{r}}(0.53)$ was obtained, since the reference is the S1 scintillation yield from XENON100.

S1 LCE Simulation in X-region

Light collection efficiency (LCE) is defined as the ratio of the number of scintillation photons hitting the PMT photocathode to the total number of scintillation photons generated in

Table 5.1: Geometric subdivision of X-regions depending on S1 field quenching.

Region Description	Geometric Cut (mm)	E (kV/cm)	Relative $S_\mathrm{r}(E)$ to $S_\mathrm{r}(0.53)$
Below the cathode and above the screening mesh (FQ I)	$-306 > z > -316$	16	0.28/0.57
Below the screening mesh and above the top surface of bottom PMTs (FQ II)	$-316 > z > -324$	0.9	0.51/0.57
Between the bottom PMTs (FQ III)	$-324 > z > -362$ && $r < 120$	0	1/0.57
Below the top surface of bottom PMTs and outside the PMT array (FQ IV)	$-324 > z > -362$ && $r > 120$	0.9	0.51/0.57

LXe in the simulation. Since the detection of the scintillation photons is influenced by their absorption, scattering, refraction in the liquid-gas surface, and reflection by the detector materials (Sec. 2.3.5), these properties must be set *a priori* for the LCE simulation. Tab. 5.2 lists the optical parameters used for the simulation. The momentum of the scintillation photon was allowed to vary 1 % with the 10 % probability at 178 nm (6.98 ± 0.07 eV). The values for PTFE reflectivity, LXe absorption length, and LXe Rayleigh scattering length were obtained from a dedicated LCE simulation in the TPC with other parameters fixed.

Since the LCE has a position dependence, the X-region below the cathode was subdivided into three different regions according to their LCE: above the bottom PMT array (LCE I), between the bottom PMTs (LCE II), and outside of the bottom PMT array (LCE III), as shown in Fig. 5.3 (left). The X-region at large radii (LCE IV) was described with one LCE function. Tab. 5.3 lists the geometric subdivision of the X-regions. For an efficient computing, S1 LCE simulations in the X-region between the bottom PMTs and outside of the bottom PMT array were performed separately at different subregions, taking advantage of repetitive geometrical pattern. The number of generated scintillation photons

Table 5.2: Optical parameters for the `S1` LCE simulation.

Property	Value (6.91, 6.98, 7.05 eV photons)
Copper Reflectivity	0.15, 0.2, 0.15
PTFE Refractive Index	1.63, 1.61, 1.58
PTFE Reflectivity	0.85
PTFE Specular Lobe	0.01
PTFE Specular Spike	0.01
PTFE Back Scatter	0.01
PTFE Efficiency	1
Grid Mesh Refractive Index	1.63, 1.61, 1.58
Grid Mesh Absorption Length	2.10 nm
Cirlex Reflectivity	0.5
Photo Cathode Refractive Index	1.50, 1.56, 1.60
Photo Cathode Absorption Length	1 nm
SS304LSteel Reflectivity	0.15, 0.2, 0.15
Quartz Refractive Index	1.5, 1.56, 1.60 [a]
Quartz Rayleigh Scattering Length	30 m [a]
LXe Absorption Length	150 cm
LXe Rayleigh Scattering Length	50 cm
LXe Refractive Index	1.63, 1.61, 1.58

[a] http://www.sciner.com/Opticsland/FS.htm

at each geometric point was 10000.

Table 5.3: Geometric subdivision of X-regions depending on S1 LCE.

X-region Description	Geometric Cut (mm)
Between the bottom PMTs (LCE I)	$-324 > z > -362$ && $r < 120$
Below the top surfaces of bottom PMTs but outside of the array (LCE II)	$-324 > z > -362$ && $r > 120$
Below the cathode and above the top surface of bottom PMTs (LCE III)	$-306 > z > -324$
At large radii (LCE IV)	$152.4 > r > 151.8$

Fig. 5.5 shows the scintillation photon generation lines for S1 LCE simulation in LCE I (left) and its zoom (right). Due to the repetitive pattern of PMTs, investigating three lines was enough to obtain the LCE in this region. x or y variations along the lines are verified to be negligible. The difference between the red line and the green line was verified to be less than 10 %. Conversely, the LCE variation along z is much more drastic. Therefore, the z variation of the red line and that of blue line were compared. In Fig. 5.6, both red line and blue line shows similar behavior and red line was chosen to represent the S1 LCE I(z) due to its better linearity at high z.

For the region below the bottom PMTs and outside of the bottom PMT array (LCE II), 5 points were chosen to infer the LCE in this region. Fig. 5.7 shows the 5 points for the scintillation photon generation (left) and the LCE(z) obtained from each point (right). Compared to Fig. 5.6, S1 LCE II(z_{max}) is lower than S1 LCE I(z_{max}) and S1 LCE II(z) variation is milder than S1 LCE I(z) variation. This is expected because the solid angle outside of the bottom PMT array is smaller than between the bottom PMTs, and the gap between the PMTs is much narrower than the one outside of the PMT array. Since the trends are similar among the points, the red point was chosen to select the average S1 LCE II(z) behavior.

For the region below the cathode but above the top surface of the bottom PMTs (LCE

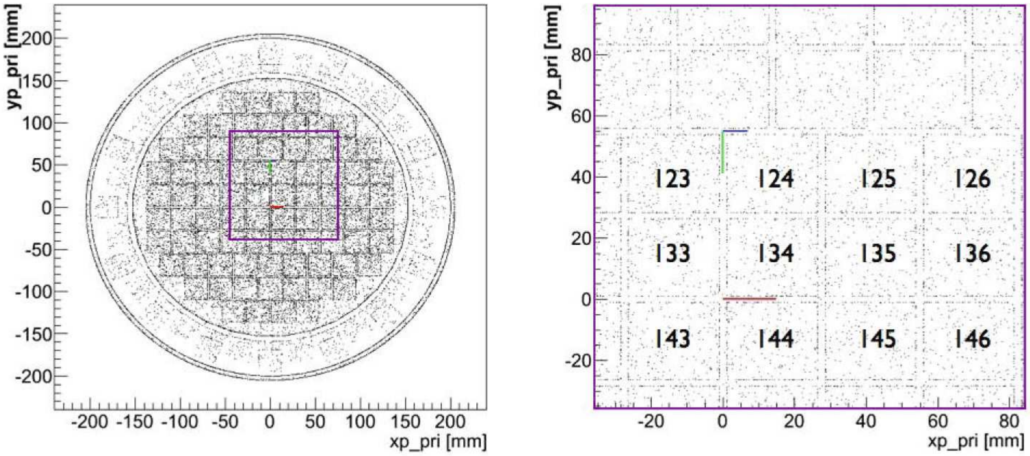

Figure 5.5: LCE simulation lines in the region between bottom PMTs (left) and its zoom (right). Due to the geometric pattern of the bottom PMTs, generating scintillation photons along 3 colored lines was enough to investigate LCE behavior in this region. The numbers in the right figure correspond to the PMT numbers.

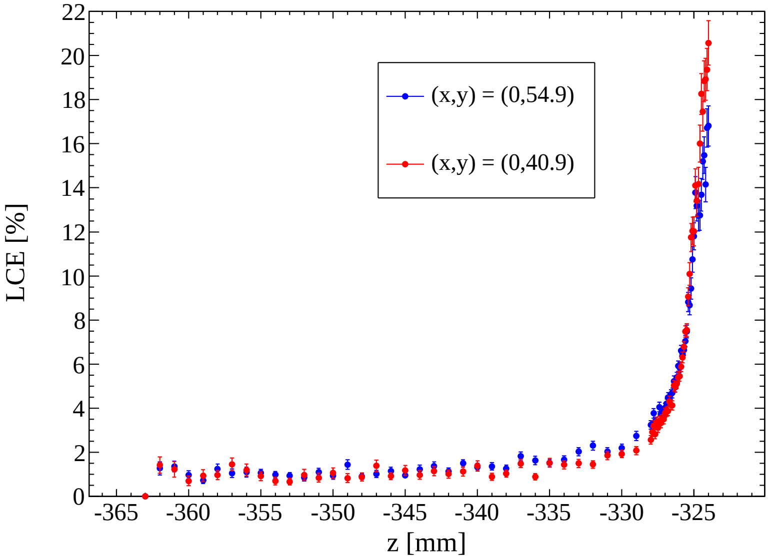

Figure 5.6: LCE variation along z in LCE I. Both red line and blue line show similar behavior in general. Both LCE values go to 0 at $z = -363\,\mathrm{mm}$. The red line was chosen to represent S1 LCE I(z) due to its better linearity at high z.

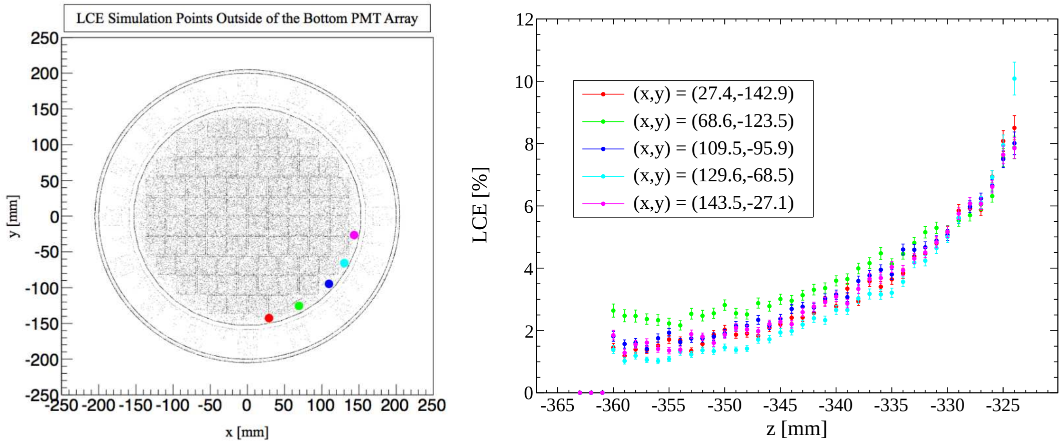

Figure 5.7: LCE simulation points (left) and LCE variation along z (right) below and outside of the bottom PMTs array. The trends are similar at each position and the red point was chosen as S1 LCE II(z).

III), both r and z dependences were taken into account. Due to the cylindrical symmetry of the LXe volume seen by the top and bottom PMTs, (x,y) dependence was enfolded in r. The scintillation photon generation was done in grids in the region with r intervals of 1 cm and z intervals of 2 mm. Fig. 5.8 shows the S1 LCE III(r,z) along with the z position of the bottom PMT screening mesh. The radius of the LXe volume is 152.4 mm. No significant LCE variation is observed across the screening mesh due to its high optical transparency 92.6 % [Mei, 2011]. S1 LCE III is uniform for $r < 130$ mm and $z > -322$ mm with a value of ~ 30 %. High LCE in this region is also expected due to the large solid angle to bottom PMTs.

Finally, at large radii inside the TPC, S1 LCE was obtained with the approximation of a 0.6 mm thick tube-shape based on Fig. 5.3 (right), with a mass of 0.5 kg LXe. In the beginning, the simulation was performed without field shaping rings implemented in the detector geometry. The overestimation of the LCE was quickly realized since the LCE at large radii is expected to be lower than the value in the TPC center. Therefore, investigation of the geometry was carried out and it was discovered that the field shaping rings were missing. After implementing the field shaping rings in the geometry, two sets of LCE simulation were performed with different width of r with the same shape in order to compare

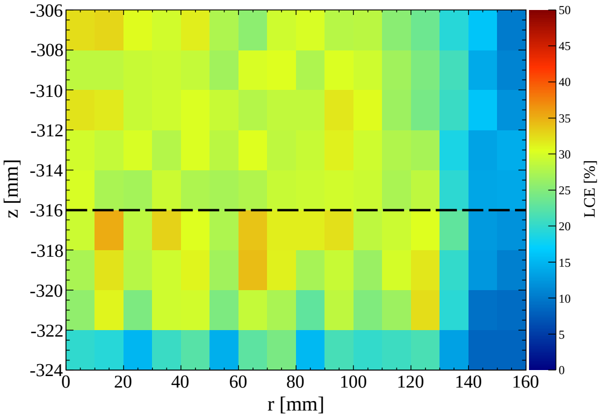

Figure 5.8: (r, z) dependence of S1 LCE below the cathode above bottom PMT array, S1 LCE III(r,z). Dashed line shows the position of the bottom PMT screening mesh. S1 LCE III(r,z) is a bit higher than the S1 LCE(r,z) just above cathode due to larger solid angle but its spatial dependence is similar. This observation enabled us later to compare γ-X model with the data (Sec. 5.2.3) and to check the tagging efficiency of the anomalous event cut (Sec. 5.4.3).

the simulated LCE with the LCE obtained from the data. If the simulated result with larger widths of r is in agreement with the one with a radius of S2 insensitive region, it is possible to compare the Monte Carlo simulation to the data with proper values of W_{ph}, QE, and $S_{\mathrm{r}}(E)$.

Fig. 5.9 shows the LCE simulation result with the impact of the field shaping ring implementation in the detector geometry and the radius width at large radii. As shown in the figure, the addition of copper field shaping rings results in significant LCE reduction in this region at most factor ~ 2. This proves the importance of implementation of detailed geometry which can influence the scintillation photon detection in the LCE simulation, but has a negligible effect on the radioactive source calibration simulation. Secondly, the LCE simulation result with $r > 150\,\mathrm{mm}$ is consistent with $r > 151.8\,\mathrm{mm}$. That is, it is possible to compare the simulation result with data by approximating the z dependence of the LCE at $r > 151.8\,\mathrm{mm}$ to be the same as that at $r > 150\,\mathrm{mm}$, although by definition of the S2 insensitive region, the position information is not known for the data. S1 LCE IV(z) was

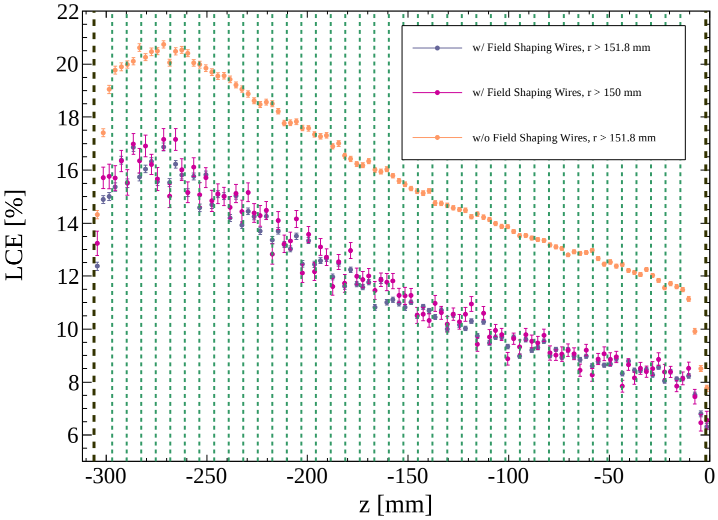

Figure 5.9: z dependence of LCE at large radii from a simulation. Legend explains the colored points in the figure. Black dashed lines at -306 mm and -2 mm indicate cathode and gate grid positions, respectively. Dashed green lines show copper field shaping ring positions. This simulation result highlights two things. First, the importance of detailed geometry in the LCE simulation which influences the scintillation photon detection. Second, the LCE simulation result with $r > 150$ mm (S2 sensitive region) is consistent with $r > 151.8$ mm (S2 insensitive region), and hence it is possible to approximate the LCE at $r > 151.8$ mm to be the same as the LCE at $r > 150$ mm in the data. This enables the comparison between the data and the simulation.

obtained from LCE obtained using $r > 151.8\,\mathrm{mm}$ (light blue).

Verification of S1 LCE Simulation

Since Fig. 5.9 showed the LCE simulation result with $r > 150\,\mathrm{mm}$ is consistent with $r > 151.8\,\mathrm{mm}$, comparison of LCE at large radii from the simulation with the one from the data was performed.

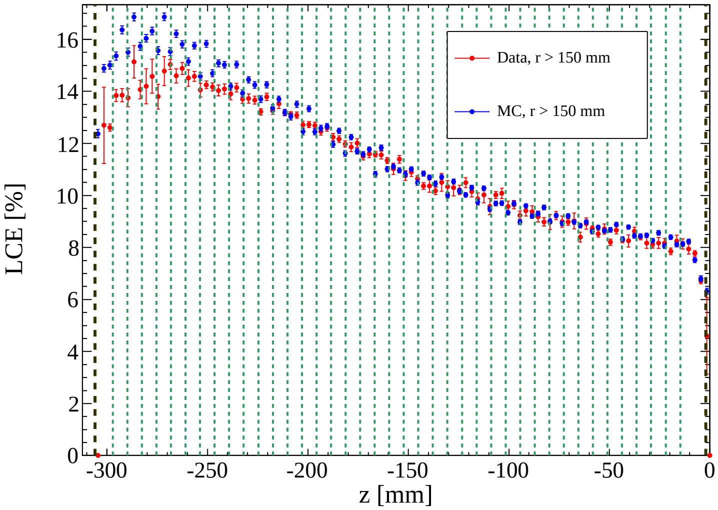

Figure 5.10: LCE variation along z at large radii comparison between ^{137}Cs data (red) and Monte Carlo simulation (blue). Black dashed lines at $-306\,\mathrm{mm}$ and $-2\,\mathrm{mm}$ indicate cathode and gate grid positions, respectively. Dashed green lines show copper field shaping ring positions.

Fig. 5.10 shows the S1 LCE at $r > 150\,\mathrm{mm}$ comparison between data and Monte Carlo simulation. To obtain the LCE from the data, ^{137}Cs calibration data taken at low anode voltage (2.2 kV) was used to acquire the S1 scintillation yield. Low anode voltage is required to avoid S2 signal saturation of the 662 keV full absorption peak, which biases the (x, y) position reconstruction. Because we are interested only in the S1 scintillation yield at large radii, high energy γ rays from ^{137}Cs were used, since they produce more scintillation photons in total, and provide less statistical fluctuations than the low energy γ rays with more uniform irradiation from an ^{241}AmBe(α, n) source.

To infer S1 LCE from the data, we need to deconvolve $W_{\rm ph}$, QE, and $S_{\rm r}$ from Eq. 5.1. Note that the Monte Carlo simulation is the same as the one in Fig. 5.9. The drift field of XENON100 is 0.53 kV/cm and its variation along z due to nonperfect electric field lines is estimated to be $\sim$ 0.01 kV/cm. Hence, $S_{\rm r}(0.53) = 0.58$ was used, obtained from the measurement with 122 keV γ ray. The average QE in the TPC of 0.28 was used, as explained in Sec. 5.2.3. To obtain $W_{\rm ph}$ at 122 keV, an independent simulation with scintillation photon generation in the center of the TPC was performed and the S1 LCE at this position (which represents the volume-averaged LCE) was obatined to be 17.7 % (using the values of $S_{\rm r}(0.53)$ and QE mentioned and the volume-averaged S1 scintillation yield of XENON100 at 122 keV at the time of measurement, 2.2 pe/keV). The obtained $W_{\rm ph}$ is 13.1 eV, consistent with value (13.8 ± 0.9 eV) found in [Doke *et al.*, 2002]. Using these values, S1 LCE from the data was compared with the one from simulation. The maximum difference between the simulation and data is $\sim$ 16 %, near the cathode. Since the radial position of an event is constructed inwards before the electric field correction, the radial position of an event is pushed “outward” after the correction, and the LCE from the data is supposed to be higher than that from Monte Carlo simulation. In addition, near the bottom of the TPC, the effective QE is supposed to increase due to more scintillation photons being seen by the bottom PMTs which would also result in overestimation of the LCE from the data. What we observe from Fig. 5.10 is opposite the expected behavior. The reason is not understood well, besides that it is related to the electric field correction. However, the data above $z > -220$ mm is consistent with the simulation and we are confident with the input values we are using to obtain S1 LCE and the obtained S1 LCE.

5.2.4 S2 Generation: Using the Gaussianity of Electronic Recoil Band

As we have seen in Sec. 4.4, the major population of electronic recoil band events from ^{60}Co and ^{232}Th data shows Gaussianity in the $\log_{10}$(S2/S1) vs S1 plane. We also have generated S1 in Sec. 5.2.3 using the energy conversion given by Eq. 5.1 with proper inputs according to the spatial dependence. Hence, it is possible to construct S2 using the S1 obtained in Sec. 5.2.3 and the Gaussian description of $\mu_{\rm er}$(S1) and $\sigma_{\rm er}$(S1) in $\log_{10}$(S2/S1). The spatial dependence of $\mu_{\rm er}$(S1) and $\sigma_{\rm er}$(S1) was studied before deciding the functional forms. No significant r dependence was observed but z above -60 mm showed quenched $\mathsf{S2}$ at $\mathsf{S1} \gtrsim 100$ pe. To obtain $\mu_{\mathrm{er}}(\mathsf{S1})$ and $\sigma_{\mathrm{er}}(\mathsf{S1})$, a fiducial volume cut of $r < 135$ mm and $-276\,\mathrm{mm} < z < -33\,\mathrm{mm}$ was used. The obtained functions were also used to compute an estimate of the electronic background from the data for the first science run [Aprile *et al.*, 2011b]. The band is fit and parametrized in two intervals in $\mathsf{S1}$, between 2−30 pe and between 30−200 pe, with the requirement that the two fits yield the same value at 30 pe. The low energy part of the band is characterized as an exponential plus a second degree polynomial function, while the high energy part of the band is fit with a fourth degree polynomial. Although the energy region of interest for a WIMP search is at low energies, high energy behavior of the band was also obtained so as to study possible interactions in the X-region with poor LCE, such as between the bottom PMTs (LCE II).

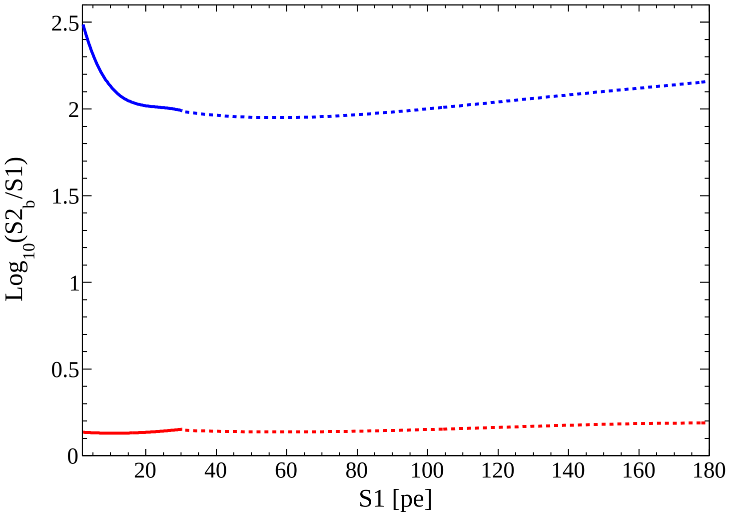

Figure 5.11: Modeled functional forms of $\mu_{\mathrm{er}}(\mathsf{S1})$ (blue) and $\sigma_{\mathrm{er}}(\mathsf{S1})$ (red). Different functions were used to describe the low energy (solid line) and high energy (dashed line) behaviors. Credit: XENON100 collaboration.

Fig. 5.11 shows the functions used to describe $\mu_{\mathrm{er}}(\mathsf{S1})$ (blue) and $\sigma_{\mathrm{er}}(\mathsf{S1})$ (red). At 30 pe, both $\mu_{\mathrm{er}}(\mathsf{S1})$ and $\sigma_{\mathrm{er}}(\mathsf{S1})$ exhibit discontinuities in the first derivative. However, this is a matter of choice of the functional forms in different energy ranges, and it does not affect the electronic recoil band description. Several functional forms were tried and a function which provides the best fit was chosen among the trial functions.

Using the functions shown in Fig. 5.11, S2 was randomly generated with Gaussian mean $\mu_{\rm er}(\mathsf{S1})$ and $\sigma_{\rm er}(\mathsf{S1})$ for given S1 in the TPC. Here we ignore anticorrelation between S1 and S2, which comes from the fixed quanta of excitons and ions ($N_{\rm tot} = N_{\rm ex} \pm N_{\rm i}$) which happens at the microscopic level, as mentioned in Sec. 5.2.1.

5.2.5 γ-X Selection

Now we have information on both S1 and S2 which can describe discrimination. One thing to notice about S2 is that it is obtained from single scatter events selected in the electronic recoil band and hence, it is only valid for single scatters in the TPC. The same selection is required in the Monte Carlo simulation.

If a multiple scatter happens at the same z, but different (x, y) as shown in the double scatter event in the TPC in Fig. 5.1, it is possible to identify multiple scatters in (x, y) plane by computing the χ^2 of S2 PMT hit pattern. However, it is impossible to know the exact contribution of each scatter to the S2. Therefore, the criterion to distinguish two S2 peaks is the z difference between them.

Although a point-like interaction is expected from a low-energy electronic recoil at the position of the interaction, due to the width of the S2 pulse, which is dominated by the gas gap below the anode, and the S2 peak-finding resolution of the data processing program, distinction of two S2 peaks is only possible when they are separated more than 3 mm in z. This distance was verified by plotting the distance between double scatter events with ^{60}Co calibration data. In addition, several sets of Monte Carlo simulation comparing single scatter rates of ^{60}Co were performed with different z values to determine the single scatter events. The simulation results were robust against the change in this value as long as it is smaller than 3 mm, within $\sim 10\,\%$. Therefore, any steps within 3 mm of z are clustered as one interaction and treated as one scatter in the simulation.

A pure single scatter refers to an event with a single interaction in the TPC and no additional interactions in the X-region, and they follow the Gaussianity in the discrimination parameter. A γ-X event is defined as a single scatter in the TPC accompanied by additional scatters in the X-region (either below the cathode or at large radii). Using the results obtained from the previous sections, the $\mathsf{S1}$ in the X-region can be computed taking into account LCE, S_r, and QE relative to the values in the TPC.

$$\mathsf{S1}_{\gamma\mathrm{X}} = \mathsf{S1}_\mathrm{X} + \mathsf{S1}_\mathrm{TPC} \tag{5.2a}$$

$$\mathsf{S1}_\mathrm{p.s} = \mathsf{S1}_\mathrm{TPC} \tag{5.2b}$$

$$\mathsf{S2}_{\gamma\mathrm{X}} = \mathsf{S2}_\mathrm{p.s} = \mathsf{S2}_\mathrm{TPC} \tag{5.2c}$$

where $\mathsf{S1}_\mathrm{X}$ is the $\mathsf{S1}$ contribution from the X-region, and $\mathsf{S1}_\mathrm{TPC}$ is the $\mathsf{S1}$ contribution from the single scatter in the TPC. Since X-region is an $\mathsf{S2}$ insensitive region, $\mathsf{S2}$ is only from the TPC and it is the same for both γ-X and pure single scatter events. As shown in Eq. 5.2a, the additional contribution of $\mathsf{S1}_\mathrm{X}$ results in quenched $\mathsf{S2}/\mathsf{S1}$ for γ-X events compared to pure single scatter events.

5.3 Verification of the Model: Double Scatters from ^{60}Co Calibration Data

By definition, verification of a γ-X event is impossible from the data, which is exactly why γ-X events are problematic and is the whole point of this study. Nevertheless if one can detect events with a similar topology, it is possible to compare the results from the simulation with those from the data. By noticing that events with X-interactions below the cathode and above the top surface of the bottom PMTs (LCE III) and a γ interaction in the TPC are similar to those with one scatter just above the cathode and another scatter in the bulk of the detector, a verification of the γ-X model with the double scatters from ^{60}Co electronic recoil band calibration data was performed.

Double scatter events with one interaction (fake X interaction) in the volume just above the cathode with the same dimensions as LCE III (as if the volume below the cathode and above the bottom PMTs was lifted to just above the cathode), and another interaction (γ interaction) in the bulk of the detector above the fake X region were selected. No veto cut was applied, so as to increase the statistics, and the energy range of $\mathsf{S1}$ from both interactions was chosen as $4\,\mathrm{pe} < \mathsf{S1} < 30\,\mathrm{pe}$. The equivalent fake γ-X selection cuts were applied to the simulation. The fractions of fake γ-X events to the total double scatters for the data and Monte Carlo simulations were found to be $10.6^{+4.8}_{-3.9}$ and $8.5^{+6.5}_{-4.4}$ %, respectively. The uncertainties are rather large due to poor statistics, but the result from Monte Carlo simulation is consistent with that from data.

It is worthwhile to notice that this verification was done with only certain parts of X-region, i.e., below the cathode above the bottom PMT array. Although this region contributes the most to γ-X due to its sizable Xe mass compared to other volumes, what we verified holds only for this X-region. But, at the same time, this is the only region for which we can compare the simulation with the data. A comparison at large radii could not be performed with the double scatter technique due to the poor statistics in this small volume.

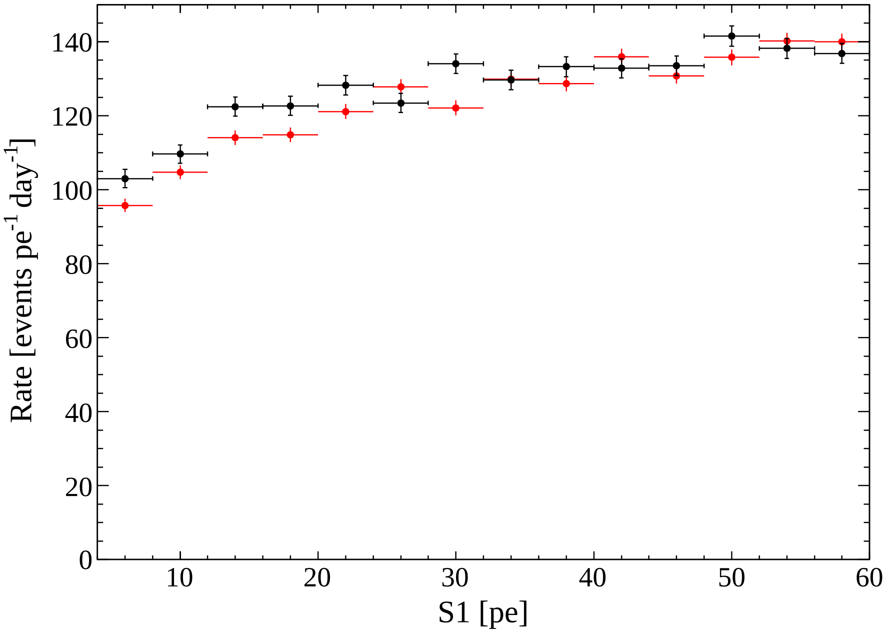

Figure 5.12: Single scatter rate comparison between Monte Carlo simulation (red) and data (black) from ^{60}Co in 48 kg FV. Single scatter event selection cut efficiency was reflected in the data. At low energies the rate from the data shows a higher value than that from Monte Carlo simulation, but the discrepancy is < 10 %.

Fig. 5.12 shows the single scatter rate comparison between Monte Carlo simulation (red) and data (black) from ^{60}Co calibration in 48 kg FV, with the event selection cuts used in [Aprile *et al.*, 2011b]. For this comparison, the active veto cut was applied since we do not suffer poor statistics and the overall cut efficiency for the data was obtained including the active veto cut. The active veto cut for Monte Carlo simulation was that the energy deposition in the veto is smaller than 200 keV, since the effect of the active veto is to flatten the energy deposition in the veto below this energy, as shown in [Aprile *et al.*, 2011e]. The results show good agreement between Monte Carlo simulation and data in general, and the largest difference was found to be less than 10 %. This proves that S1 generation and single scatter selection for the simulation described in Sec. 5.2.3 and Sec. 5.2.5, respectively, are reliable.

However, we did not proceed to estimate the contribution of γ-X events in the electronic recoil background using the background simulation since it turned out the band shape for the calibration data is different from that for the background data for the second science run. The band shape directly influences to the estimation of γ-X events with the method we described in this chapter.

5.4 Development of Anomalous Event Rejection Cut

5.4.1 S1 PMT Pattern Likelihood Method

Since γ-X events have additional scattering sites producing S1, their S1 PMT patterns are different from those of true single scatters. To discriminate against γ-X events, we have developed a method using the log likelihood ratio of measured S1 PMT patterns over expected single scatter patterns obtained from calibration data. Because it directly compares the information from background data with calibration data, this method is robust against systematic uncertainties attributed to detector response such as the QE of the PMTs, vertex reconstruction, or LCE.

The PMT pattern likelihood parameter was developed by computing the Poisson likelihood of the S1 PMT pattern of an event under examination with the "standard" S1 PMT pattern of single scatter events happening at the same (x, y, z) position. The standard S1 PMT pattern was determined using the full absorption peak of low anode voltage (2.2 kV)

^{137}Cs calibration data to avoid S2 saturation as mentioned in Sec. 5.2.3 to ensure consistent behavior of (x, y) position reconstruction algorithms. Again, we take advantage of using the full absorption peak of ^{137}Cs to have a clean single scatter sample and to have the highest possible S1 in order to minimize the photon counting fluctuations in the standard S1 PMT pattern. The whole 3D sensitive volume was coarsely binned to get a sufficient number of events in each spatial bin such that the mean values of the S1 PMT patterns have statistical fluctuations below 10 %. The PMT pattern likelihood parameter is the sum of three parts: the likelihood of the top PMT array only; the likelihood of the bottom PMT array only; and the likelihood of the (top total)/(bottom total) ratio with response normalization for the likelihood of top PMT array and the likelihood of bottom PMT array with S1 total seen by each array, respectively.

Due to the S1 dependence of the PMT pattern likelihood parameter, the associated cut was defined as a function of S1. Its performance was checked with ^{60}Co events that leak below the nuclear recoil median in the 40 kg fiducial volume. With the definition of rejection as the number of events failing the cut over the total number of leakage events, 41.0 and 71.8 % rejections were found at $\mathsf{S1} < 20\,\mathrm{pe}$ and $20\,\mathrm{pe} \leqq \mathsf{S1} < 200\,\mathrm{pe}$, respectively. The details of the S1 PMT pattern likelihood cut are explained in [Mei, 2011].

5.4.2 Position Dependence of S1 PMT Pattern Likelihood Cut

After development of the S1 PMT Pattern Likelihood cut, “Xs1patternlnl”, the estimated γ-X events contribution from the simulation was compared with the events tagged by Xs1patternlnl using ^{60}Co data with single scatter in the 48 kg fiducial volume. The estimation from the simulation was found to be 4 times smaller than the one from the data. With an additional cut requiring events to be below the 99.5 % electronic recoil band rejection of Xs1patternlnl (leakage events), the discrepancy is less pronounced but still 2× smaller than the one from the data. Several trials were made with different functional forms of energy dependence of S1 scintillation yield to take into account of the possible incorrectness of assumptions in the model, but Monte Carlo simulation always provided a smaller fraction. To understand this discrepancy, we checked the position dependence of Xs1patternlnl and compared it with the γ-X position distribution.

Fig. 5.13 (left) shows the spatial distribution of the fraction of events tagged by Xs1patternlnl with respect to the total single scatters in the data. Fig. 5.13 (right) shows the γ-X events fraction with respect to the events with a single scatter in the sensitive volume for the Monte Carlo simulation. ^{60}Co calibration with an energy range $\mathsf{S1} < 160\,\text{pe}$ and energy deposit in the TPC $< 80\,\text{keV}$ was used for data and Monte Carlo simulation, respectively. Energy conversion to S1 was not performed in this comparison due to possible uncertainties on the energy conversion to S1, and it resulted in a higher fraction of γ-X events in the simulation. The spatial distribution comparison with S1 generation using the conversion explained in Sec. 5.2.3 in the simulation showed better agreement.

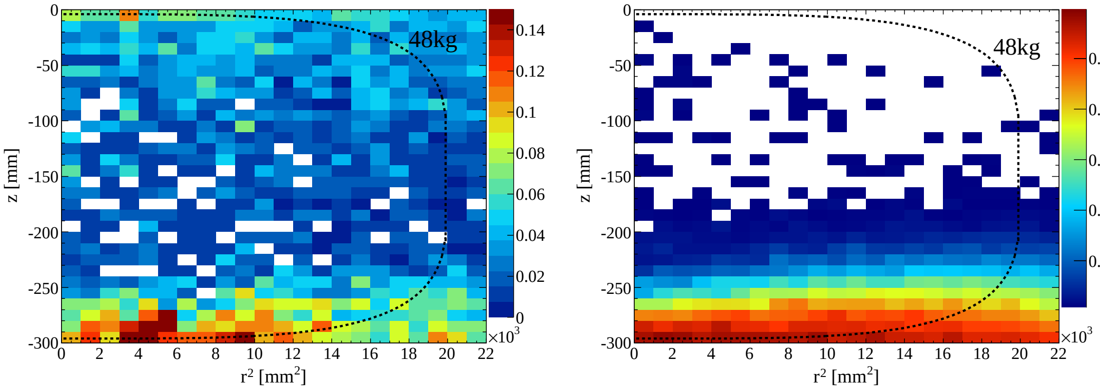

(a) Data

(b) Monte Carlo Simulation

Figure 5.13: Position distribution of the fraction of events tagged by Xs1patternlnl with respect to the total single scatters in the data (left). The γ-X events fraction with respect to the events with a single scatter in the sensitive volume from the Monte Carlo simulation (right). ^{60}Co calibration with an energy range $\mathsf{S1} < 160\,\text{pe}$ and energy deposit in the TPC $< 80\,\text{keV}$ was used for data and Monte Carlo simulation, respectively. The 48 kg fiducial volume used for the first science run is shown as dashed line. Left figure credit: XENON100 collaboration.

As shown in the figure, there exists qualitative agreement of a pronounced population at low z between the data and Monte Calro simulation. This can be interpreted as part of the anomalous events tagged by Xs1patternlnl follows the expected position distribution from γ-X topology. It is also reasonable to say that there seems to be a less pronounced but additional population on top of the detector, which is not shown in the simulation result.

5.4.3 γ-X Like Events Tagging Efficiency of S1 PMT Pattern Likelihood Cut

In addition to check the spatial distribution of anomalous events tagged by Xs1patternlnl, the tagging efficiency of Xs1patternlnl was computed with the γ-X like double scatters, using the same idea described in the verification of the γ-X model (Sec. 5.3). If the tagging efficiency is high, we can be confident that Xs1patternlnl would mostly cut γ-X events. This time, AmBe data were used since neutrons have higher probability of double scattering in the detector than γ rays.

To select γ-X like double scatters, events with one scatter in $-304 < z < -286$ and the other scatter in $-286 \leqq z < -180$ were chosen since γ-X events with X below the cathode are mostly distributed near the bottom of the TPC. A radial cut $r < 140\,\mathrm{mm}$ was also applied to ensure legitimate S2 and S1 signals. The tagging efficiency of Xs1patternlnl was found to be $2.3^{+0.7}_{-0.5}\,\%$ at low energies ($3\,\mathrm{pe} < \mathrm{S1} < 30\,\mathrm{pe}$) and $8.8^{+2.4}_{-2.1}\,\%$ where $30\,\mathrm{pe} < \mathrm{S1} < 50\,\mathrm{pe}$. This result suggests that Xs1patternlnl is mostly cutting out not γ-X but something else, whichever deviates from the “standard” single scatter S1 PMT pattern.

5.5 Discussion

We have presented in this chapter our effort to understand the anomalous background of XENON100. With the known mechanism from the previous experiment (XENON10), we have built a model based on it with assumptions on the energy calibration due to the lack of measurements and verified the model with calibration data. We did not proceed to make a prediction of anomalous events in the background in the first science run since the electronic recoil band shape of the background data was different from the calibration data, which was used to obtain S2 in the simulation. It turned out the band shape difference between the calibration and the dark matter data was attributed to the main electronic background contribution in the first science run was β particles from ^{85}Kr. For the second science run, during which the ^{85}Kr contamination was kept low and the main electronic recoil background was the Compton electrons arises from the residual radio isotopes in the detector materials, the electronic recoil band shape from the calibration data was consistent with the one from the background data.

In parallel to the work from the simulation, an anomalous event rejection cut was developed using the S1 PMT pattern based on the same mechanism of γ-X events, i.e., apparent single scatter in waveform but multiple scatter in nature. Lots of efforts were made to understand the properties of the events removed by this anomalous event rejection cut and whether it provides results consistent with the simulation prediction. From waveform watching, it was shown that at low energies ($\mathsf{S1} < 20\,\mathrm{pe}$), Xs1patternlnl is tagging noise-like events rather than tagging γ-X events.

Anomalous background events of XENON100 cut by Xs1patternlnl seem to be composed of γ-X events with rather low tagging efficiency, less than 10 %, and events with unknown origin. We have understanding of γ-X events at a certain level and can predict some of its properties, such as their pronounced spatial distribution at low z (due to its vicinity of X-region) but we are aware that many assumptions related to energy calibration of the signal need to be verified. It is simply impossible not to make assumptions for the moment due to the lack of measurements and this limits the model. For the events with unknown origin, it is beyond our understanding and we are making effort to investigate other possible mechanisms.

Given this situation, we use the electronic band description from the calibration data after applying all the cuts including Xs1patternlnl to predict the electronic recoil background (see Sec. 7.1.3). Anomalous background events happen in the tail of the main Gaussian distributed electronic recoil background and not as an isolated population (otherwise we would modify our signal region to take this into account and to lower the background). Several parametrizations for these events have been studied and yield very similar results. The anomalous events are parametrized using a flat distribution in the discrimination parameter and a decreasing exponential in S1. This parametrization agrees with the observed distribution of events in the calibration data as has been verified with a dedicated likelihood analysis.

Chapter 6

Measurement of the Scintillation Yield of Low-Energy Electrons in Liquid Xenon

Understanding the ionization and scintillation response of LXe to low-energy ($< 10\,\mathrm{keV}$) particles is crucial for the data interpretation of LXe-based WIMP searches. Inferring the energy of a particle from the measured signals requires a precise knowledge of the response to low-energy nucler recoils, produced by WIMPs or background neutrons, and electronic recoils, produced by electromagentic background. While several measurements of the relative scintillaion efficiency of nuclear recoils in LXe have been performed [Aprile *et al.*, 2005; Aprile *et al.*, 2009; Plante *et al.*, 2011], with the latest measurements giving the most precise values to date for this quantity and for recoil energies as low as 3 keV, hardly any measurements exist for electronic recoils at low energies. Recently at Columbia University, we measured the scintillation yield of electronic recoils in the energy range of 2.1 to 120.2 keV, as a part of an ongoing effort in the XENON collaboration.

A recoiling electron in LXe produces a track of ionized and excited Xe atoms (excitons). Both excitons and Xe ions that recombine with electrons lead to the formation of excited dimers which subsequently deexcite and produce scintillation photons (see Sec. 2.3.1). The ratio of the number of excitons to the number of ions produced, $N_{\mathrm{ex}}/N_{\mathrm{i}}$, is between 0.06

and 0.20 [Doke *et al.*, 2002] and hence the contribution to the scintillation signal from direct excitation is small. If an electric field is applied, the fraction of scintillation light that originates from recombining electron-ion pairs is reduced. This fraction can be varied by changing the strength of the applied electric field. However, even at zero electric field, not all electrons recombine in a time scale practical for the collection of the scintillation photons produced [Doke *et al.*, 1988]. In LXe, the nonlinearity in the scintillation signal from electronic recoils at zero electric field is understood as being the result of the energy dependence of the recombination probability.

Measurements of the scintillation yield of electrons of low energy ($\lesssim 100\,\mathrm{keV}$) in LXe are scarce. At these energies, in most cases, scintillation light yield measurements have been carried out with monoenergetic sources [Barabanov *et al.*, 1987b; Obodovskii and Ospanov, 1994; Yamashita *et al.*, 2004], where photoelectric absorption is the dominant interaction. As mentioned in Sec. 4.2, to set up any energy scale (either for electronic or nuclear recoils), irradiation of a detector with a monoenergetic γ-ray source is required. Because γ rays interact with LXe via electronic recoil, one might think calibration of the detector with photoabsorbed γ-rays from radioactive sources would be the easiest way to set up the energy scale for the electronic recoil background. However, using photoabsorbed γ rays to measure the scintillation yield has disadvantages. First, multiple energetic electrons are produced as a result of the photoabsorption: a photoelectron with an energy $E_\gamma - E_b$, the incident γ-ray energy minus the electron binding energy, and a host of deexcitation Auger electrons or X-rays photoabsorbed afterwards. The scintillation yield obtained is then the convolution of the distribution of electron energies produced with the scintillation response of LXe to electrons, which is different from that of an electron of that energy, due to the nonlinearity of the scintillation signal response. On the other hand, a γ-ray Compton scatter produces a single energetic electron with an energy very close to $E_\gamma - E'_\gamma$, the incident γ-ray energy minus the scattered γ-ray energy. This is because Compton scattering is essentially equally probable for all atomic electrons instead of only for those with significant binding energies, as is the case for photoelectric absorption. Furthermore, the low-energy electromagnetic background in a LXe dark matter detector is induced by Compton-scattered high-energy γ rays from the radioactivities present largely in construction materials and the environment.

A second difficulty arising in measurements with external low-energy γ rays is the shallow penetration depth into the active volume of the LXe detector. Due to the spatial depedence of the light detection efficiency, measurements performed with external low-energy γ rays yield partial active volume response, which is in general different from the whole active volume response.

Measurements of the scintillation yield of low-energy electrons in LXe have also been performed via internal irradiation with conversion electrons from the ^{83m}Kr isomer [Manalaysay *et al.*, 2010; Kastens *et al.*, 2009]. Despite solving the problems of low-energy external sources, the extremely limited number of isotopes that can be used for such irradiations prevents the measurement of the scintillation yield over a continuous energy range.

In this chapter, we present the measurement of the scintillation response of LXe to electronic recoils at zero electric field in the energy range of 2.1 to 120.2 keV using the Compton coincidence technique, introduced by Valentine and Rooney [Valentine and Rooney, 1994; Rooney and Valentine, 1996], and further improved by Choong *et al.* [Choong *et al.*, 2008]. A LXe scintillation detector with a very high light detection efficiency was irradiated with γ rays from an external ^{137}Cs source and the energy of the scattered γ rays was measured with a high-purity germanium (HPGe) detector placed at various scattering angles. The excellent energy resolution of the HPGe detector allows the selection of events where recoils of known energies are produced in the LXe detector. The Compton coincidence technique coupled with a high light detection efficiency LXe detector permitted us to probe down to energies as low as 2.1 keV, the lowest recoil energy measured to date in our knowledge and limited by unavoidable accidental coincidence in the high-purity germanium (HPGe) detector.

We also measured the scintillation yield of low-energy electrons in LXe to the ^{83m}Kr isomer, and used the scintillation yield of the 32.1 keV transition as a reference to report the relative scintillaion yield results of Compton coincidence measurements. We find that the scintillation yield of the 32.1 keV transition is compatible with that obtained from the Compton coincidence measurement. On the other hand, the yield for the 9.4 keV transition is much higher than that measured for a Compton electron of the same energy. We interpret the enhancement in the scintillation yield as due to the enhanced recombination rate in the presence of Xe ions left from the 32.1 keV transition, which precedes the 9.4 keV one by 220 ns, on average.

The experimental setup is described in Sec. 6.1, the LXe detector in Sec. 6.2, and data acquisition in Sec. 6.3. The calibrations of the PMTs and HPGe detector are explained in Sec. 6.4 and Sec. 6.5, respectively. The Compton coincidence measurements and data analysis are described in Sec. 6.6, 6.7, and 6.8. The response to monoenergetic γ-ray sources is described in Sec. 6.9.1, the internal ^{83m}Kr irradiation in Sec. 6.9.2. The results are presented in Sec. 6.10, discussion in Sec. 6.11, followed by conclusion in Sec. 6.12.

6.1 Experimental Setup

The measurement of the scintillation response of LXe to electronic recoils was performed by irradiating the LXe detector with γ rays from a 370 MBq ^{137}Cs source and measuring the energy of the scattered γ rays with a HPGe detector.

Fig. 6.1 shows a picture (left) and schematic (right) of the experimental setup. In this setup, ^{137}Cs source emits 661.7 keV γ rays that scatter in the LXe target volume and are then detected by the HPGe detector, in coincidence. The energy of the Compton electron produced, E_{er}, can be selected by kinematics (given by Eq. 2.4):

$$E_{\mathrm{er}} = E_{\gamma} - E_{\gamma'} \tag{6.1a}$$

$$E_{\mathrm{er}} = E_{\gamma} - \frac{E_{\gamma}}{1 + \frac{E_{\gamma}}{m_e c^2}(1 - \cos\theta)} \tag{6.1b}$$

where E_{γ} is the energy of the incoming γ ray (661.7 keV in this case), $E_{\gamma'}$ is the energy of the outgoing γ ray, m_e is the electron rest mass energy, and θ is the scattering angle. A measurement of $E_{\gamma'}$, for an outgoing γ ray that did not interact anywhere else, enables E_{er} to be measured. Because of the excellent energy resolution of the HPGe detector, it is possible to select nearly monoenergetic electronic recoils from the continuous spectrum of Compton electrons produced. By varying the angle at which the HPGe detector is positioned and the range of scattered γ energies selected, one can choose the energy at which the electron response is measured. The HPGe detector angle θ_{HPGe} was adjusted to favor recoils in the

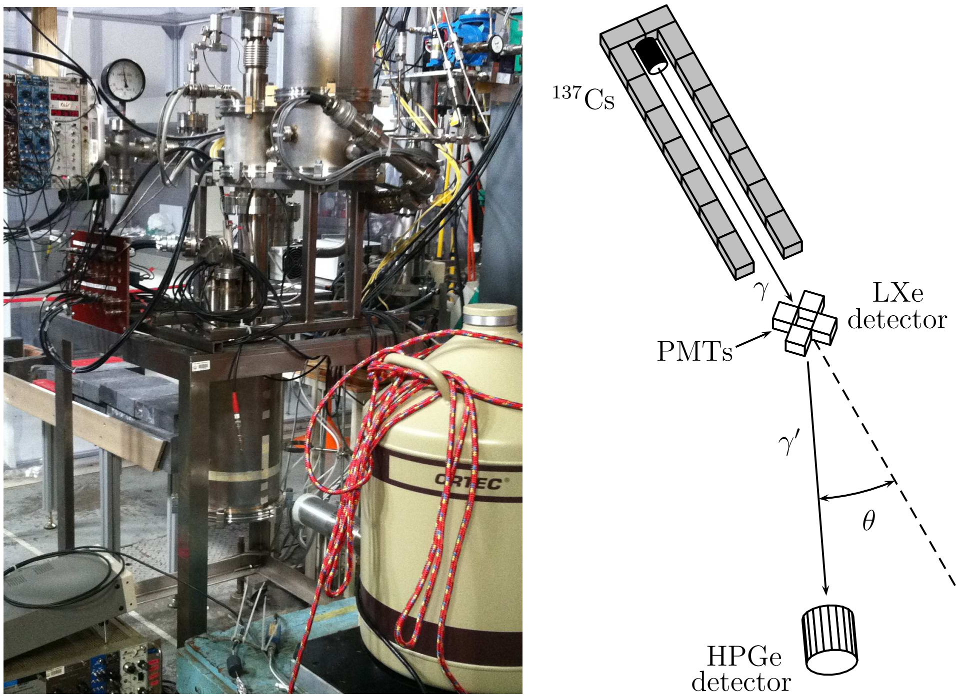

Figure 6.1: Picture (left) and schematic (right) of the experimental setup. A 370 MBq ^{137}Cs source is placed 85 cm from a LXe target viewed by six PMTs (only four shown, top and bottom PMTs are omitted for clarity). The energies of γ rays that scatter near an angle θ_{HPGe} are measured with a HPGe detector. The excellent energy resolution of the HPGe detector allows the selection of events where a Compton electron of the desired energy is produced in the LXe detector. Figure (right) from [Aprile *et al.*, 2012e].

desired energy range (see Tab. 6.2).

The ^{137}Cs source was enclosed in a lead cylinder with a 5-cm diameter and 7-cm height. To check the uniformity of the source activity, the trigger rate of the LXe detector was measured using a 5-mm diameter collimator in front of the source with 5-cm thickness. The variation of the source strength across the circular face was measured to be within 4 %.

The scattered γ rays were tagged with an ORTEC p-type coaxial HPGe detector. The diameter and total depth of the Ge crystal are 5.8 and 4.8 cm, respectively. The typical full width half-maximum (FWHM) energy resolution at 1.33 MeV and the peak-to-Compton ratio achievable are specified by ORTEC to be less than 2.09 keV and better than 51:1 respectively.

The ^{137}Cs source was aligned with respect to the center of the LXe detector active volume using an autoleveling laser. The desired HPGe detector floor positions were measured with a 1.5-m aluminium rule and a plumb line. The vertical position of the HPGe detector was set with the laser. The location of the ^{137}Cs source was fixed at a distance of 85 cm from the center of the active volume of the LXe detector. Lead bricks surrounding the path between the source and the LXe detector were used to attenuate the flux of γ rays not incident on the active volume of the LXe detector. The distance between the LXe detector and the HPGe detector varied from 14 to 62 cm (see Tab. 6.2). The uncertainty in the position of the HPGe detector was estimated to be less than 3 mm.

6.2 LXe Detector Design

The main idea for the LXe detector design is a maximization of the light detection efficiency in the active volume in order to reach the low energy threshold required to measure the LXe response at low recoil energies. This was achieved by increasing photocathode coverage of the active volume with high quantum efficiency (QE) PMTs. Another consideration for the detector design was a minimization of materials outside of the active volume so as to reduce the probability that particles scatter in detector materials before and after an interaction in the active volume. This setup has previously been used to measure the scintillation properties of nuclear recoils in LXe [Plante, 2012; Plante *et al.*, 2011].

6.2.1 Detector Inner Structure: PMTs and PTFE Frame

The active volume is a cube of side length 2.6 cm covered by six 2.5 cm square Hamamatsu R8520-406-Sel PMTs mounted in a polytetrafluoroethylene (PTFE) frame, which enables covering of 93 % of the solid angle. Fig. 6.2 shows a picture of the LXe inner structure (left) and schematic drawing of the LXe detector (right).

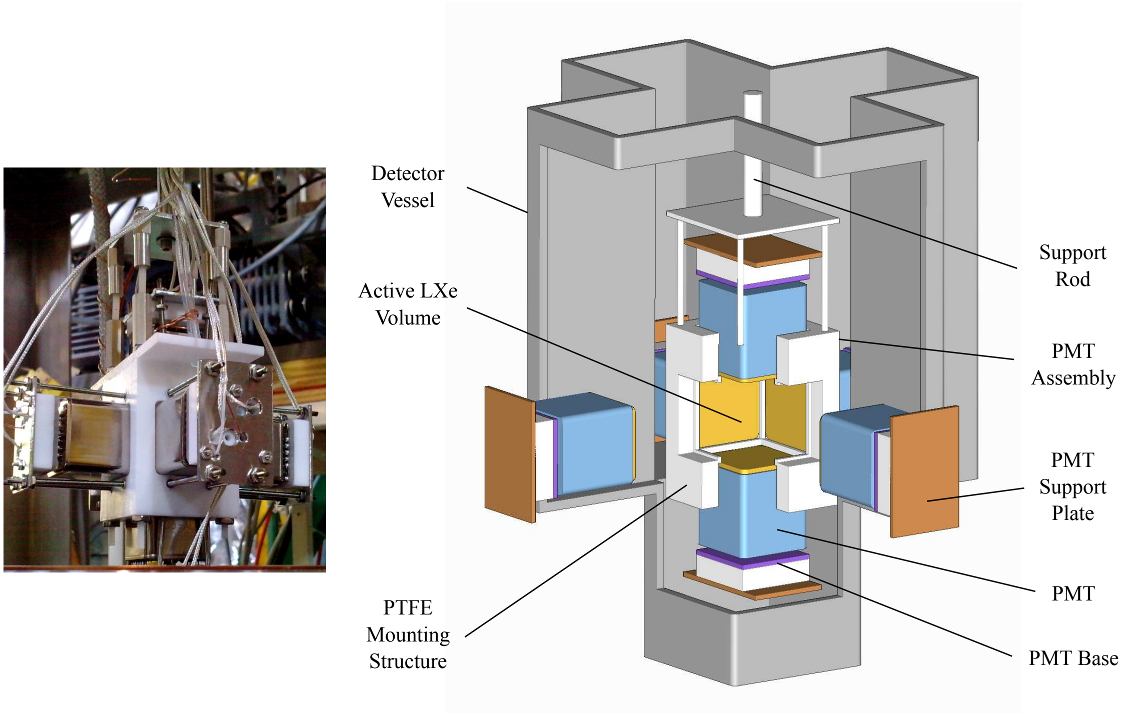

Figure 6.2: Picture of the LXe detector inner structure (left) and schematic drawing of the LXe detector (right). The cubic active LXe volume is covered by PMTs on each side. A rectangular PTFE piece on top of the PTFE mounting along with the LED was omitted in the schematic for clarity. Figure (right) from [Plante *et al.*, 2011].

The PMTs are the same type as those used in the XENON100 experiment [Aprile *et al.*, 2012c] but selected for high QE. The PMTs have a bialkali photocathode designed for low-temperature operation down to −110°C, and have an average room temperature QE of 32 % at 178 nm, the wavelength at which Xe scintillates [Jortner *et al.*, 1965]. The measured QE values were provided by Hamamatsu. The high QE of the PMTs and the large photocathode coverage of the arrangement yields a very high light collection efficiency and thus enables a low-energy threshold. The voltage divider network of the PMT bases is biased with positive high voltage to keep the PMT metal body and photocathode at ground potential, thereby ensuring that no electric field is present in the LXe active volume, which is mandatory for the zero-field measurement. Details of the ground-cathode scheme PMT base voltage divider and a linear PMT response in the regime of our interest are well explained in [Plante, 2012].

The PTFE frame serves as a mounting structure and alignment guide for the PMTs. Each PMT covers one side of the cubic active volume. Small 1-mm edges in the PTFE frame define the 2.6-cm cubic active volume and also partially envelope the boundary of the PMT, not covered by the photocathode. The PMT bases are mounted on aluminium PMT support plates with a PTFE block between the base and the support plate. The support plates are fixed to the PTFE frame with four threaded stainless steel rods. The rods can be used to precisely adjust the PMT positions and hold the support plates firmly in place. The PMT assembly is enclosed in a stainless steel detector vessel, surrounded by a vacuum cryostat. The detector vessel has a custom cross shape that emulates the contours of the PMT assembly to minimize the materials in the vicinity of the active volume and thus minimize the probability that incoming particles from the source scatter before or after an interaction in the active volume. The PTFE mounting structure is suspended from the top by a stainless steel rod fixed to a linear displacement motion feedthrough. The vertical position of the assembly within the detector vessel can be adjusted from the outside with the motion feedthrough.

An extra rectangular PTFE piece is fixed on top of the PTFE mounting structure and holds a blue light-emitting diode (LED) to calibrate the PMT gains, as shown in Fig. 6.2 (left). PTFE is partially transparent to the LED light and acts as a diffuser. A single intensity for the LED pulse is enough to generate an appropriate amount of light and calibrate all PMTs simultaneously.

PMT signal and high voltage cables share a common multipin electrical feedthrough. $50\,\Omega$ RG178 coaxial cables with their outer FEP jacket removed are used to deliver the signals from the PMT bases to the feedthrough. MDC Vacuum KAP3 in-vacuum insulated wires are used for the high voltage connections [Plante, 2012].

6.2.2 Cryogenic System, Gas Handling and Purification System

The LXe detector vessel was filled with 1.82 kg of LXe, the amount required for the liquid level to reach 1 cm above the active volume. The total LXe mass in the active volume is 50 g. A schematic of the cryogenic and gas system used for this experiment is shown in Fig. 6.3. During operation, the xenon is purified in the gas phase by circulating it through a hot getter with a diaphragm pump. The purified gas is reliquefied efficiently using a heat exchanger [Giboni *et al.*, 2011]. The LXe temperature is kept constant with an Iwatani PDC08 pulse tube refrigerator delivering 24 W of cooling power at −106°C. More details on the cooling system for this experiment are presented in [Giboni *et al.*, 2011]. For

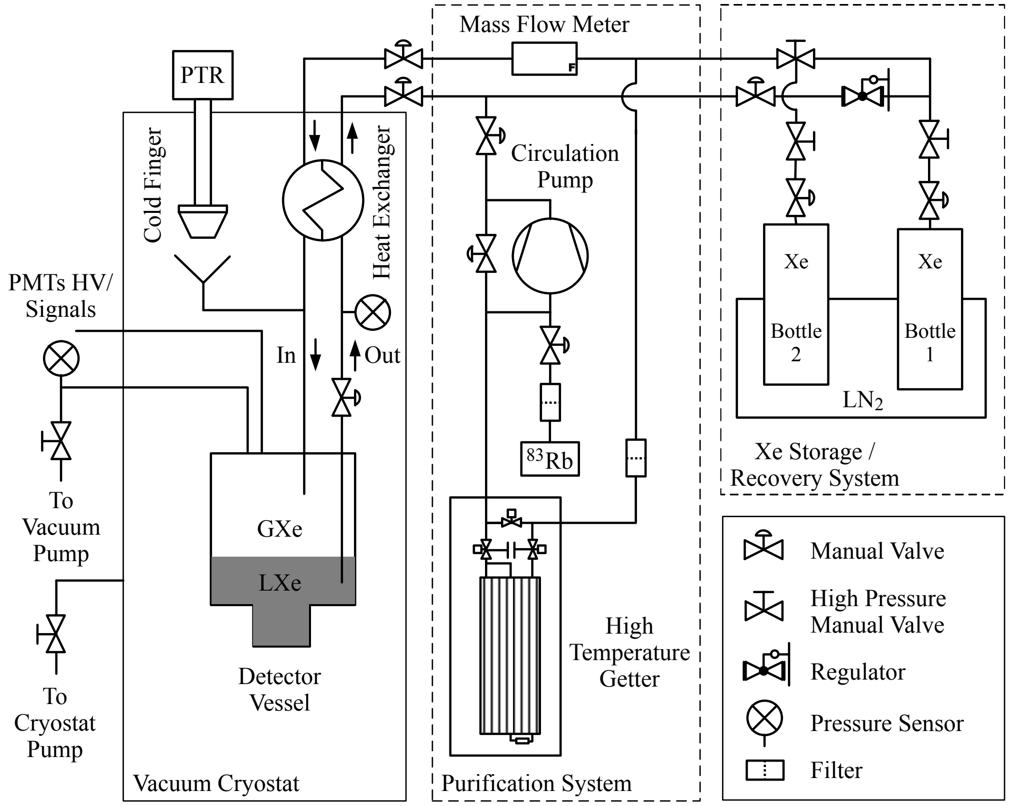

Figure 6.3: Schematic of the cryogenic and gas system with ^{83}Rb source mounted. Figure from [Plante *et al.*, 2011] and updated by G. Plante.

the measurements presented here, the LXe temperature was maintained at $-95°\mathrm{C}$ which corresponds to a vapor pressure of 2 atm. The LXe detector operating conditions were stable throughout the entire data-taking period with observed LXe temperature and gaseous xenon pressure variations (standard deviation over mean) of less than 0.7 and 0.6 %, respectively.

6.2.3 Scintillation Light Detection Efficiency

The expected scintillation light detection efficiency of the LXe detector was investigated with a light propagation simulation based on the GEANT4 Monte Carlo simulation toolkit. This simulation takes into account the geometry of the PMTs and the PTFE holding structure, the reflectivity of the materials in contact with the active LXe volume, the QE and collection efficiency of the PMTs, and an estimate of the angular response of the PMTs [Hamamatsu Photonics K.K., 2006]. Details of the simulation can be found in [Plante, 2012], with the final simulation results shown in Fig. 6.4.

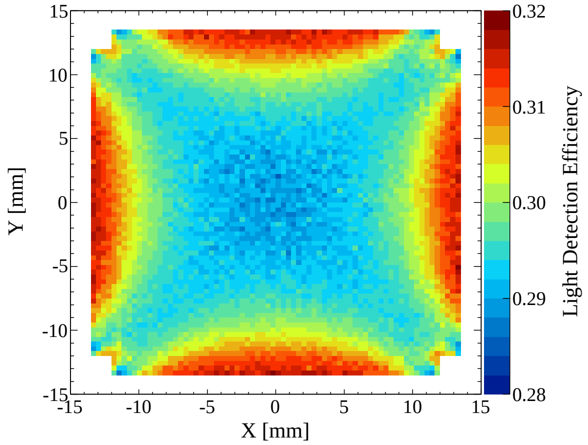

Figure 6.4: Simulated average scintillation light detection efficiency as a function of (x, y) taking into account the angular response of PMTs. Figure from [Plante, 2012].

The light detection efficiency is largely uniform in the bulk of the target volume with exceptions near the PMTs. The light detection efficiency near the surfaces of the PMT windows is pronounced mostly due to a large solid angle to the photocathodes. This resulted in higher scintillation yield without any spatial cut especially for the data with the external

^{57}Co source which emits 122 keV photoabsorbed γ rays, whose penetration depth in LXe is ~ 3 mm. Hence, to obtain the volume-averaged scintillation yield of 122 keV photoabsorbed γ rays from ^{57}Co, spatial cuts were applied (see Sec. 6.9.1).

6.3 Data Acquisition System and Trigger Description

The signals from the six PMTs were fed into a Phillips 776 ×10 amplifier with two amplified outputs per channel. The first output of each channel was digitized by a 14-bit CAEN V1724 100 MS/s flash analog-to-digital converter (ADC) with 40 MHz bandwidth while the second output was fed to a Phillips 706 leading edge discriminator. The discriminator thresholds were set at a level of -20 mV, which corresponds to 0.7 photoelectrons (pe). The logic signals of the six discriminator outputs were added with a CAEN N401 linear fan-in and discriminated to obtain a twofold PMT coincidence condition. The twofold PMT coincidence logic signal was then passed to a 10 μs holdoff circuit to prevent retriggering on the tail of the LXe scintillation signal, and constituted the LXe trigger.

The signal of the HPGe detector was amplified with an ORTEC A257N preamplifier and shaped with an ORTEC 450 research amplifier using 1 μs and 0.5 μs differentiation and integration time constants, respectively. The output of the research amplifier was split with a passive resistive fan-out. One copy went directly to the flash ADC and the other copy was discriminated at a threshold level of -30 mV, and forms the HPGe trigger signal.

Finally, for the Compton coincidence measurements presented here, the trigger was given by the coincidence within a 200-ns window of the LXe and the HPGe trigger signals.

The energy dependence of the efficiency of the LXe trigger was measured using a ^{22}Na source and a NaI(Tl) detector with the technique described in [Plante *et al.*, 2011]. The result obtained is compatible with the measurement of [Plante *et al.*, 2011], confirming that the recoil energy spectra do not suffer efficiency losses in the energy region of interest. For some of the data sets taken at higher energies ($\theta_{\mathrm{HPGe}} = 8.6^\circ$, 16.1°), the threshold levels were set to -40 mV so as to reduce the fraction of noise triggers. These increased thresholds also do not decrease the event acceptance in the energy region of interest, as shown in Fig. 6.6.

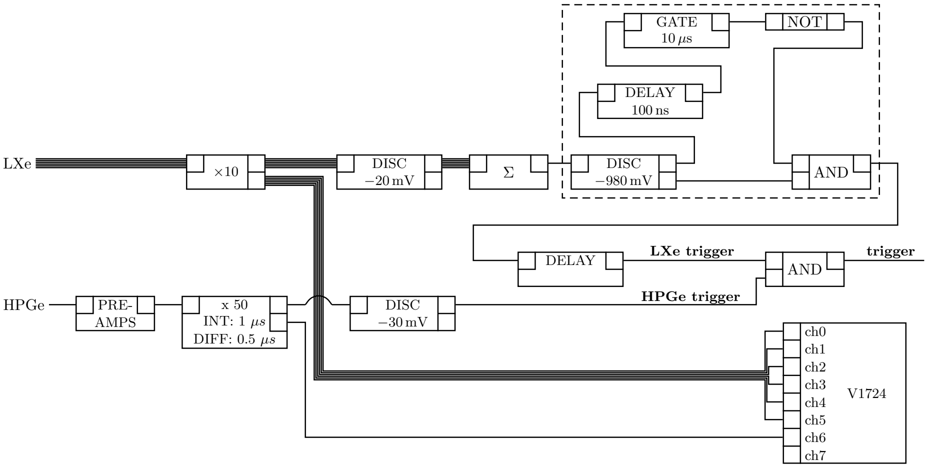

Figure 6.5: DAQ and trigger diagram.

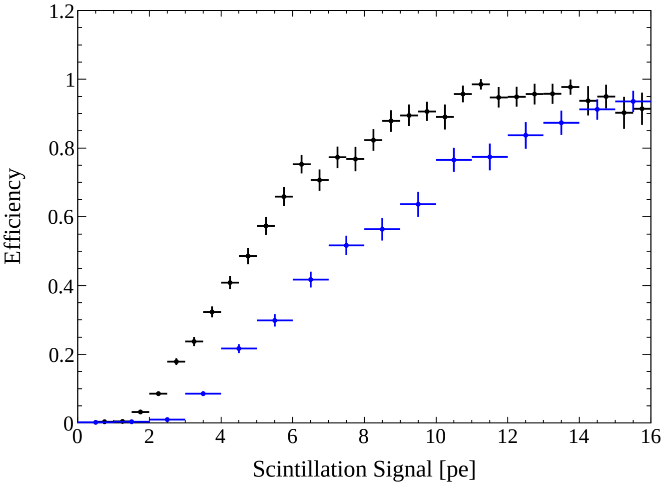

Figure 6.6: Measured trigger efficiency as a function scintillation signal with −20 mV (black) and −40 mV (blue) threshold. Wider binning was used due to limited statistics for the −40 mV measurement. The higher threshold delays reaching 100 % trigger efficiency as expected. Given that the threshold level was set as −20 mV for the low energy measurements and the mean of the lowest energy spectrum to obtain the scintillation yield is around 35 pe (see Fig. 6.15 (left, top)), recoil energy spectra do not suffer efficiency losses in the energy region of interest. Plot by G. Plante.

6.4 PMT Calibration

A blue LED embedded in the PTFE mounting structure (see Fig. 6.2 (left)) was used to calibrate the gain of each PMT. Fig. 6.7 shows a typical single-photoelectron spectrum of one of the PMTs. As shown in the figure, the light level was adjusted such that the ratio of zero-photoelectron peak (noise pedestal) to the single-photoelectron peak is about two orders of magnitude larger than the single-photoelectron peak. Since a detection of a few photons is governed by Poisson statistics, the possibility of double-photoelectron peak contamination in this spectrum can be computed by the Poisson probability

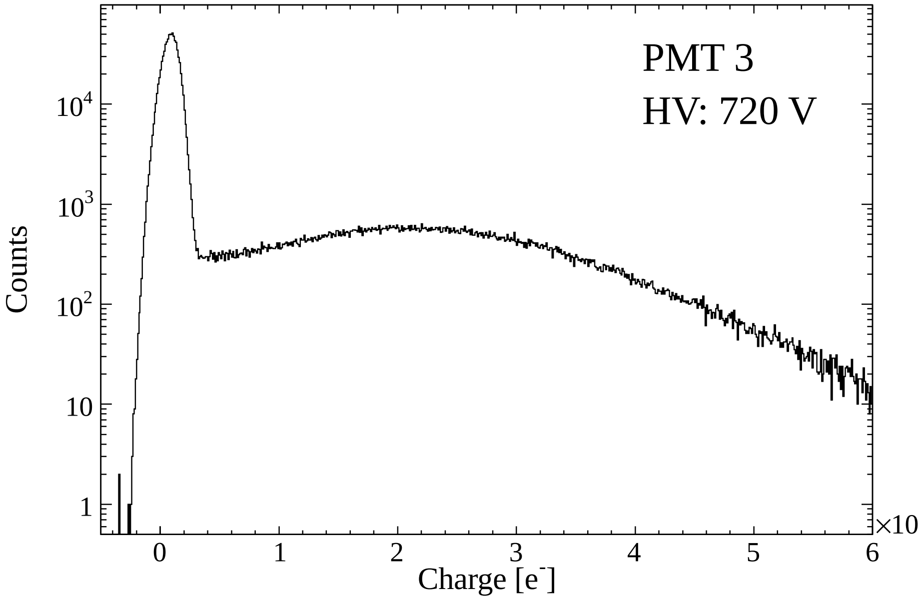

Figure 6.7: Single-photoelectron spectrum of PMT 3. The zero-photoelectron peak is about two orders of magnitude larger than the single-photoelectron peak and the possibility of double-photoelectron peak contamination in this spectrum is negligible. In this specific case, the Gaussian mean for the zero-photoelectron peak is 0.086×10^6 and the Gaussian mean of the single-photoelectron peak is 2.102×10^6 and hence the gain was computed as 2.016×10^6.

$$\mathrm{P}(k; \lambda) = \frac{\lambda e^{-\lambda}}{k!} \tag{6.2}$$

where λ is expected value and k is the number of occurrence. In the case of $\mathrm{P}(0;\lambda)/\mathrm{P}(1;\lambda) \approx 100$, λ is ≈ 0.01 and $\mathrm{P}(2;0.01)/\mathrm{P}(1;0.01) \approx 0.002$ and hence, the double-peak contamination in this spectrum is negligible.

The gain value for each LED data set was determined by fitting both the single-photoelectron peak and the noise pedestal with Gaussian functions. The gain was taken as the difference between the means of each Gaussian. The PMT gain calibration was performed at regular intervals during data taking. At the beginning of the experiment, the high voltage for each PMT was set so as to equalize the gain as much as possible with a limitation of the maximum allowed high voltage for safe operation.

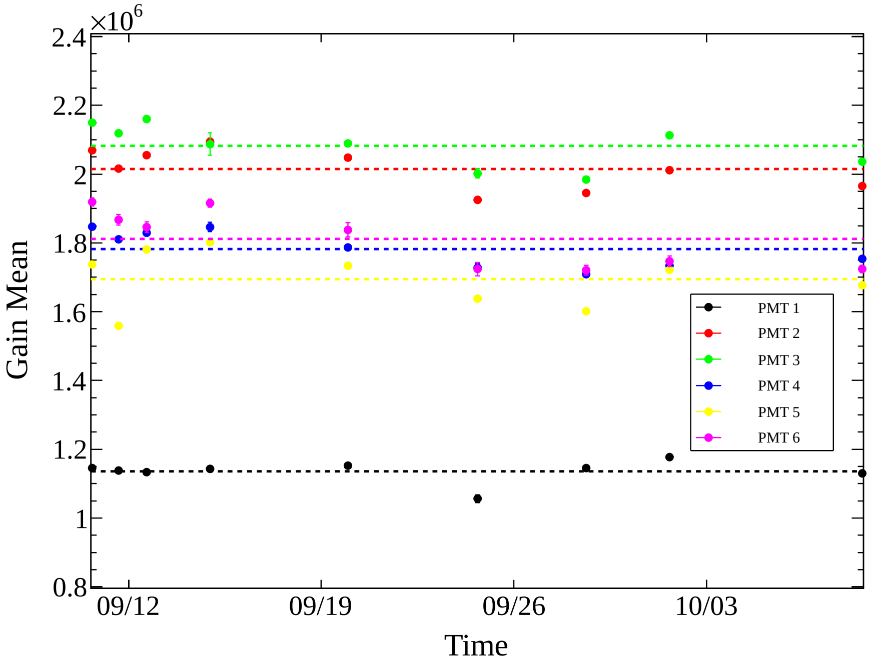

Figure 6.8: Gain measurements for each PMT (sold circles) along with their averages (dashed lines). The averages of measured values were used as PMT gains for whole data taking period. The uncertainty of each PMT gain was computed as the variation on the mean in the individual gain measurements. The total contribution to the uncertainty of the measured scintillation signal was computed as square sum of the uncertainties of each PMT.

Fig. 6.8 shows the gain measurements for each PMT and its averaged mean for the

Compton coincidence measurements. For the analysis presented here, the gain of each PMT was taken as its average measured gain over the whole data taking period and its uncertainty as the variation in the individual gain measurements. The uncertainty of the gain of each PMT varies between 1 % and 1.6 %. The total contribution to the uncertainty of the measured scintillation signal is 3 %, when taking into account that the scintillation yield is obtained from the sum of all PMT signals. Tab. 6.1 lists the individual PMT gains and uncertainties for the Compton coincidence measurements (run_07) and the external γ ray source measurements (run_08). The reason the PMT gains of run_08 exhibit larger uncertainties is due to less gain measurements.

Table 6.1: Individual PMT gains and uncertainties for run_07 and run_08.

PMT #	run_07	run_08
1	1.136×10^6 (±0.96 %)	1.143×10^6 (±0.24 %)
2	2.014×10^6 (±0.97 %)	2.073×10^6 (±1.71 %)
3	2.082×10^6 (±1.00 %)	2.163×10^6 (±2.30 %)
4	1.783×10^6 (±1.00 %)	1.922×10^6 (±0.13 %)
5	1.694×10^6 (±1.61 %)	1.855×10^6 (±0.20 %)
6	1.811×10^6 (±1.53 %)	2.043×10^6 (±1.85 %)

6.5 HPGe Detector Calibration

The excellent energy resolution of the HPGe detector makes it possible to select with high efficiency events where γ rays Compton scatter once and deposit a fixed energy in the LXe detector. Since the energy of the electronic recoil in the LXe detector is directly determined by the measured energy in the HPGe detector, it is important to verify the stability of the HPGe detector response throughout the measurements.

The HPGe detector was calibrated through dedicated measurements with the ^{137}Cs source between each Compton coincidence measurement. The linearity of the energy calibration was verified with 511 keV γ rays from a ^{22}Na source.

In addition, the stability of the HPGe detector calibration was monitored during each

Compton coincidence measurement via accidental coincidence events. Accidental coincidence events from uncorrelated LXe and HPGe triggers occur when two different γ rays interact in the LXe detector and the HPGe detector within the 200-ns coincidence window time. Since the accidental coincidence HPGe energy spectrum is essentially the same, albeit with a smaller rate, as an energy spectrum taken with the HPGe trigger, the 661.7 keV full absorption peak from ^{137}Cs γ rays incident on the HPGe detector can thus be used to monitor the stability of the calibration (see Fig. 6.11 (right)).

Fig. 6.9 shows the evolution of the absolute signal size of the 661.7 keV full absorption peak in the HPGe channel of the flash ADC from the accidental coincidence events, along with the HPGe detector calibration factors used for the data analysis and their uncertainties. As shown in the figure, the dc offset adjustment shows a correlation with the full absorption peak position of the accidental coincidence events. Therefore, the average of the value with the same dc offset was used to obtain HPGe detector calibration factor, with the exception of the 34.4° setup with 40 cm distance between the LXe detector and the HPGe detector due to the poor statistics on the accidental coincidence events in this configuration. For the Compton coincidence measurements presented here, the maximum variation in the corrected HPGe detector calibration factor was 0.2 %. It was taken into account for the uncertainty computation of the scintillation yield (see Sec. 6.10.1). For some of the data sets, there exist long term variations (< 0.5 mV) in the baseline of the HPGe channel which resulted in worsened resolution of the full absorption peaks.

Fig. 6.10 shows the HPGe spectrum of the $\theta_{\mathrm{HPGe}} = 0°$ Compton coincidence measurement after the HPGe calibration factor correction. The obtained resolution of the full absorption peak is 1.4 keV. Due to the angular acceptance of the LXe and HPGe detectors for this measurement, the left side of the peak contains real coincidence resulting in an asymmetric shape of the full absorption peak.

The energy resolution at 661.7 keV, obtained via accidental coincidence events, varied between 1.0 and 1.7 keV (see Tab. 6.2). This resolution variation could have been eliminated if the amplifier gain had been optimized to use the full dynamic range of the flash ADC.

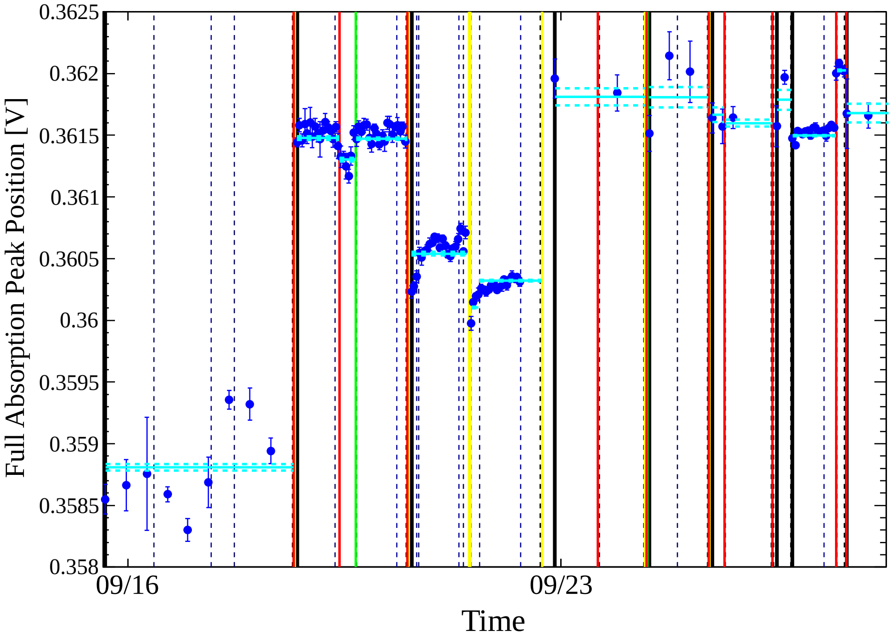

Figure 6.9: Absolute signal size variation of the 661.7 keV full absorption peak in the HPGe channel of the flash ADC from the accidental coincidence events. Thick-colored lines indicate the dc offset adjustments due to the change in the number of channels in flash ADC. Red, green, yellow lines are the dc offset adjustments for ^{57}Co, LED, dedicated HPGe detector calibration data, respectively. Thick black lines indicate the changes of HPGe angle (θ_{HPGe}) in the Compton coincidence measurements. The beginning of the each data set is shown as dashed line. As shown in the figure, the dc offset adjustment shows a correlation with the full absorption peak position of accidental coincidence events. The average values with the same dc offsets used for the HPGe calibration factor are shown in cyan lines, along with their uncertainties (cyan dashed lines). The only exception is the 34.4° measurement with the 40-cm distance between the LXe detector and HPGe detector due to poor statistics on the accidental coincidence events (around 09/24). This uncertainty in the HPGe detector calibration factor was taken into account for the total uncertainty computation (see Sec. 6.10.1).

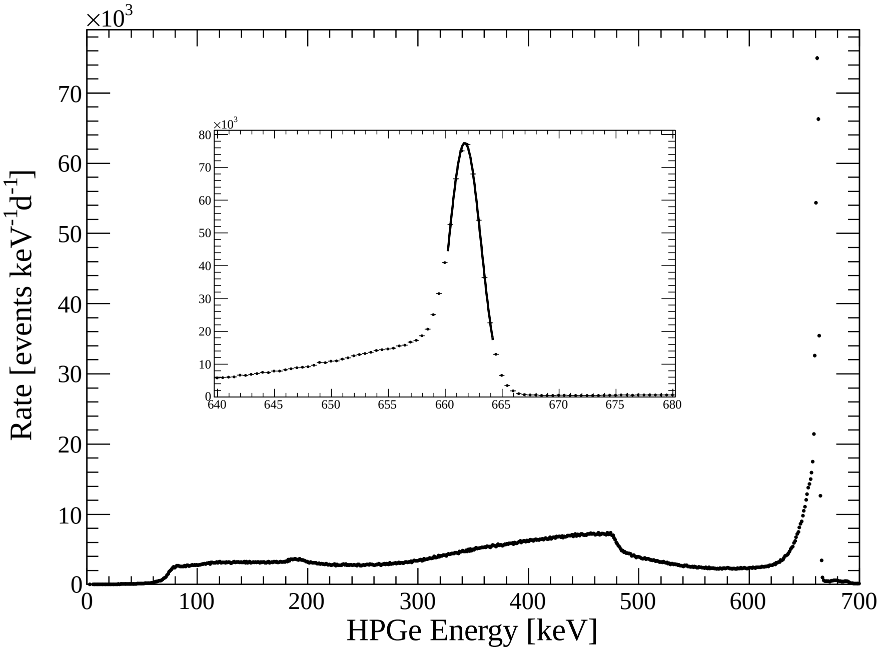

Figure 6.10: HPGe spectrum for the 0° Compton coincidence setup with Gaussian fit on the full absorption peak. The obtained energy resolution is 1.4 keV.

6.6 Measured Electronic Recoil Distributions

Compton coincidence data sets were taken with the HPGe detector positioned at eight different scattering angles, $\theta_{\rm HPGe}$: 0°, 5.6°, 8.6°, 12.0°, 16.1°, 21.3°, 28.1°, and 34.4°, with the LXe and HPGe detector distances varying between 14 and 62 cm, resulting in electronic recoil spectra with energies ranging from 2.0 to 120.2 keV. At each angle, a range of electronic recoil energies are deposited in the LXe detector due to the angular acceptance of the LXe target and that of the HPGe detector. Therefore, the HPGe detector positions were chosen so as to obtain recoil energies covering this entire energy range with sufficient statistics. Tab. 6.2 lists the HPGe detector positions used for each angle. In addition, a second 34.4° data set was taken with a different LXe and HPGe detector distance to investigate the possible contribution of the HPGe detector position to the systematic uncertainty on the scintillation yield. Finally, two data sets with different trigger configurations were taken at 0° to help study background contributions at recoil energies below 5 keV, one with a LXe detector trigger only, and one with a HPGe detector trigger only.

Table 6.2: HPGe detector positions, measured full absorption peak energy resolutions, and selected electronic recoil energy ranges for all Compton coincidence data sets. The variation of the measured resolution is discussed in Sec. 6.5. Table from [Aprile *et al.*, 2012e].

$\theta_{\rm HPGe}$	HPGe Detector Distance (cm)	HPGe Detector Resolution (keV)	$E_{\rm er}$ Range (keV)
0°	14	1.4	2.2 – 26.5
5.6°	60	1.0	2.0 – 12.9
8.6°	40	1.0	5.1 – 28.8
12.0°	40	1.0	10.0 – 27.2
16.1°	62	1.3	21.8 – 36.2
21.3°	40	1.0	33.9 – 60.2
28.1°	40	1.1	63.2 – 90.2
34.4°	19	1.7	77.2 – 122.2
34.4°	40	1.0	112.2 – 114.2

Since electronic recoils with a range of energies are accessible in one measurement with the HPGe detector at a given position, and since in all cases the energy resolution of the HPGe detector is much narrower than this energy range, the scintillation response at many different recoil energies can be extracted from a single data set. Moreover, the scintillation response at the same energy can be extracted from data sets which have overlapping recoil energy ranges.

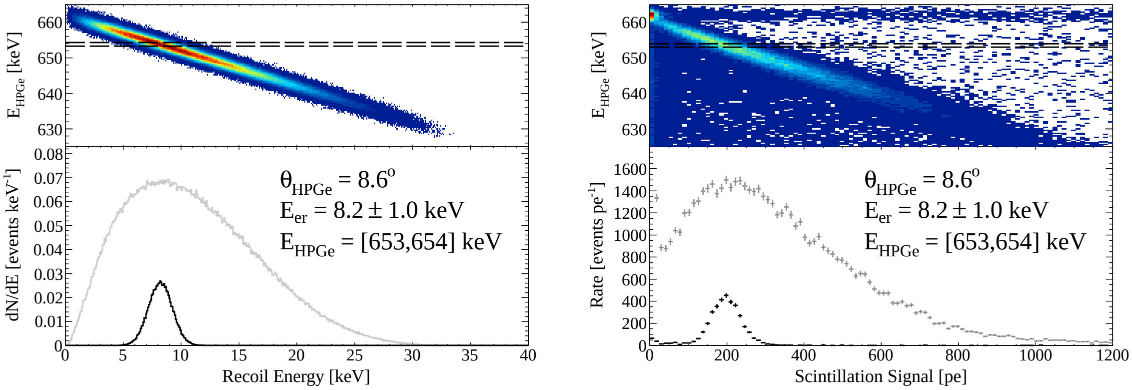

Figure 6.11: Simulated (left, top) and measured (right, top) distributions of HPGe detector energies and Compton electron recoil energies, or LXe scintillation signals in the case of the measurement, along with their projections (bottom, gray points) for the 8.6° Compton coincidence setup. A known electronic recoil energy spectrum (black points) is obtained by selecting simulated events with HPGe detector energies between 653 and 654 keV (horizontal dashed lines). With this energy selection the spread in electronic recoil energies is dominated by the HPGe detector energy resolution of 1 keV at 661.7 keV measured for this dataset (Sec. 6.5). Using the same energy selection (horizontal dashed lines), the scintillation response of LXe to 8 keV electronic recoils can be extracted from the 8.6° Compton coincidence measurement. Additional backgrounds neglected in the simulation are present in the data but become important only at recoil energies below 5 keV, as explained in the text. Figure from [Aprile *et al.*, 2012e].

The distribution of HPGe detector energies, E_{HPGe}, and Compton electron recoil energies in the LXe detector, E_{er}, for the 8.6° Compton coincidence setup are shown in Fig. 6.11

for both data (right panel) and a simplified Monte Carlo simulation (left panel). The distribution of energy deposits in both detectors is shown in the top panel, while the bottom one shows only the deposition in the LXe detector (gray line). This simplified simulation, described in Sec. 6.7.1, only includes γ-ray interactions with the detector targets, ignoring all the other materials, and takes into account the energy resolution of the HPGe detector. As expected, the energy of the scattered γ ray and that of the recoiling Compton electron sum up to the energy of the γ-ray incident on the LXe detector, E_γ. Recoils over a range of energies are produced in the LXe detector due to the angular acceptance of both detectors, as expected. A distribution of known electronic recoil energies (black line in the bottom panel) can be obtained by selecting a narrow range of scattered γ-ray energies (horizontal dashed lines) measured by the HPGe detector. The spread in electronic recoil energies after the selection is given by the convolution of the energy range chosen, ΔE_{HPGe}, with the HPGe detector resolution near E_γ. The scintillation response at a given electronic recoil energy is obtained by calculating the mean scintillation signal measured in the LXe detector when applying this HPGe detector energy selection.

Fig. 6.11 (right, top), shows the measured distribution of HPGe detector energies and LXe detector scintillation signals for the 8.6° Compton coincidence data set. Comparing this with the distribution from the simplified simulation, three different event populations are visible : events with $E_{\mathrm{er}}+E_{\mathrm{HPGe}}$ equal, lower, and higher than E_γ. The event population where $E_{\mathrm{er}} + E_{\mathrm{HPGe}} = E_\gamma$, within the limits of the HPGe detector resolution, corresponds to events where the incident γ ray scatters once in the active LXe volume, producing a Compton electron of energy E_{er}, and is fully absorbed in the HPGe detector. Consequently, the scintillation response of LXe to electronic recoils with nearly monoenergetic energies can be inferred from these events.

The event population where $E_{\mathrm{er}} + E_{\mathrm{HPGe}}$ is lower than E_γ corresponds, for the most part, to events where the scattered γ ray deposits only a fraction of its energy in the HPGe detector, due to the finite size of the crystal. That is, each possible scattered γ-ray energy is responsible for a spectrum of energies in the HPGe detector, with a full absorption peak, a Compton continuum, a multiple Compton scattering region, the latter two being responsible for the event population with a HPGe energy lower than the scattered γ-ray energy. Events where γ rays scatter in other materials before interacting in the HPGe detector additionally contribute to this population. A Monte Carlo simulation based on the GEANT4 toolkit, also described in Sec. 6.7.2, was used to estimate the contribution of such events in the energy range of the single scatter peak for various electronic recoil spectra.

Finally, the event population where $E_{\mathrm{er}} + E_{\mathrm{HPGe}}$ is higher than E_γ corresponds to events with an accidental coincidence between the LXe detector and the HPGe detector. This population is especially pronounced at $E_{\mathrm{HPGe}} \approx 662\,\mathrm{keV}$ in Fig. 6.11 (right), as expected since the accidental coincidence spectrum should have a peak at the incident γ-ray energy. As mentioned in Sec. 6.5, events from this population were used to monitor the stability of the HPGe energy calibration during the Compton coincidence measurements.

The increase in rate at low recoil energies compared to the simulated data is attributed to events where the γ ray interacts only in the LXe outside the active volume but where resulting scintillation light is visible in the active volume. The feature is also observed with all external γ-ray sources. The average probability for a photon outside the active LXe volume to reach a PMT photocathode was estimated at 1×10^{-4} via a light propagation Monte Carlo simulation. An exponential feature consistent with that observed in data can also be reproduced in simulations by including the expected scintillation signal from energy deposits outside the active LXe volume. As is apparent from Fig. 6.11 (right, top) the largest background in the measurement of the scintillation response of LXe with this technique is from chance coincidences at low electronic recoil energies.

6.7 Monte Carlo Simulation

For optimum efficiency, two different Monte Carlo simulations were used to analyze different aspects of the expected event distributions for Compton coincidence measurements. The first is a simplified Monte Carlo simulation that considers only events in which the incident γ ray interacts in the LXe detector, and deposits its full energy in the HPGe detector. The second simulation is based on the GEANT4 toolkit [Agostinelli *et al.*, 2003] and includes a realistic description of the LXe detector, detector vessel, vacuum cryostat, support frame, and HPGe detector. It was used to obtain the expected electronic recoil energy spectra as a function of HPGe energy, and thus enabled a direct comparison with the measured spectra and the identification and quantification of the different backgrounds present.

6.7.1 Simplified Monte Carlo Simulation

The simplified Monte Carlo simulation incorporates the geometry of the active LXe volume and of the HPGe detector crystal, the position of the ^{137}Cs source, as well as the actual positions of the HPGe detector used for the various Compton coincidence data sets. The simulation proceeds by generating random positions within the volume of the LXe detector, taking into account the Compton scattering mean free path, and on the front surface of the HPGe detector, and then calculating the recoil energy that corresponds to each pair of random LXe and HPGe interaction points via the Compton scattering formula. The energy deposited in the HPGe detector is then simply taken as the incident γ-ray energy, E_γ, minus the recoil energy in the LXe detector, thus assuming that the scattered γ ray deposited its full energy in the HPGe detector. This is then convolved with the Gaussian energy resolution. The standard deviation used for each Compton coincidence data set is the value measured using the corresponding accidental coincidence spectrum (see Sec. 6.5). Calculating the expected recoil energy from this simulation assumes that the incident γ ray travels directly from the source to the LXe detector, scatters once in the LXe detector, and travels directly to the HPGe detector, thereby neglecting any interactions in materials outside of the LXe active volume. Furthermore, since scattering angles are not sampled from the photon differential scattering cross section, the calculation neglects any angular dependence in the cross section over the range of scattering angles geometrically allowed by both detectors. Nevertheless, the expected mean energy of the recoil peak from the simplified simulation was found to be in agreement at the 1 % level with that of the GEANT4-based simulation, as shown in Tab. 6.3. In addition, the simulated spectra agree with each other at all recoil energies above 2 keV. Disagreement on the order of 10 % appears for the 2-keV recoil peak below 1 keV.

As mentioned earlier, the resulting mean and spread of the electronic recoil peak in the LXe, for each HPGe energy selection window applied to a Compton coincidence data set, were calculated using the simplified simulation by applying the appropriate energy selections

Table 6.3: Gaussian fit mean comparison between the simplified Monte Carlo (Simple MC) and GEANT4-based Monte Carlo (GEANT MC) simulations in the full width half-maximum (FWHM).

HPGe Energy	Fit Range (keV)	Simple MC (keV)	GEANT4 MC (keV)
$[659, 660]$	$[0.6, 3.6]$	2.16 ± 0.05	2.14 ± 0.04
$[658, 659]$	$[1.6, 4.6]$	3.13 ± 0.05	3.11 ± 0.05
$[657, 658]$	$[2.4, 6.0]$	4.13 ± 0.04	4.13 ± 0.05
$[656, 657]$	$[3.6, 6.6]$	5.14 ± 0.05	5.17 ± 0.05

to each simulated data set. This recoil energy correction factor is shown in Fig. 6.12. The effect of the misalignment of the HPGe detector on the mean energy of the recoil peak was investigated by varying the position of the HPGe detector in the simulation. Mean recoil energies are found to vary by less than 2 %. Finally, the effective change in the response of the LXe detector due to the variation of the spatial distribution of events in the LXe with the HPGe energy selection was estimated by calculating the average light detection efficiency over the spatial distribution of events for different HPGe energy selections. The spatial variation of the light detection efficiency used for the calculation was obtained from an independent light propagation Monte Carlo simulation, explained in Sec. 6.2.3.

6.7.2 GEANT4-based Monte Carlo Simulation

The GEANT4-based Monte Carlo simulation uses the same description of the LXe detector as the one used to simulate the expected nuclear recoil energy distributions for the measurement of the scintillation efficiency of low-energy nuclear recoils in LXe that was performed with the same detector [Plante *et al.*, 2011]. The geometry and response of the HPGe detector was verified by comparing simulated energy spectra with measured spectra from dedicated ^{137}Cs calibrations of the HPGe detector (see Fig. 6.13). The information recorded in the simulation includes the energy, position, time, type of particle and physical process responsible for each energy deposit in the LXe detector, as well as the total energy, time, and type of particle for each energy deposit in the HPGe detector.

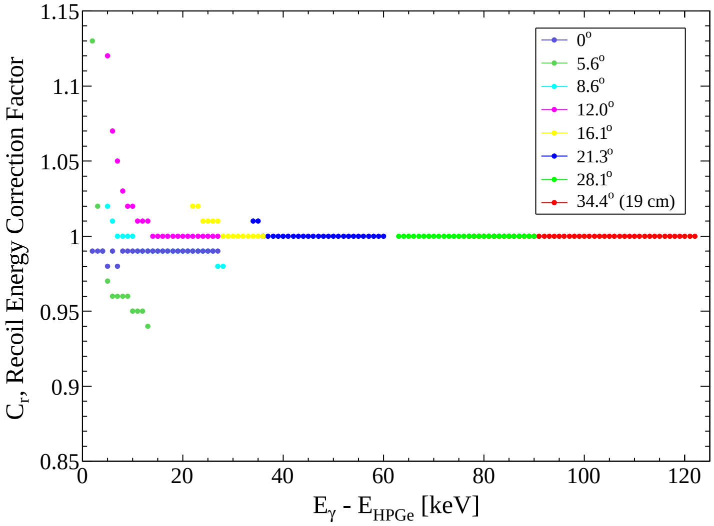

Figure 6.12: Recoil energy correction factor, C_r. The recoil energy E_er was determined by $E_\mathrm{er} = (E_\gamma$ - $E_\mathrm{HPGe})/C_\mathrm{r}$. The maximum (minimum) correction factor is 1.13 (0.94) for 5.6° measurement due to its large distance between the LXe detector and the HPGe detector. The distance between the LXe detector and the HPGe for the 16.1° measurement is similar to that of 5.6° measurement but the energy range cut based on the background contamination reduces the energy range of 16.1° measurement. Most of the cases the correction factor remains close to 1. See the text for details.

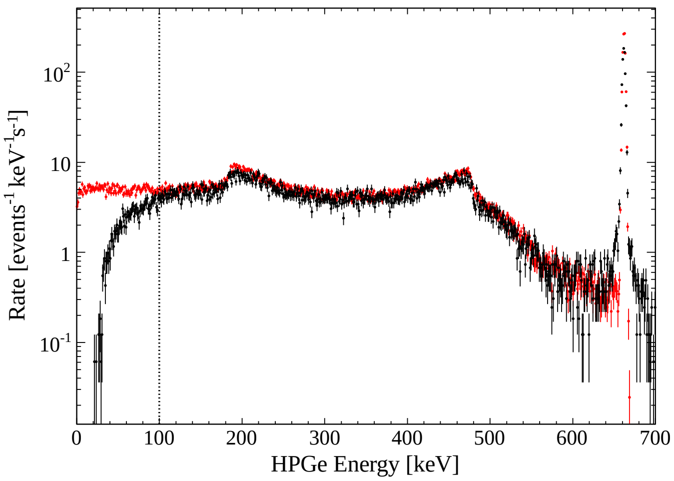

Figure 6.13: Spectral comparison between the simulation and data for the dedicated HPGe detector calibration with an 296 kBq point-like ^{137}Cs source placed at 14.2 cm from the detector. The black dashed line indicates the HPGe detector threshold (30 mV). Good agreement is shown not only for the full absorption peak but also for the Compton edge and back-scattered peak. The rate for the simulation was adjusted taking into account of the detection efficiency of the HPGe detector. The possible origin of the detection efficiency is a high rate in the detector. Plot by R. Persiani.

Fig. 6.14 shows the simulated electronic recoil energy spectra for the 0° Compton coincidence setup, obtained from the GEANT4-based simulation using E_{HPGe} energy selections $[659, 660]$, $[658, 659]$, $[657, 658]$, $[656, 657]$ keV, resulting in mean recoil energies of 2.2 ± 1.4, 3.2 ± 1.4, 4.2 ± 1.4, and 5.3 ± 1.4 keV, respectively. The black spectra consist of events in which the γ scattered only in the active LXe volume before interacting in the HPGe detector whereas the red spectra consist of events in which the γ ray additionally interacted in other materials, either before or after scattering in the active LXe volume, before interacting in the HPGe detector. The contribution of these multiple scatter events to the electronic recoil peak is less than 3 %. Their energy spectrum is not peaked since the presence of additional scatters spoils the HPGe energy and LXe recoil energy correlation. Note, however, that since the selection is for a fixed HPGe energy, their maximum recoil energy is constrained to be lower than the maximum energy of the recoil peak. Multiple scatters in the active

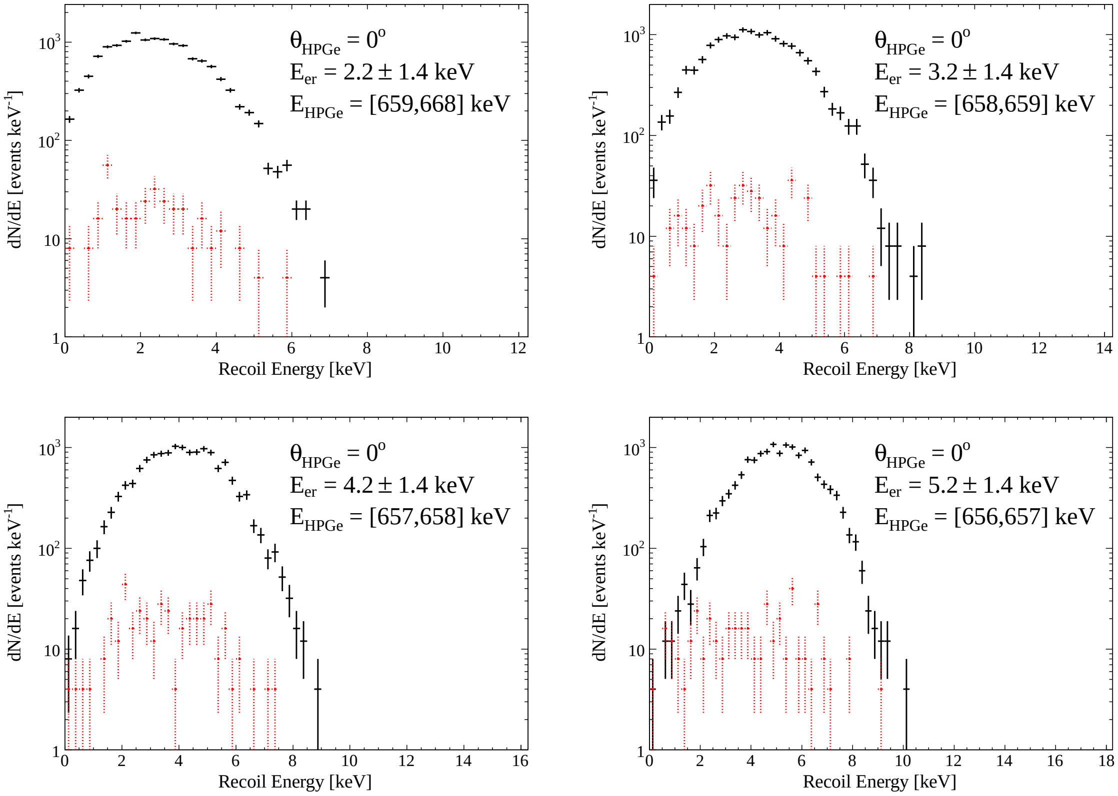

Figure 6.14: Simulated electronic recoil spectra for the 0° Compton coincidence setup, using E_{HPGe} energy selections $[659, 660]$, $[658, 659]$, $[657, 658]$, and $[656, 657]$ keV, resulting in mean recoil energies of 2.2 ± 1.4, 3.2 ± 1.4, 4.2 ± 1.4, and 5.3 ± 1.4 keV respectively. The black histograms show the spectrum of events where the incident γ ray interacts in the active LXe volume, and nowhere else, and deposits in the HPGe detector an energy within the HPGe selection window. The red histogram corresponds to events where the γ ray additionally interacts in other materials, either before or after scattering in the active LXe volume, before interacting in the HPGe detector. The contamination of the recoil peak by events with γ-ray interactions in other materials is less than 3 %. Figure from [Aprile *et al.*, 2012e].

LXe volume are highly suppressed due to the small size of the target with respect to the Compton scattering mean free path in LXe for ^{137}Cs γ rays ($\sim 5.5\,\mathrm{cm}$). These spectra can be compared to the measured LXe scintillation spectra shown in Fig. 6.15, keeping in mind that the background contribution from accidental coincidence events is not included in the simulation. At energies of 3.2 keV and above, the measured electronic recoil peak is well separated from the background from accidental coincidences. This low contamination from events with scatters in other materials shows that the design goal of minimizing the amount of materials in the vicinity of the active LXe volume has been achieved, in agreement with [Plante *et al.*, 2011].

The electronic recoil spectra with mean recoil energies of 2.2 ± 1.4, 3.2 ± 1.4, 4.2 ± 1.4 keV were also used to calculate the uncertainty in the LXe scintillation response at low energies arising from the assumption of an exponential background model (Sec. 6.8). The details of the calculation are described in Sec. 6.10.

6.8 The Scintillation Yield

For each of the angles (θ_{HPGe}) at which Compton coincidence measurements were taken, the distribution of HPGe detector energies and LXe scintillation signals were divided in 1-keV slices along the E_{HPGe} axis, and the resulting LXe scintillation spectra were analyzed for each of the selected energies.

Fig. 6.15 shows the LXe scintillation spectra obtained for the four lowest electronic recoil energies from the 0° Compton coincidence data set. For recoil energies below 2 keV, the background in the signal region is too high to extract the scintillation yield in LXe. The spectra consist of a recoil peak, which corresponds to events where the incident γ ray scattered in the active LXe volume only and deposited its full energy in the HPGe detector, and different backgrounds depending on the electronic recoil energy range selected. For spectra at low recoil energies, the background mostly comes from accidental coincidence events from the full absorption peak of ^{137}Cs in the HPGe detector and few photoelectrons scintillation signals from the LXe detector, believed to originate from interactions in the LXe outside the active volume, as discussed earlier. For spectra at recoil energies above

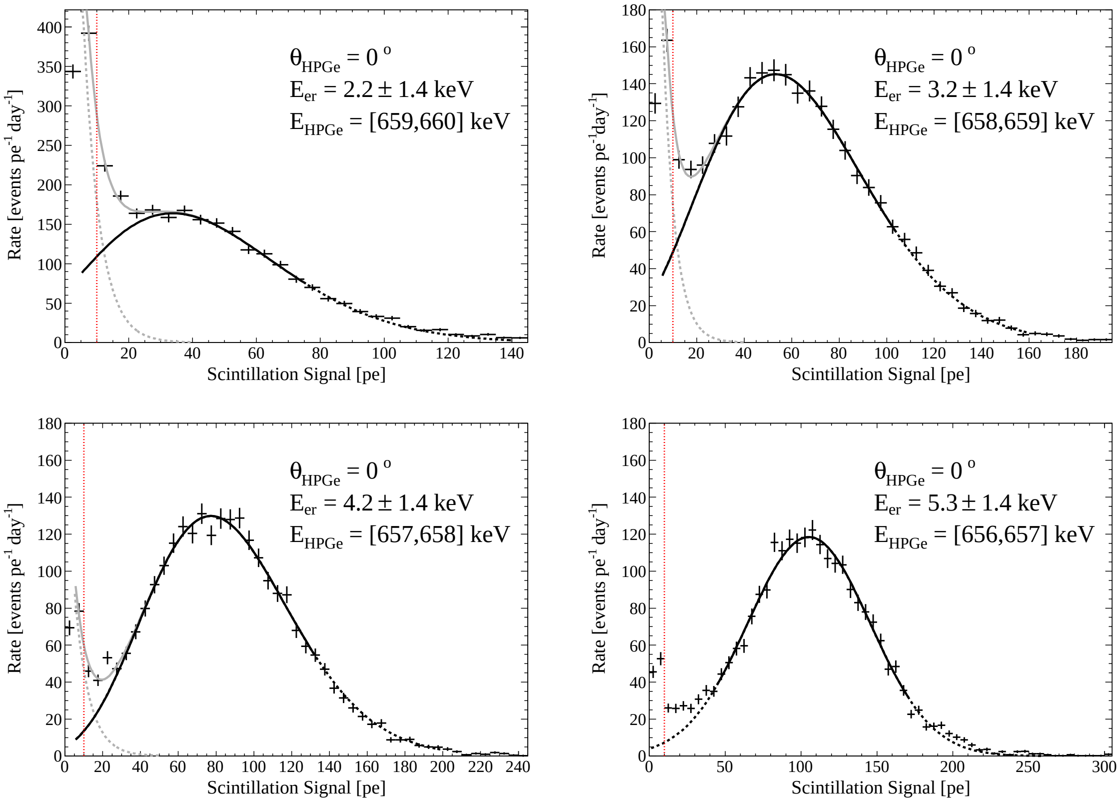

Figure 6.15: LXe scintillation spectra (points) for the energies of 2.2 ± 1.4, 3.2 ± 1.4, 4.2 ± 1.4 and 5.3 ± 1.4 keV from the 0° Compton coincidence data set with the same HPGe energy selection windows used in the Monte Carlo analysis. As a reference, the measured $> 99\,\%$ trigger efficiency is indicated by the vertical red dashed line. For recoil energies E_{er} below 5 keV, the scintillation spectra were fitted with the sum (gray line) of a "scaled" continuous Poisson function (black line), and an exponential function (dashed gray line), as described in the text. The range used for each fit is indicated by the extent of the solid black line. For recoil energies above 5 keV, the spectra were fitted with Gaussian functions (black line). Figure from [Aprile *et al.*, 2012e].

5 keV, the background largely comes from events in which scattered γ rays with energies higher than that expected for the HPGe energy selection deposit only a fraction of their energy in the HPGe detector, resulting in an approximately flat background from zero to the recoil peak. Ultimately, spectra at recoil energies above or below the range of energies expected from the angular acceptance of the LXe and HPGe detectors are dominated by events where the γ ray scattered in other materials and by accidental coincidence events between a partial energy deposit in both detectors.

For spectra at recoil energies below 5 keV, the recoil peaks are slightly asymmetric, exhibiting a longer tail at higher energies. Additionally, the background from accidental coincidence events is significant and must be taken into account to obtain the correct LXe scintillation response. Consequently, the spectra were fitted with the sum of a "scaled" continuous Poisson function, that is, a function of the form $f_{\mu,a}(x) = e^{-\mu}\mu^{ax}/\Gamma\left(ax+1\right)$, to describe asymmetry in the recoil spectra with the help of scaling parameter and an exponential function, which represents the background coming from chance coincidence events. Fig. 6.15 (top left, top right, bottom left) shows the results of fits to spectra at electronic recoil energies of 2.2 ± 1.4, 3.2 ± 1.4, and 4.2 ± 1.4 keV from the 0° Compton coincidence data set, respectively. Note that the uncertainty on the electronic recoil energy stated here (and throughout) corresponds to the spread in recoil energies after the HPGe energy selection (see Fig. 6.11), which is dominated by the HPGe energy resolution, and not the uncertainty on the mean energy of the recoil peak, which is considerably smaller.

For spectra at recoil energies above 5 keV, the recoil peaks are symmetric and the fraction of events arising from background is small. Hence these spectra were fitted with Gaussian functions over the range of the recoil peaks. Fig. 6.15 (bottom right) shows the result at 5.3 ± 1.4 keV from the 0° Compton coincidence data set. The background from scattered γ rays with partial energy deposited in the HPGe detector is apparent to the left of the recoil peak.

As explained in Sec. 6.6, each Compton coincidence data set can be used to infer the scintillation response over a wide range of energies, limited mostly by the angular acceptance of the LXe and HPGe detectors at the position used for each measurement. For recoil energies near the extremes of the range of energies for a given configuration, the background from multiple scatter and accidental coincidence events dominates over the recoil peak. The range of electronic recoil energies over which the scintillation response was calculated was chosen for each data set so that the fraction of events attributable to background in the recoil peak would remain below 20 %. To estimate the background contribution to the peak, the area in the regions between 2 and $4\,\sigma$ above and below the peak was computed. This value was then scaled to the width of the peak fitting range and divided by the total event rate in this range. This background contamination estimation method is valid as long as the background varies smoothly in energy, as was observed to be the case in all spectra above recoil energies of 5 keV. Tab. 6.2 lists the resulting ranges over which the scintillation response was calculated for each Compton coincidence data set.

The mean electronic recoil energy does not exactly correspond to E_γ minus the central value of the HPGe energy range selected, because the event rate varies as a function of the recoil energy (see Fig. 6.11), due to the geometrical acceptance of the detectors. In a region where the event rate increases as a function of recoil energy, for γ-ray scattering angles smaller than the angle at which the HPGe detector is positioned, the mean electronic recoil energy obtained from the HPGe energy selection will be higher than expected since more events at higher recoil energies will be included in the selection. Similarly, the mean electronic recoil energy obtained will be lower than expected in a region where the event rate decreases as a function of recoil energy. The finite energy resolution of the HPGe detector accentuates this effect since even more events from higher or lower energies will be shuffled. The mean and spread of the electronic recoil energy for a given HPGe energy selection was calculated using the simplified Monte Carlo simulation described in Sec. 6.7.1, applying the same selection criteria than for the data.

The HPGe energy selection also has an effect on the spatial distribution of events within the LXe detector. Events for which the γ-ray scattering angle is close to θ_{HPGe}, and hence those for which the HPGe energy selection window is close to $E_{\mathrm{er}}(\theta_{\mathrm{HPGe}})$, will be distributed somewhat uniformly in the center of the LXe detector. As the central value of HPGe energy selection is decreased however, the events will progressively cluster near the side of the LXe detector towards higher scattering angles. Similarly, events will progressively cluster near the side of the LXe detector towards lower scattering angles when the central value of the

HPGe energy selection is increased. Fig. 6.16 and Fig. 6.17 show the simulated spatial distribution with different HPGe energy selections for the 0° and 8.6° Compton coincidence setups, respectively, which clearly verifies the mentioned effect.

The relative bias in the measured scintillation response from this effect was estimated using the simplified Monte Carlo simulation and found to be smaller than 0.7 %, mostly due to the small spatial variation of the light detection efficiency of the LXe detector (Sec. 6.2.3). This effect is further suppressed since the energy range over which the scintillation response is calculated is already restricted by limiting the maximum background contamination of the electronic recoil energy peak. Recoil energy ranges corresponding to highly clustered event distributions are thus avoided.

6.9 Scintillation Response to Monoenergetic Sources

Several radioactive sources were used to evaluate the response of the LXe detector. Specifically, ^{137}Cs, ^{22}Na, and ^{57}Co external sources were used to obtain the γ-ray response of the LXe detector while ^{83m}Kr was used as an internal source for the response to fast electrons.

6.9.1 Response to External γ-ray Sources

The measurements with external sources were performed by attaching the sources to the cryostat vessel at the height of the LXe active volume. These measurements were taken without the additional ×10 amplification (Sec. 6.3) of the PMT signal to prevent saturation of the flash ADC, which has a maximum input voltage of 2.25 V. In the normal configuration, saturation starts to occur for signals of 10^3 pe on a single PMT, whereas in this configuration the response from the 1.275 MeV γ ray from ^{22}Na, with a mean signal per PMT of 4.6×10^3 pe, could be measured without any saturation effect.

Fig. 6.19 shows a scintillation spectrum obtained with the ^{137}Cs source. The peak at 16×10^3 pe corresponds to the 661.7 keV full absorption peak while the other peaked feature at 5×10^3 pe is the backscatter peak, mainly due to γ rays that scatter in materials immediately surrounding the LXe active volume before photoelectric absorption in the outer layers of the active volume. The roll-off at low energies is due to the increased effective

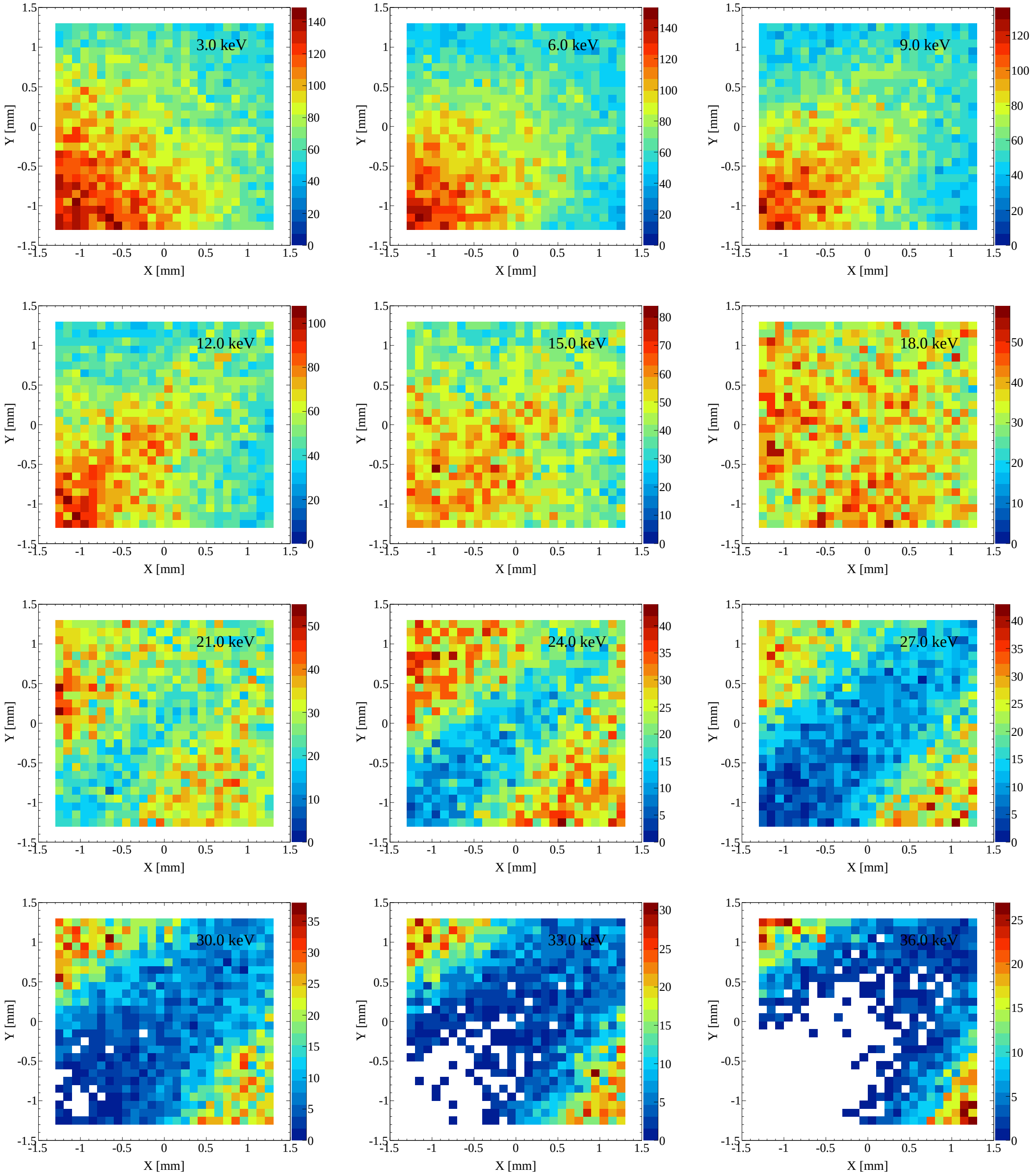

Figure 6.16: Simulated spatial distribution of events with HPGe energy selection of 1-keV slices, 3-kev intervals for the 0° Compton coincidence setup. It is clearly shown that events distribute to the edge of the detector, where the light detection efficiency is higher than the center of the detector, as the recoil energy increases. Plots by G. Plante.

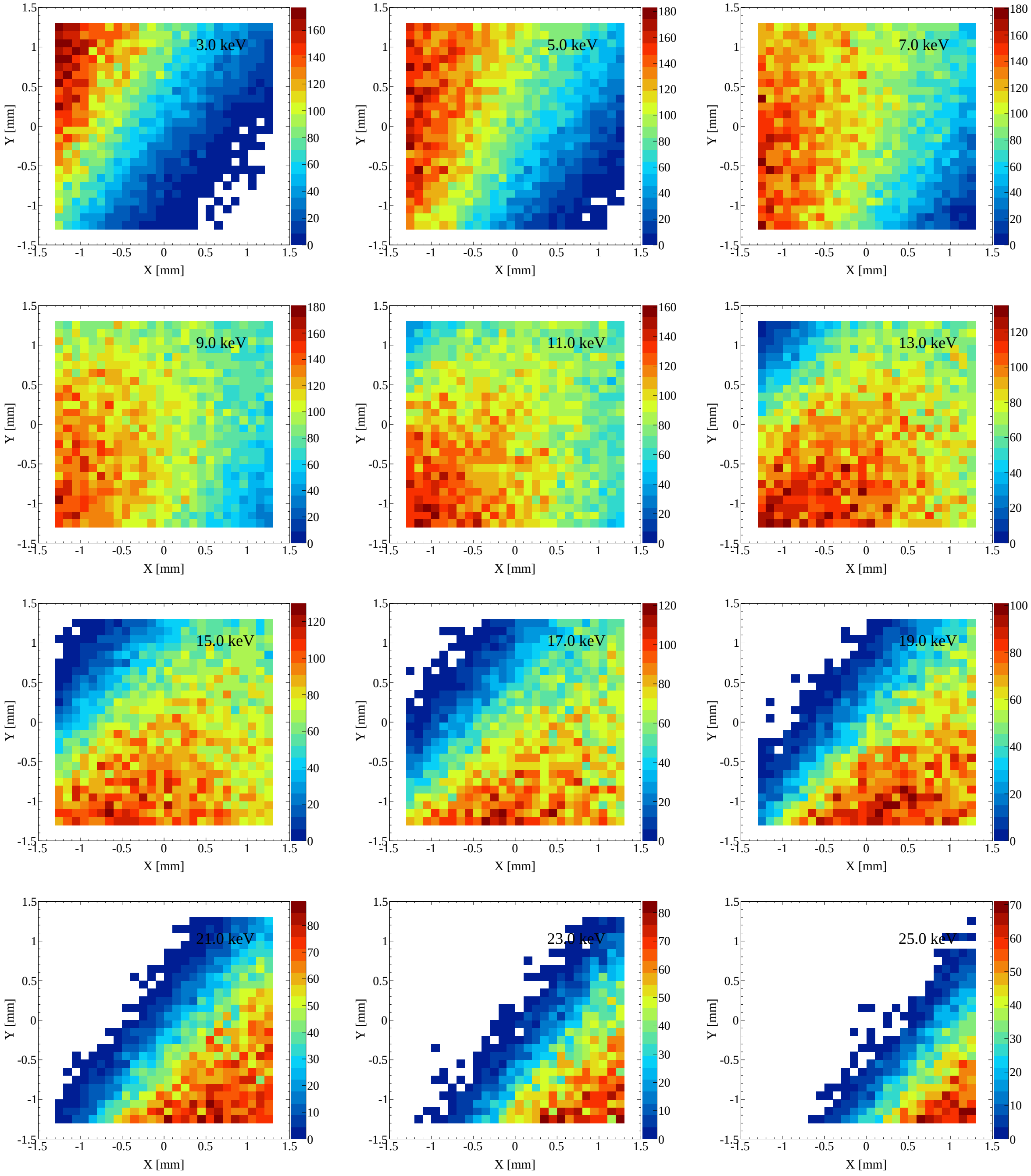

Figure 6.17: Simulated spatial distribution of events with HPGe energy selection of 1-keV slices, 2-keV intervals for the 8.6° Compton coincidence setup. As the recoil energy increases, the events move from high y and low x to low y and high x. Plots by G. Plante.

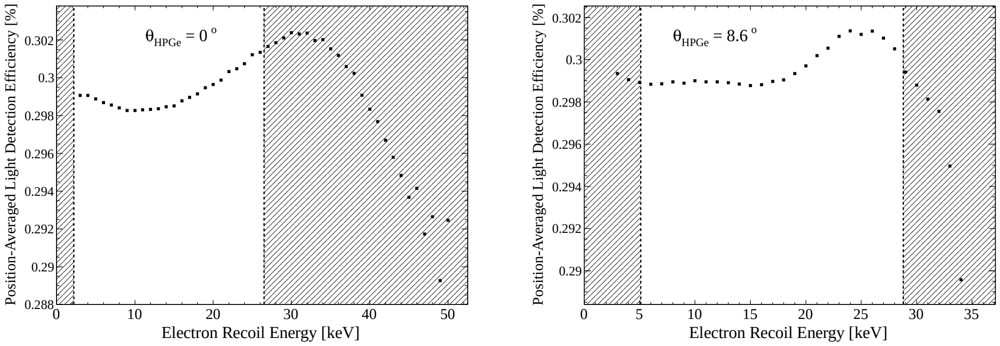

Figure 6.18: Position-averaged light detection efficiency as a function of recoil energy for the 0° (left) and 8.6° (right) Compton coincidence setups. As shown in Fig. 6.16 and Fig. 6.17, the spatial dependence of the events results in the variation of effective light detection efficiency according to the recoil energy. The shaded regions were excluded for the analysis due to their background contribution in the recoil spectra larger than 20 % as explained in the text, and hence the total variation in the light detection efficiency is smaller than 0.5 %. Plots from G. Plante and updated.

trigger threshold when the additional ×10 amplification is not applied to the PMT signals (black points). At low energy, in the spectrum with the additional ×10 amplification, the event rate rises exponentially (gray points). As discussed in Sec. 6.6 the suspected origin of these events is the small probability for scintillation photons produced outside the active LXe volume to leak into it. This feature at low energy is observed in all spectra obtained with external γ-ray sources.

The large photocathode coverage and the use of PTFE as scintillation light reflector on the few remaining surfaces assures a good uniformity of the light collection efficiency throughout the active volume. Even so, there is a slight increase in the light collection efficiency near the surface of the PMT windows. The light propagation simulation mentioned in Sec. 6.7.1 estimates this increase as $\sim$ 6 % with respect to the volume-averaged light collection efficiency. This spatial nonuniformity in the LXe can systematically increase the measured scintillation yield of low-energy γ rays from external sources such as ^{57}Co. To mitigate this effect, three cuts on the relative light ratio between two opposing PMTs are

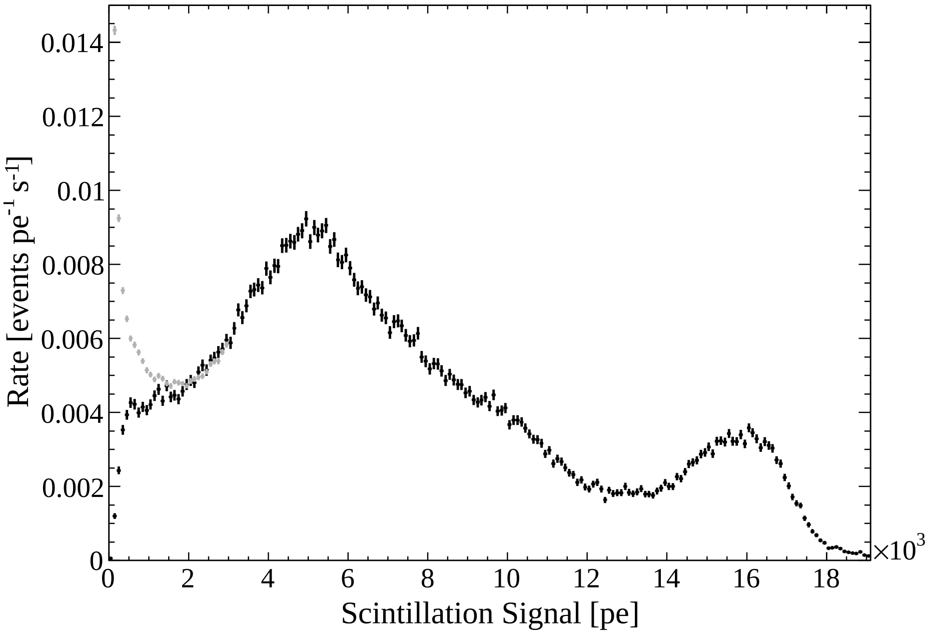

Figure 6.19: LXe scintillation spectrum obtained with the 370 MBq ^{137}Cs γ source without (black) and with (gray) additional ×10 amplification. The peak at 16×10^3 pe corresponds to the 661.7 keV full absorption peak, while the other peaked feature at 5×10^3 pe is mainly due to the backscatter peak. The event rate increase at low energies is visible in the spectrum with additional amplification, as is also observed in the accidental coincidence spectra from the Compton coincidence measurements. Figure from [Aprile *et al.*, 2012e].

applied to the ^{57}Co data to select interactions that occur further from the PMT windows. Thanks to implementing the cube-shaped active volume with 6 PMTs covering each sides, the relative light ratio between two opposing PMTs can be used to estimate the distance between the two PMTs and hence cartesian coordinate equivalent position can be established. Although the exact distance depends on the each PMT performance, our purpose is not to know the distance exactly to infer fiducial volume but rather to discard events too close to PMTs which can bias the inferrence of scintillation yield. The volume-averaged scintillation yield obtained at 122 keV is 23.60 ± 0.03(stat) $\pm\, 0.85$(sys) pe/keV, consistent with the value of [Plante *et al.*, 2011].

Tab. 6.4 lists the measured scintillation yields for the various external γ-ray sources used to evaluate the scintillation response of the LXe detector. The statistical uncertainty comes from the fit of the spectra and the variation with different fitting ranges on the spectra. The systematic uncertainty includes contributions from the measured variations in the PMT gains and in the response at different source positions.

Table 6.4: Measured scintillation yields for various external γ-ray sources and for the internal irradiation with ^{83m}Kr.

Source	Energy (keV)	Type	Scintillation Yield (pe/keV)
^{22}Na	1274.6	γ	22.26 ± 0.08(stat) $\pm\, 0.77$(sys)
^{137}Cs	661.7	γ	23.84 ± 0.08(stat) $\pm\, 0.85$(sys)
^{22}Na	511	γ	23.76 ± 0.18(stat) $\pm\, 1.07$(sys)
^{57}Co	122	γ	23.60 ± 0.03(stat) $\pm\, 0.85$(sys)
^{83m}Kr	32.1	e^-	27.38 ± 0.12(stat) $\pm\, 0.82$(sys)
^{83m}Kr	9.4	e^-	28.80 ± 0.08(stat) $\pm\, 0.86$(sys) [a]

[a] This value depends on the time difference between 32.1 and 9.4 keV transitions, see Sec. 6.11 for details.

6.9.2 Internal ^{83m}Kr Irradiation

The ^{83m}Kr isomer, produced in the decay of ^{83}Rb via pure electron capture, decays to the ground state through two subsequent transitions of 32.1 and 9.4 keV, with half-lives of 1.83 h and 154 ns, respectively. Tab. 6.5 lists the possible deexcitation channels and their branching ratios for the two transitions, as well as the different energies of the electrons emitted in each channel. Branching ratios were obtained from theoretical internal conversion coefficients calculated by the `BrIcc` program [Kibedi *et al.*, 2008] and fluorescence yields from [Hubbell *et al.*, 1994]. In both cases, most of the time the energy is carried by internal conversion and Auger electrons.

Table 6.5: Deexcitation channels and branching ratios of the 32.1 keV and 9.4 keV transitions of ^{83m}Kr. For both transitions, most of the time the energy is carried by internal conversion electrons (CE) and Auger electrons (A) instead of γ rays. Numbers in parentheses correspond to electron energies in keV.

Transition Energy	Decay Mode	Branching Ratio [%]
32.1 keV	$\mathrm{CE}_{M,N}(32)$	11.5
	$\mathrm{CE}_L(30.4) + \mathrm{A}(1.6)$	63.8
	$\mathrm{CE}_K(17.8) + \mathrm{X}_{K\alpha}(12.6) + \mathrm{A}(1.6)$	15.3
	$\mathrm{CE}_K(17.8) + \mathrm{A}(10.8) + 2\mathrm{A}(1.6)$	9.4
	γ	< 0.1
9.4 keV	$\mathrm{CE}_L(7.5) + \mathrm{A}(1.6)$	81.1
	$\mathrm{CE}_M(9.1)$	13.1
	γ	5.8

The use of ^{83m}Kr as a calibration source allows a uniform internal irradiation of the LXe detector, eliminating most of the problems mentioned earlier concerning low-energy calibrations with external γ-ray sources. Additionally, the scintillation signals produced in LXe by the two subsequent ^{83m}Kr transitions can be separated in time and thus provide precise scintillation yield measurements with negligible background contribution [Manalaysay *et al.*, 2010], even at low source activities. Since the bulk of the energy in the 32.1 keV transition of ^{83m}Kr is most often carried by a 30.4 keV conversion electron, its scintillation response should provide an independent verification of the scintillation yield at that energy obtained in the Compton coincidence measurement. Similarly, the scintillation response of the 9.4 keV transition is expected to be similar to that obtained in the Compton coincidence measurement.

The source used for the irradiation was composed of zeolite beads containing ^{83}Rb, which emanate ^{83m}Kr from ^{83}Rb decays. The ^{83}Rb activity of the source used was 3.45 kBq. The source was located in a stainless steel cylinder connected to the gas system through a 2-μm filter and isolated with a valve (see Fig. 6.3). The rate of ^{83m}Kr decays observed was 8 mHz, much lower than the activity of the source. This large reduction in observed rate is attributed to a low efficiency in the convective transport of ^{83m}Kr atoms into the active volume of the LXe detector. The bulk motion of LXe itself in and out of the active volume is limited by the small open area between PMTs and the PTFE holding structure (Sec. 6.2.1). Nevertheless, the distinctive signature of the two ^{83m}Kr transitions allows a clear selection of these events above background, as shown in Fig. 6.20 (left). Fig. 6.20 (right) shows the differential event rate with the time difference between the two transitions. The measured half-life between the two transitions is 154 ± 6 ns, in agreement with previously measured values [Ahmad *et al.*, 1995; Ruby *et al.*, 1963].

Fig. 6.21 shows the measured scintillation spectra for the 9.4 and 32.1 keV transitions. The scintillation response for the 9.4 keV transition is compatible with a Gaussian, whereas the response for the 32.1 keV is not and shows a longer tail at low scintillation values. The 32.1 keV transition is expected, in about 25 % of cases, to undergo internal conversion with a K-shell electron, and thus emit a larger number of lower energy electrons than in the case of internal conversion with an L-shell electron (see Tab. 6.5). If the scintillation yield of electrons were to vary with energy then the response of the 32.1 keV transition could have two components. Therefore, the response of the 32.1 keV transition is taken as the mean of two Gaussian functions constrained to have the appropriate branching ratios. The scintillation yield value obtained is $27.38 \pm 0.12(\text{stat}) \pm 0.82(\text{sys})$ pe/keV, with a resolution (σ/E) of 6.9 %. The scintillation yield of the 9.4 keV transition obtained is

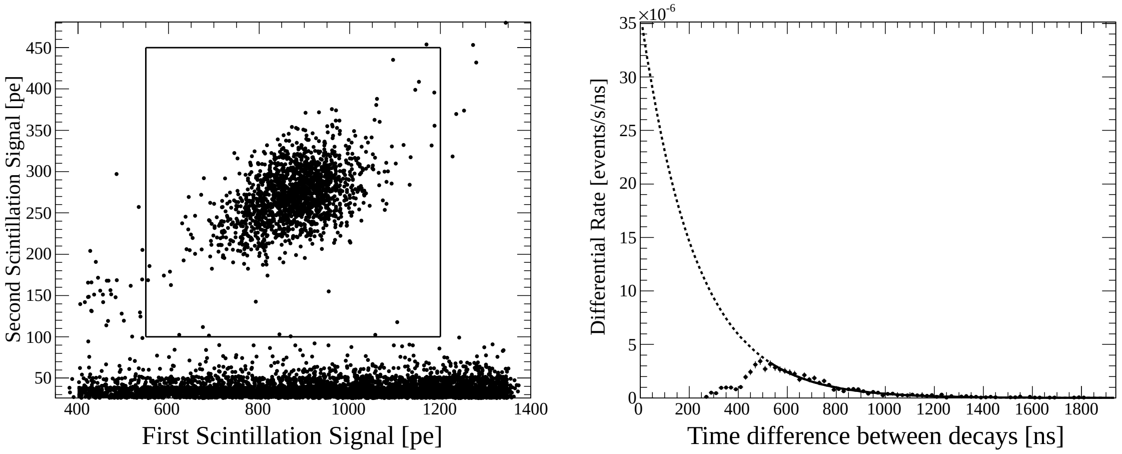

Figure 6.20: ^{83m}Kr events selection cut in the first scintillation signal (32.1 keV transition) and the second scintillation signal (9.4 keV transition) (left) and the time difference between the transitions with the event selection cut shown as a box in the left (right) . In the left, the population in the box shows a clear distinction from the background population at low second scintillation signal which does not present any correlation with the first scintillation signal. In the right, the half-life between the two transitions was obtained by fitting the measured differential rate (thick line). Due to the peak finding algorithm efficiency of the data processing program, the events with the time difference less than 500 ns were not tagged 100 % and the tagging efficiency goes to 0 at the time difference between transitions below $\sim$ 250 ns. Thus to infer the observed activity, the exponential fit to the data points was extrapolated below a time difference of 500 ns (dashed line). The obtained half-life between the two transitions and the observed activity of ^{83}Rb source are 154 ± 6 ns and 8 mHz, respectively.

$28.80 \pm 0.08(\mathrm{stat}) \pm 0.86(\mathrm{sys})\,\mathrm{pe/keV}$, with a resolution ($\sigma/E$) of 11.8 %. The measured

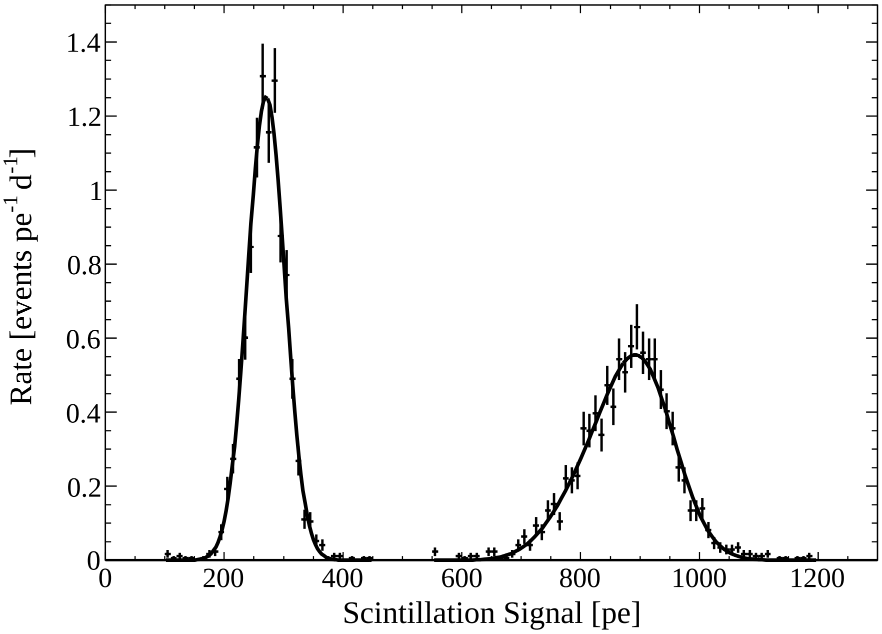

Figure 6.21: Measured scintillation spectra (data points) for the 9.4 and 32.1 keV deexcitation transitions of ^{83m}Kr, along with their fits (lines). The asymmetry of the scintillation spectrum of the 32.1 keV transition can be explained by a decrease in the response of LXe with decreasing energies. The used fit for the 32.1 keV transition is two Gaussian functions constrained with the branching ratios of 75 and 25 %. Figure from [Aprile *et al.*, 2012e].

variation in the PMT gains during the internal radiation with ^{83m}Kr, is taken as the systematic uncertainty in the light yield. The ratio of the measured scintillation yields of the 32.1 and 9.4 keV decays is 1.052 ± 0.005, a value consistent with the results of [Manalaysay *et al.*, 2010], which found 1.056 ± 0.011. In [Kastens *et al.*, 2009], the scintillation yields measured lead to a slightly lower ratio of 0.976 ± 0.001.

The measured scintillation yields from the internal irradiation with ^{83m}Kr are summarized in Tab. 6.4, along with the results for external γ-ray sources.

6.10 Results

The precise determination of the absolute scintillation yield requires the precise knowledge of many properties related to the scintillation photon detection probability: the detailed geometry of the active LXe volume, the reflectivity of the materials, and the collection efficiency of the PMTs and their QE (and its possible variation with temperature). Thus, relative yields are reported. The reference chosen is the scintillation yield of the 32.1 keV transition of ^{83m}Kr. The use of a low-energy, uniform, internal source as a reference has major advantages over an external γ-ray source such as ^{57}Co: the systematic uncertainty on the ^{57}Co scintillation yield (Sec. 6.9.1) arising from the highly localized event distribution in LXe can be eliminated. Additionally, since the reference source is internal and uniformly distributed within the active volume, it readily solves the problem of the small penetration depth of low-energy γ rays in the calibration of the inner volume of large detectors.

The obtained values of the relative scintillation yield of electronic recoils at zero field, $\mathcal{R}_e$, are listed in Tab. 6.7. The specific Compton coincidence data sets used to calculate $\mathcal{R}_e$ values are also listed for each electronic recoil energy, labeled by the scattering angle θ_{HPGe} between the ^{137}Cs source and the center of the LXe and HPGe detectors.

6.10.1 Uncertainty Computation

The statistical uncertainty on $\mathcal{R}_e$ comes from the fit of the electronic recoil peak while the systematic contributions arise from uncertainties in the PMT gains, σ_{g_i}, the HPGe calibration factor, $\sigma_{C_{\mathrm{HPGe}}}$, and the background subtraction, σ_b. The systematic uncertainties arising from the variation in the fitting range and the spread in electronic recoil energies were found to have a negligible impact and are therefore not included. However, the observed variance of $\mathcal{R}_e$ values for the same electronic recoil energy from different measurements was found to be greater than that given by the contributions mentioned above. Consequently, an additional term, $\sigma^2_{\mathcal{R}_e,\mathrm{s}}$, is included in the expression for the total uncertainty on $\mathcal{R}_e$ to account for this. The total uncertainty on $\mathcal{R}_e$ is therefore expressed as

$$\sigma^2_{\mathcal{R}_e} = \sigma^2_{\mathcal{R}_e,\mathrm{fit}} + \sum_i \left(\frac{\partial \mathcal{R}_e}{\partial g_i}\right)^2 \sigma^2_{g_i} + \left(\frac{\Delta \mathcal{R}_e}{\Delta C_{\mathrm{HPGe}}}\right)^2 \sigma^2_{C_{\mathrm{HPGe}}} + \left(\frac{\Delta \mathcal{R}_e}{\Delta b}\right)^2 \sigma^2_b + \sigma^2_{\mathcal{R}_e,\mathrm{s}}. \quad (6.3)$$

The uncertainty in the PMT gains is taken as the variation in the measured gains during the data-taking period. The variation in $\mathcal{R}_e$ values with respect to the HPGe detector calibration was calculated through a finite difference approximation, $\Delta\mathcal{R}_e/\Delta C_{\mathrm{HPGe}}$, by repeating the analysis using the calibration factors $C_{\mathrm{HPGe}} \pm \sigma_{C_{\mathrm{HPGe}}}$, as shown in Fig. 6.9. For electronic recoil energies below 5 keV (θ_{HPGe} : 0°, 5.6°), the contribution from the uncertainty in the background subtraction was estimated by repeating the analysis with a different prescription for the background model. Specifically, since low-energy background events are expected to arise from accidental coincidences between LXe and HPGe detector triggers, as explained in Sec. 6.6, an alternate background model based on the energy spectrum of accidental coincidence events was used. The LXe scintillation signal and HPGe energy random variates, distributed according to the measured LXe and HPGe detector ^{137}Cs spectra, were used to generate the expected background from accidental coincident events. The background contamination was calculated such that the resulting LXe scintillation signal spectrum, with the background spectrum subtracted, matched the rate obtained from the GEANT4 Monte Carlo simulation, as shown in Fig. 6.22. A recoil energy region virtually free of background, from 10 to 20 keV, was used to normalize the simulated rate. $\Delta\mathcal{R}_e/\Delta b$ due to the background subtraction scaling factor $b \pm \sigma_b$, similar to $\Delta\mathcal{R}_e/\Delta C_{\mathrm{HPGe}}$, and the difference from the values without background subtraction were taken into account for the uncertainty due to the background. Since the generated background only holds for the 0° measurement, the same relative uncertainty on the background subtraction was assumed for the 5.6° measurement data, although less background contamination is expected for the 5.6° setup.

The additional uncertainty contribution $\sigma^2_{\mathcal{R}_e,\mathrm{s}}$ is taken as a linear function of the recoil energy, from 7.1 % at 2 keV down to 3 % at 53 keV, and vanishing for recoil energies above 78 keV, as shown dark purple line in Fig. 6.23. Fig. 6.23 shows the unbiased sample variance with the subtraction of known uncertainty components, ${\sigma_0}^2$, explicitly,

$$
{\sigma_0}^2 = \sigma^2_{\mathcal{R}_e,\mathrm{fit}} + \sum_i \left(\frac{\partial\mathcal{R}_e}{\partial g_i}\right)^2 \sigma^2_{g_i} + \left(\frac{\Delta\mathcal{R}_e}{\Delta C_{\mathrm{HPGe}}}\right)^2 \sigma^2_{C_{\mathrm{HPGe}}} + \left(\frac{\Delta\mathcal{R}_e}{\Delta b}\right)^2 \sigma^2_b .
$$

For the energy ranges that only one angle measurement exists, the unbiased sample variance value was set to 0 in the figure. The size of the unbiased sample variance is negligible at

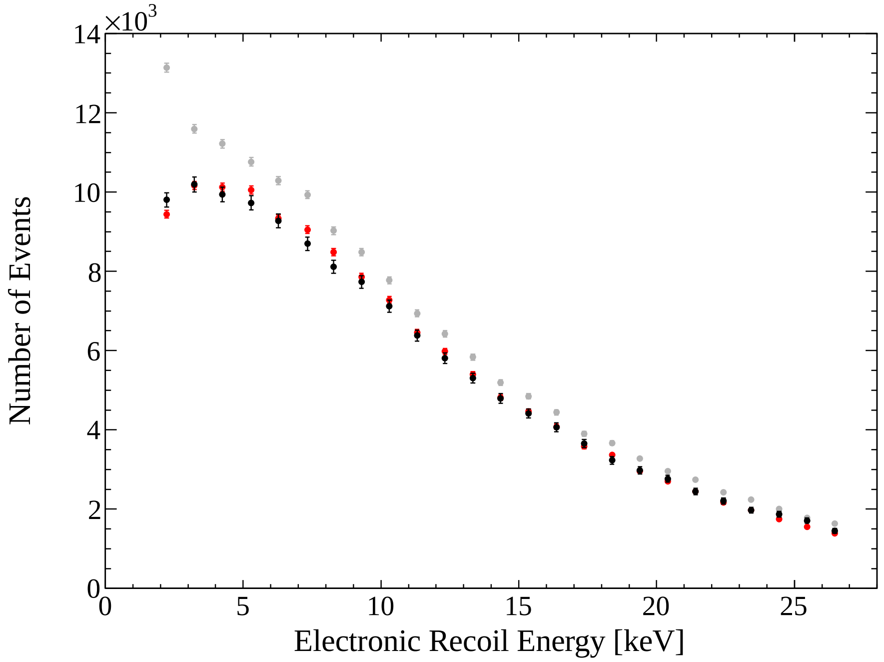

Figure 6.22: Number of events comparison between data and GEANT4 Monte Carlo simulation with live time scaling on the simulation from 10 to 20 keV, a recoil energy region virtually free of background, for the 0° compton coincidence setup. The number of events was computed with 1 keV interval HPGe energy selections as used in the analysis. The simulation (red) was performed without taking into account accidental coincidence events. The data spectra were fitted with with exponential background and "scaled" continuous Poisson signal functions as shown in Fig. 6.15. Gray dots indicate the numbers of events for total spectra and the black dots are inferred from "scaled" continuous Poisson signal functions. As shown in the figure, Monte Carlo prediction (red) on the signal agrees well with that from the data fit (black) and hence, the background subtraction scaling factor was obtained individually for 2.2 keV, 3.2 keV, and 4.2 keV from the difference between gray dots and red dots. The results were used for the uncertainty computation due to background subtraction at recoil energies below 5 keV.

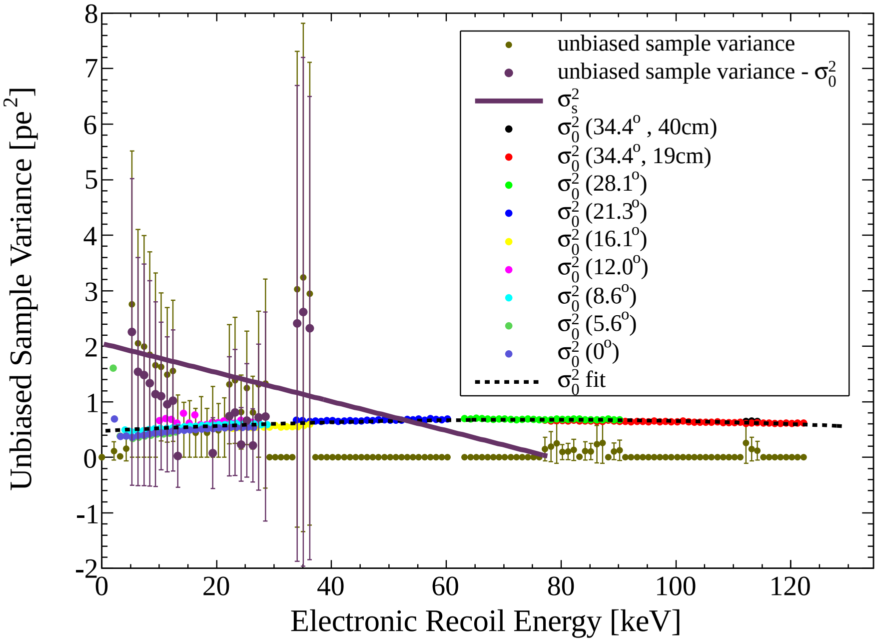

Figure 6.23: Modeling of uncertainty with unknown origin using unbiased sample variance. Sum of uncertainties with known origins ($\sigma_0{}^2$) for each angle measurement are shown as indicated in the legend in the figure along with its fit with the third order polynomial function (dashed black line). The large $\sigma_0{}^2$ at 2 keV for the 5.6° coincidence setup is attributed to large statistical uncertainty. Unbiased sample variance (dark yellow dots) with the subtraction of $\sigma_0{}^2$ (dark purple dots) was used to model the uncertainty contribution due to unknown origin (dark purple line). For the energy ranges with only one angle measurement exists, the unbiased sample variance values were set to 0. It was described as a linearly decreasing function with electronic recoil energy. The significantly large values in unbiased sample at ~ 35 keV are due to systematically low $\mathcal{R}_e$ for the 16.1° measurement (see Fig. 6.24).

high energies (above 80 keV), but for the lowest recoil energies it shows a significantly higher contribution. It is especially pronounced at ~ 35 keV, due to the systematically low $\mathcal{R}_e$ for the 16.1° measurement (see Fig. 6.24).

Tab. 6.6 lists all the uncertainty contributions for each angle measurement and each energy selection. For electronic recoil energies below 53 keV, the largest contribution to the uncertainty comes from the unbiased sample variance. The next largest contribution to the uncertainty at those energies comes from the uncertainty in the PMT gains (3 %), which is the same for all measurements. At 2 keV, the contribution from the statistical uncertainty (2.8 %) and those of the background subtraction (0.8 %) and HPGe detector calibration (0.6 %) are next in size. At recoil energies above 53 keV, the contribution from the PMT gains dominates while the contributions from other effects are negligible.

Table 6.6: Uncertainty contribution for all the measurements with 1 keV E_{HPGe} energy selection. $\frac{\partial \mathcal{R}_e}{\partial g}\sigma_g$ is defined as $\left(\sum_i \left(\frac{\partial \mathcal{R}_e}{\partial g_i}\right)^2 \sigma_{g_i}^2\right)^{\frac{1}{2}}$. $\frac{\Delta \mathcal{R}_e}{\Delta b}\sigma_b$ for the measurements below 5 keV is composed of two components, the difference obtained from the variation of the background scaling factor (a) and the difference between the mean values obtained with and without background subtraction (b), see the text for details.

θ_{HPGe}	E_{er} (keV)	$\sigma_{\mathcal{R}_e,\mathrm{fit}}$	$\frac{\partial \mathcal{R}_e}{\partial g}\sigma_g$	$\frac{\Delta \mathcal{R}_e}{\Delta C_{\mathrm{HPGe}}}\sigma_{C_{\mathrm{HPGe}}}$	$\frac{\Delta \mathcal{R}_e}{\Delta b}\sigma_b$ (a,b)	$\sigma_{\mathcal{R}_e,\mathrm{s}}$	$\sigma_{\mathcal{R}_e}$
0°	2.2	2.8	3.0	0.6	0.1, 0.8	7.1	8.3
0°	3.2	1.0	3.0	0.3	<0.1, 0.3	7.2	7.9
0°	4.3	0.7	3.0	0.2	<0.1, 0.2	6.9	7.5
0°	5.3	0.5	3.0	0.2	0	7.0	7.6
0°	6.3	0.4	3.0	0.1	0	6.6	7.2
0°	7.3	0.4	3.0	0.2	0	6.5	7.1
0°	8.3	0.4	3.0	0.1	0	6.2	6.9
0°	9.3	0.3	3.0	0.1	0	6.1	6.8
0°	10.3	0.3	3.0	<0.1	0	6.0	6.7
0°	11.3	0.3	3.0	0.2	0	5.8	6.5
0°	12.3	0.3	3.0	0.1	0	5.7	6.4
0°	13.3	0.3	3.0	0.1	0	5.6	6.3

Table 6.6 – Continued

θ_{HPGe}	E_{er} (keV)	$\sigma_{\mathcal{R}_e,\mathrm{fit}}$	$\frac{\partial\mathcal{R}_e}{\partial g}\sigma_g$	$\frac{\Delta\mathcal{R}_e}{\Delta C_{\mathrm{HPGe}}}\sigma_{C_{\mathrm{HPGe}}}$	$\frac{\Delta\mathcal{R}_e}{\Delta b}\sigma_b$ (a,b)	$\sigma_{\mathcal{R}_e,\mathrm{s}}$	$\sigma_{\mathcal{R}_e}$
0°	14.3	0.3	3.0	0.1	0	5.5	6.3
0°	15.4	0.3	3.0	0.1	0	5.4	6.2
0°	16.4	0.3	3.0	< 0.1	0	5.3	6.1
0°	17.4	0.3	3.0	0.1	0	5.3	6.0
0°	18.4	0.3	3.0	0.1	0	5.2	6.0
0°	19.4	0.3	3.0	0.1	0	5.2	5.9
0°	20.4	0.3	3.0	0.1	0	5.0	5.9
0°	21.4	0.3	3.0	< 0.1	0	5.0	5.8
0°	22.4	0.4	3.0	0.1	0	4.9	5.8
0°	23.4	0.4	3.0	< 0.1	0	4.9	5.7
0°	24.4	0.4	3.0	0.1	0	4.8	5.7
0°	25.5	0.4	3.0	0.1	0	4.8	5.6
0°	26.5	0.4	3.0	< 0.1	0	4.7	5.6
5.6°	2.0	5.0	3.0	2.2	0.1, 0.8	7.0	9.4
5.6°	3.2	1.2	3.0	0.3	< 0.1, 0.3	7.3	8.0
5.6°	4.3	0.8	3.0	0.7	< 0.1, 0.2	7.1	7.8
5.6°	5.4	0.7	3.0	0.3	0	7.2	7.8
5.6°	6.5	0.6	3.0	0.3	0	6.9	7.6
5.6°	7.5	0.6	3.0	0.3	0	6.7	7.4
5.6°	8.5	0.6	3.0	0.2	0	6.5	7.1
5.6°	9.6	0.6	3.0	0.2	0	6.3	7.0
5.6°	10.7	0.6	3.0	< 0.1	0	6.2	6.9
5.6°	11.8	0.7	3.0	0.2	0	6.1	6.9
5.6°	12.9	0.9	3.0	0.5	0	6.0	6.8
8.6°	5.1	0.6	3.0	0.4	0	6.2	6.9
8.6°	6.2	0.5	3.0	0.6	0	6.1	6.8
8.6°	7.2	0.4	3.0	0.4	0	5.9	6.7
8.6°	8.2	0.4	3.0	0.3	0	5.8	6.5

Table 6.6 – Continued

θ_{HPGe}	E_{er} (keV)	$\sigma_{\mathcal{R}_e,\mathrm{fit}}$	$\frac{\partial\mathcal{R}_e}{\partial g}\sigma_g$	$\frac{\Delta\mathcal{R}_e}{\Delta C_{\mathrm{HPGe}}}\sigma_{C_{\mathrm{HPGe}}}$	$\frac{\Delta\mathcal{R}_e}{\Delta b}\sigma_b$ (a,b)	$\sigma_{\mathcal{R}_e,\mathrm{s}}$	$\sigma_{\mathcal{R}_e}$
8.6°	9.2	0.3	3.0	0.4	0	5.6	6.4
8.6°	10.2	0.3	3.0	0.2	0	5.5	6.3
8.6°	11.3	0.3	3.0	0.2	0	5.5	6.2
8.6°	12.3	0.3	3.0	0.1	0	5.4	6.2
8.6°	13.3	0.3	3.0	0.2	0	5.3	6.0
8.6°	14.3	0.3	3.0	0.2	0	5.2	6.0
8.6°	15.4	0.3	3.0	0.2	0	5.1	5.9
8.6°	16.4	0.3	3.0	< 0.1	0	5.1	5.9
8.6°	17.4	0.3	3.0	0.2	0	5.0	5.8
8.6°	18.4	0.3	3.0	0.1	0	4.9	5.7
8.6°	19.4	0.3	3.0	0.1	0	4.8	5.7
8.6°	20.4	0.3	3.0	0.2	0	4.8	5.6
8.6°	21.4	0.3	3.0	0.1	0	4.7	5.6
8.6°	22.4	0.4	3.0	0.2	0	4.7	5.5
8.6°	23.4	0.4	3.0	0.1	0	4.6	5.5
8.6°	24.4	0.5	3.0	0.1	0	4.6	5.5
8.6°	25.5	0.5	3.0	< 0.1	0	4.6	5.5
8.6°	26.5	0.5	3.0	0.1	0	4.5	5.4
8.6°	27.8	0.5	3.0	0.1	0	4.5	5.4
8.6°	28.8	0.5	3.0	0.1	0	4.4	5.4
12.0°	10.0	1.3	3.0	1.1	0	5.6	6.6
12.0°	11.1	1.3	3.0	1.4	0	5.6	6.6
12.0°	12.1	1.3	3.0	1.1	0	5.5	6.4
12.0°	13.1	1.2	3.0	0.8	0	5.5	6.4
12.0°	14.2	1.1	3.0	1.9	0	5.3	6.5
12.0°	15.2	1.0	3.0	0.9	0	5.3	6.2
12.0°	16.2	1.0	3.0	1.6	0	5.2	6.2
12.0°	17.2	0.8	3.0	0.3	0	5.1	6.0

Table 6.6 – Continued

θ_{HPGe}	E_{er} (keV)	$\sigma_{\mathcal{R}_e,\mathrm{fit}}$	$\frac{\partial \mathcal{R}_e}{\partial g}\sigma_g$	$\frac{\Delta \mathcal{R}_e}{\Delta C_{\mathrm{HPGe}}}\sigma_{C_{\mathrm{HPGe}}}$	$\frac{\Delta \mathcal{R}_e}{\Delta b}\sigma_b$ (a,b)	$\sigma_{\mathcal{R}_e,\mathrm{s}}$	$\sigma_{\mathcal{R}_e}$
12.0°	18.2	0.6	3.0	0.6	0	5.1	5.9
12.0°	19.2	0.8	3.0	0.5	0	4.9	5.8
12.0°	20.2	0.7	3.0	0.5	0	4.8	5.7
12.0°	21.2	0.9	3.0	0.8	0	4.8	5.7
12.0°	22.2	0.7	3.0	0.8	0	4.8	5.7
12.0°	23.2	0.8	3.0	0.2	0	4.7	5.6
12.0°	24.2	0.8	3.0	0.9	0	4.7	5.7
12.0°	25.2	0.8	3.0	0.2	0	4.6	5.5
12.0°	26.2	0.8	3.0	0.5	0	4.5	5.5
12.0°	27.2	0.7	3.0	0.7	0	4.4	5.4
16.1°	21.8	1.0	3.0	0.2	0	5.2	6.1
16.1°	22.8	0.8	3.0	0.3	0	5.1	6.0
16.1°	24.0	0.8	3.0	0.2	0	5.0	5.9
16.1°	25.0	0.9	3.0	0.7	0	5.1	6.0
16.1°	25.9	0.7	3.0	0.2	0	4.9	5.7
16.1°	27.0	0.8	3.0	0.3	0	4.8	5.7
16.1°	28.2	0.8	3.0	0.1	0	4.8	5.7
16.1°	29.2	0.8	3.0	0.1	0	4.7	5.6
16.1°	30.2	0.7	3.0	0.7	0	4.6	5.6
16.1°	31.2	0.8	3.0	0.4	0	4.6	5.6
16.1°	32.2	0.8	3.0	0.2	0	4.5	5.5
16.1°	33.2	0.6	3.0	0.4	0	4.5	5.4
16.1°	34.2	0.6	3.0	0.2	0	4.4	5.3
16.1°	35.2	0.8	3.0	0.4	0	4.3	5.3
16.1°	36.2	1.1	3.0	0.4	0	4.3	5.4
21.3°	33.9	0.6	3.0	0.3	0	3.9	5.0
21.3°	34.9	0.6	3.0	0.1	0	3.9	5.0
21.3°	36.2	0.5	3.0	0.1	0	3.9	4.9

Table 6.6 – Continued

θ_{HPGe}	E_{er} (keV)	$\sigma_{\mathcal{R}_e,\mathrm{fit}}$	$\frac{\partial\mathcal{R}_e}{\partial g}\sigma_g$	$\frac{\Delta\mathcal{R}_e}{\Delta C_{\mathrm{HPGe}}}\sigma_{C_{\mathrm{HPGe}}}$	$\frac{\Delta\mathcal{R}_e}{\Delta b}\sigma_b$ (a,b)	$\sigma_{\mathcal{R}_e,\mathrm{s}}$	$\sigma_{\mathcal{R}_e}$
21.3°	37.2	0.5	3.0	0.4	0	3.9	4.9
21.3°	38.2	0.4	3.0	0.2	0	3.8	4.8
21.3°	39.2	0.4	3.0	0.1	0	3.7	4.8
21.3°	40.2	0.5	3.0	0.2	0	3.7	4.8
21.3°	41.2	0.4	3.0	0.2	0	3.7	4.7
21.3°	42.2	0.5	3.0	0.1	0	3.6	4.7
21.3°	43.2	0.4	3.0	0.3	0	3.5	4.6
21.3°	44.2	0.4	3.0	0.1	0	3.5	4.6
21.3°	45.2	0.4	3.0	0.1	0	3.4	4.6
21.3°	46.2	0.4	3.0	0.3	0	3.4	4.5
21.3°	47.2	0.4	3.0	0.1	0	3.3	4.5
21.3°	48.2	0.4	3.0	0.3	0	3.2	4.4
21.3°	49.2	0.4	3.0	0.1	0	3.2	4.4
21.3°	50.2	0.3	3.0	0.1	0	3.1	4.3
21.3°	51.2	0.4	3.0	0.1	0	3.1	4.3
21.3°	52.2	0.4	3.0	0.3	0	3.0	4.3
21.3°	53.2	0.4	3.0	0.1	0	2.9	4.2
21.3°	54.2	0.5	3.0	0.1	0	2.9	4.2
21.3°	55.2	0.4	3.0	0.2	0	2.8	4.1
21.3°	56.2	0.4	3.0	0.1	0	2.8	4.1
21.3°	57.2	0.4	3.0	0.2	0	2.7	4.0
21.3°	58.2	0.4	3.0	0.1	0	2.6	4.0
21.3°	59.2	0.4	3.0	0.1	0	2.6	3.9
21.3°	60.2	0.5	3.0	0.1	0	2.5	3.9
28.1°	63.2	0.6	3.0	0.4	0	2.3	3.8
28.1°	64.2	0.6	3.0	0.3	0	2.2	3.8
28.1°	65.2	0.7	3.0	0.3	0	2.1	3.7
28.1°	66.2	0.5	3.0	0.4	0	2.1	3.7

Table 6.6 – Continued

θ_{HPGe}	E_{er} (keV)	$\sigma_{\mathcal{R}_e,\mathrm{fit}}$	$\frac{\partial\mathcal{R}_e}{\partial g}\sigma_g$	$\frac{\Delta\mathcal{R}_e}{\Delta C_{\mathrm{HPGe}}}\sigma_{C_{\mathrm{HPGe}}}$	$\frac{\Delta\mathcal{R}_e}{\Delta b}\sigma_b$ (a,b)	$\sigma_{\mathcal{R}_e,\mathrm{s}}$	$\sigma_{\mathcal{R}_e}$
28.1°	67.2	0.5	3.0	0.1	0	2.0	3.6
28.1°	68.2	0.5	3.0	0.1	0	1.9	3.5
28.1°	69.2	0.4	3.0	0.1	0	1.8	3.5
28.1°	70.2	0.4	3.0	0.4	0	1.7	3.5
28.1°	71.2	0.4	3.0	0.1	0	1.6	3.4
28.1°	72.2	0.3	3.0	0.1	0	1.5	3.3
28.1°	73.2	0.4	3.0	0.1	0	1.3	3.3
28.1°	74.2	0.4	3.0	0.2	0	1.2	3.2
28.1°	75.2	0.4	3.0	0.1	0	1.1	3.2
28.1°	76.2	0.4	3.0	0.2	0	0.9	3.1
28.1°	77.2	0.4	3.0	0.1	0	0.7	3.1
28.1°	78.2	0.3	3.0	0.1	0	0.3	3.0
28.1°	79.2	0.4	3.0	0.2	0	0	3.0
28.1°	80.2	0.4	3.0	0.2	0	0	3.0
28.1°	81.2	0.4	3.0	0.3	0	0	3.0
28.1°	82.2	0.3	3.0	0.4	0	0	3.0
28.1°	83.2	0.5	3.0	0.4	0	0	3.0
28.1°	84.2	0.4	3.0	0.1	0	0	3.0
28.1°	85.2	0.4	3.0	0.3	0	0	3.0
28.1°	86.2	0.4	3.0	0.1	0	0	3.0
28.1°	87.2	0.3	3.0	0.2	0	0	3.0
28.1°	88.2	0.4	3.0	0.4	0	0	3.0
28.1°	89.2	0.3	3.0	0.1	0	0	3.0
28.1°	90.2	0.4	3.0	0.3	0	0	3.0
34.4° (19cm)	77.2	0.5	3.0	0.3	0	0.7	3.1
34.4° (19cm)	78.2	0.4	3.0	0.3	0	0	3.0
34.4° (19cm)	79.2	0.4	3.0	0.2	0	0	3.0
34.4° (19cm)	80.2	0.4	3.0	0.2	0	0	3.0

Table 6.6 – Continued

θ_{HPGe}	E_{er} (keV)	$\sigma_{\mathcal{R}_e,\mathrm{fit}}$	$\frac{\partial\mathcal{R}_e}{\partial g}\sigma_g$	$\frac{\Delta\mathcal{R}_e}{\Delta C_{\mathrm{HPGe}}}\sigma_{C_{\mathrm{HPGe}}}$	$\frac{\Delta\mathcal{R}_e}{\Delta b}\sigma_b$ (a,b)	$\sigma_{\mathcal{R}_e,\mathrm{s}}$	$\sigma_{\mathcal{R}_e}$
34.4° (19cm)	81.2	0.3	3.0	0.1	0	0	3.0
34.4° (19cm)	82.2	0.3	3.0	0.5	0	0	3.0
34.4° (19cm)	83.2	0.3	3.0	0.1	0	0	3.0
34.4° (19cm)	84.2	0.4	3.0	0.2	0	0	3.0
34.4° (19cm)	85.2	0.3	3.0	0.2	0	0	3.0
34.4° (19cm)	86.2	0.4	3.0	0.3	0	0	3.0
34.4° (19cm)	87.2	0.4	3.0	< 0.1	0	0	3.0
34.4° (19cm)	88.2	0.3	3.0	0.2	0	0	3.0
34.4° (19cm)	89.2	0.3	3.0	0.1	0	0	3.0
34.4° (19cm)	90.2	0.3	3.0	0.1	0	0	3.0
34.4° (19cm)	91.2	0.3	3.0	< 0.1	0	0	3.0
34.4° (19cm)	92.2	0.4	3.0	0.2	0	0	3.0
34.4° (19cm)	93.2	0.3	3.0	0.3	0	0	3.0
34.4° (19cm)	94.2	0.3	3.0	0.1	0	0	3.0
34.4° (19cm)	95.2	0.3	3.0	0.1	0	0	3.0
34.4° (19cm)	96.2	0.3	3.0	0.3	0	0	3.0
34.4° (19cm)	97.2	0.3	3.0	< 0.1	0	0	3.0
34.4° (19cm)	98.2	0.3	3.0	0.2	0	0	3.0
34.4° (19cm)	99.2	0.3	3.0	0.1	0	0	3.0
34.4° (19cm)	100.2	0.4	3.0	0.2	0	0	3.0
34.4° (19cm)	101.2	0.3	3.0	0.2	0	0	3.0
34.4° (19cm)	102.2	0.3	3.0	0.1	0	0	3.0
34.4° (19cm)	103.2	0.3	3.0	0.1	0	0	3.0
34.4° (19cm)	104.2	0.2	3.0	0.1	0	0	3.0
34.4° (19cm)	105.2	0.3	3.0	0.2	0	0	3.0
34.4° (19cm)	106.2	0.3	3.0	0.1	0	0	3.0
34.4° (19cm)	107.2	0.3	3.0	0.2	0	0	3.0
34.4° (19cm)	108.2	0.3	3.0	< 0.1	0	0	3.0

Table 6.6 – Continued

θ_{HPGe}	E_{er} (keV)	$\sigma_{\mathcal{R}_e,\text{fit}}$	$\frac{\partial \mathcal{R}_e}{\partial g}\sigma_g$	$\frac{\Delta \mathcal{R}_e}{\Delta C_{\text{HPGe}}}\sigma_{C_{\text{HPGe}}}$	$\frac{\Delta \mathcal{R}_e}{\Delta b}\sigma_b$ (a,b)	$\sigma_{\mathcal{R}_e,\text{s}}$	$\sigma_{\mathcal{R}_e}$
34.4° (19cm)	109.2	0.3	3.0	0.1	0	0	3.0
34.4° (19cm)	110.2	0.3	3.0	< 0.1	0	0	3.0
34.4° (19cm)	111.2	0.3	3.0	0.2	0	0	3.0
34.4° (19cm)	112.2	0.3	3.0	0.1	0	0	3.0
34.4° (19cm)	113.2	0.3	3.0	0.1	0	0	3.0
34.4° (19cm)	114.2	0.3	3.0	0.1	0	0	3.0
34.4° (19cm)	115.2	0.3	3.0	0.1	0	0	3.0
34.4° (19cm)	116.2	0.3	3.0	0.1	0	0	3.0
34.4° (19cm)	117.2	0.3	3.0	0.1	0	0	3.0
34.4° (19cm)	118.2	0.3	3.0	0.1	0	0	3.0
34.4° (19cm)	119.2	0.3	3.0	0.1	0	0	3.0
34.4° (19cm)	120.2	0.3	3.0	0.1	0	0	3.0
34.4° (19cm)	121.2	0.3	3.0	0.2	0	0	3.0
34.4° (19cm)	122.2	0.3	3.0	0.1	0	0	3.0
34.4° (40cm)	112.2	0.4	3.0	0.1	0	0	3.0
34.4° (40cm)	113.2	0.4	3.0	0.3	0	0	3.0
34.4° (40cm)	114.2	0.4	3.0	0.1	0	0	3.0

6.10.2 Obtain $\mathcal{R}_e$ from Multiple Measurements

When multiple $\mathcal{R}_e$ values were obtained at a given electronic recoil energy from different Compton coincidence data sets, the results were averaged taking the total uncertainty of each value into account.

Fig. 6.24 shows scintillation yields with their total uncertainties listed in Tab. 6.6, along with the average scintillation yields with 1 keV HPGe energy intervals, after requiring the background contamination in the spectra should be lower than 20 % (see Sec. 6.8). 16.1° measurement exhibits systematically lower scintillation yields compared to the adjacent θ_{HPGe} measurements. The reason of this lower scintillation yields for 16.1° measurement

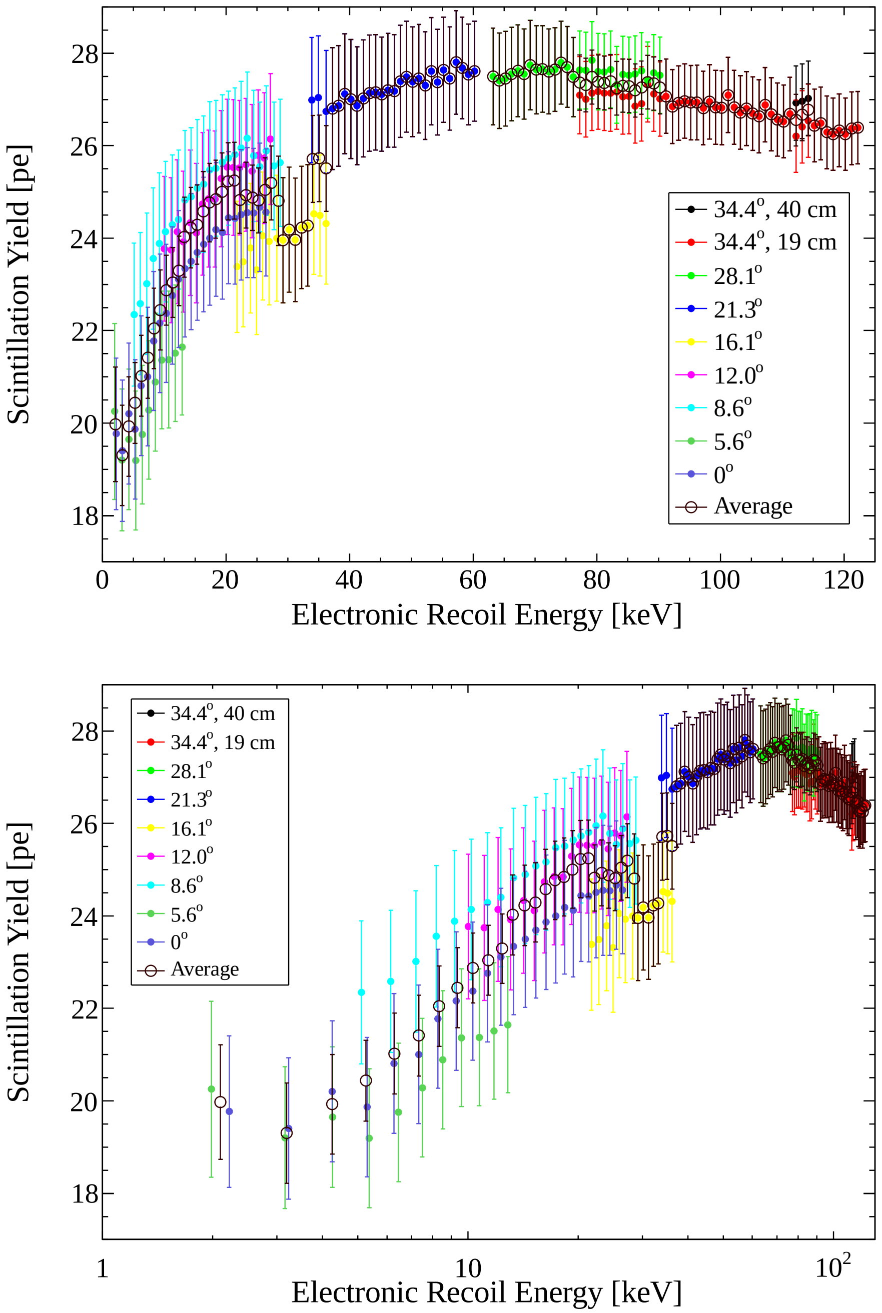

Figure 6.24: Scintillation yields of all the measurements with their total uncertainties listed in Tab. 6.6 (σ_{tot}), along with the average scintillation yields. 16.1° measurement shows systematically lower scintillation yields compared to the adjacent θ_{HPGe} measurements, resulting in a dip in the energy range where only this measurement exists.

is not known. By chance, this energy range is coincide with the K-shell X-ray of LXe (34.6 keV), which photoabsorbed γ-ray cross section varies abruptly but we do not find a reason Compton electrons interact preferentially to K-shell electron of LXe. We rather think this is due to the systematically lower scintillation yields from the 16.1° measurement and this dip could have been not present if we had multiple measurements in this range. The average scintillation yields and their uncertainties were computed taking into account of scintillation yields and their uncertainties from each measurements in the same E_{HPGe} interval. For the final results shown in Fig. 6.25, the average scintillation yields were averaged over ranges of electronic recoil energies where $\mathcal{R}_e$ did not vary appreciably.

Fig. 6.25 shows the results as a function of electronic recoil energy (solid circles), obtained from the average of Fig. 6.24, along with the measured (open circle, open triangle) and predicted (open squares) relative scintillation yields of the 32.1 and 9.4 keV transitions of ^{83m}Kr. The results are summarized in Tab. 6.7. The predicted relative yields of the two transitions were computed from the Compton coincidence results shown in the figure and the electron energies emitted (Tab. 6.5). The large uncertainty at ~ 30 keV is again due to the systematically low scintillation yields of the 16.1° measurement. One thing to keep in mind is that the electronic recoil energies for ^{83m}Kr transitions do not share the exactly same electronic recoil energies (x-axis) with the results from Compton electrons, but close enough (see Tab. 6.5). As shown in the figure, the measured value of 9.4 keV transition shows significant discrepancy with the predicted value while the measured value of 32.1 keV transition is consistent with the measured value within the uncertainty of Compton coincidence measurement. This is discussed in the following section.

6.11 Discussion

To our knowledge, these results are the first measurements of the scintillation response of LXe to nearly monoenergetic low-energy electrons over a wide range of energies. The Compton coincidence technique allows for the production of electronic recoils which most closely resemble the background of large LXe dark matter detectors, without the need to deconvolve the response for any atomic shell effects present in the case of the response to

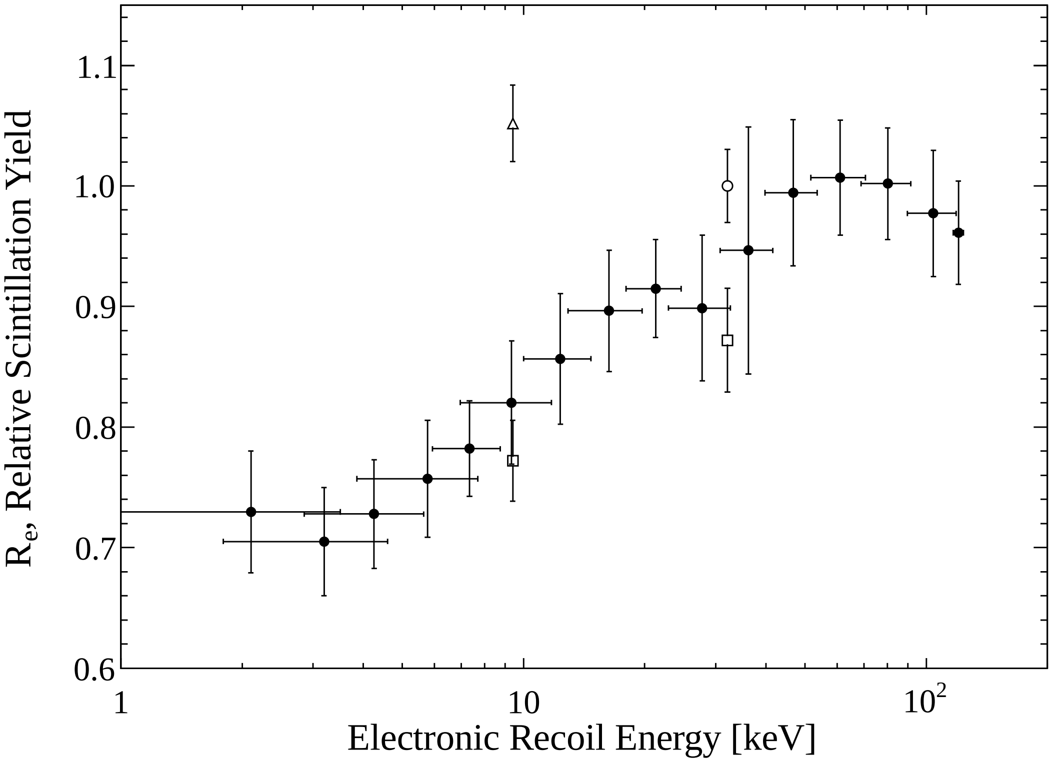

Figure 6.25: Measured values (solid circles) of the relative scintillation yield of electronic recoils, $\mathcal{R}_e$, with respect to the scintillation yield of the 32.1 keV transition of ^{83m}Kr (open circle), along with that of the 9.4 keV transition (open triangle). The predicted relative yield of the two transitions, computed from the Compton coincidence results and the electron energies emitted (Table 6.5) also indicated (open squares). The anomalous scintillation yield of the 9.4 keV transition of ^{83m}Kr, compared to that of an electronic recoil of the same energy, can be understood by the transient state of the LXe after the absorption of the electrons emitted in the 32.1 keV transition, as explained in the text. Figure from [Aprile *et al.*, 2012e].

Table 6.7: Values of the relative scintillation yield of electronic recoils at zero field, $\mathcal{R}_e$, together with their uncertainties, obtained from different sets of Compton coincidence measurements, labeled by the scattering angle θ_{HPGe} between the ^{137}Cs source and the center of the LXe and HPGe detectors. Table from [Aprile *et al.*, 2012e].

E_{er} (keV)	Measurements (θ_{HPGe})	$\mathcal{R}_e$
2.1 ± 1.4	0.0°, 5.6°	0.730 ± 0.050
3.2 ± 1.4	0.0°, 5.6°	0.705 ± 0.045
4.3 ± 1.4	0.0°, 5.6°	0.728 ± 0.045
5.8 ± 1.9	0.0°, 5.6°, 8.6°	0.757 ± 0.048
7.3 ± 1.4	0.0°, 5.6°, 8.6°	0.782 ± 0.040
9.3 ± 2.4	0.0°, 5.6°, 8.6°, 12.0°	0.820 ± 0.051
12.3 ± 2.3	0.0°, 5.6°, 8.6°, 12.0°	0.857 ± 0.054
16.3 ± 3.4	0.0°, 5.6°, 8.6°, 12.0°	0.896 ± 0.050
21.3 ± 3.3	0.0°, 8.6°, 12.0°, 16.1°	0.915 ± 0.041
27.8 ± 4.9	0.0°, 8.6°, 12.0°, 16.1°	0.899 ± 0.060
36.2 ± 5.4	16.1°, 21.3°	0.947 ± 0.103
46.7 ± 6.9	21.3°	0.994 ± 0.061
61.1 ± 9.4	21.3°, 28.1°	1.007 ± 0.048
80.2 ± 11.4	21.3°, 28.1°, 34.4°	1.002 ± 0.046
104.2 ± 14.4	28.1°, 34.4°	0.977 ± 0.052
120.2 ± 3.4	34.4°	0.961 ± 0.043

low-energy photoabsorbed γ rays.

Our results suggest that the scintillation yield of electronic recoils at zero field initially increases as the electron energy decreases from 120 to about 60 keV but then decreases by about 30 % from 60 to 2 keV, contrary to the intuition that it should continue to increase with ionization density. This odd behavior is expected, however, since the electron-ion recombination probability has been shown to become independent of the ionization density for low-energy electronic recoils [Dahl, 2009]. For electronic recoil track sizes smaller than the electron thermalization length in LXe, an increase in ionization density is not accompanied by an increase in recombination probability as ionization electrons thermalize in a volume larger than that of the track. In fact, the energy at which the turnover is observed in our measurement corresponds very closely to the energy at which the average electronic recoil track size calculated in [Dahl, 2009] reaches 4.6 μm, the estimated value for the electron thermalization length in LXe [Mozumder, 1995]. This length scale is also used in the NEST model [Szydagis *et al.*, 2011] to bridge the low- and high-energy regime recombination models. At zero field, these electrons either recombine at much longer time scales [Kubota *et al.*, 1978b; Kubota *et al.*, 1979; Doke *et al.*, 1988], attach to impurities, or eventually leave the active volume of the detector, in all cases contributing to a reduction in the amount of scintillation light from recombination.

The scintillation yield obtained from the Compton coincidence measurement is compatible with the measured yield of the 32.1 keV transition of ^{83m}Kr, in which the bulk of the energy released, as described in Sec. 6.9.2, is most often (75 %) carried by a 30 keV internal conversion electron. The scintillation yield of the 9.4 keV transition of ^{83m}Kr, however, is not compatible with the value from the Compton coincidence measurement. Assuredly, such a marked disagreement between the two measured values prompted a search for possible unaccounted systematic effects in one or both measurements. A notable difference between an energetic electron produced in the LXe detector by a γ-ray Compton scatter and a conversion electron from the 9.4 keV transition is that the latter is produced a very short time, 220 ns on average, after another energetic electron transferred its energy to the LXe. On that time scale, electrons and positive ions from the track of the 32.1 keV transition conversion electron which have not recombined might still populate the immediate vicinity of the Kr atom. In the context of the Thomas-Imel model [Thomas and Imel, 1987], in which recombination depends on the number of Xe ions, and not on ionization density, the enhancement in the scintillation yield could be understood as being due to the effective increase in number of ions left over from the previous interaction. The fact that the predicted relative yields of the two transitions (Fig. 6.25, open squares), computed from the Compton coincidence results and the electron energies emitted (Tab. 6.5) are both lower than the measurements, is also consistent with the above interpretation. That is, subsequent deexcitations in the cascade have enhanced scintillation yields, compared to those of isolated recoiling electrons of the same energy, since they occur very close in time and in the immediate vicinity of previous tracks.

If the scintillation yield of the 9.4 keV transition of ^{83m}Kr were to decrease with an increasing time difference between the two transitions, this would provide a strong indication that the transient state of the LXe is responsible for the anomalously high scintillation yield of the 9.4 keV transition, compared to that measured for Compton electrons of a similar energy. Fig. 6.26 shows the measured scintillation yields for both transitions as a function of the time difference between the two scintillation signals. The scintillation yield of the first transition (32.1 keV) shows no time dependence while that of the second transition (9.4 keV) exhibits a decrease of 12 % from time differences of 300−900 ns. This raises doubts on the suitability of ^{83m}Kr as a calibration source in LXe at 9.4 keV, at least at zero electric field.

The efficiency of the data processing software in separating scintillation signals, which themselves have decay times on the order of 45 ns [Hitachi *et al.*, 1983] at zero field, from two energy deposits very close in time, such as the two transitions of ^{83m}Kr, necessarily implies a loss in detection efficiency at short time differences. This efficiency loss, likely different for measurements from different groups, coupled to a time-dependent decrease in the scintillation yield of the 9.4 keV transition, could explain the discrepancy between the ratio of scintillation yields of the 9.4 keV and 32.1 keV transition of ^{83m}Kr of this work and the one in [Kastens *et al.*, 2009], a quantity which one would otherwise expect to be virtually free of most systematic effects.

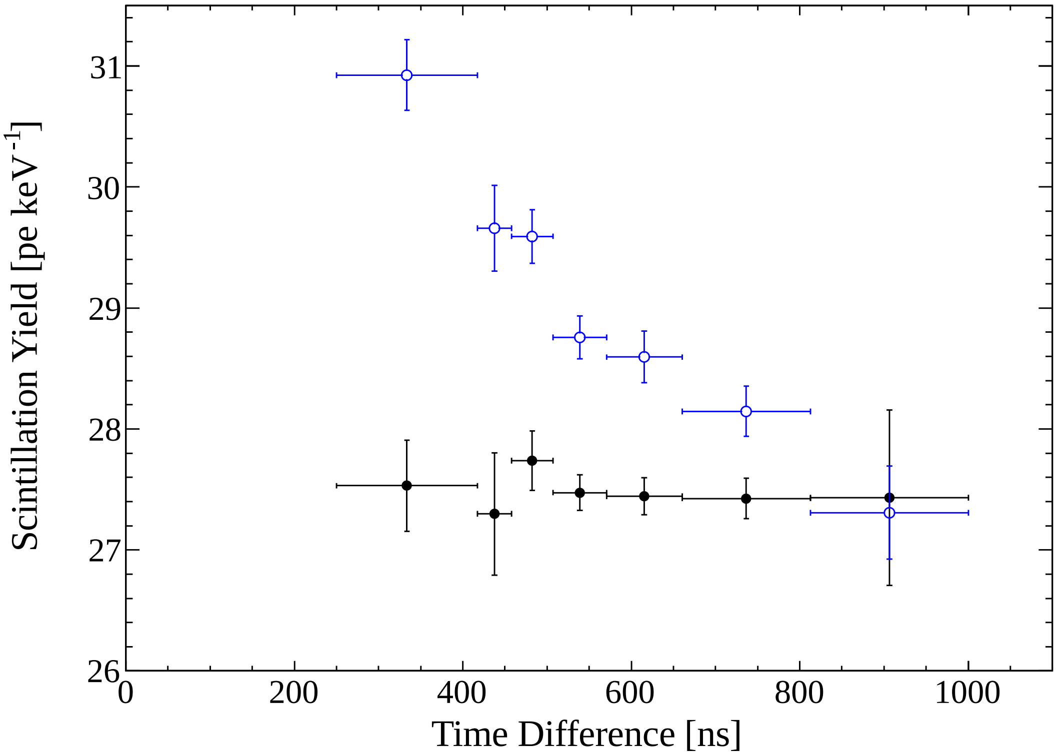

Figure 6.26: Scintillation yields of the 9.4 keV (open blue circles) and 32.1 keV (solid black circles) transitions of ^{83m}Kr as functions of the time difference between the two scintillation signals. While the measured yield of the 32.1 keV transition is constant with increasing time difference, that of the 9.4 keV transition decreases. This is a strong indication that the transient state of the LXe is responsible for the discrepancy observed with respect to the yield measured with the Compton coincidence method at this energy. Figure from [Aprile *et al.*, 2012e].

6.12 Conclusion

We have chosen to report relative instead of absolute yields to eliminate systematic uncertainties in the total light detection efficiency of the LXe detector from the measurement. The precise reason for the very high absolute light yield obtained is not known, although two very likely effects are a temperature dependence of the QE of the PMTs for LXe scintillation light [Aprile *et al.*, 2012d], and a change in the effective QE of the PMTs as a function of the angle of an incident photon [Hamamatsu Photonics K.K., 2006], the latter being a much more pronounced effect for a compact detector such as the one used in this measurement. We have chosen to report our results relative to the scintillation yield of the 32.1 keV transition of ^{83m}Kr to minimize the uncertainty from any position dependence in the light detection efficiency.

We have shown that the improved Compton coincidence technique [Choong *et al.*, 2008], with a high energy resolution HPGe detector, can be used to provide a source of electronic recoils with a precise energy and small energy spread ($\sim 1\,\mathrm{keV}$). This technique allows for the measurement of the response of LXe to electrons with energies as low as a few keV, and is only limited by the resolution of the HPGe detector near the Compton scattered γ-ray energy.

Chapter 7

Dark Matter Results from 225 Live Days of XENON100 Data

XENON100 has been taking data since 2009, and the first limits were placed using 11.2 live-days of data from the commissioning phase (`run_07`) [Aprile *et al.*, 2010] and 100.9 live-days of data taken during the first science run, between 2009 and 2010 (`run_08`). Following the published results from 100.9 live-days [Aprile *et al.*, 2011b], which set the most stringent limit for WIMP-nucleon inelastic scattering (even with a higher Kr background than the design goal), a new distillation of the xenon was performed and the detector resumed data taking at the beginning of 2011. The results for this new science data, comprising 224.6 live-days taken over 13 months during 2011 and 2012 (`run_10`), set the most stringent limits on the spin-independent elastic WIMP-nucleon scattering cross section for WIMP masses above $8\,\mathrm{GeV}/c^2$ [Aprile *et al.*, 2012a].

In this chapter, we will discuss the analysis steps for the dark matter science data focusing on the `run_10` results. As mentioned in Sec. 4.4, band calibration is a prerequisite for the dark matter data analysis because the final electronic recoil background rejection is performed in the discrimination parameter vs energy space. Therefore, we will report the studies on the electronic and nuclear recoil bands calibration and science (dark matter) data.

Fig. 7.1 shows a summary of the accumulated science and band calibration data from

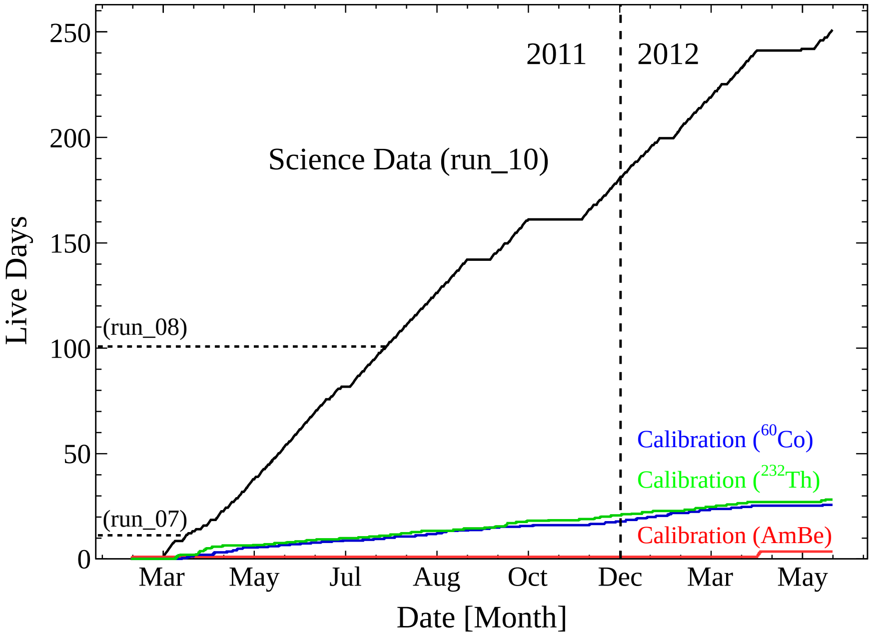

Figure 7.1: Summary of the accumulated science (black) and calibration (blue, green, red) data from `run_10`, along with the amount of science data for the previous runs (parallel dashed lines). The main interruptions of science data taking are attributed to detector maintenance (see Fig. 4.1). Overall, the duty cycle of XENON100 in `run_10` was 81 %. ^{60}Co and ^{232}Th data (48 live-days) are used for the electronic recoil band calibration, to characterize the electronic recoil background. ^{241}AmBe(α, n) data (2.7 live-days) is used for the nuclear recoil band calibration to characterize the WIMP behavior. A significant amount of electronic recoil band calibration data is required to profile the electronic recoil background behavior, especially to estimate the fraction of electronic recoil events that leak into the nuclear recoil band with reliable statistics. Nuclear recoil band calibration was performed before and after the run. The science data taking started about 18 days after the neutron calibration, taking into account the half-lives of activated xenon. The half-lives of activated xenon are relatively short (see Tab. 2.5) and irradiation of the detector with a neutron source is not a problem for the operation of the detector. Credit: XENON100 collaboration.

`run_10`, along with the amount of science data from the previous runs. The total amount of science data for the `run_10` analysis is more than twice of that for `run_08`. In addition, the data taking over 13 months enabled a probe of a full annual cycle. For the electronic recoil band calibration, 35 times more data was accumulated in the energy region of interest, equivalent to ~ 2800 days of electronic recoil background exposure in the fiducial volume (FV) chosen, considering the lower electronic recoil background of this run. Nuclear recoil band calibration was performed before and after the run to avoid activation of the xenon and the detector materials.

One of the most significant improvements of the `run_10` data compared to previous runs is that the energy threshold was lowered thanks to a trigger modification. This has been directly measured using the method described in Sec. 3.9 (also see Fig. 3.17), and leads to virtually no loss of events in the energy region of interest. The S2 threshold was lowered ~ 2 times from 300 to 150 pe. S1 threshold was lowered from 4 to 3 pe ($6.6\,\mathrm{keV_{nr}}$).

Lastly, the higher LXe purity level of `run_10` compared to previous runs reduced the uncertainty in the S2 signal correction (see Fig. 4.1). The maximum correction size is 15 %. The width of the S2 signal is also corrected in (x, y, z) such that it is independent of inhomogeneities in the meshes.

7.1 Analysis

The raw data was processed with the event processing software (see Sec. 3.4.3 of [Plante, 2012] for details). For the (x, y) position reconstruction, a Neural Network algorithm was used. The (x, y) positions calculated from a Support Vector Machine (SVM) and a χ^2 algorithm were used for a consistency check. 3D vertex reconstruction of a particle interaction in the TPC and signal corrections to remove their position dependence were performed for the data analysis, as explained in Sec. 4.1.3 and Sec. 4.1.4, respectively. Data with gas pressure and the liquid temperature variations larger than 0.7 and 0.16 % were excluded from the analysis (see Fig. 3.15). Data with anomalously increased electronic noise or very localized light emission in (x, y) position were excluded as well. This resulted in 224.6 live-days for the final science data. To avoid analysis bias, the science data was blinded from 2 to 100 pe in S1 by keeping only the upper 90 % of the electronic recoil band, equivalent to masking more than 90 % of the signal region.

7.1.1 Event Selection and Acceptance

The energy window for the dark matter analysis of run_10 is 3−30 pe in S1, corresponding to 6.6−43.3 $\mathrm{keV_{nr}}$ from the $\mathcal{L}_{\mathrm{eff}}$ parametrization (see Fig. 4.9). The lower bound is determined by the software threshold to select legitimate S1 pulses free from noise, with reasonable S1 twofold coincidence cut (Xs1coin) acceptance. The upper bound comes from the expectation that the WIMP-induced nuclear recoil spectrum decreases exponentially as the recoil energy increases. Most of the WIMP-induced nuclear recoils are below this upper bound.

The data selection cuts can be divided into several categories: basic quality cuts, single scatter cuts, consistency check cuts, and fiducial volume cut. The cut acceptance of a specific cut, defined as the fraction of events passing the cut under examination, was evaluated to compute the correct exposure, using the energy range and the fiducial volume used for the data analysis. In most cases, the neutron calibration data was used for the computation of the cut acceptance since the nuclear recoils are expected behave like WIMPs. A few exceptions are the ones for which the neutron calibration data do not represent the science data taking condition.

Basic Quality Cuts

The purpose of basic quality cuts is to remove non-physical or noise-like events, mostly at very low energy. The basic quality cuts include the followings: Signal to noise cut (Xsignalnoise), S1 width cut (Xs1width), corrected S2 asymmetry cut (Xlownoise), entropy of the individual S1 signal in each PMT (Xentropy0), removing the events localized in (x, y) using the S2 signal sum of the top PMTs (Xs2top), discrimination parameter cut (Xhighlog), and position of S2 peak cut (Xs2peakpos0).

In addition to the cuts mentioned above, two more cuts belong to basic quality cuts. S1 twofold coincidence cut requires that at least two non-noisy PMTs must register the S1 signal with an individual signal size above 0.35 pe within a ±20 ns time window centered on the highest digitizer sample of the S1 signal (Xs1coin). The lower S2 threshold cut (Xs2peak) requires that the minimum size of the S2 signal must be $> 150\,\mathrm{pe}$, which generates a $> 99\,\%$ trigger efficiency.

Single Scatter Cuts

Because the interaction rate of a WIMP with a target nucleus is expected to be very low, the events of interest for WIMP searches are single scatter events. Ideally, only two peaks would be present in the waveform, one S1 pulse and one S2 pulse. However, in reality, there exist factors which can produce additional true or fake S1 and S2 signals, especially related to very low energy events. Additional S1-like features can arise from PMT dark counts, very small S2 signals due to single electrons, or the real coincident interactions. Additional S2-like features are often attributed to delayed extraction of single electrons or photoionization of impurities.

Single scatter cuts consist of a single S1 cut (Xs1single), a single S2 cut (Xs2single), and a veto coincident cut (Xveto). Xs1single requires that any other S1 peaks in the waveform, besides the main S1 peak with the largest PMT coincidence, must be due to electronic noise or PMT dark counts (i.e., PMT coincidence is one), or due to an unrelated S2 signal. S1 peaks due to unrelated S2 signals can be identified in the waveform with the distance between this S1 peak and the S2 peak beyond the maximum drift length of the TPC, which is unphysical. Another source of event registration with unrelated S2 signal is a coincident interaction on the top of the target volume because of backscattering of high-energy γ rays with the detector materials. The second source is characterized by anomalously high S2/S1 ratio and can be discarded with a cut on the S2/S1 ratio. Therefore, the events with unrelated S2 signal are kept to maintain a high acceptance of low-energy events when it is clear that additional S1 peaks are irrelevant to the S2 peak in the waveform. Xs2single requires that any other S2 peaks in the waveform must be small enough to be consistent with delayed single electron emission. Lastly, Xveto rejects events with a S1 signal in the veto volume larger than $0.35\,\mathrm{pe}$, which is in coincidence with the S1 peak selected in the target volume.

Fiducial Volume Cut

As for the run_08 analysis, a generalized super ellipsoid defined in the r^2-z plane was used for the fiducial volume cut. Its formula is described as,

$$\mathrm{FV}(r, z) = \left|\frac{z - z_0}{a_z}\right|^m + \left|\frac{(r - r_0)^2}{a_{r^2}}\right|^n < 1 \tag{7.1}$$

with $m, n > 0$. The general strategy for the choice of optimum fiducial volume is maximization of the sensitivity given all known backgrounds. In run_08, the intrinsic background from ^{85}Kr was dominating, and is uniformly distributed in the detector. Hence, a larger fiducial volume was a better choice, only limited by the regions near surfaces where the response of the detector is not understood. The fiducial volume mass for run_08 was 48 kg. However, for run_10, background from the detector materials played a major role and an optimum fiducial volume was chosen compromising between WIMP detection sensitivity and WIMP limit sensitivity. The fiducial volume used for run_10 is 34 kg.

Consistency Cuts

Consistency cuts require the events to be consistent with single scatter interactions in various parameters. They also require consistency among the reconstructed positions from different algorithms, and consistency between the reconstructed position and its expectation from Monte Carlo simulations.

The S2 width cut (Xs2width) rejects events whose S2 pulse width is inconsistent with that expected from the proportional scintillation signal of an electron cloud created at the z position and drifted to the liquid surface. S1 PMT pattern likelihood cut (XPL013_97) explained in Sec. 5.4 removes events whose S1 PMT pattern is different from the one obtained with single scatter events using the full absorption peak of low anode ^{137}Cs data. The position reconstruction algorithm cut (Xposrec) removes events with large discrepancies in the reconstructed position from different algorithms. The χ^2 cut on the comparison between reconstructed position and its expectation (Xs2chisquare) removes events with unusually high χ^2 between reconstructed position and its expectation from the Monte Carlo simulation. The details about each cut are explained in [Aprile *et al.*, 2012b]. Table 7.1 summarizes all the cuts used in the run_10 analysis.

Table 7.1: Data selection cuts used in `run_10`. Leading "X" represents a cut and trailing number indicates the version of the cut (with exceptions labeled by $*$).

Name	Description
Xsignalnoise3&4	Selection on signal-to-noise ratio.
Xs1width0	Removes noise-like S1 with selection on S1 pulse width at 10% height.
Xlownoise_m*	Removes noise-like S1 with selection on the ratio of corrected S2 signal difference between the top and bottom PMTs to the total S2 signal.
Xentropy0	Selection on the entropy of S1 waveform.
Xs2top0	Removes unusual event localization in x-y position, requires some part of the S2 signal must be seen by the top PMTs.
Xs2peaks2	Requires S2 signal size larger than 150 pe to maintain $> 99\%$ trigger efficiency.
Xs1coin2	Requires at least 2 PMTs seeing the S1 signal.
Xhighlog1	Removes events showing anomalously high discrimination parameter due to random coincidence between noise-like S1 and S2.
Xs2peakpos0	Removes events whose S2 peak position is not in the center of waveform but is in the first half of the waveform, since the corresponding S1 might be missing.
Xs1single4	Selects events with single S1 pulse.
Xs2single3	Selects events with single S2 pulse.
XVeto2	Removes events with energy deposition in the active veto
XFV34kg	Selects events in the 34 kg FV defined by a generalized super-ellipsoid in the r^2-z plane.
Xs2width8	Selection on the drift time dependence of S2 pulse width, removes unphysical events.
XPL013_97*	Selects events with single-scatter-like S1 PMT pattern.
Xposrec1	Removes events with large discrepancies in the reconstructed position from different algorithms.
Xs2chisquare0	Removes events with unusually high χ^2 in position reconstruction compared to an expectation from Monte Carlo simulations.

Cut Acceptance

Most of the individual cut acceptances were obtained using nuclear recoil calibration data since the events recorded in these data behave in the way expected from WIMPs. However, in some cases a certain feature of the nuclear recoil calibration data is different from that of WIMPs. For example, the number of multiple scatters in the nuclear recoil calibration data is quite large while it is hardly expected from WIMPs. In addition, ^{241}AmBe(α, n) irradiation of the detector was performed for a very short period of time, while dark matter data was taken during the whole year with varying noise conditions. Therefore, cut acceptances of a few cuts related to single scatter selection and noise, such as Xsignalnoise3&4, Xentropy0, Xs2single3, and Xs1single4, were obtained using electronic recoil calibration data or the non-blind part of the science data.

After deciding the kind of data used to evaluate the acceptance of each cut, the next step is to define a WIMP-like data sample. One way is to assume that all events removed by two or more cuts are bad events, but the events failing only one cut are good events. In this approach, we consider that the event sample defined by all the cuts except the one we are looking at constitutes a sample of valid events, and hence the events removed by the test cut are considered to be wrongly removed. The acceptance for that cut in particular is computed by dividing the number of events passing the cut by the total number of events. However, this approach is valid only if all the cuts are orthogonal (i.e., not correlated). Some of the cuts have a correlation with other cuts, e.g., Xsignalnoise and Xentropy, Xchisquare and Xposrec. For these cuts, the cut acceptance was computed excluding the corresponding correlated cut.

Many of the cuts, such as Xs2width and XPL013_097 were constructed to maintain a high acceptance on single scatter nuclear recoils by defining a cut at fixed quantiles in the distributions. Most of the cuts have a moderate energy dependence, less than 5% variations over the energy range considered, and a high acceptance. The only exceptions are Xs1coin and Xs2peak.

While a Monte Carlo simulation was used to compute the Xs1coin acceptance for the analysis of `run_07` and `run_08`, a data driven approach using coincident interactions in the veto was adopted to evaluate Xs1coin acceptance for the `run_10` analysis. The idea is that a coincident interaction in the veto can distinguish a PMT dark count event from a real interaction event. This works since the accidental coincidence rate of interactions in the veto and a dark count peak in the TPC is very small. This new method yields a slightly lower acceptance compared to using the Monte Carlo simulation results, but its impact on the results presented in [Aprile *et al.*, 2010; Aprile *et al.*, 2011b] is negligible.

Xs2peak was mainly responsible for the acceptance loss at low energies for the previous runs, since the variance of the nuclear recoil band is large at low energies. With reduced S2 lower threshold, acceptance loss at low energies due to Xs2peak is far less pronounced in run_10 ($< 5\,\%$ at 3 pe of unsmeared S1). Xs2peaks2 is independent of possible fluctuations in S1 and has to be applied to the S1 spectrum before taking into account the S1 resolution. Therefore, an unsmeared S1 cut acceptance has to be obtained. Xs2peak acceptance is computed with three procedures: First, obtain the correlation between the corrected S1 and S2 signals using the nuclear recoil calibration data. Using a scaled Poisson function similar to the one used in Chap. 6, the low energy spectra of corrected S2 were obtained for different values of S1. Second, using a Monte Carlo simulation integrating the detector response of electron life time and $\mathcal{L}_{\rm eff}$ parametrization, uncorrected S2 spectra were obtained. With the obtained uncorrected S2 spectra, the S1 resolution-smeared S2 cut acceptance was computed, which is equivalent to what we obtain from the data. Last, the simulated AmBe spectrum was converted to unsmeared S1 using $\mathcal{L}_{\rm eff}$ parametrization and convoluted with various trial acceptances, until the acceptance derived from the smeared data agrees with the one observed in the AmBe data.

Applying Xs2peak before smearing of S1 leads to an acceptance which depends on the recoil energy spectrum, and consequently depends on WIMP masses, once converted into the observed S1 signal. It can be understood as follows: the minimum WIMP mass which can be detected with a 3 pe S1 threshold ($6.6\,{\rm keV_{nr}}$) is $\sim 13\,{\rm GeV}/c^2$ with $v_{\rm esc} = 544\,{\rm km/s}$ (see Sec. 1.3.1). Any WIMPs with lower masses can be detected in XENON100 only by their upwards fluctuation in S1. Given the low scintillation photon detection efficiency, ~ 0.0034 pe/photon, fluctuations of the measured S1 signal near threshold are well approximated by Poisson statistics. However, even if the measured S1 signal fluctuates above threshold, the associated S2 signal does not fluctuate above the S2 threshold in general. Although the

S1 signal of low mass WIMPs can fluctuate above threshold, the probability that the S2 signal be above the trigger threshold (Xs2peak) decreases for lower WIMP masses. Fig. 7.2 (bottom) shows the WIMP mass dependence of the cumulative cut acceptance. This figure is for the run_08 analysis with lower S2 threshold of 300 pe. But the same method was used for computing Xs2peak acceptance and that of run_10 shows the same behavior.

The overall cut acceptance was computed as the product of all the individually computed acceptances, besides the fiducial volume cut whose acceptance is taken into account by assigning an uncertainty on the fiducial mass.

Fig. 7.2 (top) shows the combined cut acceptance (solid blue), the lower S2 threshold cut (dashed red), along with and the cut acceptance to nuclear recoils with 99.75 % electronic recoil rejection line for the cross-check with the optimum interval gap method (dotted green) for run_10.

7.1.2 Profile Likelihood Method

A classical way of setting limits in rare events searches depends on the expected background in a pre-defined signal region and on the uncertainty of the prediction. When no background is expected, usually a 90 % confidence upper limit is computed using a Poisson distribution with a mean of the observed number of events. If the background is known with reasonable accuracy, the Feldman-Cousins approach [Feldman and Cousins, 1998] is used for the calculation of the 90 % confidence upper limit. If possibly unknown backgrounds exist, Yellin's optimum interval method [Yellin, 2002] or the maximum-patch method [Henderson *et al.*, 2008] (the latter being a two dimensional generalization of the former) are often used. However, these methods are designed to set upper limits only, unlike the Feldman-Cousin's method. As the possibility of detecting dark matter is rapidly increasing with various experimental efforts, it is natural to transition to a statistical tool which can claim detection. In any case, understanding of the background is essential to any method that is used to quantify the significance of a discovery claim.

The Profile Likelihood (PL) method is a statistical model using the profile likelihood ratio as a test statistic in a frequentist approach. This statistical model can be used to either set an exclusion limit or to quantify a discovery claim. A main distinction from the

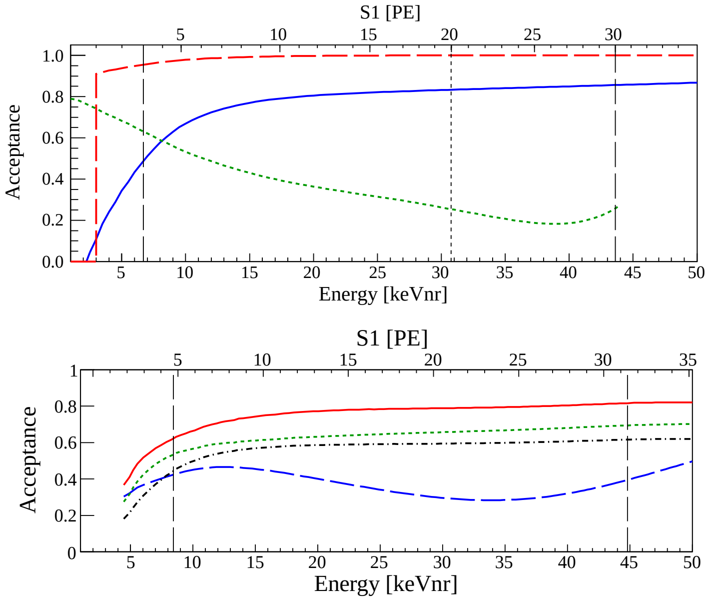

Figure 7.2: Combined cut acceptance (solid blue), the S2 threshold cut S2 $> 150\,$pe (dashed red), and the cut acceptance to nuclear recoils with $99.75\,\%$ electronic recoil rejection line for the cross-check with the optimum interval gap method (dotted green) for run_10 (Top). Since the S2 threshold cut is independent of possible fluctuations in S1, it has to be applied to the S1 spectrum before taking into account the S1 resolution, resulting in a WIMP mass dependent combined cut acceptance. It was conservatively set to 0 at 1 pe. Bottom figure shows WIMP mass dependence of combined cut acceptance for several WIMP masses ($m_\chi \geq 50\,\mathrm{GeV}/c^2$ (solid red), $m_\chi = 10\,\mathrm{GeV}/c^2$ (dotted green), $m_\chi = 7\,\mathrm{GeV}/c^2$ (dash-dotted black)), along with the cut acceptance to nuclear recoils equivalent to the dotted green on top figure (dashed blue). The bottom figure was used for the run_08 analysis, but the WIMP mass dependent cut acceptance behavior is the same as run_10 . Top figure is from [Aprile *et al.*, 2012a] and bottom figure is from [Aprile *et al.*, 2011b].

optimum interval method is that the PL provides a discovery potential. Another significant difference is systematic uncertainties, such as uncertainties in the energy scale and astrophysical uncertainties, are included in the PL method. Therefore, the results are derived with the proper treatment of statistical and systematic uncertainties in contrast to applying hard cuts in a signal acceptance region. Details about the use of PL in the XENON100 data analysis can be found in [Aprile *et al.*, 2011c].

It was decided beforehand to use the PL method to derive the dark matter results. Both signal and background-only hypotheses were tested for exclusion and discovery, respectively. PL avoids the need to *a priori* define the signal acceptance region (benchmark region). Nevertheless, it was defined for the parallel analysis with the optimum interval method to cross check the results, and for a direct comparison of the expected background with the observed events.

7.1.3 Background Prediction

A benchmark WIMP search region to quantify the background expectation and to be used for the optimum interval method was defined from 3 to 20 pe (6.6 to 30.5 $\mathrm{keV_{nr}}$) in S1. The upper 99.75 % electronic recoil rejection line in the discrimination parameter vs S1 space set the upper bound of the benchmark region. The lower bound of the benchmark region was set by the lines corresponding S2 $>$ 150 pe and a lower border running along the 97 % nuclear recoil quantiles (see Fig. 7.3).

The background in the benchmark region has contributions from the statistical leakage and anomalous leakage from electronic recoil background, and neutron-induced nuclear recoils. The statistical leakage events from the electronic recoil background mainly come from the high-energy γ-ray induced Compton electrons, due to the residual radioactive isotopes in the detector materials. Another contribution to the statistical leakage events is attributed to intrinsic radioactive impurities in the LXe, such as ^{85}Kr and ^{222}Rn, as explained in Sec. 4.3.

Anomalous leakage events have a feature of their non-Gaussian distribution in the discrimination parameter. In Chap. 5, we extensively discussed this type of background. However, the prediction of an estimate of anomalous leakage events was not performed us-

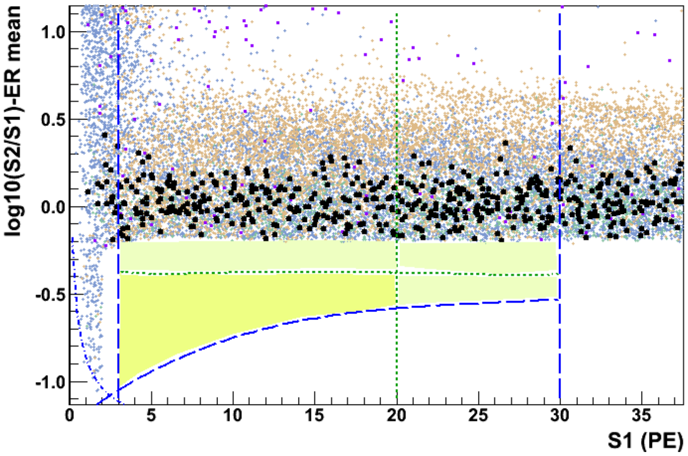

Figure 7.3: A signal acceptance region for the cross check with the optimum interval method (dark yellow), along with energy window for the PL analysis. The discrimination parameter $\log_{10}(\mathsf{S2}_b/\mathsf{S1})$ was flattened by subtracting the electronic recoil mean. Lower and upper analysis energy thresholds of 3 pe (6.6 $\mathrm{keV_{nr}}$) and 30 pe (43.3 $\mathrm{keV_{nr}}$) for the PL analysis are shown as blue vertical dashed lines. The upper analysis energy threshold used for the optimum interval method (and hence the benchmark WIMP search region) is 20 pe (30.5 $\mathrm{keV_{nr}}$), shown as a green vertical dashed line. The lower S2 threshold cut ($\mathsf{S2} > 150$ pe) constitutes the lower bound at lower energies, which hardly impacts above 3 pe. A lower border running along the 97 % nuclear recoil quantiles (dashed blue line) constitutes the lower bound at higher energies. An additional hard cut on the discrimination parameter at 99.75 % electronic recoil rejection defines the upper bound of the benchmark WIMP search region (green quasi-horizontal dashed line). The events in the 48 kg FV removed by the basic quality cuts besides those related to low energy thresholds (blue), the single scatter cuts (green), the low energy threshold cuts (Xs2peaks2 & Xs1coin1, brown), and the consistency cuts (purple) from the 225 live-days of dark matter data are shown as well. Credit: XENON100 collaboration.

ing the simulation model discussed in that chapter due to the non-verification of some of the assumptions on the model without relevant measurements. Therefore, both statistical and anomalous leakage events were computed together using the electronic band calibration data, with the same cuts used for the dark matter results analysis. The calibration data was scaled to the dark matter exposure by normalizing it to the number of events seen above the blinding cut in the energy region of interest. The estimated electronic recoil background including statistical leakage events and anomalous leakage events was (0.79 ± 0.16) in the benchmark region.

The nuclear recoil background was determined from Monte Carlo simulations, using the measured screening results of the detector materials [Aprile *et al.*, 2011d]. The origins of the neutron background integrated in the simulations were $(\alpha$,n) and spontaneous fission reactions, and muons. The muon energy and angular dependence at LNGS were taken into account for the muon-induced neutron background, which constitutes 70 % of the total neutron background. The expectation obtained from the simulation was $(0.17^{+0.12}_{-0.07})$ events for the given exposure and nuclear recoil acceptance in the bench mark region. This leads to a total background expectation of (1.0 ± 0.2) events, with the 34 kg FV and 224.6 live-days of exposure.

The background model for the PL analysis uses the same assumptions and input spectra from Monte Carlo simulation and calibration data. Using the high-energy sideband and the vetoed data with S1 between 3−30 pe, the validity of the background model was confirmed before unblinding.

7.2 Results

As mentioned previously, the science data was blinded to avoid analysis bias. All the calibration data and background data away from the WIMP search region (sideband) were used to optimize the cuts, to determine the acceptance, to fine-tune the WIMP search region, to estimate the background events, and to improve the analysis tools. However, "opening the box" or unblinding the data was allowed only after all the parameters were determined and all the tools were set.

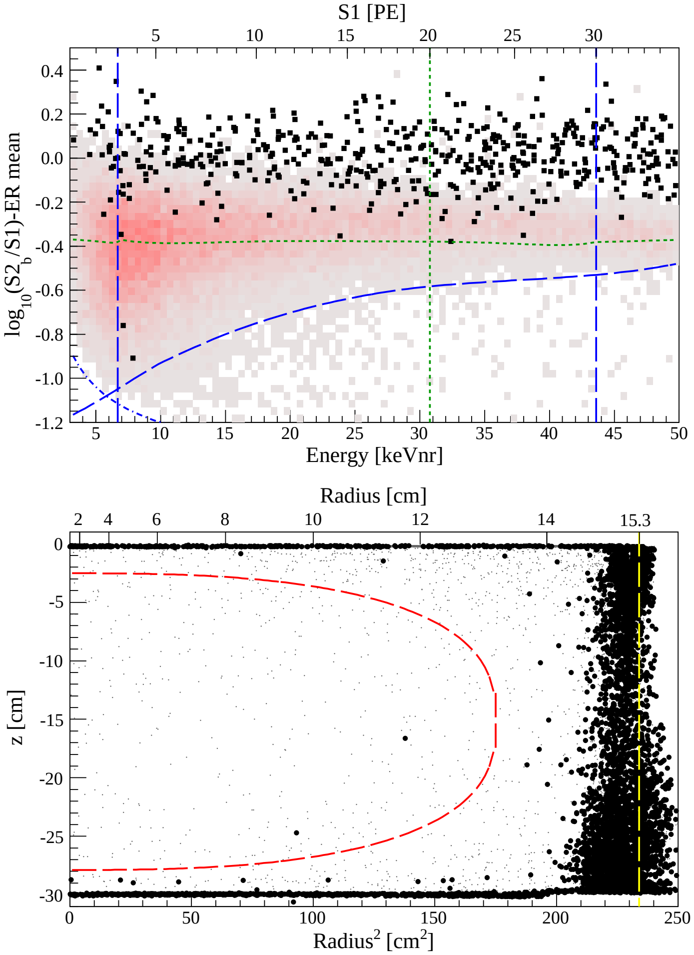

Figure 7.4: Event distribution in the discrimination parameter $\log_{10}(\mathsf{S2}_b/\mathsf{S1})$ vs energy space, flattened by subtracting the electronic recoil mean, after unblinding using all analysis cuts with the 34 kg fiducial volume cut, shown as black dots (top). All the lines are the same as explained in Fig. 7.3. The histogram in red indicates the nuclear recoil band from the neutron calibration. As shown in the figure, two events were found in the benchmark WIMP search region after unblinding, where (1.0 ± 0.2) background events are expected. The spatial distribution of the events inside the TPC with using $6.6-43.3\,\mathrm{keV_{nr}}$ energy window (bottom). The 34 kg FV is shown as red dashed line. Gray points are above the 99.75 % rejection line, black dots fall below the rejection line. Figure from [Aprile *et al.*, 2012a].

224.6 live-days of run_10 science data was unblinded on July 8th, 2012. Fig. 7.4 shows the event distribution in the discrimination parameter vs energy space (top) and the spatial event distribution inside the TPC (bottom) after unblinding. There are no leakage events below 3 pe. Two events were observed in the benchmark WIMP search region. Both fall into the lowest pe bin in the analysis, with energies of 7.1 $\mathrm{keV_{nr}}$ (3.3 pe) and 7.8 $\mathrm{keV_{nr}}$ (3.8 pe). Their S2/S1 value is at the lower edge of the nuclear recoil band from neutron calibration. Fig. 7.5 and Fig. 7.6 show the summed waveform and S2 signal PMT distribution of the two events observed in the benchmark WIMP search region.

The PL analysis yields a p-value of $\geq 5\,\%$ for all WIMP masses for the background-only hypothesis, i.e., no signal excess due to WIMPs. The Poisson probability that the expected background in the benchmark region fluctuates to 2 events or more is 26.4 %, which confirms this conclusion.

A 90 % confidence level exclusion limit for spin-independent WIMP-nucleon cross sections σ_χ was calculated with the following assumptions: an isothermal WIMP halo with a local density of $\rho_\chi = 0.3\,\mathrm{GeV}/c^3$, a local circular velocity of $v_0 = 220\,\mathrm{km/s}$, and a Galactic escape velocity of $v_{\mathrm{esc}} = 544\,\mathrm{km/s}$ [Smith *et al.*, 2007]. Systematic uncertainties in the energy scale, by the $\mathcal{L}_{\mathrm{eff}}$ parametrization described in Sec. 4.2.3, and in the background expectation were profiled out and incorporated into the limit. The S1 energy resolution, governed by the Poisson fluctuations of the photoelectron generation in the PMT, was taken into account. The expected sensitivity in absence of any signal is shown by the green/yellow ($1\sigma/2\sigma$) band in Fig. 7.7. The 90 % confidence upper limit on the spin-independent WIMP-nucleon elastic cross section as a function of WIMP masses is presented as the thick blue line. It excludes a large fraction of previously unexplored parameter space, including the region theoretically favored by constrained minimal supersymmetric standard models (CMSSM) [Strege *et al.*, 2012; Fowlie *et al.*, 2012; Buchmueller *et al.*, 2012].

The results from run_10 science data, set the most stringent limits for $m_\chi > 8\,\mathrm{GeV}/c^2$ with a minimum $\sigma_\chi = 2.0 \times 10^{-45}\,\mathrm{cm}^2$ at a WIMP mass of $m_\chi = 55\,\mathrm{GeV}/c^2$. The results from the optimum interval analysis using an acceptance-corrected exposure of 2323.7 kg × days, weighted with a spectrum of a $m_\chi = 100\,\mathrm{GeV}/c^2$ WIMP, are consistent

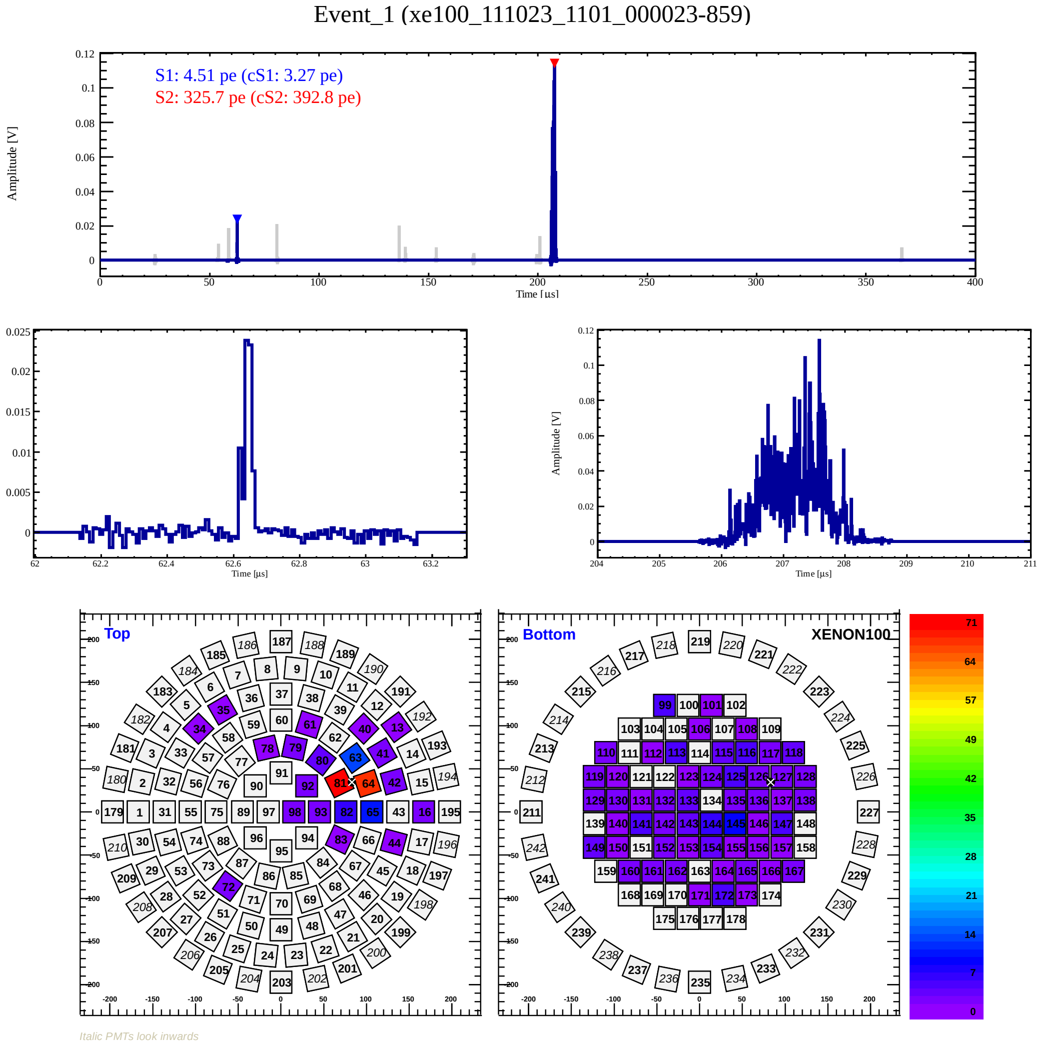

Figure 7.5: Summed waveform, zoom of S1 and S2 (top) of the WIMP candidate event no. 1. S1 and S2 are indicated by blue and red triangles, respectively. Gray peaks represent the signals which only one ADC has been digitized, which correspond to PMT dark counts. These are not considered in the analysis. S2 signal PMT distribution of the same event (bottom). Credit: XENON100 collaboration.

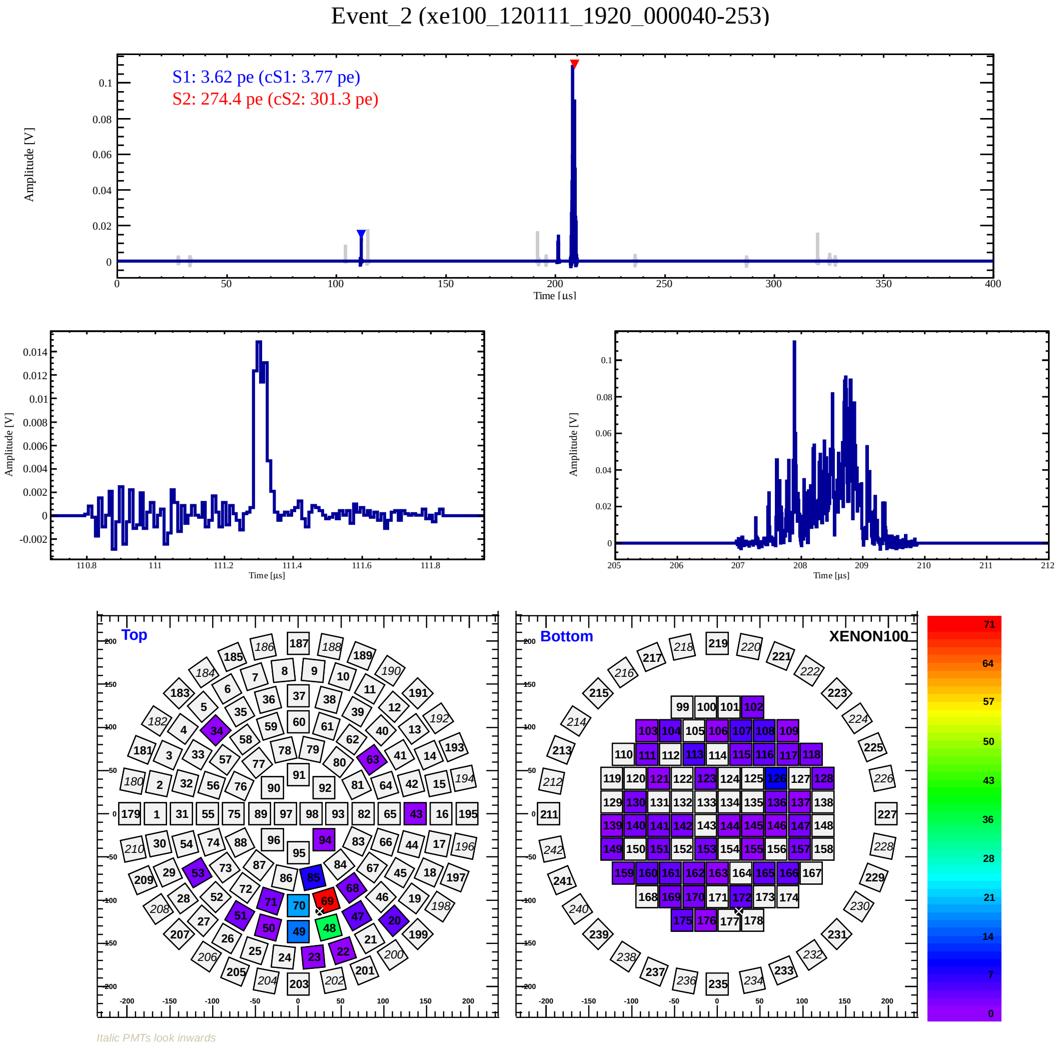

Figure 7.6: Summed waveform (top) and S2 signal PMT distribution (bottom) of the WIMP candidate event no. 2. The small peak around 200 μs before S2 peak is most likely a S2 pulse from a single electron. Credit: XENON100 collaboration.

with the results from Fig. 7.7 within the differences of the methods. The new XENON100 result continues to challenge the interpretation of the DAMA [Savage *et al.*, 2009], CoGeNT [Aalseth *et al.*, 2011], and CRESST-II [Angloher *et al.*, 2012] results as being due to light mass WIMPs.

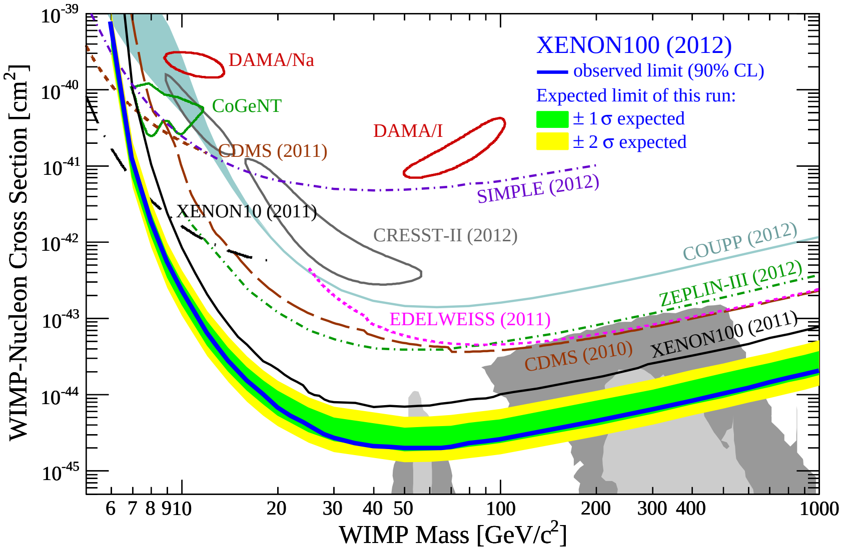

Figure 7.7: 90 % confidence upper limit on the spin-independent WIMP-nucleon elastic cross section (σ_χ) as a function of WIMP masses (m_χ) from the 224.6 live-days of XENON100 data (blue line), along with that from the previous data (black line) [Aprile *et al.*, 2011b]. The expected sensitivity is shown by the green/yellow band ($1\sigma/2\sigma$). Other experimental results from DAMA [Savage *et al.*, 2009], CoGeNT [Aalseth *et al.*, 2011], CRESST-II (2012) [Angloher *et al.*, 2012], CDMS (2010/2011) [Ahmed *et al.*, 2010; Ahmed *et al.*, 2011], EDELWEISS (2011/2012) [Armengaud *et al.*, 2011; Armengaud *et al.*, 2012], XENON10 (2011) [Angle *et al.*, 2011], SIMPLE (2012) [Felizardo *et al.*, 2012], COUPP (2012), [Behnke *et al.*, 2012], and ZEPLIN-III [Akimov *et al.*, 2012] are also shown. The regions ($1\sigma/2\sigma$) favored by supersymmetric models (CMSSM) [Strege *et al.*, 2012; Fowlie *et al.*, 2012; Buchmueller *et al.*, 2012] are shown as gray (light/dark). Figure from [Aprile *et al.*, 2012a].

7.3 Concluding Remarks

In this thesis, we have presented the research carried out in the context of the XENON100 dark matter search experiment. Starting with the motivation of dark matter searches (Chap. 1) and an introduction of LXe as an attractive WIMP detection medium (Chap. 2), we have described the detector design, the detector and its subsystems (Chap. 3), calibration of the detector (Chap. 4), anomalous background events (Chap. 5), details of a measurement of the scintillation yield of low-energy electrons in LXe (Chap. 6), and finally the dark matter exclusion limits (Chap. 7).

A natural next step for the XENON100 experiment is scaling up of the detector with larger target mass, for larger exposure and for greater background suppression. XENON100 itself is a scaled up version of XENON10, which demonstrated that a dual-phase LXe detector provides excellent ability to explore WIMP parameter space. From the experience of scaling up from XENON10 to XENON100, we have accumulated knowledge in building a larger detector. The main challenges that accompany building a large scale detector are purification of LXe, configuration of drift field, and quenched light collection efficiency. The purification of LXe, by removing impurities those attenuate scintillation and ionization signals and radioactive impurities, is critical to allow for observation of small signals and to maintain low background. In addition, a technique to measure very low background would be also required, especially related to ^{85}Kr contamination. As the drift length of the TPC becomes longer, higher electron lifetime is required for S2 signal detection. Certainly, a higher purification rate of LXe would be necessary to purify LXe at the desired level for a larger detector. Another thing that comes with a longer drift length is higher voltage to maintain the same drift field strength, which is difficult to achieve. Lastly, as the detector size becomes larger, the scintillation photon collection efficiency becomes lower. Simulations would be required before the detector design is finalized to find the maximum light collection efficiency configuration. The light collection efficiency is also related to the transparencies of the meshes, which is relevant to drift field configuration. Increasing optical transparency of a mesh helps to achieve higher light collection efficiency but causes more electric field leakage through the mesh. This electric field leakage needs to be corrected later and its effect would be more pronounced with higher drift field. Hence, the simulations of both light collection efficiency and electric field would be necessary for the final design of the detector. In addition, calibration of the detector with external radioactive sources would be more difficult as the detector size becomes larger. Spatially uniform calibration of the detector by using a gaseous source with short life-time such as ^{83m}Kr would be helpful to solve this problem. In case of using ^{83m}Kr, it can be removed by a Kr column, part of the detector subsystem.

Besides building a large-scale detector, measurements of the signal responses of LXe to both nuclear and electronic recoils with a dedicated dual-phase setup will be necessary, especially at low energies. They are mandatory to set the energy scale of WIMP-like signals and that of background, utilizing S2 signal. In addition, the measurements with dual-phase detectors are required to understand electronic and nuclear recoil backgrounds, as we have seen from the case of anomalous background events in XENON100. To claim a discovery, a robust understanding of backgrounds is mandatory.

The limit from XENON100 data cut out some of the CMSSM parameter space allowed by the initial Large Hadron Collider (LHC) data. Given that both direct dark matter search experiments and collider experiments will have improved results in the near future, it will be surely interesting to see if the results from both sides agree. In the end, it is possible that WIMP dark matter is a false hypothesis. Whether it is true or not, the experimental effort of XENON100 contributed to a better understanding of dark matter, and we will keep continuing the journey to broaden our knowledge about the universe.

Part I

Bibliography

Bibliography

[Aad *et al.*, 2009] G. Aad, E. Abat, B. Abbott, J. Abdallah, A. A. Abdelalim, A. A. Abdesselam, et al. Expected Performance of the ATLAS Experiment - Detector, Trigger and Physics. 2009.

[Aalseth *et al.*, 2008] C. E. Aalseth, P. S. Barbeau, D. G. Cerdeño, J. Colaresi, J. I. Collar, P. de Lurgio, G. Drake, et al. Experimental constraints on a dark matter origin for the DAMA annual modulation effect. *Phys.Rev.Lett.*, 101:251301, 2008.

[Aalseth *et al.*, 2011] C. E. Aalseth, P. S. Barbeau, J. Colaresi, J. I. Collar, J. Diaz Leon, et al. Results from a Search for Light-Mass Dark Matter with a P- type Point Contact Germanium Detector. *Phys. Rev. Lett.*, 106:131301, 2011.

[Ackerman *et al.*, 2011] N. Ackerman, B. Aharmim, D. J. Auty, P. S. Barbeau, K. Barry, et al. Observation of Two-Neutrino Double-Beta Decay in ^{136}Xe with EXO-200. *Phys.Rev.Lett.*, 107:212501, 2011.

[Aglietta *et al.*, 1998] M. Aglietta, B. Alpat, E. D. Alyea, P. Antonioli, G. Badino, et al. Muon "depth-intensity" relation measured by the lvd underground experiment and cosmic-ray muon spectrum at sea level. *Phys. Rev. D*, 58:092005, 1998.

[Agostinelli *et al.*, 2003] S. Agostinelli, J. Allison, K. Amako, J. Apostolakis, H. Araujo, et al. GEANT4: A Simulation Toolkit. *Nucl. Instrum. Meth. Phys. Res., Sect. A*, 506:250–303, 2003.

[Ahmad *et al.*, 1995] I. Ahmad, K. E. Rehm, E. P. Kanter, W. Kutschera, W. R. Phillips, et al. Half-lives of isomeric states in Fe-57 and Kr-83. *Phys.Rev.*, C52:2240–2241, 1995.

[Ahmed *et al.*, 2009] Z. Ahmed, D. S. Akerib, S. Arrenberg, M. J. Attisha, C. N. Bailey, L. Baudis, D. A. Bauer, et al. Search for Weakly Interacting Massive Particles with the First Five-Tower Data from the Cryogenic Dark Matter Search at the Soudan Underground Laboratory. *Phys.Rev.Lett.*, 102:011301, 2009.

[Ahmed *et al.*, 2010] Z. Ahmed, D. S. Akerib, S. Arrenberg, C. N. Bailey, D. Balakishiyeva, L. Baudis, et al. Dark Matter Search Results from the CDMS II Experiment. *Science*, 327:1619–1621, 2010.

[Ahmed *et al.*, 2011] Z. Ahmed, D. S. Akerib, S. Arrenberg, C. N. Bailey, D. Balakishiyeva, L. Baudis, et al. Results from a Low-Energy Analysis of the CDMS II Germanium Data. *Phys.Rev.Lett.*, 106:131302, 2011.

[Akimov *et al.*, 2002] D. Akimov, A. Bewick, D. Davidge, J. Dawson, A.S. Howard, et al. Measurements of scintillation efficiency and pulse shape for low-energy recoils in liquid xenon. *Phys.Lett.*, B524:245–251, 2002.

[Akimov *et al.*, 2012] D. Y. Akimov, H. M. Araujo, E. J. Barnes, V. A. Belov, A. Bewick, et al. WIMP-nucleon cross-section results from the second science run of ZEPLIN-III. *Phys.Lett.*, B709:14–20, 2012.

[Alton *et al.*, 2011] D. Alton, D. Durben, M. Keeter, K. Zehfus, S. Brice, et al. DarkSide-50: A Direct Search for Dark Matter with New Techniques for Reducing Background, 2011.

[Ambrosio *et al.*, 1995] M. Ambrosio, R. Antolini, G. Auriemma, R. Baker, A. Baldini, G. C. Barbarino, B. C. Barish, et al. Vertical muon intensity measured with MACRO at the Gran Sasso Laboratory. *Phys.Rev.*, D52:3793–3802, 1995.

[Angle *et al.*, 2008a] J. Angle, E. Aprile, F. Arneodo, L. Baudis, A. Bernstein, et al. First Results from the XENON10 Dark Matter Experiment at the Gran Sasso National Laboratory. *Phys.Rev.Lett.*, 100:021303, 2008.

[Angle *et al.*, 2008b] J. Angle, E. Aprile, F. Arneodo, L. Baudis, A. Bernstein, et al. Limits on spin-dependent WIMP-nucleon cross-sections from the XENON10 experiment. *Phys.Rev.Lett.*, 101:091301, 2008.

[Angle *et al.*, 2011] J. Angle, E. Aprile, F. Arneodo, L. Baudis, A. Bernstein, et al. A search for light dark matter in XENON10 data. *Phys.Rev.Lett.*, 107:051301, 2011.

[Angloher *et al.*, 2012] G. Angloher, M. Bauer, I. Babykina, A. Bento, C. Bucci, et al. Results from 730 kg days of the CRESST-II Dark Matter search. *Eur. Phys. J*, C72:1971, 2012.

[Aprile and Doke, 2010] E. Aprile and T. Doke. Liquid Xenon Detectors for Particle Physics and Astrophysics. *Rev.Mod.Phys.*, 82:2053–2097, 2010.

[Aprile *et al.*, 1993] E. Aprile, A. Bolotnikov, D. Chen, and R. Mukherjee. W value in liquid krypton. *Phys. Rev. A*, 48:1313–1318, 1993.

[Aprile *et al.*, 2004] E. Aprile, K.-L. Giboni, P. M. Majewski, K. Ni, and M. Yamahista. Proportional Light in a Dual-phase Xenon Chamber. 51(5):1986–1990, 2004.

[Aprile *et al.*, 2005] E. Aprile, K.L. Giboni, P. Majewski, K. Ni, M. Yamashita, et al. Scintillation response of liquid xenon to low energy nuclear recoils. *Phys.Rev.*, D72:072006, 2005.

[Aprile *et al.*, 2006] E. Aprile, C. E. Dahl, L. de Viveiros, R. J. Gaitskell, K. L. Giboni, J. Kwong, K. Ni, T. Shutt, and M. Yamashita. Simultaneous Measurement of Ionization and Scintillation from Nuclear Recoils in Liquid Xenon as Target for a Dark Matter Experiment. *Phys. Rev. Lett.*, 97:081302, 2006.

[Aprile *et al.*, 2007a] E. Aprile, A. E. Bolotnikov, A. I. Bolozdynya, and T. Doke. *Noble gas detectors.* John Wiley & Sons, 2007.

[Aprile *et al.*, 2007b] E. Aprile, K. L. Giboni, P. Majewski, K. Ni, and M. Yamashita. Observation of anticorrelation between scintillation and ionization for mev gamma rays in liquid xenon. *Phys. Rev. B*, 76:014115, 2007.

[Aprile *et al.*, 2009] E. Aprile, L. Baudis, B. Choi, K. L. Giboni, K. E. Lim, et al. New Measurement of the Relative Scintillation Efficiency of Xenon Nuclear Recoils Below 10 keV. *Phys.Rev.*, C79:045807, 2009.

[Aprile *et al.*, 2010] E. Aprile, K. Arisaka, F. Arneodo, A. Askin, L. Baudis, et al. First Dark Matter Results from the XENON100 Experiment. *Phys. Rev. Lett.*, 105:131302, 2010.

[Aprile *et al.*, 2011a] E. Aprile, J. Angle, F. Arneodo, L. Baudis, A. Bernstein, et al. Design and Performance of the XENON10 Dark Matter Experiment. *Astropart.Phys.*, 34:679–698, 2011.

[Aprile *et al.*, 2011b] E. Aprile, K. Arisaka, F. Arneodo, A. Askin, L. Baudis, et al. Dark Matter Results from 100 Live Days of XENON100 Data. *Phys.Rev.Lett.*, 107:131302, 2011.

[Aprile *et al.*, 2011c] E. Aprile, K. Arisaka, F. Arneodo, A. Askin, L. Baudis, et al. Likelihood Approach to the First Dark Matter Results from XENON100. *Phys. Rev.*, D84:052003, 2011.

[Aprile *et al.*, 2011d] E. Aprile, K. Arisaka, F. Arneodo, A. Askin, L. Baudis, et al. Material screening and selection for XENON100. *Astropart.Phys.*, 35:43–49, 2011.

[Aprile *et al.*, 2011e] E. Aprile, K. Arisaka, F. Arneodo, A. Askin, L. Baudis, et al. Study of the electromagnetic background in the XENON100 experiment. *Phys.Rev.*, D83:082001, 2011.

[Aprile *et al.*, 2012a] E. Aprile, M. Alfonsi, K. Arisaka, F. Arneodo, C. Balan, L. Baudis, B. Bauermeister, et al. Dark Matter Results from 225 Live Days of XENON100 Data. *Phys.Rev.Lett.*, 109:181301, 2012.

[Aprile *et al.*, 2012b] E. Aprile, M. Alfonsi, K. Arisaka, F. Arneodo, C. Balan, L. Baudis, et al. Analysis of the XENON100 Dark Matter Search Data. 2012.

[Aprile *et al.*, 2012c] E. Aprile, K. Arisaka, F. Arneodo, A. Askin, L. Baudis, et al. The XENON100 Dark Matter Experiment. *Astropart.Phys.*, 35:573–590, 2012.

[Aprile *et al.*, 2012d] E. Aprile, M. Beck, K. Bokeloh, R. Budnik, B. Choi, et al. Measurement of the Quantum Efficiency of Hamamatsu R8520 Photomultipliers at Liquid Xenon Temperature. *JINST*, 7:P10005, 2012.

[Aprile *et al.*, 2012e] E. Aprile, R. Budnik, B. Choi, H. A. Contreras, K. L. Giboni, L. W. Goetzke, J. E. Koglin, R. F. Lang, K. E. Lim, A. J. Melgarejo Fernandez, R. Persiani, G. Plante, and A. Rizzo. Measurement of the Scintillation Yield of Low-Energy Electrons in Liquid Xenon. *Phys.Rev.*, D86:112004, 2012.

[Aprile, 2012] E. Aprile. The XENON1T Experiment at LNGS. Proceedings of UCLA DM 2012 (to be published), 2012.

[Armengaud *et al.*, 2011] E. Armengaud, C. Augier, A. Benoit, L. Berge, J. Blumer, A. Broniatowski, et al. Final results of the EDELWEISS-II WIMP search using a 4-kg array of cryogenic germanium detectors with interleaved electrodes. *Phys.Lett.*, B702:329–335, 2011.

[Armengaud *et al.*, 2012] E. Armengaud, C. Augier, A. Benoit, L. Berge, J. Blumer, A. Broniatowski, et al. A search for low-mass WIMPs with EDELWEISS-II heat-and-ionization detectors. *Phys.Rev.*, D86:051701, 2012.

[Arneodo *et al.*, 2000] F. Arneodo, B. Baibusinov, A. Badertscher, P. Benetti, Elisa Bernardini, et al. Scintillation efficiency of nuclear recoil in liquid xenon. *Nucl. Instrum. Meth.*, A449:147–157, 2000.

[Asaf and Steinberger, 1974] U. Asaf and I. T. Steinberger. Photoconductivity and electron transport parameters in liquid and solid xenon. *Phys. Rev. B*, 10:4464–4468, 1974.

[Asztalos *et al.*, 2004] Stephen J. Asztalos, R. F. Bradley, L. Duffy, C. Hagmann, D. Kinion, et al. An Improved RF cavity search for halo axions. *Phys.Rev.*, D69:011101, 2004.

[Asztalos *et al.*, 2010] S. J. Asztalos, R. F. Bradley, L. Duffy, C. Hagmann, D. Kinion, et al. A SQUID-based microwave cavity search for dark-matter axions. *Phys.Rev.Lett.*, 104:041301, 2010.

[Atrazhev *et al.*, 2005] V. M. Atrazhev, A. V. Berezhnov, D. O. Dunikov, I. V. Chernysheva, V. V. Dmitrenko, and G. Kapralova. Electron Transport coefficients in Liquid Xenon, in Dielectric Liquids. *ICDL 2005, 2005 IEEE International Conference on*, pages 329–332, 2005.

[Bakale *et al.*, 1976] G. Bakale, U. Sowada, and W. F. Schmidt. Effect of an Electric Field on Electron At- tachment to Sulfur Hexafluoride, Nitrous Oxide, and Molecular Oxygen in Liquid Argon and Xenon. *J. Phys. Chem.*, 80:2556, 1976.

[Baldini *et al.*, 2005] A. Baldini, C. Bemporad, F. Cei, T. Doke, M. Grassi, et al. Absorption of scintillation light in a 100 l liquid xenon gamma ray detector and expected detector performance. *Nucl.Instrum.Meth.*, A545:753–764, 2005.

[Barabanov *et al.*, 1987a] I. R. Barabanov, V. N. Gavrin, and A. M. Pshukov. Liquid Xenon Scintillation Spectrometer. *Nucl. Instrum. Meth. Phys. Res.*, A254:355–360, 1987.

[Barabanov *et al.*, 1987b] I. R. Barabanov, V. N. Gavrin, and A. M. Pshukov. Liquid Xenon Scintillation Spectrometer. *Nucl. Instrum. Meth. Phys. Res., Sect. A*, 254:355–360, 1987.

[Battesti *et al.*, 2008] R. Battesti, B. Beltran, H. Davoudiasl, M. Kuster, P. Pugnat, et al. Axion searches in the past, at present, and in the near future. *Lect.Notes Phys.*, 741:199–237, 2008.

[Bednyakov *et al.*, 1994] V. A. Bednyakov, H. V. Klapdor-Kleingrothaus, and S. Kovalenko. On SUSY dark matter detection with spinless nuclei. *Phys.Rev.*, D50:7128–7143, 1994.

[Begeman *et al.*, 1991] K. G. Begeman, A. H. Broeils, and R. H. Sanders. Extended rotation curves of spiral galaxies: Dark haloes and modified dynamics. *Mon.Not.Roy.Astron.Soc.*, 249:523, 1991.

[Beger *et al.*, 2005a] M. Beger, M. Coursey, M. Zucker, and J. Chang. ASTAR, Stopping Power and Range Tables for Helium Ions. `http://physics.nist.gov/PhysRefData/Star/Text/ASTAR.html`, 2005a.

[Beger *et al.*, 2005b] M. Beger, M. Coursey, M. Zucker, and J. Chang. ESTAR, Stopping Power and Range Tables for Electrons. `http://physics.nist.gov/PhysRefData/Star/Text/ESTAR.html`, 2005b.

[Beger *et al.*, 2010] M. Beger, J.H. Hubbell, S.M. Seltzer, J. Chang, J.S. Coursey, R. Sukumar, D.S. Zucker, and K. Oslen. XCOM: Photon Cross Section Database. `http://physics.nist.gov/xcom`, 2010.

[Behnke *et al.*, 2012] E. Behnke, J. Behnke, S. J. Brice, D. Broemmelsiek, J. I. Collar, A. Conner, et al. First Dark Matter Search Results from a 4-kg CF_3I Bubble Chamber Operated in a Deep Underground Site. *Phys.Rev.*, D86:052001, 2012.

[Bekenstein, 2004] J. D. Bekenstein. Relativistic gravitation theory for the MOND paradigm. *Phys.Rev.*, D70:083509, 2004.

[Belogurov *et al.*, 1995] S. Belogurov, A. Bolozdynya, D. Churakov, A. Koutchenkov, V. Morgunov, V. Solovov, G. Safronov, and G. Smirnov. High Pressure Gas Scintillation Drift Chamber with Photomultipliers Inside of Working Medium. *1995 IEEE*, 1:519–523, 1995.

[Benetti *et al.*, 2008] P. Benetti, R. Acciarri, F. Adamo, B. Baibussinov, M. Baldo-Ceolin, et al. First results from a Dark Matter search with liquid Argon at 87 K in the Gran Sasso Underground Laboratory. *Astropart.Phys.*, 28:495–507, 2008.

[Beringer *et al.*, 2012] J. Beringer, J. F. Arguin, R. M. Barnett, K. Copic, O. Dahl, D. E. Groom, et al. 2012 Review of Particle Physics. *Phys.Rev.*, D86:010001, 2012.

[Bernabei *et al.*, 2001] R. Bernabei, P. Belli, R. Cerulli, F. Montecchia, A. Incicchitti, et al. Light response of a pure liquid xenon scintillator irradiated with 2.5-MeV neutrons. *Eur.Phys.J.direct*, C3:11, 2001.

[Bernabei *et al.*, 2003] R. Bernabei, P. Belli, F. Cappella, R. Cerulli, F. Montecchia, et al. Dark matter search. *Riv.Nuovo Cim.*, 26N1:1–73, 2003.

[Bernabei *et al.*, 2008] R. Bernabei, P. Belli, F. Cappella, R. Cerulli, C. J. Dai, et al. First results from DAMA/LIBRA and the combined results with DAMA/NaI. *Eur.Phys.J.*, C56:333–355, 2008.

[Bertone, 2010] Gianfranco Bertone. *Particle dark matter: Observations, models and searches.* Cambridge, 2010.

[Boulay, 2012] M. G. Boulay. DEAP-3600 Dark Matter Search at SNOLAB. *J.Phys.Conf.Ser.*, 375:012027, 2012.

[Bradac *et al.*, 2008] M. Bradac, S. W. Allen, T. Treu, H. Ebeling, R. Massey, et al. Revealing the properties of dark matter in the merging cluster MACSJ0025.4-1222. 2008.

[Bradley *et al.*, 2003] R. Bradley, J. Clarke, D. Kinion, L. J. Rosenberg, K. van Bibber, et al. Microwave cavity searches for dark-matter axions. *Rev.Mod.Phys.*, 75:777–817, 2003.

[Brown *et al.*, 2009] M. L. Brown, P. Ade, J. Bock, M. Bowden, G. Cahill, P. G. Castro, et al. Improved measurements of the temperature and polarization of the cosmic microwave background from QUaD. *Astrophys.J.*, 705:978–999, 2009.

[Buchmueller *et al.*, 2012] O. Buchmueller, R. Cavanaugh, A. De Roeck, M. J. Dolan, J. R. Ellis, et al. Higgs and Supersymmetry. *Eur.Phys.J.*, C72:2020, 2012.

[Burles and Tytler, 1998] S. Burles and D. Tytler. Measurements of the deuterium abundance in quasar absorption systems. 1998.

[Burles *et al.*, 1999] S. Burles, K. M. Nollett, and M. S. Turner. Big bang nucleosynthesis: Linking inner space and outer space. 1999.

[Chadwick *et al.*, 2006] M. B. Chadwick, P. Oblozinsky, M. Herman, N. M. Greene, R. D. McKnight, et al. ENDF/B-VII.0: Next Generation Evaluated Nuclear Data Library for Nuclear Science and Technology. *Nuclear Data Sheets*, 107:29313060, 2006.

[Chang *et al.*, 2009] S. Chang, G. D. Kribs, D. Tucker-Smith, and N. Weiner. Inelastic Dark Matter in Light of DAMA/LIBRA. *Phys.Rev.*, D79:043513, 2009.

[Chasman *et al.*, 1968] C. Chasman, K. W. Jones, H. W. Kraner, and Werner Brandt. Band-Gap Effects in the Stopping of Ge-72* Atoms in Germanium. *Phys.Rev.Lett.*, 21:1430–1433, 1968.

[Chepel *et al.*, 2006] V. Chepel, V. Solovov, F. Neves, A. Pereira, P. J. Mendes, et al. Scintillation efficiency of liquid xenon for nuclear recoils with the energy down to 5-keV. *Astropart.Phys.*, 26:58–63, 2006.

[Choi, 2012] Bin Choi. *The Light Response of the XENON100 Time Projection Chamber and the Measurements of the Optical Parameters with the Xenon Scintillation Light*. PhD thesis, Columbia Univeristy, 2012.

[Choong *et al.*, 2008] W.-S. Choong, K. M. Vetter, W. W Moses, G. Hull, S. A. Payne, N. J. Cherepy, and J. D. Valentine. Design of a Facility for Measurnig Scintillator Non-proportionality. *IEEE Trans. Nucl. Sci.*, 55:1753, 2008.

[Chwolson, 1924] O. Chwolson. Über eine mögliche Form fiktiver Doppelsterne. *Astronomische Nachrichten*, 221:329–330, 1924.

[Clowe *et al.*, 2004] D. Clowe, A. Gonzalez, and M. Markevitch. Weak lensing mass reconstruction of the interacting cluster 1E0657-558: Direct evidence for the existence of dark matter. *Astrophys.J.*, 604:596–603, 2004.

[Clowe *et al.*, 2006] D. Clowe, M. Bradac, A. H. Gonzalez, M. Markevitch, S. W. Randall, et al. A direct empirical proof of the existence of dark matter. *Astrophys.J.*, 648:L109–L113, 2006.

[Conti *et al.*, 2003] E. Conti, R. DeVoe, G. Gratta, T. Koffas, S. Waldman, J. Wodin, D. Akimov, G. Bower, M. Breidenbach, and others. Correlated fluctuations between luminescence and ionization in liquid xenon. *Phys. Rev.*, B68:054201, 2003.

[Dahl, 2009] Carl Eric Dahl. *The Phyiscs of Background Discrimination in Liquid Xenon, and First Results from XENON10 in the Hunt for WIMP Dark Matter.* PhD thesis, Princeton Univeristy, 2009.

[Diaferio *et al.*, 2008] A. Diaferio, S. Schindler, and K. Dolag. Clusters of galaxies: setting the stage. 2008.

[Dodelson, 2003] Scott Dodelson. Modern cosmology. 2003.

[Dodelson, 2011] S. Dodelson. The Real Problem with MOND. *Int.J.Mod.Phys.*, D20:2749–2753, 2011.

[Doke and Masuda, 1999] T. Doke and K. Masuda. Present status of liquid rare gas scintillation detectors and their new application to gamma-ray calorimeters. *Nucl.Instrum.Meth.*, A420:62–80, 1999.

[Doke *et al.*, 1988] T. Doke, H.J. Crawford, A. Hitachi, J. Kikuchi, P.J. Lindstrom, K. Masuda, E. Shibamura, and T. Takahashi. LET Dependence of Scintillation Yields in Liquid Argon. *Nucl. Instrum. Methods Phys. Res., Sect. A*, 269:291, 1988.

[Doke *et al.*, 2002] T. Doke, A. Hitachi, J. Kikuchi, K. Masuda, H. Okada, and E. Shibamura. Absolute Scintillation Yields in Liquid Argon and Xenon for Various Particles. *Jpn. J. Appl. Phys.*, 41:1538, 2002.

[Drees and Nojiri, 1993] M. Drees and M. Nojiri. Neutralino - nucleon scattering revisited. *Phys.Rev.*, D48:3483–3501, 1993.

[Drukier and Stodolsky, 1984] A. Drukier and L. Stodolsky. Principles and Applications of a Neutral Current Detector for Neutrino Physics and Astronomy. *Phys.Rev.*, D30:2295, 1984.

[Du *et al.*, 2004] X. Du, K. Bailey, Z.-T. Lu, Mueller, P., O'Connor, T.P., and L. Young. An atom trap system for practical ^{81}Kr-dating. *Rev. Sci. Instrum.*, 75:3224, 2004.

[Dunkley *et al.*, 2009] J. Dunkley, E. Komatsu, M. R. Nolta, D. N. Spergel, D. Larson, G. Hinshaw, et al. Five-Year Wilkinson Microwave Anisotropy Probe (WMAP) Observations: Likelihoods and Parameters from the WMAP data. *Astrophys.J.Suppl.*, 180:306–329, 2009.

[Edwards *et al.*, 2008] B. Edwards, H. M. Araujo, V. Chepel, D. Cline, T. Durkin, et al. Measurement of single electron emission in two-phase xenon. *Astropart.Phys.*, 30:54–57, 2008.

[Einstein, 1936] A. Einstein. Lens-Like Action of a Star by the Deviation of Light in the Gravitational Field. *Science*, 84:506–507, 1936.

[Eisenstein *et al.*, 2005] D. J. Eisenstein, I. Zehavi, D. W. Hogg, R. Scoccimarro, M. R. Blanton, R. C. Nichol, et al. Detection of the baryon acoustic peak in the large-scale correlation function of SDSS luminous red galaxies. *Astrophys.J.*, 633:560–574, 2005.

[Engel, 1991] J. Engel. Nuclear form-factors for the scattering of weakly interacting massive particles. *Phys.Lett.*, B264:114–119, 1991.

[Feldman and Cousins, 1998] G. J. Feldman and R. D. Cousins. A Unified approach to the classical statistical analysis of small signals. *Phys.Rev.*, D57:3873–3889, 1998.

[Felizardo *et al.*, 2012] M. Felizardo, T. A. Girard, T. Morlat, A. C. Fernandes, A. R. Ramos, et al. Final Analysis and Results of the Phase II SIMPLE Dark Matter Search. *Phys.Rev.Lett.*, 108:201302, 2012.

[Fowlie *et al.*, 2012] Andrew Fowlie, Malgorzata Kazana, Kamila Kowalska, Shoaib Munir, Leszek Roszkowski, et al. The CMSSM Favoring New Territories: The Impact of New LHC Limits and a 125 GeV Higgs. 2012.

[Giboni *et al.*, 2011] K. L. Giboni, E. Aprile, B. Choi, T. Haruyama, R. F. Lang, et al. Xenon Recirculation-Purification with a Heat Exchanger. *JINST*, 6:P03002, 2011.

[Goodman and Witten, 1985] M. W. Goodman and E. Witten. Detectability of Certain Dark Matter Candidates. *Phys.Rev.*, D31:3059, 1985.

[Gushchin *et al.*, 1982] E. M. Gushchin, A. A. Kruglov, and I. M. Obodovski. Electron dynamics in condensed argo and xenon. *Sov.Phys.JETP*, 55:4, 1982.

[Hamamatsu Photonics K.K., 2006] Hamamatsu Photonics K.K. *Photomultiplier Tubes: Basics and Applications*. Hamamatsu Photonics K.K., 3rd edition, 2006.

[Helm, 1956] R. H. Helm. Inelastic and Elastic Scattering of 187-Mev Electrons from Selected Even-Even Nuclei. *Phys.Rev.*, 104:1466–1475, 1956.

[Henderson *et al.*, 2008] S. Henderson, J. Monroe, and P. Fisher. The Maximum Patch Method for Directional Dark Matter Detection. *Phys.Rev.*, D78:015020, 2008.

[Hilt and Schmidt, 1994] O. Hilt and W. F. Schmidt. Ionic Mobilities in Liquid Xenon. *IEEE Trans. Dielectr. Electr. Insul.*, 1:648, 1994.

[Hime, 2011] A. Hime. MiniCLEAN Dark Matter Experiment. 2011.

[Hitachi *et al.*, 1983] A. Hitachi, T. Takahashi, N. Funayama, K. Masuda, J. Kikuchi, et al. Effect of ionization density on the time dependence of luminescence from liquid argon and xenon. *Phys.Rev.*, B27:5279–5285, 1983.

[Hitachi, 2005] A. Hitachi. Properties of liquid xenon scintillation for dark matter searches. *Astropart. Phys.*, 24:247–256, 2005.

[Horn *et al.*, 2011] M. Horn, V. A. Belov, D. Y. Akimov, H. M. Araujo, E. J. Barnes, A. A. Burenkov, V. Chepel, A. Currie, et al. Nuclear recoil scintillation and ionisation yields in liquid xenon from ZEPLINIII data. *Phys. Lett.*, B, 2011.

[Hu, 2001] Wayne Hu. CMB Intermediate Guide. `http://background.uchicago.edu/~whu/intermediate/intermediate.html`, 2001.

[Huang and Freeman, 1978] S. S.-S. Huang and G. R. Freeman. Electron Mobilities in Gaseous, Critical, and Liquid Xenon: Density, Electric Field, and Temperature Effects: Quasilocalization. *J. Chem. Phys.*, 68:1355, 1978.

[Hubbell *et al.*, 1994] J. H. Hubbell, P. N. Trehan, N. Singh, B. Chand, D. Mehta, M. L. Garg, R. R. Garg, S. Singh, and S. Puri. A Review, Bibliography, and Tabulation of K, L, and Higher Atomic Shell XRay Fluorescence Yields. *J. Phys. Chem. Ref. Data*, 23:339, 1994.

[Ishida *et al.*, 1997] N. Ishida, M. Chen, T. Doke, K. Hasuike, A. Hitachi, et al. Attenuation length measurements of scintillation light in liquid rare gases and their mixtures using an improved reflection suppresser. *Nucl. Instrum. Meth. Phys. Res., Sect. A*, 384:380, 1997.

[Jarosik *et al.*, 2011] N. Jarosik, C. L. Bennett, J. Dunkley, B. Gold, M. R. Greason, et al. Seven-Year Wilkinson Microwave Anisotropy Probe (WMAP) Observations: Sky Maps, Systematic Errors, and Basic Results. *Astrophys.J.Suppl.*, 192:14, 2011.

[Jones and Kraner, 1975] K. W. Jones and H. W. Kraner. Energy lost to ionization by 254-eV Ge-73 atoms stopping in Ge. *Phys.Rev.*, A11:1347–1353, 1975.

[Jones and Kunhardt, 1995] H. M. Jones and E. E. Kunhardt. Development of pulsed dielectric breakdown in liquids. *J. of Phys. D: Appl. Phys.*, 28:178, 1995.

[Jortner *et al.*, 1965] J. Jortner, L. Meyer, S. A. Rice, and E. G. Wilson. Localized excitations in condensed ne, ar, kr, and xe. *J. Chem. Phys.*, 42:4250, 1965.

[Jungman *et al.*, 1996] G. Jungman, M. Kamionkowski, and K. Griest. Supersymmetric dark matter. *Phys.Rept.*, 267:195–373, 1996.

[Kastens *et al.*, 2009] L. W. Kastens, S. B. Cahn, A. Manzur, and D. N. McKinsey. Calibration of a Liquid Xenon Detector with Kr-83m. *Phys.Rev.*, C80:045809, 2009.

[Kibedi *et al.*, 2008] T. Kibedi, T. W. Burrows, M. B. Trzhaskovskayac, P. M. Davidsona, and C. W. Nestor Jr. Evaluation of theoretical conversion coefficients using Brlcc. *Nucl. Instrum. Meth.*, A589:202–229, 2008.

[Kish, 2011] Alexander Kish. *Dark Matter Search with the XENON100 Experiment.* PhD thesis, University of Zurich, 2011.

[Knoll, 2000] Glenn F. Knoll. *Radiation detection and measurement.* 2000. 3rd ed.

[Kolb and Turner, 1988] E. W. Kolb and M. S. Turner. *The early universe.* Frontiers in Physics, 1988.

[Komatsu *et al.*, 2011] E. Komatsu, K. M. Smith, J. Dunkley, C. L. Bennett, B. Gold, et al. Seven-Year Wilkinson Microwave Anisotropy Probe (WMAP) Observations: Cosmological Interpretation. *Astrophys.J.Suppl.*, 192:18, 2011.

[Kowalski *et al.*, 2008] M. Kowalski, D. Rubin, G. Aldering, R. J. Agostinho, A. Amadon, R. Amanullah, et al. Improved Cosmological Constraints from New, Old and Combined Supernova Datasets. *Astrophys.J.*, 686:749–778, 2008.

[Kubota *et al.*, 1978a] S. Kubota, M. Hishida, and J. Ruan. Evidence for a triplet state of the self-trapped exciton states in liquid argon, krypton and xenon. *J. Phys. C*, 11:2645, 1978.

[Kubota *et al.*, 1978b] S. Kubota, A. Nakamoto, T. Takahashi, T. Hamada, E. Shibamura, M. Miyajima, K Masuda, and T. Doke. Recombination luminescence in liquid argon and in liquid xenon. *Phys. Rev. B*, 17:2762, 1978.

[Kubota *et al.*, 1979] S. Kubota, M. Hishida, M. Suzuki, and J. Ruan(Gen). Dynamical behavior of free electrons in the recombination process in liquid argon, krypton, and xenon. *Phys. Rev. B*, 20:3486–3496, 1979.

[Larson *et al.*, 2011] D. Larson, J. Dunkley, G. Hinshaw, E. Komatsu, M. R. Nolta, et al. Seven-Year Wilkinson Microwave Anisotropy Probe (WMAP) Observations: Power Spectra and WMAP-Derived Parameters. *Astrophys.J.Suppl.*, 192:16, 2011.

[Lee *et al.*, 2007] H. S. Lee, H. C. Bhang, J. H. Choi, H. Dao, I. S. Hahn, M. J. Hwang, et al. Limits on WIMP-nucleon cross section with CsI(Tl) crystal detectors. *Phys.Rev.Lett.*, 99:091301, 2007.

[Lewin and Smith, 1996] J. D. Lewin and P. F. Smith. Review of mathematics, numerical factors, and corrections for dark matter experiments based on elastic nuclear recoil. *Astropart.Phys.*, 6:87–112, 1996.

[Lindhard *et al.*, 1963] J. Lindhard, M. Nielsen, M. Scharff, and P. V. Thomsen. Integral Equations Governing Radiation Effects. *Mat. Fys. Medd. Dan. Vid. Selsk.*, 33:1–42, 1963.

[Lippincott *et al.*, 2008] W. H. Lippincott, K. J. Coakley, D. Gastler, A. Hime, E. Kearns, et al. Scintillation time dependence and pulse shape discrimination in liquid argon. *Phys.Rev.*, C78:035801, 2008.

[Manalaysay *et al.*, 2010] A. Manalaysay, T. Marrodan Undagoitia, A. Askin, L. Baudis, A. Behrens, et al. Spatially uniform calibration of a liquid xenon detector at low energies using 83m-Kr. *Rev.Sci.Instrum.*, 81:073303, 2010.

[Manzur *et al.*, 2010] A. Manzur, A. Curioni, L. Kastens, D. N. McKinsey, K. Ni, and T. Wongjirad. Scintillation efficiency and ionization yield of liquid xenon for mono-energetic nuclear recoils down to 4 keV. *Phys. Rev.*, C81:025808, 2010.

[Marchionni *et al.*, 2010] A. Marchionni, C. Amsler, A. Badertscher, V. Boccone, A. Bueno, and others. ArDM: a ton-scale LAr detector for direct Dark Matter searches. 2010.

[Matarrese *et al.*, 2011] S. Matarrese, M. Colpi, V. Gorini, and U. Moschella. *Dark matter and dark energy.* Springer, 2011.

[McKinsey *et al.*, 2010] D. N. McKinsey, D. Akerib, S. Bedikian, A. Bernstein, A. Bolozdynya, A. Bradley, et al. The LUX Dark Matter Search. *J.Phys.Conf.Ser.*, 203:012026, 2010.

[Mei *et al.*, 2008] D.-M. Mei, Z.-B. Yin, L.C. Stonehill, and A. Hime. A Model of Nuclear Recoil Scintillation Efficiency in Noble Liquids. *Astropart.Phys.*, 30:12–17, 2008.

[Mei, 2011] Yuan Mei. *Direct Dark Matter Search with the XENON100 Experiment.* PhD thesis, Rice University, 2011.

[Melia, 2007] Fulvio Melia. *The galactic supermassive black hole.* Princeton University Press, 2007.

[Messous, 1995] Y. Messous. Calibration of a Ge crystal with nuclear recoils for the development of a dark matter detector. *Astropart.Phys.*, 3:361–366, 1995.

[Miyajima *et al.*, 1974] M. Miyajima, T. Takahashi, S. Konno, T. Hamada, S. Kubota, H. Shibamura, and T. Doke. Average energy expended per ion pair in liquid argon. *Phys. Rev. A*, 9:1438–1443, 1974.

[Miyajima *et al.*, 1993] M. Miyajima, S. Sasaki, and H. Tawara. Numbers of scintillation photons produced in NaI(Tl) and plastic scintillator by gamma-rays. *IEEE Trans. Nucl. Sci.*, 40:417–423, 1993.

[Mozumder, 1995] A. Mozumder. Free-ion yield and electron-ion recombination rate in liquid xenon. *Chem.Phys.Lett.*, 245:359–363, 1995.

[Nakamura, 2010] K. Nakamura. Review of particle physics, 22. Dark Matter (2012 edition). *J.Phys.G*, G37:075021, 2010.

[Obodovskii and Ospanov, 1994] I. M. Obodovskii and K. T. Ospanov. Scintillation output of liquid xenon for low-energy γ-quanta. *Instrum. Exp. Tech*, 37:42, 1994.

[Ozone, 2005] Kenji Ozone. *Liquid Xenon Scintillation Detector for the New* $\mu \rightarrow e\gamma$ *Search Experiment*. PhD thesis, University of Tokyo, 2005.

[Pack *et al.*, 1992] J. L. Pack, R. E. Voshall, A.V. Phelps, and L. E. Kline. Longitudinal Electron Diffusion Coefficients in Gases: Noble Gases. *J. Appl. Phys.*, 71:5363, 1992.

[Peccei and Quinn, 1977] R. D. Peccei and H. R. Quinn. CP Conservation in the Presence of Instantons. *Phys.Rev.Lett.*, 38:1440–1443, 1977.

[Peebles *et al.*, 1991] P. J. E. Peebles, D. N. Schramm, E. L. Turner, and R. G. Kron. The Case for the hot big bang cosmology. *Nature*, 352:769–776, 1991.

[Peiffer *et al.*, 2008] P. Peiffer, T. Pollmann, Stefan Schonert, A. Smolnikov, and S. Vasiliev. Pulse shape analysis of scintillation signals from pure and xenon-doped liquid argon for radioactive background identification. *JINST*, 3:P08007, 2008.

[Penzias and Wilson, 1965] A. A. Penzias and R. W. Wilson. A Measurement of excess antenna temperature at 4080-Mc/s. *Astrophys.J.*, 142:419–421, 1965.

[Percival *et al.*, 2010] W. J. Percival, B. A. Reid, N. A. Eisenstein, Daniel J. B., T. Budavari, et al. Baryon Acoustic Oscillations in the Sloan Digital Sky Survey Data Release 7 Galaxy Sample. *Mon.Not.Roy.Astron.Soc.*, 401:2148–2168, 2010.

[Plante *et al.*, 2011] G. Plante, E. Aprile, R. Budnik, B. Choi, K.-L. Giboni, et al. New Measurement of the Scintillation Efficiency of Low-Energy Nuclear Recoils in Liquid Xenon. *Phys.Rev.*, C84:045805, 2011.

[Plante, 2012] Guillaume Plante. *The XENON100 Dark Matter Experiment: Design, Construction, Calibration and 2010 Search Results with Improved Measurement of the Scintillation Response of Liquid Xenon to Low-Energy Nuclear Recoils*. PhD thesis, Columbia Univeristy, 2012.

[Profumo and Sigurdson, 2007] S. Profumo and K. Sigurdson. The Shadow of Dark Matter. *Phys.Rev.*, D75:023521, 2007.

[Reichardt *et al.*, 2009] C. L. Reichardt, P. A. R. Ade, J. J. Bock, J. R. Bond, J. A. Brevik, et al. High resolution CMB power spectrum from the complete ACBAR data set. *Astrophys.J.*, 694:1200–1219, 2009.

[Rentzepis and Douglas, 1981] P. M. Rentzepis and D. C. Douglas. The Case for the hot big bang cosmology. *Nature*, 293:165, 1981.

[Riess *et al.*, 2009] A. G. Riess, L. Macri, S. Casertano, M. Sosey, H. Lampeitl, et al. A Redetermination of the Hubble Constant with the Hubble Space Telescope from a Differential Distance Ladder. *Astrophys.J.*, 699:539–563, 2009.

[Riess *et al.*, 2011] A. G. Riess, L. Macri, S. Casertano, H. Lampeitl, H. C. Ferguson, et al. A 3 % Solution: Determination of the Hubble Constant with the Hubble Space Telescope and Wide Field Camera 3. *Astrophys.J.*, 730:119, 2011.

[Rooney and Valentine, 1996] B. D. Rooney and J. D. Valentine. Benchmarking the Compton Coincidence Technique for Measuring Electron Response Non-Proportionality in Inorganic Scintillators. *IEEE Trans. Nucl. Sci*, 43(3):1271–1276, 1996.

[Ruby *et al.*, 1963] S. L. Ruby, Y. Hazoni, and M. Pasternak. Lifetimes of the Low-Energy $M1$ Transitions in La^{137} and Kr^{83}. *Phys. Rev.*, 129:826–828, 1963.

[Savage *et al.*, 2009] C. Savage, G. Gelmini, P. Gondolo, and K. Freese. Compatibility of DAMA/LIBRA dark matter detection with other searches. *JCAP*, 0904:010, 2009.

[Schmidt, 2001] W. F. Schmidt. The basic properties of liquid xenon as related to its application in radiation detectors. pages 1–16, 2001.

[Schwentner *et al.*, 1985] N. Schwentner, E.-E. Koch, and J. Jortner. *Electronic Excitations in Condensed Rare Gases*. Springer Tracts in Modern Physics, 1985.

[Scott and Smoot, 2011] D. Scott and G. F. Smoot. Cosmic Microwave Background. `http://pdg.lbl.gov/2011/reviews/rpp2011-rev-cosmic-microwave-background.pdf`, 2011.

[Seguinot *et al.*, 1992] J. Seguinot, T. Ypsilantis, G. Passardi, and J. Tischhauser. Liquid xenon ionization and scintillation: Studies for a totally active vector electromagnetic calorimeter. *Nucl.Instrum.Meth.*, A323:583–600, 1992.

[Sekiya, 2011] H. Sekiya. XMASS. *J.Phys.Conf.Ser.*, 308:012011, 2011.

[Shibata *et al.*, 2008] M. Shibata, T. Arai, A. Fukuda, H. Funahashi, T. Haseyama, S. Ikeda, K. Imai, Y. Isozumi, T. Kato, and Y. Kido. Practical Design for Improving the Sensitivity to Search for Dark Matter Axions with Rydberg Atoms. *J. Low Temp. Phys*, 151(3):1043, 2008.

[Sigurdson *et al.*, 2004] K. Sigurdson, M. Doran, A. Kurylov, R. R. Caldwell, and M. Kamionkowski. Dark-matter electric and magnetic dipole moments. *Phys.Rev.*, D70:083501, 2004.

[Sikivie, 1983] P. Sikivie. Experimental Tests of the Invisible Axion. *Phys.Rev.Lett.*, 51:1415, 1983.

[Silva *et al.*, 2010] C. Silva, J. Pinto da Cunha, A. Pereira, V. Chepel, M. I. Lopes, et al. Reflectance of Polytetrafluoroethylene (PTFE) for Xenon Scintillation Light. *J. Appl. Phys.*, 107:064902, 2010.

[Smith *et al.*, 2007] M. C. Smith, G. R. Ruchti, A. Helmi, R. F. G. Wyse, J. P. Fulbright, et al. The RAVE Survey: Constraining the Local Galactic Escape Speed. *Mon.Not.Roy.Astron.Soc.*, 379:755–772, 2007.

[Smoot *et al.*, 1992] G. F. Smoot, C. L. Bennett, A. Kogut, E. L. Wright, J. Aymon, et al. Structure in the COBE differential microwave radiometer first year maps. *Astrophys.J.*, 396:L1–L5, 1992.

[Sofue and Rubin, 2001] Y. Sofue and V. Rubin. Rotation curves of spiral galaxies. *Ann.Rev.Astron.Astrophys.*, 39:137–174, 2001.

[Solovov *et al.*, 2004] V. N. Solovov, V. Chepel, M. I. Lopes, and A. Hitachi. Measurement of the refractive index and attenuation length of liquid xenon for its scintillation light. *Nucl.Instrum.Meth.*, A516:462–474, 2004.

[Sorensen and Dahl, 2011] P. Sorensen and C. E. Dahl. Nuclear recoil energy scale in liquid xenon with application to the direct detection of dark matter. *Phys.Rev.*, D83:063501, 2011.

[Sorensen *et al.*, 2009] P. Sorensen, A. Manzur, C. E. Dahl, J. Angle, E. Aprile, et al. The scintillation and ionization yield of liquid xenon for nuclear recoils. *Nucl.Instrum.Meth.*, A601:339–346, 2009.

[Strege *et al.*, 2012] C. Strege, G. Bertone, D. G. Cerdeno, M. Fornasa, R. Ruiz de Austri, et al. Updated global fits of the cMSSM including the latest LHC SUSY and Higgs searches and XENON100 data. *JCAP*, 1203:030, 2012.

[Szydagis *et al.*, 2011] M. Szydagis, N. Barry, K. Kazkaz, J. Mock, D. Stolp, M. Sweany, M. Tripathi, et al. NEST: a comprehensive model for scintillation yield in liquid xenon. *JINST*, 6:10002, 2011.

[Takahashi *et al.*, 1975] T. Takahashi, S. Konno, T. Hamada, M. Miyajima, S. Kubota, et al. Average energy expended per ion pair in liquid xenon. *Phys.Rev.*, A12:1771–1775, 1975.

[Thomas and Imel, 1987] J. Thomas and D. A. Imel. Recombination of electron-ion pairs in liquid argon and liquid xenon. *Phys.Rev.*, A36:614–616, 1987.

[Tremaine and Gunn, 1979] S. Tremaine and J. E. Gunn. Dynamical Role of Light Neutral Leptons in Cosmology. *Phys.Rev.Lett.*, 42:407–410, 1979.

[Valentine and Rooney, 1994] J. D. Valentine and B. D. Rooney. Design of a compton spectrometer experiment for studying scintillator nonlinearity and intrinsic energy resolution. *Nucl. Instrum. Meth.*, A353:37–40, 1994.

[Wasserman, 1986] I. Wasserman. POSSIBILITY OF DETECTING HEAVY NEUTRAL FERMIONS IN THE GALAXY. *Phys.Rev.*, D33:2071–2078, 1986.

[Weinberg, 1978] S. Weinberg. A New Light Boson? *Phys.Rev.Lett.*, 40:223–226, 1978.

[Wilczek, 1978] F. Wilczek. Problem of Strong p and t Invariance in the Presence of Instantons. *Phys.Rev.Lett.*, 40:279–282, 1978.

[Yamashita *et al.*, 2004] M. Yamashita, T. Doke, K. Kawasaki, J. Kikuchi, and S. Suzuki. Scintillation response of liquid xe surrounded by ptfe reflector for gamma rays. *Nucl. Instrum. Meth. Phys. Res., Sect. A*, 535(3):692–698, 2004.

[Yellin, 2002] S. Yellin. Finding an upper limit in the presence of unknown background. *Phys.Rev.*, D66:032005, 2002.

[Ziegler, 2011] J. Ziegler. SRIM, The Stopping Power and Range of Ions in Matter. `http://www.srim.org/`, 2011.

[Zwicky, 1933] F. Zwicky. Spectral displacement of extra galactic nebulae. *Helv.Phys.Acta*, 6:110–127, 1933.